

# THÈSE

Présentée pour l'obtention du titre de :

DOCTEUR de L'UNIVERSITÉ DE LORRAINE

Spécialité: Sciences de matériaux

Par :

**William Chamorro Coral**

---

## Microstructure, chemistry and optical properties in ZnO and ZnO-Au nanocomposite thin films grown by DC- reactive magnetron co-sputtering

---

Thèse soutenue publiquement le 9 Décembre 2014 à Nancy

**Membres du jury :**

Mme Caroline BONAFOS	Directrice de recherche CNRS, CEMES (Toulouse)	Rapporteur
M. Klaus ELLMER	Chercheur, Helmholtz Zentrum für Materialien und Energy (Berlin)	Rapporteur
M. David HORWAT	Maître de Conférences, IJL, Université de Lorraine (Nancy)	Directeur de thèse
M. Frank MÜCKLICH	Professeur, Lehrstuhl für Funktionswerkstoffe, Universität Des Saarlandes (Saarbrücken)	Co-Directeur de thèse
M. Christian MOTZ	Professeur, Lehrstuhl für Experimentelle Methodik der Werkstoffwissenschaften, Universität Des Saarlandes (Saarbrücken)	Examineur
M. Aotmane En NACIRI	Professeur, LCP-A2MC, Université de lorraine (Metz)	Examineur
M. Magnus ODEN	Professeur, IFM, Linköpings universitet (Linköping)	Examineur
Mme Aline ROUGIER	Directrice de recherches CNRS, ICMCB (Bordeaux)	Examineur

*Institut Jean Lamour – UMR 7198- Département CP2S – Equipe 202  
Parc de Saurupt - CS 50840- 54011 NANCY Cedex*

*Université de Lorraine – Pôle M4 : matière, matériaux, métallurgie, mécanique*

*Institut Jean Lamour –UMR 7198- Département CP2S – Equipe 202  
Parc de Saurupt - CS 50840- 54011 NANCY Cedex*

*Université de Lorraine – Pôle M4 : matière, matériaux, métallurgie, mécanique*

---

# **Microstructure, chemistry and optical properties in ZnO and ZnO-Au nanocomposite thin films grown by DC-reactive magnetron co-sputtering**

---

DISSERTATION

zur Erlangung des  
des Doktorgrades der Ingenieurwissenschaften  
der Naturwissenschaftlich-Technischen Fakultät III  
Chemie, Pharmazie, Bio- und Werkstoffwissenschaften  
der Universität des Saarlandes



UNIVERSITÄT  
DES  
SAARLANDES

von

William Chamorro Coral

Nancy (Frankreich) in 9. Dezember 2014

Tag des Kolloquiums: 9. December 2014

Dekan: Prof. Dr. Dirk Bähre

-Berichterstatter: Prof. Dr. Frank MÜCKLICH Professor, Lehrstuhl für Funktionswerkstoffe, Universität Des Saarlandes (Saarbrücken)  
Prof. Dr. Christian MOTZ Professor, Lehrstuhl für Experimentelle Methodik der Werkstoffwissenschaften, Universität Des Saarlandes (Saarbrücken)  
Prof. Dr. David HORWAT Professor, Maître de Conférences, IJL, Université de Lorraine (Nancy)

-Vorsitz: Dr. Aline ROUGIER Directrice de recherches CNRS, ICMCB (Bordeaux)

-Mitglieder des Prüfungsausschusses: Dr. Caroline BONAFOS Directrice de recherche CNRS, CEMES (Toulouse)  
Dr. Klaus ELLMER HZB-Helmoltz Zentrum für Materialien und Energie (Berlin)  
Prof. Dr. Aotmane En NACIRI Professeur, LCP-A2MC, Université de lorraine (Metz)  
Prof. Dr. Magnus ODEN Professor, IFM, Linköpings universitet (Linköping)

# Content

Content.....	1
Acknowledgements.....	5
Résumé étendu.....	7
General Introduction.....	12
1. Generalities on ZnO, Au and ZnO-Au nanocomposites .....	15
1.1. Properties of ZnO .....	15
1.1.1. Structure and vibrational modes .....	16
1.1.2. Bandgap energy.....	19
1.1.3. ZnO thin films growth .....	23
1.2. Properties of Gold.....	24
1.2.1. General considerations .....	24
1.2.2. Gold nanoparticles.....	25
1.2.2.1. Localized surface plasmon resonance.....	27
1.3. Oxide/metal nanocomposites .....	31
2. Thin film synthesis and characterization methods .....	34
2.1. The sputtering method.....	36
2.1.1. Plasma spatial regions .....	37
2.1.2. Sputtering interactions .....	39
2.1.3. Total sputtering yield and transport in the gas phase .....	41
2.1.4. Secondary electron emission (SEE).....	42
2.1.5. Magnetron sputtering.....	44
2.1.6. Reactive magnetron sputtering.....	45

---

2.2. Structure zone diagram (SZD) .....	47
2.2.1. Zones description .....	48
2.3. Experimental setup .....	50
2.4. Characterization methods .....	52
2.4.1. X-ray diffraction (XRD) .....	52
2.4.1.1. Bragg-brentano ( $\theta/2\theta$ ) geometry configuration .....	54
2.4.1.2. Pole figure and $\varphi$ scan configurations .....	55
2.4.2. Transmission electron microscopy (TEM) .....	57
2.4.3. Energy dispersive spectroscopy of X-ray (EDSX) .....	60
2.4.4. X-ray photoelectron spectroscopy (XPS) .....	61
2.4.5. Optical transmittance spectroscopy .....	62
2.4.5.1. Absorption coefficient .....	65
2.4.5.2. Tauc plot .....	65
2.4.5.3. Urbach energy .....	66
2.4.6. Ellipsometry .....	67
2.4.7. Photoluminescence spectroscopy .....	69
2.4.8. Raman spectroscopy .....	70
3. ZnO thin films: Synthesis and characterization .....	72
3.1. Elaboration of zinc oxide thin films .....	73
3.2. ZnO crystal growth .....	74
3.2.1. Structure and microstructure .....	75
3.2.2. Composition and defect chemistry .....	83
3.2.3. Oxygen ion bombardment .....	88
3.3. Near absorption edge optical properties .....	91
3.3.1 ZnO Urbach energy .....	92
3.3.2. ZnO bandgap energy .....	96
3.4. Conclusion .....	99

---

---

4. ZnO-Au nanocomposite films .....	101
4.1. Synthesis and characterization .....	101
4.2. Structure and microstructure .....	103
4.2.1. Influences of the Au content and <i>OFR</i> .....	105
4.2.2. Influence of the annealing temperature .....	108
4.3. Au <i>NPs</i> oxidation .....	113
4.3.1. Electron diffraction patterns .....	115
4.3.2. Au <sub>2</sub> O <sub>3</sub> /Au shell/core structure .....	116
4.4. Optical properties of ZnO-Au nanocomposite thin films .....	121
4.4.1. Localized surface plasmon resonance and absorption background .....	121
4.5. Physical properties of ZnO-Au nanocomposite films.....	128
4.5.1. Conductivity .....	128
4.5.2. vibrational properties .....	130
4.5.3. Photoluminescence .....	134
4.6. Conclusion.....	136
General conclusions .....	137
Annexes.....	139
Bibliography.....	149
Abstract .....	165
Zusammenfassung .....	166
Résumé.....	167



---

# Acknowledgements

Foremost, I would like to express my sincere gratitude to my advisor Mr David Horwat for the continuous support of my Ph.D work and for our discussion, his patience, motivation, enthusiasm and knowledge.

I would like to thank to the members of the jury for agreeing to participate in my PhD defense, specially to Mr Klaus Ellmer from the Helmholtz-Zentrum Berlin für Materialien und Energie (HZB) (Berlin) and Ms Caroline Bonafos, Directrice de recherche CNRS in CEMES (Toulouse) to serve as reviewers.

A very special thanks goes out to Mr Frank Mücklich and Mr Flavio Soldera for their important contribution during my PhD thesis and to all the members of the Department of Materials Science and Engineering of the Universität des Saarlandes.

Special thanks to Mr Jean François Pierson, head of the team 202, of the CP2S at the Institut Jean Lamour (IJL) to offer me the opportunity to be part of his group. Thanks to Mr Philippe Pigeat for the invaluable suggestions in this work.

I must also acknowledge Ms Sylvie Migot and Mr Jaafar Ghanbaja, and Mr Pascal Boulet and Ms Sylvie Robert for their collaboration with the Transmission Electronic Microscopy (TEM) and X-ray diffraction measurements respectively, for the discussions and their indispensable contributions to this work. Also I would like to thank Mr Patrice Miska at the Science faculty in Nancy for his help with Raman and photoluminescence measurements and to Mr Aotmane En Naciri and Mr Yann Battie for their collaboration and their help with the ellipsometry measurements and the very useful discussion. Thanks to Mr Aurélien Renard for his help with the XPS measurements. Thanks to Mr André Mézin for his collaboration with the strain measurements. Appreciation also goes to Ms Christine Gendarme for the training in the SEM and EDSX.

A special mention to Ms Valérie Tamburini, secretary of the 202 team and to Ms Martine Tailleur, Ms Anne-Marie Airault, Ms Christine Sartori, Ms Francine Tedesco, Ms

---

Geraldine Georges for their orientation and collaboration during these three years in the administrative aspect, many thanks to them.

I'd like to thank all the people that I met at the IJL with whom I discussed about academic topics but also with them whom I had the possibility to share more than an academic space. Especially I will mention the people of PVD team that welcomed me with open arms, thanks to David, Alan, Alexis, Nolwenn and Maud and thanks also to their successors, Yong, Manuel, Martin, Aurélien and Emile with whom I share most of my time here in the lab. Special thanks to Yuan who started and finished the PhD as me, thanks to your kindness and friendship. I cannot forget *Le Goûter du Jeudi*, thanks Aurore, Stephanie and all the people that participate with their excellent "contributions", also thanks to them with whom I've shared the *pause café*. Thanks to all the DocMase students for your support, the good experiences and our unforgettable Summer Schools!

I would also like to thank my family for the support they provided me through my entire life and to all my friends around the world that make more enjoyable my time during this thesis. A todos usted, gracias totales!

In conclusion, I recognize that this research would not have been possible without the financial assistance of the European Commission for 'Erasmus Mundus' PhD fellowship within the DocMASE project.

---

# Résumé étendu

## **Microstructure, la chimie et les propriétés optiques de ZnO et ZnO-Au nanocomposites couches minces produites par magnétron DC-réactive co-pulvérisation**

Les matériaux composites sont des mélanges homogènes de deux ou plusieurs éléments de natures et propriétés différentes (mécaniques, optiques, chimiques, etc). Ils offrent la possibilité d'obtenir des propriétés qu'aucun des composants pris individuellement ne présente. Ils comprennent des mélanges de polymères, de céramiques, de métaux, de biomatériaux ou leurs combinaisons. Ils sont principalement utilisés dans le domaine de l'ingénierie pour modifier les propriétés mécaniques telles que la dureté, l'élasticité ou la résistance mécanique, entre autres propriétés.

Les premiers développements des matériaux composites ont débuté à partir de composants macroscopiques (dont un exemple typique est le béton) vers des composants à l'échelle du micron et, finalement, vers des composants dispersés à l'échelle du nanomètre ou de quelques nanomètres. Ces derniers sont appelés nanocomposites. En raison d'effets de confinement et d'effets quantiques qui se produisent à l'échelle nanométrique, ils peuvent présenter de nouvelles propriétés par rapport à celles des composites dont les composants sont dispersés aux échelles macroscopiques et du micron. Parmi les matériaux nanocomposites, les hybrides semi-conducteur/métal sont très intéressants en raison de leurs propriétés catalytiques et opto-électroniques uniques et de la possibilité de les ajuster dans une large gamme. Cependant, pour profiter de ces propriétés, il est nécessaire de comprendre les interactions qui agissent au sein de ces matériaux telles que le comportement des interfaces semi-conducteurs|métal et de les relier aux propriétés fonctionnelles telles que le transport électrique, les mécanismes catalytiques, les propriétés plasmoniques ou l'exaltation de signaux spectroscopiques (Raman, photoluminescence). Ainsi, les matériaux semi-conducteurs à large bande interdite et les films minces nanocomposites métal/oxyde constituent des blocs de construction pour le développement d'une

---

nouvelle génération de dispositifs dans le domaine de la plasmonique, de l'optoélectronique, de la catalyse et de la détection.

Le but de ce travail de recherche de doctorat est de contribuer à une meilleure compréhension du comportement des films minces nanocomposites semi-conducteur/métal par l'étude de la microstructure, de la chimie et des propriétés optiques dans des couches minces ZnO et ZnO-Au nanocomposites élaborées par copulvérisation magnétron réactive continue. Le choix de chaque constituant dans les films nanocomposites a été réalisé en raison de leurs propriétés intéressantes et des avantages particuliers, ce qui conduit à un matériau présentant un potentiel élevé dans de multiples domaines d'applications. Les travaux décrits dans ce manuscrit sont organisés en quatre chapitres et une conclusion générale.

Dans le premier chapitre nous passons, tout d'abord, en revue les principales caractéristiques de l'oxyde de zinc (ZnO) et donnons les procédés d'élaboration de ce matériau. Nous continuons avec une description générale des caractéristiques de l'or en précisant l'influence de la taille de nano-objets d'or sur l'émergence de propriétés catalytiques et de l'effet de résonance plasmon de surface localisée (LSPR). Nous terminons le chapitre par une description des caractéristiques et applications des nanocomposites oxyde/métal comprenant les films nanocomposites ZnO-Au.

Dans le chapitre 2, nous décrivons en détail la méthode de pulvérisation cathodique magnétron réactive, les facteurs les plus importants pour l'élaboration des minces réalisés au cours de cette étude et détaillons certains avantages de cette méthode. Le chapitre se poursuit par une description des méthodes de caractérisation utilisées pour étudier les propriétés structurales, microstructurales, optiques, électriques et chimiques des films minces de ZnO et ZnO-Au synthétisés.

Les films ont été élaborés et caractérisés de façon à obtenir des informations utiles sur les propriétés de la matrice ZnO prise séparément sous forme de films minces et des films nanocomposites ZnO-Au. Par conséquent, dans le chapitre 3, nous décrivons les conditions expérimentales de croissance de ZnO films minces sur des substrats différents en utilisant la technique de pulvérisation cathodique réactive. Nous avons étudié plus particulièrement l'influence des conditions expérimentales sur les propriétés de croissance et les propriétés optiques des couches minces élaborées. Un

---

paramètre expérimental important pendant l'étape de synthèse a été le débit d'oxygène (OFR pour oxygen flow rate). Le chapitre est divisé en deux parties principales. Dans une première partie, nous étudions la possibilité d'obtenir des films minces monocristallins de ZnO épitaxiés sans assistance thermique sur des substrats (0001)-saphir à partir de la pulvérisation cathodique réactive, tandis que dans la deuxième partie de ce chapitre nous décrivons l'évolution de la réponse optique des films en fonction de la nature et du type de défauts ponctuels présents dans différentes conditions de croissance. Il a été possible de montrer que la croissance épitaxiale de films minces de ZnO sur substrats de saphir peut être réalisée sans assistance thermique et pour des supports dont la température auto-établie est proche de la température ambiante. Plus particulièrement, ces conditions nécessitent une croissance lente des films et de contrôler finement le débit d'oxygène (*OFR*) pendant la phase de dépôt de façon à obtenir une teneur élevée d'oxygène dans la phase gazeuse. L'épitaxie est réalisée sur des substrats de saphir orientés (0001) et produit des films minces de ZnO qui croissent selon l'axe *c* de la maille wurtzite. Nous proposons un mécanisme de croissance dans lequel le bombardement des films par des atomes d'oxygène rapides ne se produit qu'au-delà d'un débit critique lorsque la surface de la cible est suffisamment oxydée.

Les films produits avec différentes conditions de synthèse ont été caractérisés par spectroscopie de photoluminescence. Cette technique a permis d'observer un changement dans la chimie des défauts qui évolue depuis une situation où elle est dominée par des défauts de donneurs superficiels dans des conditions riches en zinc vers une situation riche en oxygène où les atomes d'oxygène en position interstitielle dominant. La possibilité de faire varier la chimie de défauts dans les films épitaxiés ouvre des possibilités pour étudier l'influence des défauts ponctuels sur les propriétés des films de ZnO en l'absence de joints de grains.

L'étude des propriétés optiques permet d'améliorer la compréhension de la relation étroite entre les énergies liées au gap d'émission et au gap d'absorption. Les résultats permettent de mieux comprendre la grande dispersion des valeurs de gap rapportées dans la littérature sur les films de ZnO, en proposant un modèle qui tient compte des défauts chimiques majoritaires. Plus particulièrement, a été mise en évidence la nécessité de considérer l'énergie Urbach pour expliquer le comportement optique des films de ZnO présentant une grande densité de défauts ponctuels. Une relation simple

---

qui relie les énergies d'absorption et d'émission a été proposée sur la base de la théorie de l'énergie Urbach impliquant les interactions exciton-phonons et exciton-défauts.

Dans le chapitre 4, nous décrivons la synthèse et la caractérisation de films nanocomposites ZnO-Au obtenus par co-pulvérisation cathodique magnétron réactive continue d'une cible de zinc et d'une cible d'or. Nous avons observé combien les propriétés structurales, microstructurales, optiques et physiques sont influencées par l'incorporation dans une matrice de ZnO, par la teneur en or et par la variation des conditions de synthèse réactive. Dans ce chapitre, nous évaluons les conditions qui permettent d'obtenir des films de nanocomposites qui présentent le phénomène de résonance plasmon de surface localisée (LSPR) par les nanoparticules d'or dans le domaine optique visible. Dans un premier temps nous avons étudié la façon dont l'incorporation d'or dans la matrice de ZnO et la variation de la quantité d'oxygène dans la phase gazeuse pendant la synthèse influencent les propriétés structurales et microstructurales. Une forte diminution de la cristallinité est observée au cours de l'incorporation d'or. Ceci s'accompagne d'une déformation de la maille cristalline de ZnO et d'une évolution de l'état de contrainte avec la teneur en or. Tous les films présentent des contraintes compressives qui tendent à être relaxées avec l'ajout d'or. Ceci peut s'expliquer par la ségrégation spontanée de l'or pour former des nanoparticules plus ductiles que la matrice ZnO et par la présence d'atomes d'or piégés dans la matrice qui déforment sa maille cristalline. La taille caractéristique des particules est proche de 3 nanomètre quelle que soit la teneur en or. Des recuits sous air ont été réalisés qui permettent de mettre en évidence une augmentation de la taille des particules d'or autour de 5 nanomètre et d'une relaxation de la maille cristalline de la matrice vers les dimensions la maille de ZnO wurtzite massive pure. Ceci suggère que les atomes d'or piégés dans la matrice libérés au cours du recuit et viennent alimenter les particules déjà formées.

L'étude a été poursuivie par des analyses chimiques qui indiquent qu'il est possible de former des nanoparticules présentant une structure cœur/coquille avec une coque d'or oxydé en  $\text{Au}_2\text{O}_3$  et un noyau d'or métallique ou des nanoparticules complètement métalliques mais chargées négativement en fonction du comportement de la matrice. Ceci peut s'expliquer par un changement du caractère chimique de la matrice ZnO qui passe d'un caractère réducteur à un caractère oxydant lorsque la chimie des défauts

---

évolue. En effet, dans le chapitre 3 il a été montré que la nature des défauts majoritaires dans ZnO évolue avec les conditions de synthèse. Nous proposons un modèle d'interaction entre les nanoparticules et la matrice dans lequel la présence de défauts donneurs (accepteurs) dans la matrice de ZnO permet réduire (oxyder) les nanoparticules d'or et de modifier les propriétés des deux composants du nanocomposite.

Ces phénomènes s'accompagnent de changements dans les différentes propriétés fonctionnelles évaluées. Nous avons plus particulièrement sondé les propriétés de d'absorption et d'émission optique, les propriétés vibrationnelles et la conductivité électrique des couches formées. L'ensemble des propriétés sont affectées par la microstructure des films soit à l'état brut d'élaboration soit après un recuit dans l'air. Dans une situation où les nanoparticules d'or sont à l'état métallique et sont chargées négativement, une absorption optique se manifeste dans le visible du fait du phénomène de résonance plasmon de surface localisée, les signaux vibrationnels (Raman) et de photoluminescence de la matrice ZnO sont exaltés et les films présentent une conductivité électrique mesurable et qui s'améliore avec l'augmentation de la teneur en or. La présence d'une coquille d'or à la surface des nanoparticules d'or éteint le signal LSPR, réduit l'exaltation des signaux Raman et de photoluminescence et rend les films résistifs.

Ce travail de recherche contribue à la compréhension des mécanismes à l'œuvre dans les films minces ZnO et ZnO-Au et de leur influence sur les propriétés d'usage de ces matériaux. Notamment, une meilleure compréhension de l'interaction à l'interface entre les nanoparticules d'or et la matrice de ZnO a pu être réalisée.

Ce travail pourra, d'une part, servir de base à une meilleure compréhension de l'influence des défauts sur les propriétés optiques de ZnO. D'autre part, il indique des directions de recherche pour le développement d'applications et la maîtrise l'ajustement des propriétés des films minces nanocomposites ZnO-Au films. Cependant, les mécanismes permettant d'expliquer l'exaltation des signaux spectroscopiques Raman et de photoluminescence à l'échelle de particules dans le domaine du nanomètre ne sont toujours pas complètement compris et doivent être étudiés plus en détail.

---

# General Introduction

Composite materials are inhomogeneous mixtures of two or more components of different nature and properties (mechanical, optical, chemical, etc). They offer the possibility to achieve properties that none of the individual components exhibit. They include mixtures of polymers, ceramics, metals or biomaterials and their combination. They are mostly employed in the engineering field to modify mechanical properties as hardness, elasticity or mechanical resistance<sup>1</sup>, among other properties.

The forefront development of composite materials have evolved from macroscopic components (which a typical example is concrete) to micro-scale components and finally to nano-scale components of a few nanometers. The latter are referred as nanocomposites. Nanocomposites can exhibit new properties compared to the bulk state or to macro- and micro-scaled composites of the same components due to confinement and quantum effects occurring at the nano-scale. They are generally composed of a matrix wherein are embedded fibers, particles or sheets of a nanoscale size. They are used for their exceptional performance in optoelectronic devices, biosensors and medical treatments but also in an increasing number of industrial fields pushing the development of new technologies. Among nanocomposite materials, the semiconductor/metal hybrids are highly interesting because of their unique catalytic and optoelectronic properties and the possibility to tune it easily. However, to take advantage of these properties it is necessary to understand the interactions in action such as semiconductor|metal interface interactions<sup>2-10</sup> and to relate them to the electrical transport characteristics, catalytic mechanisms, plasmonic effect or surface enhance Raman effects. After studying the characteristics of ZnO films, this PhD work investigates on the specific interactions and resulting physical properties occurring in ZnO-Au nanocomposite films deposited by reactive magnetron sputtering.

The aim of this PhD research work is to contribute to a better understanding of semiconductor/metal nanocomposites by studying the microstructure, chemistry and optical properties of ZnO and ZnO-Au nanocomposite thin films grown by DC-reactive magnetron co-sputtering. The choice of each component in the nanocomposite films is

---

due to their interesting individual properties and advantages, leading to a material with a high potential in multiple fields of applications.

This manuscript is organized in four chapters and a general conclusion.

In chapter 1 we review the main features of the ZnO structure and give information about its optical behavior and defect chemistry. We describe some of the elaboration methods of ZnO thin films including the magnetron sputtering. We continue with a general description of gold and the influence on the nanometric scale on the gold catalytic properties and on the emergence of the localized surface plasmon resonance (*LSPR*) effect. We end the chapter with a description of oxide/metal nanocomposites including the ZnO-Au nanocomposites and their applications.

In chapter 2 we describe in details the sputtering method, which are the most important factors for thin film elaborations conducted within this study and some of its advantages. Afterwards, we describe the characterization methods used to study the structural, microstructural, optical, electrical and chemical properties of thin ZnO and ZnO-Au films synthesized.

ZnO films were elaborated and characterized to collect useful information on the matrix relevant to the description in chapter 4 of the behavior of ZnO-Au nanocomposite films grown. Therefore, in chapter 3, we describe the experimental conditions to grow ZnO thin films on different substrates by using the reactive sputtering technique and controlling the oxygen flow rate (*OFR*). Then, we investigate the influence of experimental conditions on the growth and optical properties of ZnO thin films. The chapter is divided in two main parts. In a first part we investigate on the possibility to obtain single-domain epitaxial ZnO thin films without thermal assistance on (0001)-sapphire substrates using reactive DC magnetron sputtering. In the second part of the chapter we describe the evolution of the optical response of the grown films and the underlying role of the chemical defects present using different growth conditions on the optical properties.

In chapter 4, we describe the synthesis and characterization of ZnO-Au nanocomposite films grown by reactive DC magnetron co-sputtering. We will observe how deeply are influenced the structural, microstructural, optical and physical properties by the incorporation of gold into ZnO as matrix, by the gold content and the variation of the

---

*OFR* when compared to pure ZnO. In this chapter we evaluate more particularly the conditions to obtain nanocomposite films showing the Au *LSPR* absorption in the visible region. The study continues with chemical analyses that indicate it is possible form nanoparticles with a shell/core structure composed of an Au<sub>2</sub>O<sub>3</sub> shell and Au<sup>0</sup> core. Supported by the results obtained in chapter 3 we propose a mechanism of Au<sub>2</sub>O<sub>3</sub> shell that takes in count the interactions between ZnO and Au. Photoluminescence, electrical conduction and vibrational properties are finally analyzed to the light of the understanding gained on the microstructure and local chemical states in the films.

---

# Chapter 1

## 1. Generalities on ZnO, Au and ZnO-Au nanocomposites

In this chapter, are described the properties of zinc oxide and gold before giving a short literature review on ZnO-Au nanocomposites. The choice of each component in the nanocomposite films is due to their interesting individual properties and advantages, leading to a material with a high potential in multiple fields of applications. ZnO is a semiconductor deeply studied in optoelectronic applications and gold has exceptional optical and chemical properties in the form of particles of sizes below a few tens of nanometers.

### 1.1. Properties of ZnO

ZnO has been used for a long time as powder in the industry for rubber vulcanization, in paints, in the ceramics industry, in agriculture, as excipient or active component in drugs or as a food additive. Its use for other technological applications covers less than 8 % of the total ZnO consumption pointing out it has likely not fully expressed its potential. It has been investigated since the early 20th century with temporal interest in the 1950s and 1970s after the discovery of its piezoelectric properties. Moreover, since the beginning of the 2000s there has been a continuous and increasing interest to investigate ZnO for new applications. According to the research Web of Sciences™ database (see fig 1.13 at the end of this chapter), there has been an explosion of publications containing the word ZnO in the title since the beginning of 2000. ZnO has been studied as nanoparticles, nanowires, thin films, among others, with potential applications as a transparent electrode or luminescent layer in optoelectronic devices

---

such as solar cells, UV light emitting diodes and electrochromic devices. It has also been studied for its catalytic properties.

### 1.1.1. Structure and vibrational modes

ZnO is a II-VI wide bandgap binary semiconductor that can exist in three types of crystal structures: Rock-salt, cubic zinc-blende or hexagonal wurtzite structure. However, the most abundant phase is the hexagonal wurtzite structure. Ab-initio calculations of the cohesive and internal energy of the three crystal structures show that wurtzite is the most stable structure followed by zinc-blende and the rock salt structure explaining the abundance of the wurtzite structure. In the following we describe only this structure generally observed during thin film deposition of ZnO (fig. 1.1).

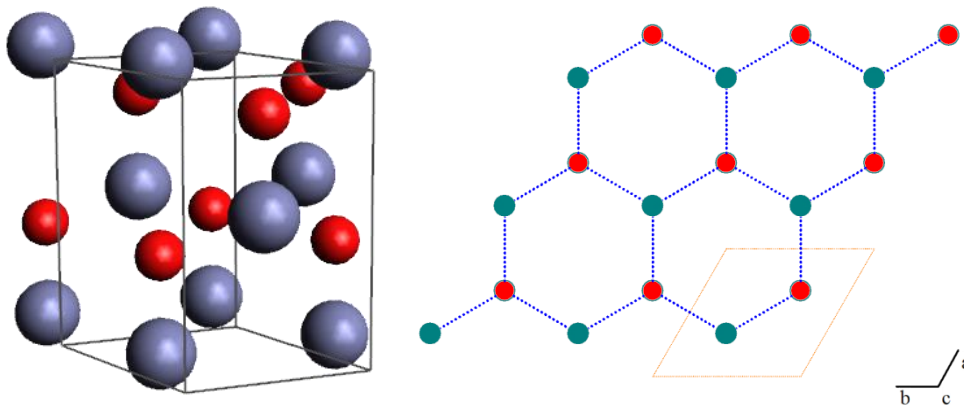


FIG. 1.1. Crystal structure of ZnO wurtzite hexagonal type. (left) side view, (right) top view showing the hexagonal symmetry. Blue and red balls represent Zn and O atoms, respectively.

The ZnO wurtzite structure has a  $C_{6v}^4$  or  $P6_3mc$  space group revealing a 6-fold symmetry and the lattice parameters for bulk ZnO are  $a=b=0.32539$  nm and  $c=0.52042$  nm. However, the lattice parameters can evolve depending on several factors such as the free-electron concentration, doping, presence of point defects, external strains or by variation of the temperature. The structure can be described as two hexagonal

---

interpenetrating networks shifted along the  $c$ -axis with a zinc (oxygen) atom surrounded by four oxygen (zinc) atoms. This tetrahedral conformation is common in materials showing  $sp^3$  hybridization as in diamond whereas in II-VI binary compounds it is related with the hybridization between the  $Zn^{2+}$  cation  $s$  and the  $O^{2-}$  anion  $p$  orbitals.

The wurtzite cell does not exhibit inversion symmetry which induces crystallographic polarity along the  $c$ -axis. The Zn-terminated and the O-terminated polar faces correspond to the  $(000\bar{1})$  and  $(0001)$  crystal planes, respectively. The piezoelectricity, spontaneous polarization as well as growth, etching, formations of defects, optical properties directly depend on, or are affected by the polarity of ZnO.

Knowledge of the vibrational properties of the ZnO crystal lattice is important for understanding in details the optical properties and, more particularly, the photoluminescence properties investigated in chapter 3. From symmetry considerations, the irreducible representation of phonons is expressed as follows:

$$\Gamma = 2A_1 + 2B_1 + 2E_1 + 2E_2 \quad (1.1)$$

The total number of phonons can be calculated as  $3s$ , with  $s$  the number of atoms. As the unitary crystal cell of ZnO contains 4 atoms, a pair for each type of atoms, 12 phonon modes exist among which are acoustic and optical modes. The  $A_1$  and  $B_1$  modes are onefold degenerated while the  $E$  modes are twofold degenerated. Also a set of the  $A_1$  and  $E_1$  modes are acoustic phonons divided in 1 longitudinal acoustic ( $LA$ ) and two transversal acoustic ( $TA$ ) modes. Hence the symmetry of optical phonons can be expressed as:

$$\Gamma_{opt} = 1A_1 + 2B_1 + 1E_1 + 2E_2 \quad (1.2)$$

The phonon modes can be divided in three longitudinal optical ( $LO$ ) and six transversal optical ( $TO$ ) modes. The  $B_1$  modes are Raman and IR inactive (silent modes).

The group theory only considers purely vibrational non-propagating modes. However, experimental results imply propagating optical phonon modes. interacting with the polarity-induced macroscopic electric field, which acts as an additional restoring force for the ion oscillation<sup>11,12</sup>. Consequently, for the  $A_1$  and  $E_1$  polar modes occurs an additional  $LO$ - $TO$  splitting.

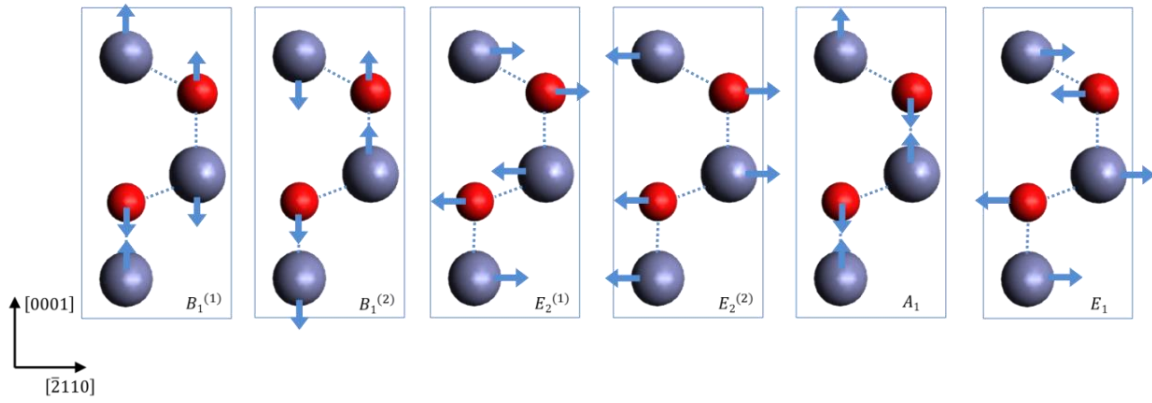


FIG. 1.2. Wurtzite ZnO optical phonon modes. Atoms displacement are indicated by the blue line. Blue and red balls represent Zn and O atoms, respectively.

Table 1.1. Symmetry of Raman active modes for wurtzite ZnO and the frequencies of the lattice vibration modes for and Raman scattering geometries. \*Inactive. Theoretical calculation<sup>13,14</sup>.

Symmetry	Raman shift (cm-1)	Energy (meV)	Scattering configuration <sup>15</sup>
$A_1$ -TO	378-380	46.8- 47.1	$x(yy)x'$
$E_1$ -TO	409-413	50.7- 51.2	$x(zy)x'$ , $x(yz)y$
$A_1$ -LO	574-579	71.2- 71.8	$z(xx)z'$
$E_1$ -LO	583-591	72.3- 73.3	$x(yz)y$
$E_2^{low}$	98-102	12.2- 12.6	$z(xx)z'$ , $x(yy)x'$
$E_2^{high}$	437-438	54.2- 54.3	$z(xx)z'$ , $x(yy)x'$
$B_1^{low}$	261*	32.4	Silent mode
$B_1^{high}$	552*	68.4	Silent mode

During lattice vibration, in the  $A_1$  and  $B_1$  symmetries, the atoms move parallel to the  $c$ -axis, while they move perpendicular to it in the  $E_1$  and  $E_2$  symmetries (see fig. 1.2). Due to this, the detection of each vibrational mode in Raman spectroscopy depends on the

---

geometry of the measurements particularly for highly oriented films. The  $E_2$  modes are non-polar and are only Raman active.

The Raman shift frequencies of active optical phonon modes are listed in Table 1.1.

### 1.1.2. Bandgap energy

Theoretical calculations determining the ZnO band diagram reveal that the valence band maxima and the conduction band minima are localized at the gamma point ( $k=0$ ) of the Brillouin zone, showing that ZnO is a direct-bandgap semiconductor. The band diagram can be described at low energies (near -9 eV) by a group of 10 bands corresponding to the Zn 3d levels, 6 bands between -5 and 0 eV corresponding to the O 2p bonding states and represent the valence band. The conduction band is represented by 2 bands that correspond to delocalized Zn 3s levels (fig. 1.3).

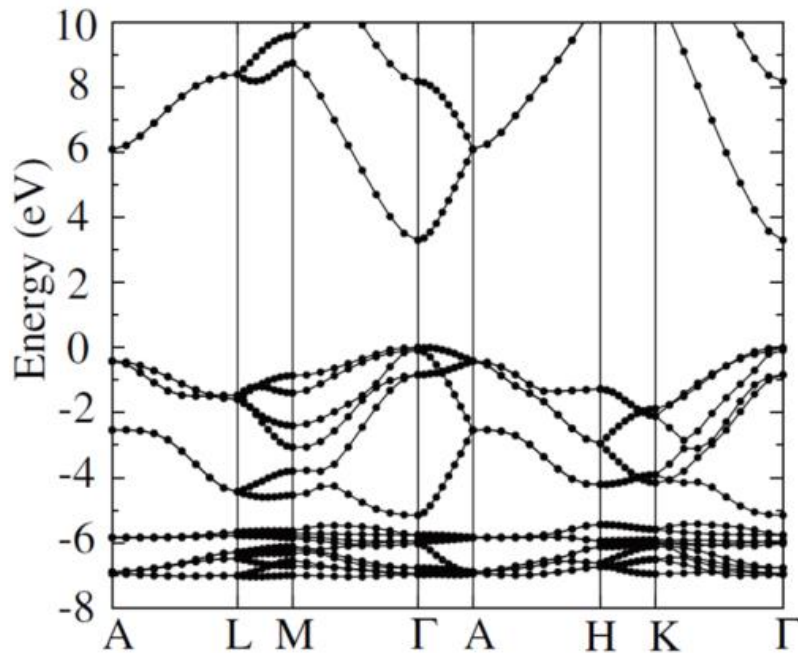


FIG. 1.3 Calculated band structure of ZnO using the HSE hybrid functional in density functional theory. The energy of the valence-band maximum (VBM) was set to zero. From <sup>16</sup>.

Spectroscopic measurements confirmed that ZnO has a direct bandgap transition with a value close to 3.4 eV for bulk ZnO<sup>17</sup>. As the top of the valence band is mainly related with the O 2*p* orbitals that are threefold degenerated into three A, B and C subbands due to crystal-field and spin-orbit interactions<sup>18,19</sup>. The band diagram representation is depicted in fig. 1.4. The A and C valence subbands have a  $\Gamma_7$  symmetry and the B band has a  $\Gamma_9$  symmetry. The energy separation of these three bands referred to the valence band maxima are 0, 4.9 and 43.7-48.6 meV, respectively<sup>20,21</sup>.

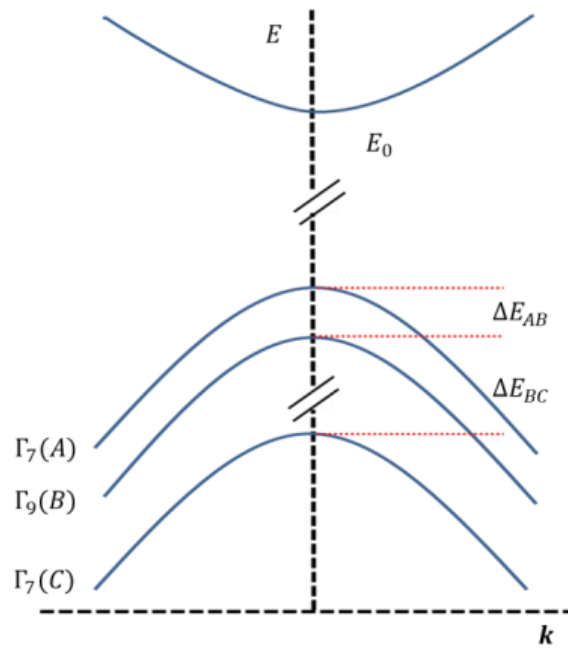


FIG. 1.4. Representation of the conduction and valence band states for ZnO with a direct transition. The valence band is split by into three subbands due to crystal field and spin-orbit interactions. Each subband has a specific symmetry.

In semiconductors the absorption and the emission processes are transitions between the valence and conduction bands in the near absorption edge. For the absorption process, photons with higher energy than the bandgap energy allow electrons to jump from the valence band to the conduction band. It leaves a hole in the valence band. In the emission process, the excited electron relaxes to its ground state, releasing a photon with a lower energy than the absorption energy. The difference in energy between both processes is due to the creation of an electron-hole pair (exciton) that behaves as a neutral quasiparticle in which the charges are coupled by columbic forces and can move

---

together (free exciton) through the crystal carrying energy but not mass. As there are A, B and C valence subbands, A, B and C excitons can be produced. Excitons are classified in Frenkel and Wannier excitons According to the exciton interaction radius<sup>22,23</sup>. The first are mostly found in molecular crystal and the second occur mainly in ionic crystals like ZnO. The larger is the interaction radius the more stable is the exciton, leading to a high exciton binding energy ( $E_{exciton}$ ) If the exciton binding energy is higher than  $k_B T$  the exciton can be detected by photoluminescence measurements at a given temperature,  $E_{exciton}$  in ZnO is close to 60 meV.

The presence of free exciton can therefore be detected at room temperature. In a perfect semiconductor crystal where there is absence of defects, the electronic band structure consist in sharp edges and only allows transitions from localized states in the valence and conduction bands<sup>24,25</sup>. The exciton binding energy corresponds then to the difference between the bandgap energy determined by absorption ( $E_{g(abs)}$ ) and bandgap energy determined by emission ( $E_{g(ems)}$ ). However, the introduction of defects could affects both processes<sup>26-29</sup>.

To access to the value of  $E_{g(abs)}$  it is necessary to obtain the absorption spectrum. For semiconductors, the absorption spectrum is described as the sum of different independent contributions and it could be divided in two main regions<sup>30-35</sup> (fig. 1. 5). At energies higher than  $E_{g(abs)}$  the material can be described by the Tauc relationship:

$$h\nu\alpha = B(h\nu - E_{g(abs)})^{1/2} \quad (1.3)$$

From which it is possible to obtain directly the absorption bandgap energy of the films. At energies below  $E_{g(abs)}$ , the absorption should be equal to zero, but it is possible to detect an absorption tail, the Urbach tail. It follows an exponential behavior:

$$\alpha = \alpha_0 \exp^{((h\nu - E_0)/E_u)} \quad (1.4)$$

Where  $\alpha_0$  and  $E_0$  are constants that depend on the material,  $h\nu$  is the photon energy and  $E_u$  is the Urbach energy.

Unintentional doping with native defects is very common in ZnO films. The native point defects caused by a displacement, removal or substitution of lattice atoms that induce deformation of the ideal structure. Identified native defects are vacancies, interstitials or

antisites (atoms of different natures, here Zn and O, exchanging their lattice positions). In ZnO it is possible to have zinc and oxygen vacancies ( $V_{Zn}$  and  $V_O$ ) both at neutral and ionized states, zinc and oxygen interstitials ( $Zn_i$  and  $O_i$ ) as well as zinc and oxygen antisites ( $Zn_O$  and  $O_{Zn}$ ). Frenkel (cation vacancy and cation interstitial) defects are also possible<sup>21,36</sup>.

The energy of formation of native defects indicates which are stable under given conditions. Theoretical calculations have shown that  $V_O$  and  $Zn_i$  are predominant under Zinc-rich conditions. However, the  $V_O$  has the lower energy of formation. At oxygen-rich conditions,  $V_{Zn}$  shows the lowest energy of formation. Knowledge about the nature of native defects in ZnO is important because its properties are strongly depending on the presence of intrinsic defects such as zinc and oxygen interstitials or vacancies<sup>16,37-40</sup>. The ZnO thin films are favored to generate n-type semiconductors and we can mention that  $p$ -type doping has become a challenge in the last years due to the difficulty to avoid a charge compensation mechanism with native defects.

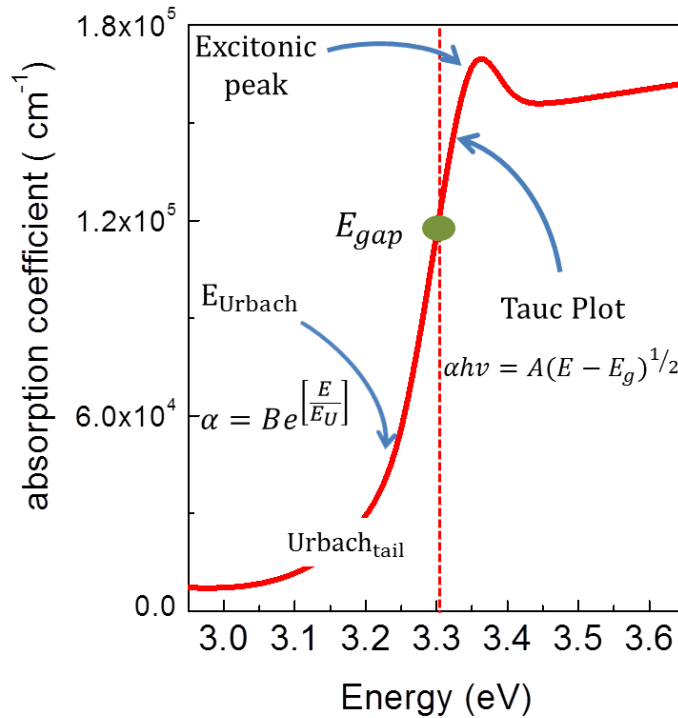


FIG. 1.5. Typical absorption spectrum of a ZnO film. In the near absorption edge, at energies higher than the  $E_{g(abs)}$  the absorption coefficient follows the Tauc relation, below the  $E_{g(abs)}$  it follows an exponential behavior.

---

### 1.1.3. ZnO thin films growth

The synthesis of ZnO is reported for various deposition methods. However, a strong dispersion of the crystal quality, the bandgap energy, the stoichiometry and the defect chemistry is encountered depending on the synthesis conditions.

With chemical methods such as electrodeposition, sol-gel, Chemical Bath Deposition, it is usual to obtain polycrystalline, nanocrystalline or amorphous ZnO films<sup>32,41,42</sup>. As the films are grown in an aqueous medium, it is very difficult to avoid OH<sup>-</sup> and H<sup>+</sup> species that act as active defects in the crystalline structure of ZnO. ZnO synthesized by sol-gel methods could be easily doped and produced in the form of different nanostructures such as nanorods, nanowires, etc at a relatively low temperature (<100 °C)<sup>41-43</sup>. ZnO nanostructures can also be obtained by CVD (chemical vapor deposition) methods. Another interest related to the growth ZnO is the possibility to obtain single crystal oriented films using different methods such as Metal-Organic Vapor Phase Epitaxy (MOVPE)<sup>44</sup>, molecular Beam Epitaxy (MBE)<sup>45</sup> or pulsed laser deposition (PLD)<sup>46,47</sup>. The growth of high quality ZnO epitaxial films generally requires substantial thermal assistance above typically 300°C during growth. Epitaxial ZnO is increasingly demanded as it prevents dangling bonds, charge carriers trapping and scattering at the grain boundaries that influence the electronic and optical properties of polycrystalline ZnO<sup>48,49</sup>.

Magnetron sputtering<sup>50,51</sup> has become a traditional method for the deposition of ZnO films. Films deposited by this method are usually textured along the *c*-axis on different substrates and depositions can be performed in DC, radio frequency (RF), medium frequency (MF) or high-power impulse magnetron sputtering (HIPIMS) modes. It is possible to use a ZnO target in presence of argon with little addition of oxygen or from a zinc metallic target sputtered in a reactive atmosphere, in our case a mixture of Ar and O<sub>2</sub> (see chapter 2, section 2.1). The advantages of using the reactive magnetron sputtering is the possibility to grow ZnO films by adjusting the chemical composition in a large extent<sup>52</sup>.

---

## 1.2. Properties of Gold

### 1.2.1. General considerations

Gold (Au) is a malleable and ductile transition metal of the group 11 in the periodic classification of elements. Its electronic configuration is  $[Xe]4f^{14}5d^{10}6s^1$ . Its crystal structure is face-centered cubic (fcc), with 4 atoms in the unit cell and a coordination number of 12. Most of the annual world demand of Au (4120 tons in 2011) is used in jewelry (48 %) followed by uses as money (41 %), comprising gold bars. Its participation in technology is only of 11 % mostly for electrical contacts in the electronic industry due to its high conductivity and corrosion resistance.

Detailed contribution of the Gold demand is depicted in fig. 1.6. Since the early 1990s, there has been a sustained interest in the use and study of nanometric gold for application in various fields such as medicine, optics and catalysis due to novel or improved properties with reference to bulk gold.

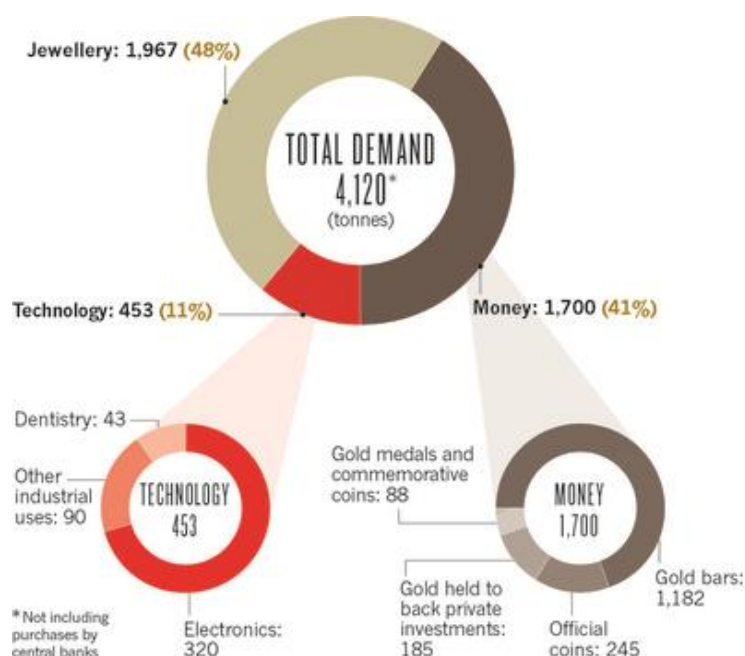


FIG. 1.6. Total world demand of gold in 2011 year showing a demand of 11% for the technology sector<sup>53</sup>.

---

### 1.2.2. Gold nanoparticles

There are several reasons for a different behavior of gold at the nanometric scale. One of it is the modification of the electronic structure. In order to explain its origin, it is necessary to recall some features of the energy band diagram of a metal. The band diagram shows superimposed valence and a conduction bands and each of the energy bands is not continuous but results from the contributions of  $N$ -atoms with  $N$ -energy levels including antibonding (high energy) and bonding (low energy) levels. When the dimensions are decreased to the nanometer scale, the number of atoms decreases dramatically and the separation between energy levels increases (fig. 1.7). The properties of materials being highly sensitive to the electronic structure, they are modified with reference to the bulk phase.

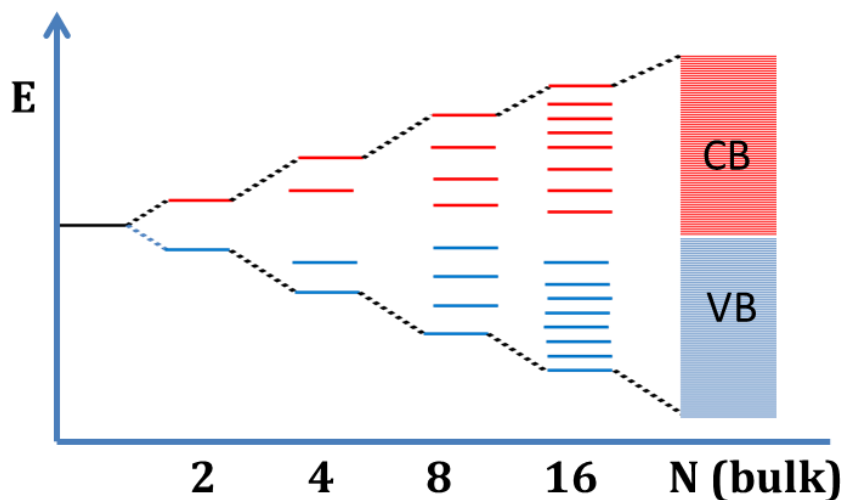


FIG. 1.7. Schematic representation of the band diagram in a metal and its evolution when the number of atoms is decreased to a few atoms per nanoparticle.

A second set of considerations are related to the geometry of nano-objects. First, as the size of nanoparticles ( $NPs$ ) decreases, the fraction of surface atoms increases. This has several consequences: surface atoms vibrate more freely leading to a higher mobility of surface atoms and drop of the melting temperature<sup>54,55</sup>. Moreover, depending on the number of atoms, it is possible to obtain different nanoparticle shapes, as is observed in

fig. 1.8a for the Au series of 10, 18, 20, 24, 38 and 42 atoms. Faceted geometries with a given number of edges, corners or steps and different bond lengths, bond angles or coordination numbers compared to periodic surfaces are thereby obtained (fig. 1.8b shows it in the case of Pt *NPs*). Therefore, the uncompensated bonding forces and coordination number evolve with the position of atoms at the particle surface and the reactivity of surface atoms is different and higher than in the bulk metal<sup>56</sup>.

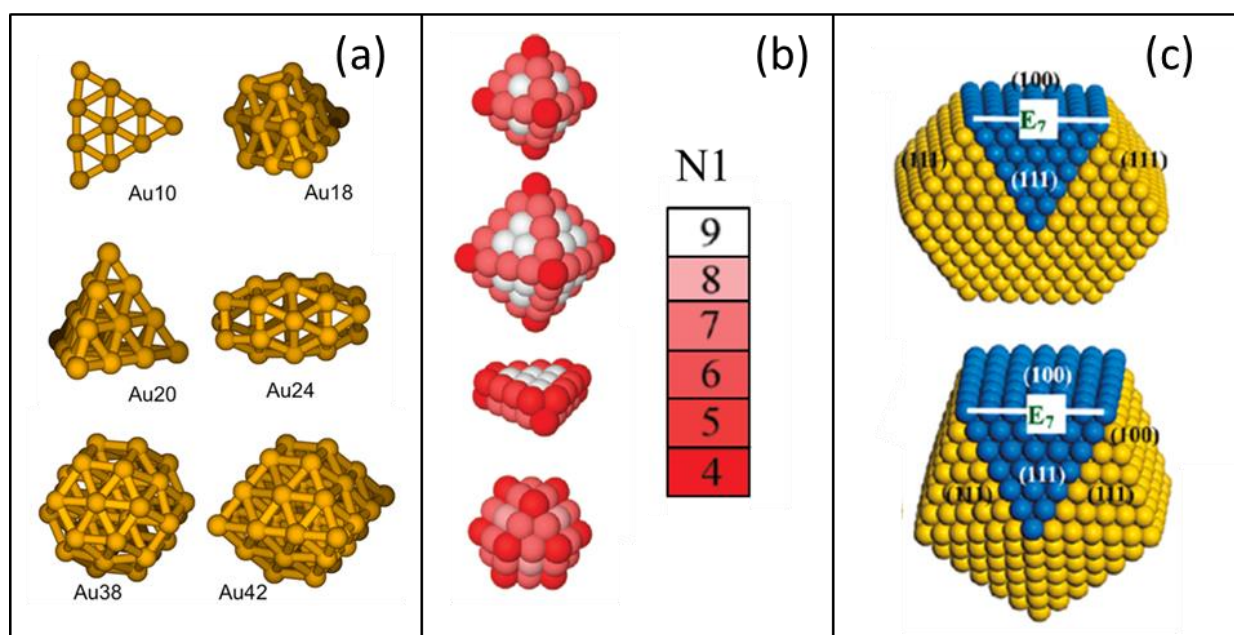


FIG. 1.8. Representation of metallic *NPs* for (a) 10 to 42 Au Atoms and their corresponding geometrical configurations<sup>57</sup>. (b) Pt *NPs* with different number of atoms and shapes, N1 present a color-table indicating the coordination number for each geometrical configuration<sup>55</sup>. (c) Dodecahedral Au<sub>781</sub> and Penta-star Au<sub>932</sub> *NPs* close to 4 nm in diameter<sup>58</sup>.

There are several studies of nanoparticles of a few atoms (nanoclusters) revealing that for cluster between 15 to 19 atoms the atoms in the Au nanocluster are all surface atoms<sup>59</sup>, but this proportion readily decreases with the increase in the size of *NPs*. However, the catalytic activity seems to be enhanced by sites with low coordination numbers only for *NPs* with sizes lower than 1 nm containing around 50 atoms<sup>55,57</sup>. Furthermore, the fraction of sites with low coordination numbers is low in particles with more than 150 atoms (~2 nm) of dodecahedral or penta-star geometries (fig. 1.8c) but the catalytic activity is high. Hence, other mechanisms than site improvement such as

---

the presence of charged Au atoms are involved in the overall catalytic activity of Au *NPs*<sup>58,59</sup>.

Relativistic effects are also considered to affect deeply the shape, catalytic activity<sup>60</sup> as well as chemistry of gold *NPs*<sup>61</sup>. This short overview on some of the effects present in gold *NPs* shows that their behavior is affected by many factors, which influences can be difficult to separate.

### **1.2.2.1. Localized surface plasmon resonance**

Another important consequence of the reduction of the size of gold objects to the nanoscale is the absorption of light at a given wavelength depending on the particle size. Gold is known to be a metal of low reactivity. However, it is possible to obtain gold compounds in highly oxidizing conditions. The most stable oxidation states of gold are  $\text{Au}^{+1}$  and  $\text{Au}^{3+}$ . A well-known recipe to dissolve gold is in an aqueous solution of concentrated  $\text{HNO}_3$  and  $\text{HCl}$  (aqua regia), producing  $\text{Au}^{3+}$  ions in solution. Nitric acid oxidizes the metallic Au and  $\text{HCl}$  forms complex anions as  $\text{AuCl}_4^-$  stabilizing the Au ions and helping to dissolve the Au.

If the  $\text{AuCl}_4^-$  aqueous solution is gently reduced by citric acid, it is possible to obtain colloidal suspensions of metallic Au nanoparticles *NPs*. Gold colloidal suspensions are colored and the obtained color is strongly dependent on the size of the Au (*NPs*). This behavior is absent in the bulk state and the visual result has been applied for centuries. It is at the origin of the color of stained glass in the middle age churches. It is possible to trace its use back to the Roman culture with the famous example of the Lycurgus cup of the IV century. The cup represents an episode from the myth of King Lycurgus who attacked Dionysus. The cup shows this moment when Lycurgus is entrapped by the branches of the vine (metamorphosed nymph Ambrosia), while Dionysus, Pan and a satyr torment him for his evil behaviour<sup>62</sup>. The cup is composed of Silver-Gold alloy *NPs* of a diameter close to 70 nm dispersed in melted silica. When the light is reflected from the surface, the cup shows an opaque Jade color. In contrast, if the light pass through the cup, it absorbs the blue radiation and the transmitted light is red (wine color) (see fig.

---

1.9). Scientific approaches to study the optical behavior of Au *NPs* start with the works of Michael Faraday studying colloidal suspensions.

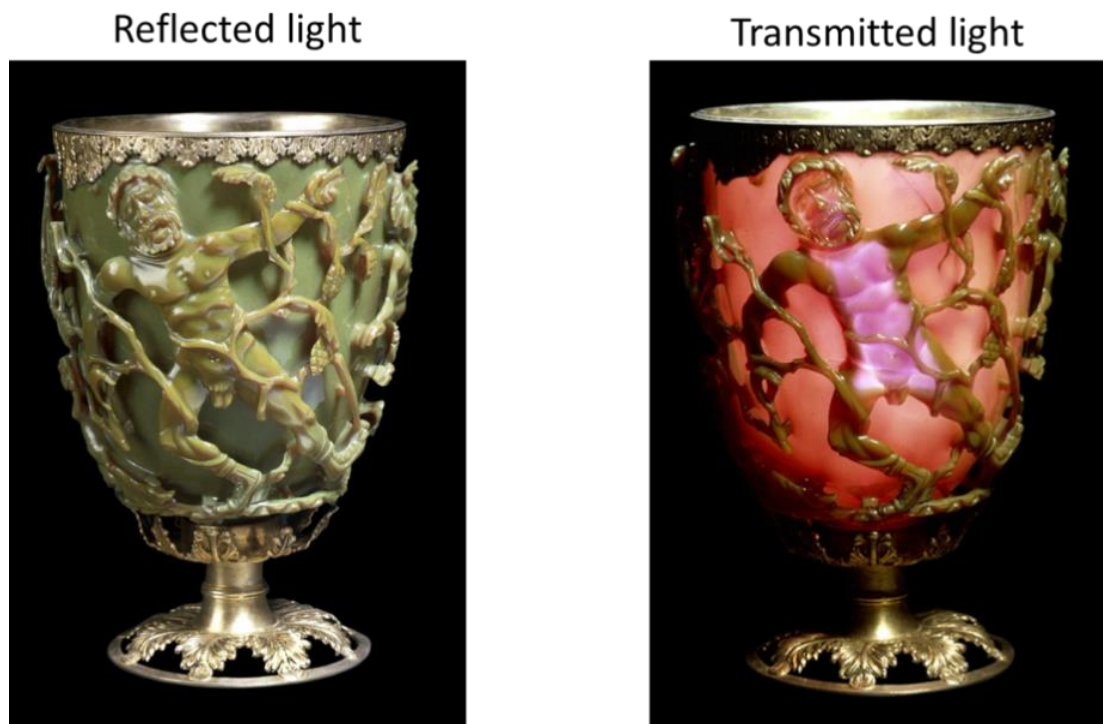


FIG. 1.9. Lycurgus Cup from the Roman era depicting the legend of the Thracian king Lycurgus wrestling with vines. (Left) jade color whit reflected light. (Right) Cup turning to red after the light passes through the cup.

Later on, in the early years of the 20<sup>th</sup> century, Gustav Mie, solved the Maxwell equations for absorption and scattering of electromagnetic radiation by spherical noble metallic nanoparticles in the early years of the 20<sup>th</sup> century<sup>63,64</sup>. He showed that noble metal, as Pd, Ag, and Au, nanoparticles can absorb electromagnetic radiation in the visible region due to the harmonic oscillation of the electrons of the *NP* surface (fig. 1.10). This effect called localized surface plasmon resonance (*LSPR*) occurs upon interaction with an electromagnetic radiation of frequency depending on the metal, the size, the shape of the *NPs* and the dielectric constant of the surrounding medium. The frequency absorbed corresponds to the plasmon frequency of the free electrons in the *NP*.

The Mie approximation can describe the behavior of spherical metallic nanoparticles with only dipole polarization. For *NPs* that are much smaller than the radiation

wavelength (usually  $2r < \lambda/10$ ), it is possible to observe only a dipole polarization mode and the extinction cross section  $\sigma_{\text{ext}}$  can be expressed as:

$$\sigma_{\text{ext}}(\omega) = 9 \frac{\omega}{c} \epsilon_m^{3/2} V \frac{\epsilon_2(\omega)}{[\epsilon_1(\omega) + 2\epsilon_m]^2 + \epsilon_2^2(\omega)} \quad (1.5)$$

With  $\omega$  the angular frequency of the exciting light,  $c$  the speed of light,  $V$  the particle volume.  $\epsilon_m$  is the dielectric function of the embedding medium.  $\epsilon(\omega) = \epsilon_1(\omega) + i\epsilon_2(\omega)$  is the dielectric functions of the absorbing material, in our case of the metal *NPs*, with  $\epsilon_1$  and  $\epsilon_2$  the real and the imaginary parts respectively. When  $\epsilon_1(\omega) = -2\epsilon_m$  the extinction cross section shows its maximum value corresponding to the resonant behavior describing the *LSPR* of a sphere in vacuum.

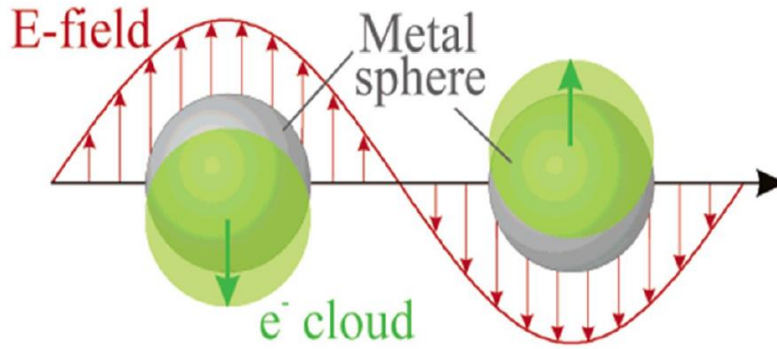


FIG. 1.10. Schematic depiction of the coherent motion of the free electrons in a spherical metallic nanoparticle when excited by an external time dependent electric field fitting the plasmon frequency.

Considering the condition of resonance ( $\epsilon_1(\omega) = -2\epsilon_m$ ) and assuming that the surrounding medium has a dielectric constant distinct to zero ( $\epsilon_m \neq 0$ ), the plasmon resonance frequency can be calculated as<sup>65-68</sup>:

$$\omega = \frac{\omega_p}{\sqrt{1+2\epsilon_m}} \quad (1.6)$$

With  $\omega_p$  the electron plasma frequency in vacuum.

In the Mie approximation neither the shape nor the size of *NPs* is directly considered. For small gold particles (radius  $< 20$  nm) exists mainly a dipole polarization but it is

---

necessary for larger sizes to consider quadrupole or higher polarization modes. Furthermore, different geometrical shapes such as rods, triangles, cubes, etc. produce different polarization modes (fig. 1.11).

The dielectric function of noble metal *NPs* such as silver and gold consists of two contributions accounting for interband contributions (due to the *5d* electrons response) and intraband contribution that take into account the influence of free electron contribution.

In the classical approach, confinement effects appear when the mean free path of conduction electron is limited by the nanoparticle size. Assuming that only the free electrons are affected by the *NPs* size, the dielectric function of metallic *NPs* can be expressed in the following way:

$$\varepsilon(\omega) = \varepsilon_{bulk} - \frac{\omega_p^2}{-\omega^2 + i\omega\Gamma_0} + \frac{\omega_p^2}{-\omega^2 + i\omega\Gamma(R)} \quad (1.7)$$

$\Gamma(R)$ , the damping constant, takes into account the scattering of the electrons at phonons, lattice defects, impurities, etc. Moreover, for metal *NPs* it is possible to take into account size effects related with the electron mean free path. It can be expressed as:

$$\Gamma(R) = \Gamma_0 + A \frac{v_F}{R} \quad (1.8)$$

With  $\varepsilon_{bulk}$ ,  $\omega_p$ ,  $v_f$  and  $\Gamma_0$  the tabulated dielectric function of the bulk, the electron plasmon frequency, the Fermi velocity of free electrons and electron damping parameter, respectively.  $A$  is a parameter that depends on the material and is fixed to 1.  $R$  is the *NP* radius.

Experimentally, the effect of the *NPs* size can be correlated with the variation in the bandwidth of the *LSPR* absorption. It is associated with the dephasing of the coherent electron oscillation (damping). Large bandwidths correspond to rapid loss of the coherence of the electron motion. For metals, the average mean free path is close to 40-50 nm. For *NPs* of sizes below this value, the surface electrons can be easily scattered and the coherence of the electron motion decrease. Decreases in the dephasing time is also observed in *NPs* embedded in a matrix compared to isolated *NPs* and can be represented with a decrease of the damping parameter.

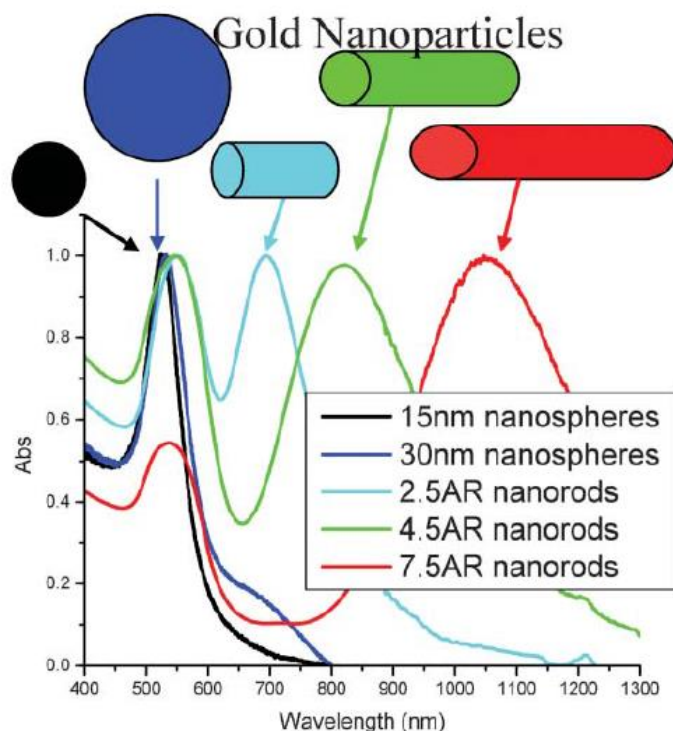


FIG. 1.11. Gold nanoparticles – absorption of various sizes and shapes<sup>69</sup>.

### 1.3. Oxide/metal nanocomposites

To take advantage of the catalytic activity or optical effects of metal *NPs* such as surface enhanced Raman spectroscopy (*SERS*), the *NPs* must be in contact with the reactants or the analyte, respectively. However, this interaction could affect the size, distribution or shape of the *NPs*, changing their properties. Moreover, if a temperature higher than room temperature is needed for the applications, the particles tend to grow by Ostwald ripening, which leads to loss or weakening of the properties of interest. These problems can be solved using a very thin oxide coating to stabilize the morphology of *NPs*. Examples of this approach are sketched in fig. 1.12 for oxide/metal shell-core structure, *NPs* distributed in an oxide surface. This approach also affects the response of the *NPs* due to the oxide|metal interface. For this reasons studying the properties of oxide / metal nanocomposites is a current important in materials science.

---

Oxide/metal nanocomposites are growingly studied due to their high potential in many fields of applications such as optoelectronic and catalytic devices.

Using the database of the Web of Sciences<sup>TM</sup> research platform and looking for publications with ZnO and Au in the title, we observe that the publications are recent, low in number but, effectively, represent a growing research field. There are even fewer publications related to ZnO-Au nanocomposite films (Inset of fig. 1.13) pointing out that most of their characteristics are still poorly understood. This may be explained by the fact that tailoring, and understanding semiconductor/metal nanostructures still remains a challenge. As will be stated in the next paragraphs, ZnO-Au nanocomposite films have a high potential of applications and deserves further investigations.

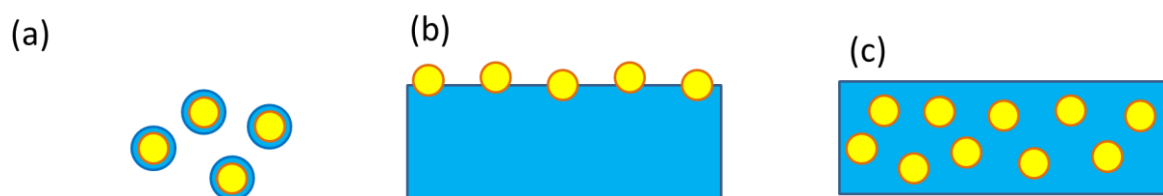


FIG. 1.12. Sketch of possible configurations for semiconducting-metal nanocomposites (a) Core-shell nanostructure, (b) Metal supported on semiconducting surface (Outside structure), (c) metal embedded in a semiconducting matrix (inside structure).

Among methods used to grow ZnO-Au nanocomposites we find electrodeposition, RF-sputtering and pulsed laser deposition<sup>70-74</sup>. To date, the ZnO-Au nanocomposite system has been mostly used for photocatalytic applications. Au *NPs* are used to improve the catalytic performance of ZnO not only in the UV but in the visible region<sup>75,76</sup>. These nanocomposites are mainly elaborated by a wet route because of the ease to produce optimal morphologies for this application. ZnO-Au nanocomposites have been also studied as electrical or optical gas sensing layers, in which reducing gases can transfer electrons through the ZnO matrix leading to charge variations detected by optical measurements of the localized surface plasmon resonance absorption (*LSPR*, see section 1.2.2.1.) or electrical measurements<sup>77-80</sup>.

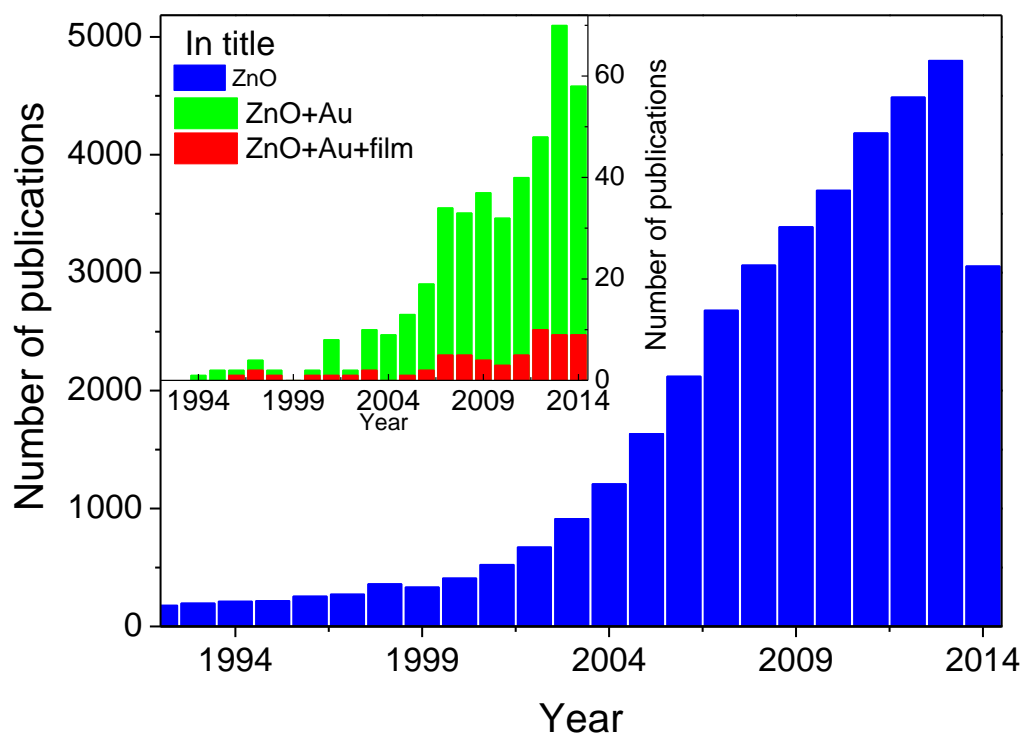


FIG. 1.13. Number of publications returned by the Web of Sciences™ research engine using ZnO in title (blue), Inset: Search in title for ZnO + Au (green) and ZnO + Au + film (red).

Gold contacts of ZnO-Au nanocomposite layers have also been studied. It has been found that the introduction of ZnO in gold electrical contact films influence the hardness without significant loss in the electron conductivity<sup>81-83</sup>. ZnO-Au can also be used in surface enhanced Raman spectroscopy (*SERS*) to enhance the Raman signal of selected molecules. It has been proved that ZnO-Au nanostructures are good *SERS*-active substrates<sup>84,85</sup>.

---

# Chapter 2

## 2. Thin film synthesis and characterization methods

Thin film is a term used to describe layers deposited onto a substrate. There is no accurate definition of “thin” and the film thickness can vary from only a few atomic layers to several micrometers according to the desired properties or applications<sup>86-88</sup>. Compared to bulk materials, a low thickness allows decreasing the amount of materials used while keeping the same properties as the bulk or even leading to better performances. New properties can also appear. In this manuscript the term “thin” is used for films of a few hundreds of nanometers (100-300 nm).

There is a wide variety of methods for the elaboration of thin films and the choice of a specific method depends on the required application. Among the methods existing to synthesize thin films, we can describe each of it according to a few criteria: e.g. whether it is based on chemical or physical processes and if it is operated at atmospheric pressure or in vacuum (high, medium or low). Nevertheless, nowadays several methods are hybrids considering the above-mentioned criteria. Examples of chemical methods in liquid medium to deposit films at atmospheric pressure are chemical bath deposition (CBD), sol-gel or electrodeposition, among others. These are widely used because of their low cost and ease of implementation. However, they are becoming increasingly less popular due to the chemical wastes they can generate and their low compatibility with other deposition methods at industrial scale. Spray-ILGAR (Ion Layer Gas reaction) and spray pyrolysis are also used to produce thin films of good quality via chemical reaction at atmospheric pressure using sprayed dispersed solutions. Among the physical methods to deposit films at atmospheric pressure is the spin coating method, consisting on the spreading of a colloidal suspension of oxides<sup>89,90</sup> or polymers<sup>91,92</sup> onto a substrate while rotating the substrate, by removing the excess of suspension and a posterior solvent evaporation.

---

Advantages of using vacuum methods over deposition at atmospheric pressure or in liquid are multiple such as the possibility to achieve high crystal quality, low impurity contents and, in the case of evaporation, to decrease the evaporation temperature, meaning a save in energy consume. In vacuum methods, the precursors of the films are in vapor phase from introduction of volatile precursors (gases), thermal evaporation, sputtering or laser ablation of a source. Vacuum methods are classified according to the interactions taking place in, or at the origin of, the vapor phase. If chemical reaction occurs in the vapor phase, it belong to the chemical vapor deposition (CVD) methods. In opposite, if no chemical reaction occurs in the vapor phase and the vapor phase is produced by a physical mean, it is related to the physical vapor deposition (PVD) methods<sup>86-88</sup>. CVD methods can be used at atmospheric, low, medium or high vacuum and produce high quality films mostly for the semiconductor industry. One drawback of such methods is the use of highly toxic volatile precursors. Since the discovery of PVD methods, the most used method has been the thermal evaporation of a source using the joule effect or electron beam heating. However, the sputtering method became very competitive in the last decades. More precisely, it became an independent branch of thin film technologies in concurrence with CVD methods and thermal evaporation after intense researches on the sputtering theory in the 1950-60s<sup>93,94</sup>. Sputtering is a plasma gas (usually argon) assisted method based on the bombardment of ions coming from the plasma that impact a target source and eject the atoms from its surface. The sputtered atoms arrive to a substrate where they condense to form the film. We use the sputtering method for several reasons. First, it enables to obtain high quality films and to limit the presence of impurities. Second, it is a relatively easily upscalable process that facilitates the transfer to the industry of results gained at the laboratory scale. There are also other reasons related to its condensation energetics, such as a high associated cooling rate leading to metastable states of interest for certain applications. In this chapter, we describe in details the sputtering method, some of its advantages and which are the most important factors for thin film elaborations conducted within this study and some of its advantages. Afterwards, we describe the characterization methods used to study the structural, microstructural, optical, electrical and chemical properties of thin ZnO and ZnO-Au films synthesized.

---

## 2.1. The sputtering method

In a schematic description, the sputtering method is comparable to a vacuum tube diode as in fig. 2.1. It consists in a chamber at low pressure  $\sim 10^1$  to  $10^{-1}$  Pa of an inert gas atmosphere, generally argon, the source of the material to deposit placed as the cathode and the chamber walls including the substrate-holder as the anode or ground. As the cathode is negatively polarized, the voltage difference between both electrodes could lead to a luminescent discharge due to the ionization of the gas generating plasma.

A DC basic discharge can be divided in three main regimes: dark, glow (luminescent) and arc discharge regimes. We are interested in the glow discharge regime at discharge currents higher than the gas breakdown voltage. This regime is divided in the normal and abnormal regions depending on the discharge current. At low current, in the normal region, the voltage is independent of the discharge current and remains nearly constant. The electrode current density does not change because the plasma does not cover completely the electrode surfaces. As the discharge current increases, the surface coverage of the electrode by the plasma increases up to complete coverage. Increasing the discharge current from this point leads to the abnormal region where the current density, plasma luminous intensity and voltage increase with the discharge current. The discharge then behaves as a normal resistance. The DC sputtering operation occurs in the abnormal discharge region. However, if the discharge current leads to high enough current densities, thermionic electron emission is allowed and the discharge leads transits to an arc discharge characterized by a drop of the discharge voltage.

In the abnormal discharge, a large voltage difference, generally of some hundreds of volts, between the anode and the cathode leads to different effects that enable to ignite and maintain a sputtering plasma. In the argon gas there is a small portion of ionized atoms (around  $10^{-4}$  atoms),  $\text{Ar}^+$  in case of an argon background gas. As the  $\text{Ar}^+$  ions approach the cathode surface it capture an electron by tunnel effect and neutralize as well as stimulate the emission of secondary electrons by potential emission. Those secondary electrons sustain the plasma discharge. The sputtering method is based on a non-linear plasma process since the collision of argon ions and/or electrons with atoms in the gas phase continues the ionization before a self-sustained plasma can be reached.

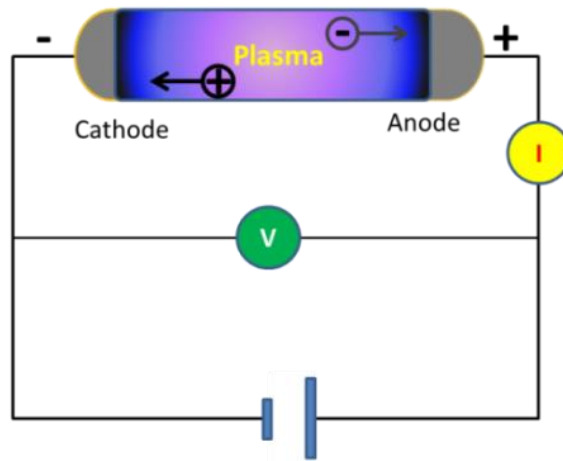


Fig. 2.1. Schematic of a vacuum tube and formation of a glow discharge.

### 2.1.1. Plasma spatial regions

The plasma is a mixture of neutral atoms, positive ions and electrons and is overall neutral with an equal number of electrons and ions (fig. 2.2). However in contact with a surface, plasma sheaths appear.

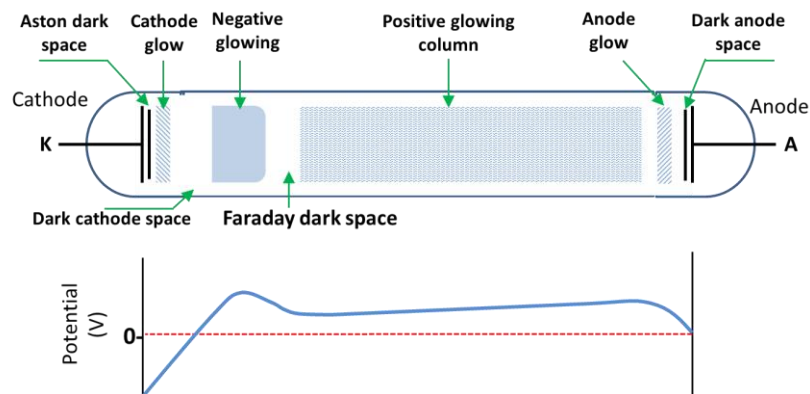


FIG. 2.2. Glow discharge and representation of the voltage profile in the plasma<sup>95</sup>.

A plasma sheath is the localized electric field that separates a plasma from a material boundary<sup>96</sup>. The plasma can be divided in three main regions. Cathode and anode

sheaths and the plasma bulk zone. The cathode sheath, in contact with the target is also called dark space. This sheath is of primary importance to understand the origin of the sputtering process. It is a positively charged zone with a high argon ions density due to the high electron mobility and high voltage drop  $V_{sheath}$ . The sheath thickness can be described by the Child law<sup>97-99</sup>:

$$s(t) = \frac{3}{4} \left[ \frac{\varepsilon_0^2 V_{sheath}^3(t)}{en_0^2(t)kT_e(t)} \right]^{1/4} \quad (2.1)$$

Whit  $\varepsilon_0$  the permittivity of free space,  $e$  the elementary charge,  $k$  the Boltzmann constant,  $n_0$  the plasma density and  $T_e$  the plasma electron temperature.

The sheath thickness is dynamic and depends on the instantaneous plasma density, the electron temperature and sheath voltage (see fig. 2.3). The presence of a sheath leads to a drastic drop in voltage in a narrow spatial zone, generating a strong electric field. In the anode sheath there is also a drop in voltage but less important due to the absence of polarization of the anode. To compensate the sheath voltage drop, the plasma bulk is slightly charged positively to maintain the electroneutrality.

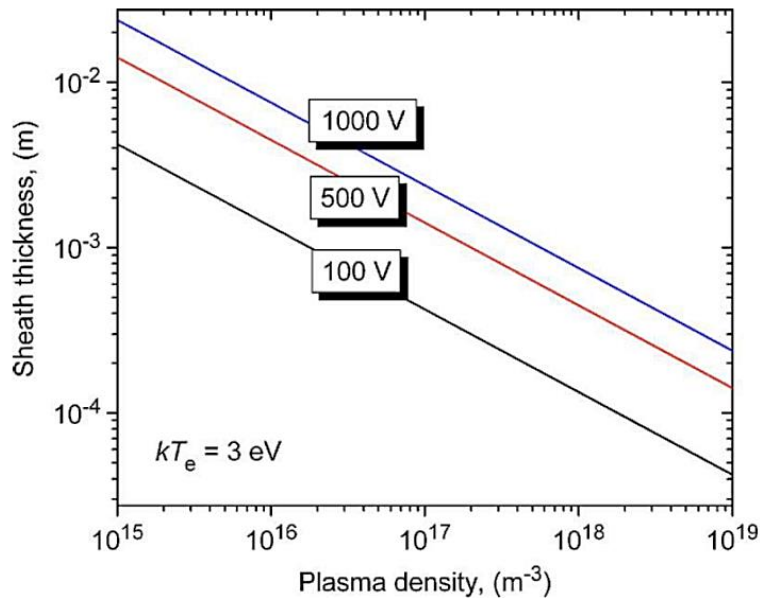
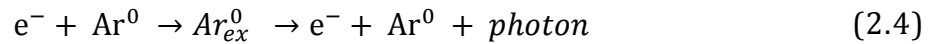


FIG. 2. 3. Child sheath thickness as a function of plasma density, with electron temperature and sheath voltage as parameters<sup>98</sup>.

---

In the cathode sheath, charged particles (electrons or argon ions) are accelerated by the electric field. Argon ions are accelerated toward the target and surface electrons into the bulk plasma region where they may collide with argon atoms. In the bulk plasma region, there are two types of interactions: The first are the elastic interactions that lead to electron scattering (equation (2.2)). The second type of interactions are the inelastic collisions wherein there is a transfer of kinetic energy from the electron to the atom. Inelastic collisions can lead to atom ionization or excitation (equations (2.3) and (2.4)). Atom ionizations produce the electron-ion pair contributing to the plasma generation and sustainment and occur in the cathode sheath region. After argon excitation, there is a decay process to a low energetic level being responsible for the luminescence of the plasma bulk region (equation (2.4)).



### 2.1.2. Sputtering interactions

Energetic argon ions bombard the target surface with a maximal energy proportional to the difference in voltage between the target ( $V_T$ ) and the plasma bulk ( $V_p$ ) and described as:

$$E_{max} \leq Z(V_p - V_T) \quad (2.5)$$

With  $Z$  the ion charge state.

Argon ion bombardment leads to different interactions with the target material as is represented in fig. 2.4 and can be summarized as follow:

- a) When Argon ions hit surface atoms (primary collisions), there is transfer of momentum among the neighboring atoms (secondary collisions) leading to collision cascades and emission of surface atoms (sputtering process).
- b) The arriving argon ions favor the emission of secondary electrons mostly by potential emission at the discharge voltages used for sputter-deposition<sup>98</sup>.

c) Argon ions have a probability to be neutralized by secondary electrons and to be implanted beneath the target surface.

d) Argon ions have a probability (complementary to the process describe in c) to be neutralized by secondary electrons and reflected by the target surface.

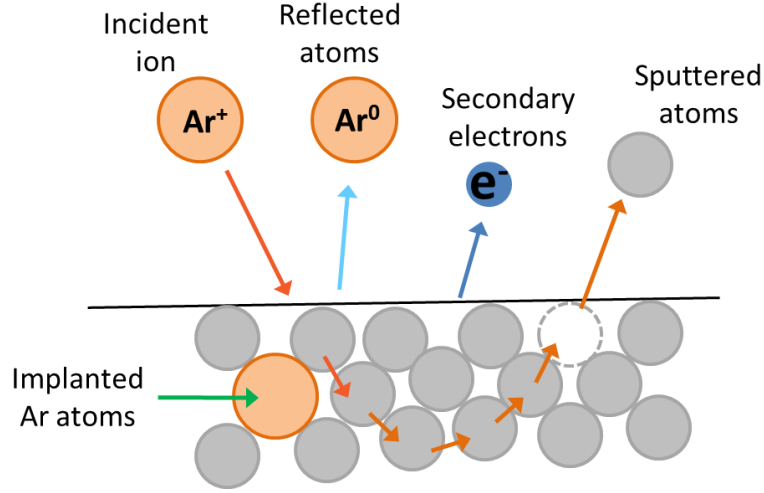


FIG. 2.4. Simplified diagram of interactions after collision of argon ions on the target surface.

Each kind of collision can be described according its energy. Sputtered atoms have an averaged energy of some tens of volts depending on the target material surface binding energy  $E_{sb}$ . The sputtered atoms kinetic energy distribution function can be described by<sup>94,100</sup>:

$$f_a(E) = \frac{cE}{(E + E_{sb})^3} \quad (2.6)$$

With a dependency of  $E^{-2}$  when  $E \gg E_{sb}$  and  $c$  a constant. Positive ions formed in the bulk plasma phase and impinging the target surface have a kinetic energy described by equation (2.5) and the voltage difference in the sheath is given by<sup>100,101</sup>:

$$(V_p - V_f) = \left( \frac{kT_e}{2e} \left( 1 + \ln \left( \frac{m_i}{2\pi m_e} \right) \right) \right) \quad (2.7)$$

With  $m_i$  and  $m_e$  the mass of the ions and electrons, respectively.

---

Reflected particles are mostly neutralized atoms originating from energetic ions formed in the bulk plasma phase. These backscattered particles leave the target surface with a maximum energy  $E_p$  that depends on the mass ratio between target atoms and the impacting ions  $(m_t/m_p)^{100,102}$ :

$$E_p = \left(\frac{A-1}{A+1}\right)^2 E_{p0} \quad (2.8)$$

With  $A=m_t/m_p$  and  $E_{p0}$  the original energy of the impacting ion.

### 2.1.3. Total sputtering yield and transport in the gas phase

The total sputtering yield  $Y$  is defined as the ratio between the number of sputtered atoms  $N_{sp}$  and the number of incident particles  $N_{ip}$  ( $Ar^+$  ions in non-reactive sputtering).

$$Y = \frac{N_{sp}}{N_{ip}} \quad (2.9)$$

This yield expresses the ease to eject an atom from the target surface.

The sputtering process is very complex and depends on the atomic mass and binding energy of the target material, the mass of the gas ions and on interactions such as the nuclear stopping cross section. There have been several empirical equations to describe the complex relation of each factor to the sputtering yield but one of the most accepted and successful description is based on the work of Yamamuha et al<sup>103</sup>. It includes parameters to describe the behavior in the case of heavy and light ions bombardment. This expression is based on the pioneering theoretical works of Sigmund<sup>93,104</sup> valid for heavy and light ions for incident energies below 1 keV. The Sputtering yield can be expressed as:

$$Y = \frac{3}{4\pi^2} \alpha \frac{4M_1M_2}{(M_1+M_2)^2} \frac{E}{U_s} \quad (2.10)$$

With  $E$  the energy of the incident ions,  $M_1$  and  $M_2$  the masses of the incident ion and the target atoms.  $\alpha$  is a dimensionless parameter that depends on the mass ratio and the ion energy and  $U_s$  is the surface binding energy (same as  $E_{sb}$  in Equation 2.5).

---

In the path from the target to the substrate, the sputtered atoms can collide with the gas carrier atoms. According to the elastic-collision theory, the energy transferred at each collision can be expressed as:

$$T_E = E_0 \frac{4M_1M_2}{(M_1+M_2)^2} \cos^2 \frac{\theta_c}{2} \quad (2.11)$$

With  $E_0$  the initial energy,  $M_1$  and  $M_2$  the mass of target and gas atoms, respectively. Head-on collisions ( $\theta_c = 0$ ) correspond to the maximum energy transferred.

Beside the transferred energy, it is important to consider the mean free path to include the energy lost by sputtered atoms, due to collisions with other particles, when they arrive to the substrate surface. According to the kinetic theory, the mean free path  $\lambda$  can be expressed as:

$$\lambda = (n\sigma)^{-1} \quad (2.12)$$

with  $n$  the number of particle targets in a given volume and  $\sigma$  the effective cross section for the collision. For energetic particles that follow a Maxwell distribution (the energy distribution of sputtered atoms tend to be shifted to a Maxwell distribution by collisions with the atoms of the gas phase), it is modified as:

$$\lambda = (\sqrt{2}n\sigma)^{-1} \quad (2.13)$$

Taking into account the expression of  $\sigma$ , we obtain:

$$\lambda = \frac{k_B T}{\sqrt{2}\pi d^2 p} \quad (2.14)$$

Whit  $p$  the pressure and  $d$  the diameter of the sputtered atoms.

#### 2.1.4. Secondary electron emission (SEE)

Bombardment of a material with a primary radiation of highly energetic particles (electrons, ions or photons) leads to the emission of secondary electrons (emitted with a low energy  $< 50$  eV) due to ionization processes. The secondary electron emission (SEE) helps to maintain the plasma discharge.

Secondary electrons are emitted when an electron from the surface neutralizes the impinging ion and a second electron from the surface absorbs the excess energy from neutralization. The energy transferred to the electron can be expressed as:

$$\Delta E \approx (E_{IZ} - E_{\phi}) \quad (2.15)$$

With  $E_{IZ}$  the ion ionization energy of the impinging ion and  $E_{\phi}$  the working function of the target.

The SEE produced by (argon) ions bombarding the cathode is called ion-induced secondary electron emission (*ISEE*). To describe the secondary electron emission process, it is possible to define the emission yield coefficient  $\gamma_{ISEE}$  as the ratio of the number of secondary electrons emitted to the number of ions approaching the surface. For clean metallic surfaces,  $\gamma_{ISEE}$  is lower than 1 and is nearly independent of the ion kinetic energy at voltages below 500 V<sup>105</sup>. However, it depends on the metal electronic properties:

$$\gamma_{ISEE} = A(BE_{IZ} - 2E_{\phi})/E_f \quad (2.16)$$

With  $A$  and  $B$  experimental constants with values close to 0.3 and 1.5, respectively, and  $E_f$  the Fermi energy of the metal<sup>106,107</sup>.

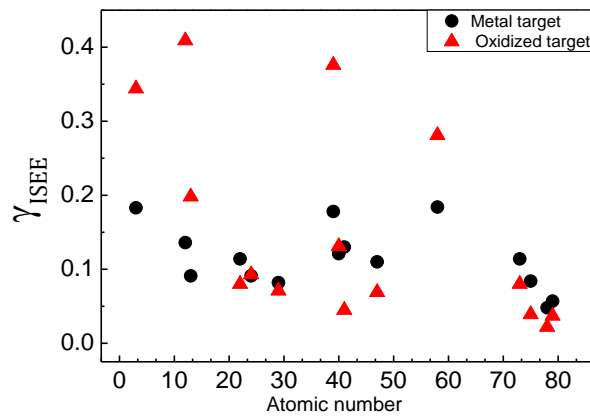


FIG. 2.5. Secondary electron emission for a series of metallic and oxidized targets (adapted from <sup>107</sup>).

When a metal target surface is oxidized, it is expected that  $\gamma_{ISEE}$  increases because most oxides have a lower work function and lower Fermi level than their corresponding metal. However, depending of the properties of the oxide, it is possible that  $\gamma_{ISEE}$

increases, decreases or remain unchanged (see fig. 2.5) with reference to the metallic surface. This is related with the incident bombarding ions and their ease to reduce the surface oxides<sup>108</sup>. For oxides that increase  $\gamma_{ISEE}$ , the measured discharge voltage at a constant current decreases due to decrease of the plasma impedance by injection of supplementary electrons. However, for oxides that are reduced by the ion bombardment the discharge voltage increases<sup>107-109</sup>.

### 2.1.5. Magnetron sputtering

In traditional (diode) sputtering, a self-sustained plasma is held at relatively high pressure, about 1 Pa, that represents a mean free path of few mm, leading to a low film growth rate and poor film quality (low density compared to bulk). To increase the film growth rate, it is necessary to decrease the number of sputtered atoms thermalized by collisions with atoms in the gas phase and/or to increase the sputtering rate. Another important point to consider is that secondary electrons are fundamental for generation and sustainment of the plasma. The magnetron sputtering configuration is well adapted to this challenge as it increases the efficiency of the sputtering process at low pressure.

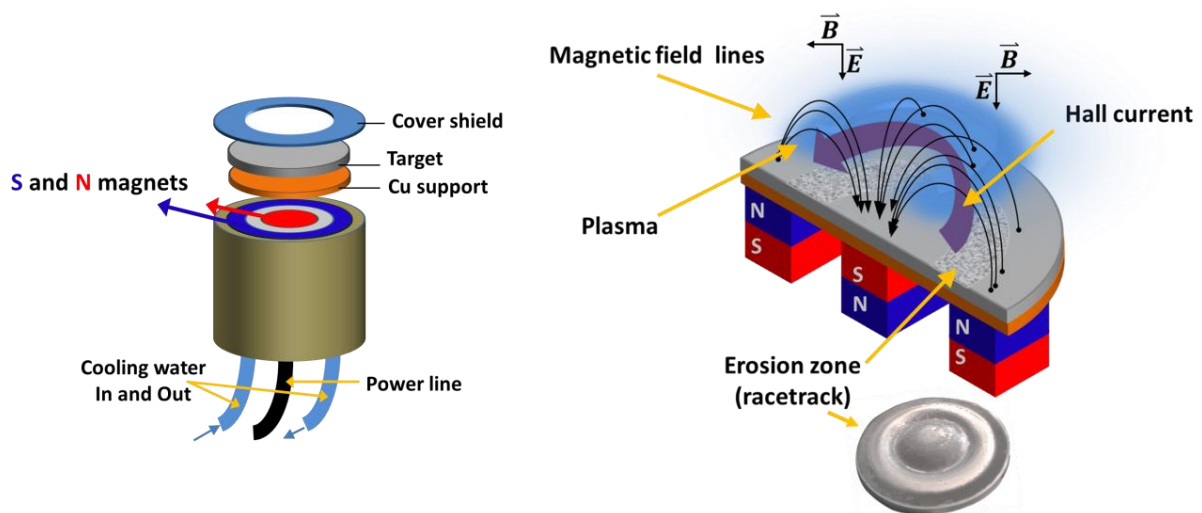


FIG. 2.6. (Left) schematic of the configuration of a magnetron. (Right) magnetron cross section indicating the magnetic field lines, the lorentz forces, the hall current, the erosion zone and the dense plasma region.

---

The planar magnetron configuration uses two concentric magnets with opposite polarities generating a magnetic field that traps and confine the electrons near the target (fig. 2.6). The magnetic field ( $\mathbf{B}$ ) being nearly perpendicular to the electric field ( $\mathbf{E}$ ), a Lorentz force ( $\mathbf{E} \times \mathbf{B}$ ) is applied to the electrons. In a simplified description of the magnetron sputtering, the electrons describe a cyclotron motion around magnetic field lines, increasing the electronic density and the ionization probability. As the electron gyration radius is smaller as the electrons approach the target surface, a closed azimuthal drift current, called hall current, is observed<sup>98,107</sup>.

Because the plasma density is higher in the cyclotron trajectory, the sputtering process is more intense in this region and provokes a more pronounced erosion of the target (racetrack) next to this plasma region.

The magnetron sputtering configuration not only allows obtaining self-sustained plasma at lower pressure but also increases the sputtering rate. The results are a higher film growth rate in a cleaner environment and, since the sputtered atoms have a high kinetic energy as they condensate in comparison with thermal evaporation and diode sputtering, films exhibit a higher density.

### **2.1.6. Reactive magnetron sputtering**

While argon, an inert gas, is used to produce the sputtering plasma, other gases can be used to react with the sputtered atoms. Mixtures of argon and reactive gas lead to reactive magnetron sputtering. The most used reactive gases are nitrogen and oxygen to produce nitrides or oxides, respectively. The sputtered atoms condensing on the substrate surface react with the reactive gas to produce the compound films. An alternative to produce compounds is by using ceramic target. However, it is necessary to work mainly in radiofrequency mode to avoid target polarization and arcing. Furthermore, with the use of ceramic targets it is only possible to change slightly the stoichiometry of the film, while reactive magnetron sputtering of metallic targets allows wider tailoring of the film properties composition and properties.

---

In the Ar/reactive gas mixture, the reactive gas flow rate determines the properties of the system and can introduce a non-linear instability during reactive sputtering of metallic targets. The reactive total gas flow must be equivalent to the sum of pumped gas flow  $q_{Pumped}$ , the reaction gas flow (getter effect) with the surroundings,  $q_{Surrounding}$  including condensed film and reactor walls and, finally, the reaction with the target surface  $q_{Target}$ . These three parameters have a nonlinear dependency with the pressure and depend on factors such as the area and the fraction of surface covered by target element(s)-oxygen compounds at both substrate and target locations.

$$q_0 = q_{Pumped} + q_{Surrounding} + q_{Target} \rightarrow \text{Non linear evolution} \quad (2.17)$$

The process can be divided in three modes<sup>110</sup>. At low reactive gas partial pressures, an elemental, or metallic, sputtering mode is observed that is referred to a bare, or nearly bare, metallic target generally associated to a high sputtering yield. In this case, most of the reactive gas species are gettered by the surroundings, avoiding the target poisoning and leading to a low sensitivity of the reactive gas partial pressure to the reactive gas flow rate.

At high reactive gas partial pressures, reactive species react completely with the target surface, poisoning the target. Apart from few cases, this results in a low sputtering yield. This mode is called the ceramic, compound or poisoned sputtering mode.

There is a transition mode between the above mentioned modes for which the target surface coverage by reactive species depends on the gas flow rate and, therefore, on the reactive gas pressure and the sputtering yield showing two competitive processes: the poisoning and sputtering or cleaning of the surface, respectively. The transition mode can be a stable or a bi-stable region typical for the reactive sputtering process, where a hysteresis loop is developed. This phenomenon is generally undesirable. The sputtering system becomes bi-stable, an abrupt decrease in the reactive gas consumption is observed upon increasing the reactive gas flow rate. It is possible to avoid this instability if the pumping speed is greater than a critical value<sup>110</sup>. Using metallic targets of elements highly reactive towards the reactive gas species favors the observation of an hysteresis loop. We do not detail more this effect because in our deposition chamber, under the working conditions of this study, no hysteresis loop was observed.

---

## 2.2. Structure zone diagram (SZD)

Film growth is a process in heterogeneous phase resulting from the condensation of the vapor or sputtered phase of a material. The film formation can be divided in several steps: The adsorption and clustering of atoms on the substrate (nucleation), incorporation of the deposited atoms by the growing nuclei (crystal growth) and coalescence or grain boundary migration (grain growth). Thermodynamic and kinetic factors are present simultaneously and influence each step of the process. As a result, different morphologies and microstructures are achieved. The *SZDs* are semi-empirical approaches to describe the microstructure of relatively thick deposited films.

In their early work, Movchan and Demchishin found that, to describe the microstructure of deposited films by evaporation, it is necessary to consider the adsorption/desorption and diffusion of atoms on the substrate. These processes depend on the surface energy and surface tension of the substrate and of the growing film. After an analysis of thin and thick films under different growth conditions, they concluded that the microstructure of deposited films can be of three types (1, 2 and 3)<sup>111</sup> depending on the homologous temperature ( $T_h$ ).  $T_h$  is expressed as the ratio between the film temperature ( $T$ ), approximated to the substrate temperature, and the melting point ( $T_m$ ) of the formed film:

$$T_h = T/T_m \quad (2.18)$$

Based on this pioneering work, Thornton incorporated an argon gas pressure axis to adapt the *SZD* to sputter-deposition because it affects the kinetic energy of the impinging atoms that determines the film microstructure. Looking closely at this two dimensions *SZD* it was found a transition zone between the zone 1 and zone 2<sup>111,112</sup>.

In their *SZD* of Barna and Adamik<sup>113,114</sup> consider the presence of impurities during the film growth, showing that they play an important role on the microstructure by interfering with grain growth and stimulating continuous nucleation. However, in most of the *SZD* the role of impurities is not considered.

As the pressure is related with the kinetic energy of impinging atoms, Messier<sup>115</sup> has replaced the argon pressure by the ion kinetic energy to well describe ion beam assisted

---

deposition methods. However, it was needed to modify the model due to the introduction of energetic deposition methods such as High Power Impulse Magnetron Sputtering (HIPIMS) or cathodic arc evaporation.

A revised SZD proposed by Anders<sup>116</sup> modifies and extends the available models based on three main changes:

- The introduction of a general temperature  $T^*$  that includes the homologous temperature ( $T_h$ ) and the transformation of potential energy carried by the impinging particles into thermal energy in the film ( $T_{pot}$ ).
- The replacement of the argon pressure by a normalized energy term  $E^*$  that includes the kinetic energy of the particles.
- Introduction of a film thickness axis  $t^*$  to better describe the influence of the previous parameters, including ion-etching.

### **2.2.1. Zones description**

The *SZD* proposed by Anders contains the four zones pre-existing in the Thornton *SZD* and add an etching zone as shown in fig. 2.7.

We describe briefly each zone below.

#### **Zone 1**

At low  $T^*$  and low  $E^*$ , the kinetic and potential energies of the impinging atoms are low. Consequently, the bulk and surface mobilities are almost inexistent and there are no favored nucleation centers. In some cases, a low  $E^*$  is related with conditions of high pressure where collision probability is high, shifting the kinetic energy of atoms impinging the substrate to lower values. These conditions lead to a morphology consisting in nanocrystalline columns separated by voids. The resulting films are porous.

## Zone T

In the transition (T) zone, the surface diffusion increases. However, diffusion inside the grains remains limited. The characteristic microstructure can be described as a dense array of fibrous grains that is developed by a competitive crystal growth. The structure is inhomogeneous along the film thickness. Increasing  $T^*$ , enhances the thermal mobility. Increasing  $E^*$  can also improve the mobility by heating or atomic displacement. Due to the thermal transfer from the particles to substrate, an increase in  $E^*$  leads to a decrease in the thermal threshold between zone 1 and zone T and to a broadening of zone T.

## Zone 2

Increasing, from the previous zone T, the kinetic energy of the impinging particles by decreasing the gas pressure (and the number of collisions) or thanks to bombardment by ions accelerated in the cathode sheath also increases the surface and bulk mobilities. However, the growth is governed by the surface diffusion process. Fibrous grains evolve to uniform columnar grains across the film thickness.

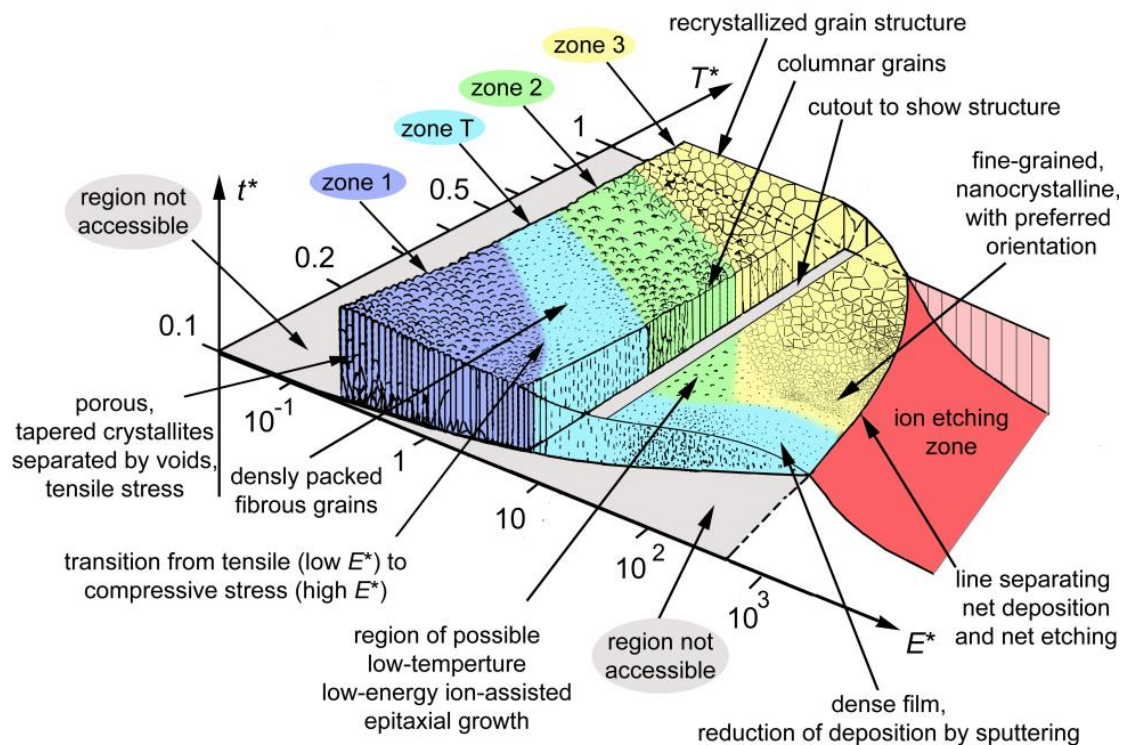


FIG. 2.7. Extended structure zone diagram including situations owing to highly energetic synthesis methods<sup>116</sup>.

---

### **Zone 3**

The increase of  $T^*$  and/or higher energy flux of accelerated ions with high kinetic and potential energies (that lead to microlocalized thermal spike regions along implantation channels) determine the film microstructure by bulk diffusion and therefore recrystallization processes. The obtained films are dense with an equiaxed structure.

### **Ion etching zone**

The *SZD* proposed by Anders explains how at high  $E^*$  accelerated ions arriving to the growing film can induce etching.

The development of *SZDs* and their wide use show the need to comprehend the influence of each experimental parameter in film growth. Supported by these semi-empirical approaches, it is easier to understand and to interpret the behavior of a particular system.

## **2.3. Experimental setup**

Thin films elaboration was performed using a 40 L volume deposition chamber. The base pressure reached is around 0.003 Pa using a mechanical pump for primary vacuum and a turbo molecular pump. ZnO syntheses were conducted in a reactive atmosphere consisting of argon-oxygen mixtures. The gas flow rates were controlled using a mass-flow controller Bronkhorst EL-FLOW model F-201CV. The argon flow rate was fixed for all the experiments while the oxygen flow rate (*OFR*) was varied. The total pressure was adjusted by the turbomolecular pump with a rotation speed of 25000 revolutions per minute (rpm) and controlled using a PENNINGVAC PTR 90 (pressure to voltage converter) pressure gauge. The average working pressure was in the range 0.03 to 0.05 Pa.

As it was described before, the use of magnetrons increases the sputtering rate. The deposition chamber is equipped with three magnetrons for co-sputtering when it is needed. The target diameter was 50 mm with an adjustable target to substrate distance. To ensure a good lateral homogeneity in thickness and composition, the targets are off-

---

centered relative the rotative substrate-holder axis and the substrate-holder was rotating at 30 rpm. To avoid lateral inhomogeneity, the samples were positioned facing the magnetron axis<sup>27,117</sup>. The substrate-holder was polarized using a radio frequency Advanced Energy Cesar® RF power supply (Frequency, 13.56 MHz, Max outpower, 300 W) to etch and clean the substrate surface (60W, 2 min) just before deposition. This procedure helps generating dangling bonds at the film surface, which promotes the film adhesion if deposition is started before the end of the etching step. The substrate-holder was not intentionally heated and the substrate temperature was evaluated using thermal level stripes (Thermax) positioned on the same circumference as the substrates on the substrate-holder. It was below 40 °C (the lower detection limit of the thermal level stripes) for all conditions. Fig. 2.8 shows a schematic of the deposition chamber and below are presented photographs of the ZnO and ZnO-Au sputtering deposition processes, showing a substrate and the off-axis position of the targets relative to the substrate-holder axis of rotation.

Direct current (DC) magnetron sputtering was used for depositions and the discharge was controlled by fixing the discharge current intensity ( $I$ ) to each target. Voltage ( $V$ ) and power ( $W$ ) values self-adjusted depending on the experimental conditions. Advanced Energy Pinnacle+ 5kW and MDX500 generators were used for Zn and pure Au targets, respectively. In order to produce ZnO and ZnO-Au films, the discharge current applied was fixed at 0.07 A on the zinc target and varied between 0.006 and 0.015 A on the gold target. The target to substrate distance ( $D_{ts}$ ) was fixed at 50 mm for the Zn target while distances from 55 to 120 mm have been used for the Au target.

The deposition time was set such that the resulting film thickness was 150 nm $\pm$ 40 nm for all deposition conditions. To measure the film thickness of a sample, the substrate was partially covered by an adhesive thermal resistive tape before deposition. Therefore, when removing the tape we obtained two well differentiated regions with bare substrate and deposited film. The film thickness was measured using a tactile profilometer Talysurf 10 Taylor-Hubson where a stylus in contact with the sample surface moves laterally. At the interface between the two regions, a step with a vertical height ( $h$ ) is measured by the stylus.

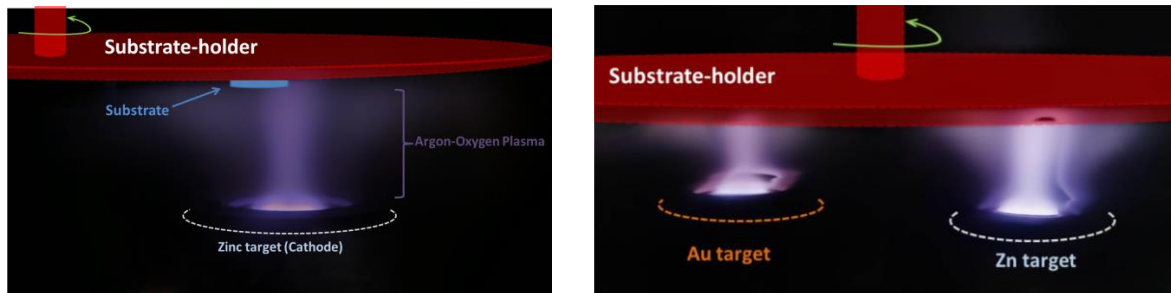
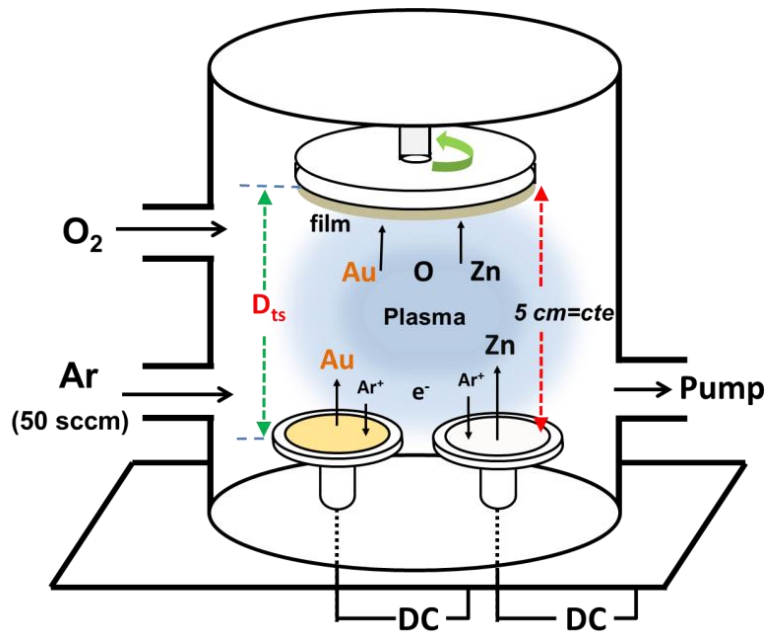


FIG. 2.8. (Above) schematic of the reactive sputtering chamber used for the growth of ZnO and ZnO-Au nanocomposite thin films. The Au target is added for the deposition of ZnO-Au films. (below) Photographs of ZnO and ZnO-Au sputtering process showing the off-axis position of the targets and of the substrate.

## 2.4. Characterization methods

### 2.4.1. X-ray diffraction (XRD)

The knowledge of the structure and microstructure of a material are essential for different reasons: It allows to confirm or to find the identity of the elaborated material. With the information extracted it is possible to obtain a better understanding of the

---

properties of the material. The X-ray diffraction (XRD) methods are very important tools in material science to characterize crystalline materials.

When an oscillating electric field of an electromagnetic radiation interacts with electrons in matter, coherent scattering can occur. In crystals, X-ray radiations are needed to interact with ordered atoms producing scattered waves. Depending on the beam angle, can exist constructive or destructive interferences determined by the Bragg law (fig. 2.9).

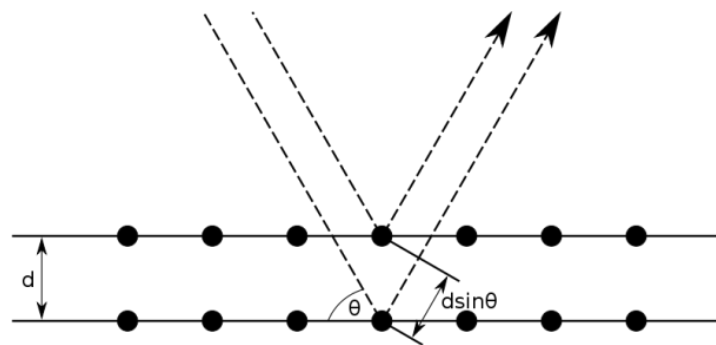


FIG. 2.9. Schematic representation of the Bragg diffraction law. The atoms in the crystal lattice are represented as black spheres.

$$2d_{hkl} \sin \theta = n\lambda \quad (2.19)$$

With  $\theta$  the scattering angle,  $\lambda$  the wavelength and  $n$  an integer determined by the order of the diffraction process.  $h$ ,  $k$  and  $l$  are called miller index that represent the specific crystallographic plane in condition of diffraction.

In crystal structures with primitive cell,  $h$ ,  $k$  and  $l$  can take any value for diffraction. However, the Bragg law is a necessary but not sufficient condition for diffraction in other crystal structures. Based on atomic scattering factors and structure factors selection rules, it is possible to know which family of planes can diffract for a specific crystal structure<sup>118</sup>.

Depending on the geometrical configuration used, it is possible to obtain information about the presence of phases, crystal quality, coherence length, internal stress, preferential orientation or texture.

---

### 2.4.1.1. Bragg-brentano ( $\theta/2\theta$ ) geometry configuration

In the X-ray diffraction methods, there are different geometrical configurations that can offer different information about a material. The Bragg-Brentano geometry is one of the most extended XRD configurations because it allows characterizing a wide range of materials. In this configuration the sample is fixed while the X-ray source and the detector are rotated around it.

We briefly describe how works a typical diffractometer. X ray emission is generated in a vacuum tube diode where electrons are emitted by thermionic effect and impact a metallic anode under an a high voltage, producing a characteristic X-ray spectrum of the anode material. A crystal monochromator separates the different wavelengths to obtain a beam composed exclusively of the  $K_{\alpha}$  emission. An AXS Bruker D8 Advance diffractometer using a Cu anode ( $\text{Cu } k_{\alpha 1} = 1.54\text{\AA}$ ) in the Bragg-Brentano geometry as presented in fig. 2.10 was used for some of the analyses presented within this study.

In the Bragg-Brentano configuration only crystallographic planes in condition of diffraction and parallel to the sample surface are measured. However, constructive interferences are possible also for small deviations from the  $\theta$  diffraction angle, resulting in peaks with a specific width that is related with the number of planes aligned in the same direction.

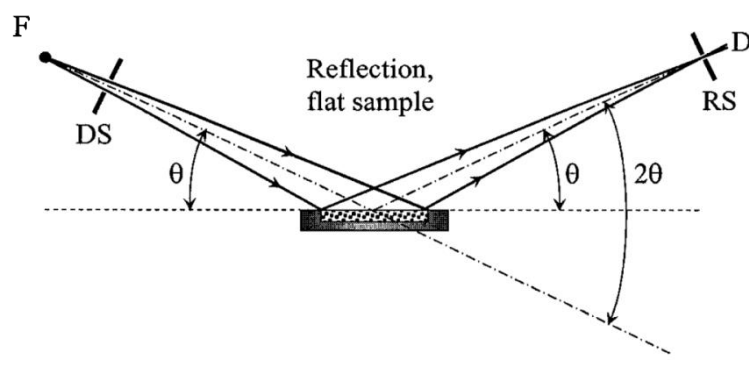


FIG. 2.10. Schematic representation of the Bragg-Brentano geometry. F- Focus of x-ray beam source, DS is the divergence slit, RS is the receiving slit, D is the detector and  $\theta$  the bragg angle. The incident beam reaches the sample surface at a determined  $\theta$  angle while the detector collects the diffracted beam at an angle  $2\theta$  of the incident beam <sup>119</sup>.

---

#### 2.4.1.2. Pole figure and $\varphi$ scan configurations

In material science, texture or preferential orientation describes the statistical distribution of grain orientation of polycrystalline samples and this property determines some electrical, magnetic and mechanical properties among others. Three types of texture components are usually distinguished in thin films: random texture, when grains have no preferred orientation; fiber texture, for which one crystallographic axis of the film is parallel to the substrate normal, while there is a rotational degree of freedom around the fiber axis; and epitaxial alignment (or in-plane texture) on single-crystal substrates, when there is coherence between the crystal lattices of the substrate and film. The substrate and film can be of same (homoepitaxy) or different (heteroepitaxy) natures. In case of epitaxial growth, a monocrystal can be formed if all regions grow with the same in-plane orientation (single domain epitaxy)<sup>120-122</sup>.

The Bragg-Brentano geometry ( $\theta/2\theta$ ) is an out-plane configuration that allows to obtain information of the h, k and l indices of planes parallel to the sample surface and it is relevant for the investigation of powder, polycrystalline or thin film samples. However, with the use of an out-plane configuration it is not possible to differentiate if an (hkl) plane orientation corresponds to a fiber texture or to an epitaxial alignment.

To obtain information on the preferential orientation of a specific (hkl) plane in the volume of the material, X-ray diffraction methods such as pole figure and  $\varphi$  scan measurements are needed. In a pole figure, the selected plane is virtually placed as the center of a sphere and can be represented as a point that is the result of the intersection between the sphere surface and a normal vector to the specific plane. This point can be described with two coordinates, the  $\psi$  and  $\varphi$  angles, as is observed in fig. 2.11a. The  $\psi$  angle can vary from 0 to 90 degrees while the  $\varphi$  angle can vary from 0 to 360 degrees.

The pole figure can be visualized in 2D projection with the help of a stereographic representation where the  $\psi$  angle is represented by the distance from the center to a point in the circumference and the  $\varphi$  angle is the rotation angle starting from the x-axis.

A four circles AXS Bruker D8 Discover diffractometer has been used for pole figure and  $\varphi$  scan measurements due to the possibility to vary the  $\theta$ ,  $2\theta$ ,  $\psi$  and  $\varphi$  angles. The diffractometer X-ray source is a Co anode (Co  $k_\alpha = 1.79\text{\AA}$ ).

If we consider, for the sake of the explanation, a 4-fold symmetry such as simple a cubic structure and follow a specific plane, e.g. [111] plane, it is possible to determine if the material has a random orientation, a fiber texture or if it shows epitaxial alignment.

In the diffractometer, to follow the spatial distribution of the specified plane in the material volume, the X-ray source ( $\theta$ ) and the detector ( $2\theta$ ) angle positions are fixed to the [111] diffraction condition, while a series of scans for different  $\psi$  and  $\varphi$  angle values are performed.

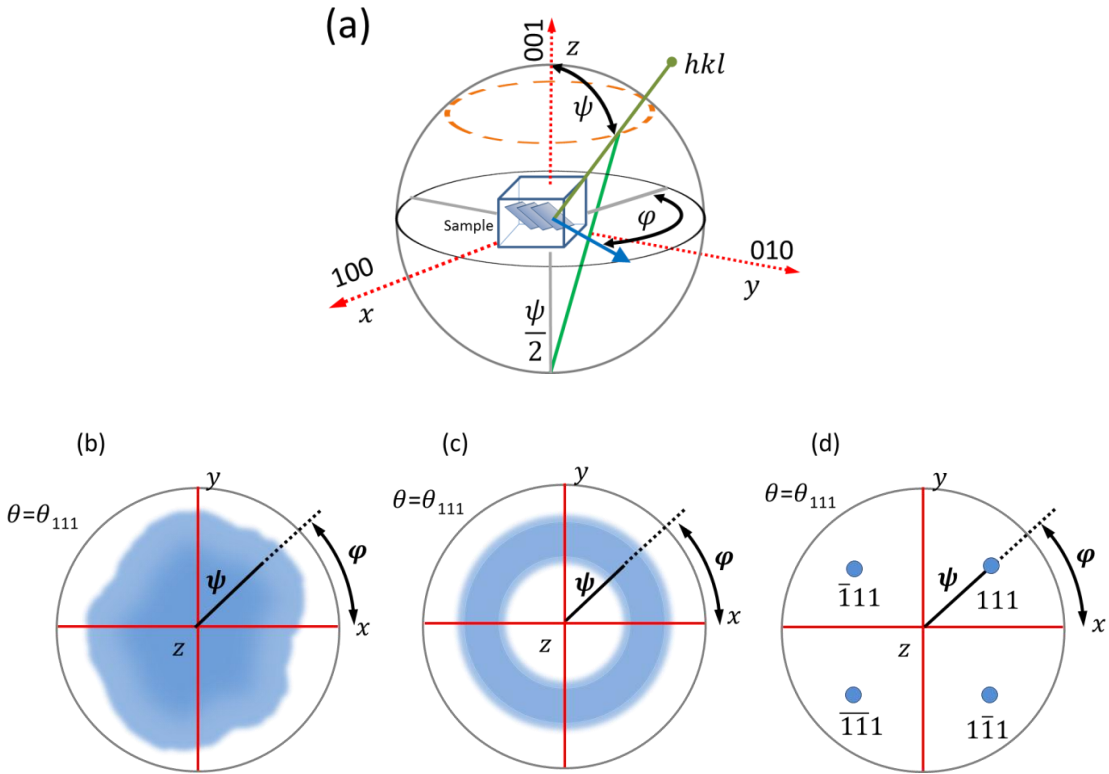


FIG. 2.11. Representation of a (a) pole figure geometry and the 2D stereographic representations of a 4-fold crystal structure material with (b) random orientation, (c) fiber texture and (d) epitaxial alignment.

For randomly oriented films (fig. 2.11b) the diffraction peak signal will appear at almost any  $\psi$  and  $\varphi$  angles, meaning that the pole figure will have randomly dispersed spots. Fiber-textured films exhibit a signal at constant  $\psi$  but variable  $\varphi$  angle values represented in an inner circumference as in fig. 2.11c. In monocrystals, the diffraction peaks only appear at a fixed value of  $\psi$  and defined  $\varphi$  angles. For a cubic structure the 4-

---

fold symmetry shows four points that corresponds to the {111} family of planes. Depending on the crystal quality, each spot can be broadened along  $\psi$  and/or  $\varphi$  angles or, in high quality films, be well defined narrow spots (fig. 2.11d)

The  $\varphi$  scan can be differentiated from pole figure measurements by the fact the  $\psi$  angle is fixed. Using the  $\psi$  angle corresponding to the spots of fig. 2.11d and performing a  $\varphi$  scan would produce a diffractogram composed of 4 peaks separated by 90 degrees, i.e. the angle between consecutive {111} planes of the cubic structure.

#### 2.4.2. Transmission electron microscopy (TEM)

Transmission Electron Microscopy is a high magnification microscopy that allows evaluating the crystal structure, grain orientation as well the microstructure in materials. An electron gun produces a beam of electrons that are accelerated and focused with magnetic lenses to pass through a sample (~80 nm-thick) interacting with it and the transmitted electrons are collected. The signal is then amplified to build a 2D image. In an oversimplified explanation, the objective lens takes the electrons from the exit surface of the sample, disperses them to create a diffraction plane (*DP*) in the back-focal plane (*BFP*) and recombines them to form an image in the image plane. The diagram shows a three lens TEM in the two basic operations: diffraction (fig. 2.12a) and imaging modes (figure 2.12b)<sup>123</sup>.

- In diffraction mode, to look at the *DP* (the *BFP* of the objective lens), it is necessary to insert an aperture into the image plane of the objective lens.
- In imaging mode, to view an image (the image plane of the objective lens), it is necessary to insert an aperture called objective aperture into the *BFP* of the objective lens.

Considering the diffraction mode and taking a look to the diagram in fig. 2.12, the *DP* collects the electrons of all the sample area, which is not an advantage because the sample is usually not perfectly flat and the beam intensity is large enough to damage the viewing screen or saturate the CCD camera. To solve this problem and obtain useful information, an object aperture is placed in one of the multiples image planes and can

regulate the beam intensity and give localized diffraction pattern information. The object aperture can delimitate a specific area of the sample and create a virtual object aperture in the same plane of the sample. This configuration is called Selected Area Electron Diffraction (SAED). In the SAED, electron beam interaction with the film includes not only absorption but also diffraction. SAED pattern is a 2D projection of the reciprocal lattice. The diffracted signal of polycrystalline materials present circles corresponding to a family of planes with specific radii of the circles owing to the Bragg law applied to electron diffraction. In monocrystalline materials, instead of circles, the pattern shows spots that represent not a family of planes but a specific type of plane.

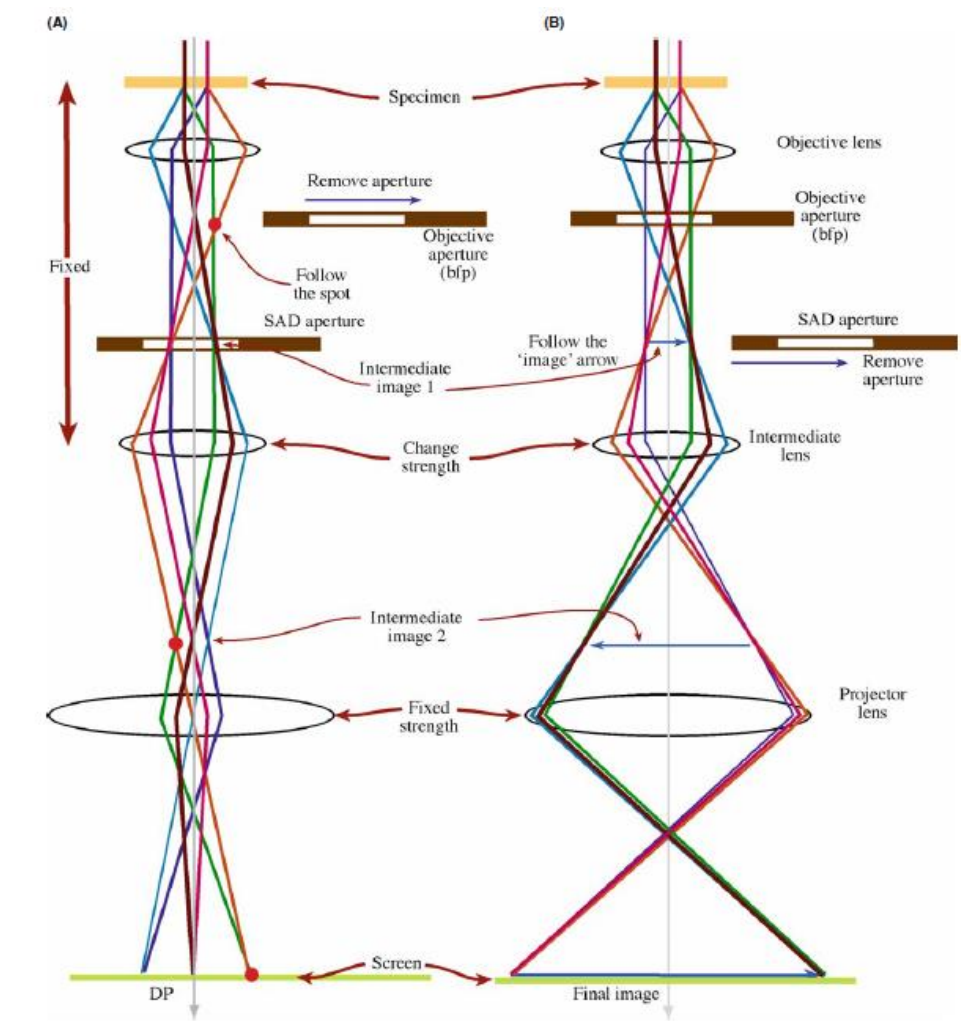


FIG. 2. 12. Diagram of Three lens TEM operating in (A) a diffraction mode and (B) an imaging mode. The figure shows the position of the objective and the SAED apertures<sup>123</sup>.

The imaging mode has two main contrast imaging methods. Bright and dark field modes. Contrast imaging methods allow having a complete description of the sample microstructure. Bright field (*BF*) imaging only includes the unscattered beam (fig. 2.13a) and corresponds to absorption of electrons in the sample. Bright contrast images show thick regions of the sample or with high atomic number in dark contrast, while thinner regions of the sample or regions with low atomic number appear brighter. Dark field (*DF*) excludes the unscattered beam from the image and only allows the passing of electron beams diffracted after their interaction with the sample. In *DF* images, the contrast is due to the intensity of the diffracted beam of a specific *hkl* plane. Bright zones represent the presence of crystallites oriented in the selected diffraction condition. In dark zones, the Bragg conditions are not fulfilled. *DF* brings information about crystal quality, grain size, epitaxy and the microstructure of a material. In *DF* images, the position of the objective aperture and the diffraction beam coincide, while the incident beam is blocked by moving the objective aperture (fig. 2.13b) or by tilting the incident beam (fig. 12.3c).

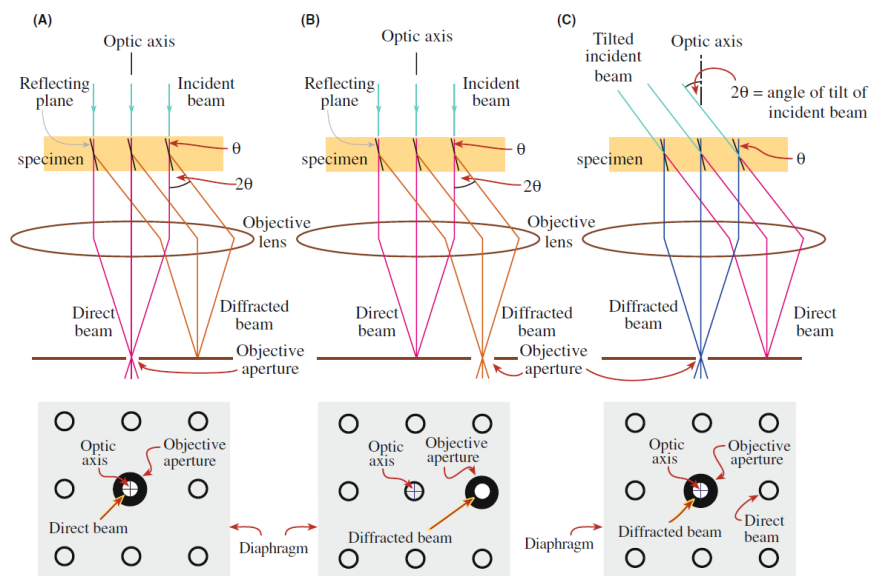


FIG. 2.13. TEM imaging operation modes of (a) bright field and dark field by (b) displacement of the objective aperture and (c) tilting of the incident beam<sup>123</sup>.

For this project, we used a Philips CM200 and a JEOL ARM 200-Cold FEG microscopes for film characterization. The working voltage of the microscopes is close to 200 kV.

---

TEM foils were prepared in a focused ion beam (FIB)/scanning electron microscope (SEM) dual beam system (FEI Strata DB235) using the '*in situ*' lift-out method. Thinning of the foil was carried out using an acceleration voltage of 30 kV at the first steps and finishing with 5 kV and a current of 16 pA. Fig. 2.14 shows the extraction of the foil and fixing to the grid for TEM measurement and an example of bright field image and SAED pattern.

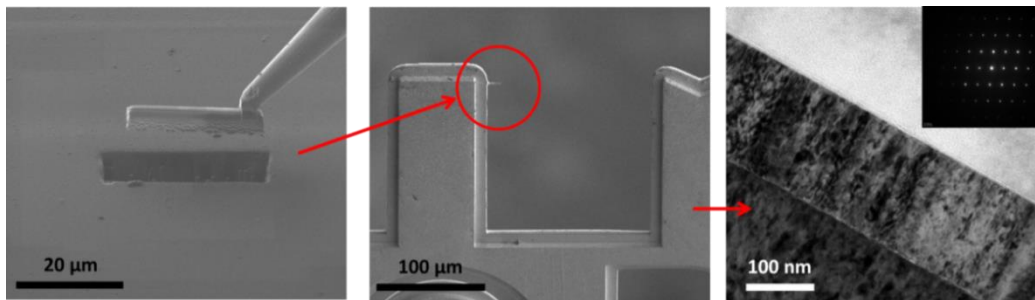


FIG. 2.14. Lift-out method step by step. Elaboration by FIB of a ZnO lamella for TEM measurements. (right) extraction of the specimen after cutting from the film bulk. (Center). Pasting of the TEM lamella to the holder grid. (Right) TEM image of a transverse section of the ZnO film and (inset) SAED pattern of the film.

### 2.4.3. Energy dispersive spectroscopy of X-ray (EDSX)

Energy dispersive spectroscopy of X-rays (EDSX) is a method usually in coupled mode with scanning electron microscopy (SEM) that allows qualitative and semi-quantitative chemical analysis. As for TEM, in SEM an electron gun is the source of the electron beam that impacts the surface sample generating different types of interactions. Secondary electron emission intensity is related with the surface morphology and this information is used to produce images.

In EDSX, it is necessary to have an electron beam with high enough energy to excite inner core electrons from a specific material. The ejection of an electron leaves an empty level. Afterwards, there is relaxation and electrons from upper levels fill the empty level, generating X-ray emission lines corresponding to specific transitions between electronic levels with a cross section depending on the electron incident energy. Each element leads to a unique emission spectrum related with k, l, m or n atomic levels.

For the ZnO films, EDSX was used to evaluate the oxygen content using a ZnO powder standard and increasing the signal from light elements. For ZnO-Au nanocomposite films, EDSX was used to determine the Au content in the films from the Zn-L and Au-M lines and following the  $\left(\frac{Au}{Au+Zn}\right)$  ratio of atomic concentrations.

#### 2.4.4. X-ray photoelectron spectroscopy (XPS)

XPS is a widely used method for surface analysis to obtain chemical information as elemental composition and chemical and electronic state of a sample.

With the aid of a monochromator, an Al-canon gun emits a K-alpha X-ray beam (1786.6 eV). The X-ray photons interact with the material and can eject an electron from atom (*A*) core levels, producing a ionization process ( $A + h\nu \rightarrow A^+ + e^-$ ). The ejected, and detected, photoelectrons originate from the surface down to a depth of 2-3 nm, making this method surface-sensitive.

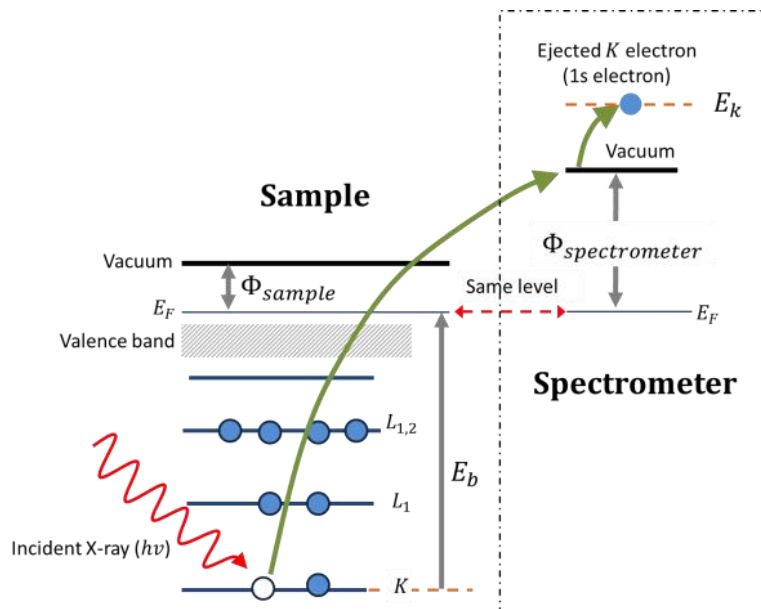


FIG. 2.15. Representation of the mechanism of photoelectron emission by a photon with energy  $h\nu$  in X-ray photoelectron spectroscopy (XPS)<sup>124</sup>.

---

The ejected electrons are emitted with a kinetic energy ( $E_k$ ) measured by the spectrometer.  $E_k$  depends on the energy of the incident photons and is not an intrinsic property of the material. However, it is possible to relate  $E_k$  with the electron binding energy ( $E_b$ ) (see fig. 2.15) The electron binding energy gives information about the element identity as well the specific energy level.  $E_b$  is related with the photon incident energy ( $h\nu$ ),  $E_k$  and the work function ( $\Phi_s$ ) of the spectrometer as shown in equation (2.20):

$$E_b = h\nu - E_k + \Phi_s \quad (2.20)$$

In an element, each oxidation state can be differentiated by its specific  $E_b$ . The changes in the chemical environment caused by the surrounding atoms can also change  $E_b$ . This change is called chemical shift.

#### 2.4.5. Optical transmittance spectroscopy

Materials could be described by their crystalline structure, microstructure and chemical composition but other intrinsic characteristics of a material are the optical properties that explain the response of the material exposed to an electromagnetic radiation.

Optical transmittance measurements were performed with a double beam Cary 5000 UV-Vis-NIR spectrophotometer. The wavelength can be varied in the range of 175 to 3300 nm. A schematic of the spectrophotometer is represented in fig. 2.16.

The absorption of photons is the basis of the transmittance methods to study and obtain properties of a specific material as the absorption bandgap energy ( $E_{g(abs)}$ ).

From transmittance measurements it is not possible to measure the optical response of a thin film alone when it is deposited onto a substrate because the latter interferes with the light. The light source emits a beam that is split in two beams of proportional intensity ( $I$ ) to the brightness ( $B$ ) of the lamp ( $I=k \times B$ ). One beam passes through a reference compartment while the other is directed to the sample compartment. Before measuring a set of samples, a baseline correction is needed to calibrate the two beams and compensate any fluctuation of the lamp emission along the whole range of

wavelengths. Air can be used as reference and represents 100 % transmittance. The measurement consists in comparing the intensity of the 2 beamlines after transmission through the compartments. It enables measuring the intensity of light transmitted through the sample at each wavelength.

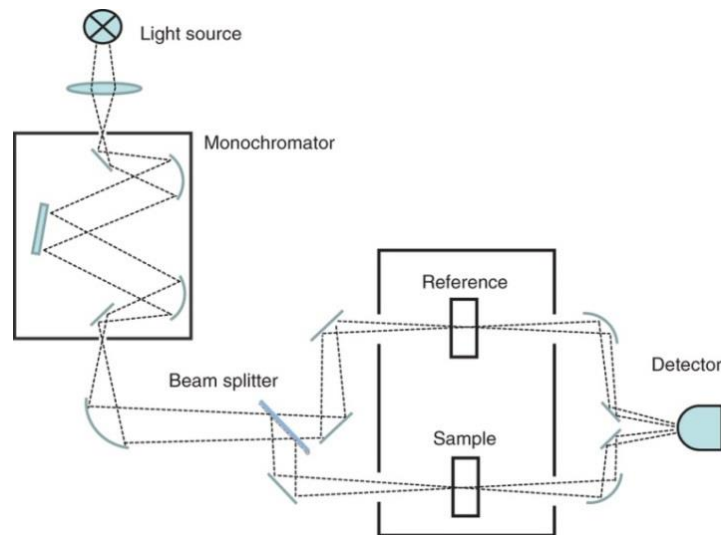


FIG. 2.16. Schematic of a double-beam absorption spectrometer<sup>125</sup>.

To obtain only the film transmittance, the performed measurements must be corrected. If we consider the beam passing through a bare substrate and passing through a film deposited onto a substrate (fig. 2.17), it is clear that the beam is attenuated when passing each interface due to reflexion and scattering phenomena.

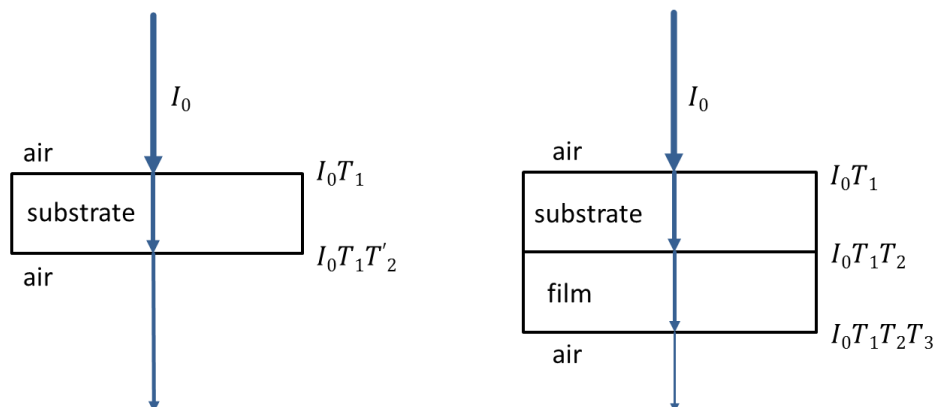


FIG. 2.17. Representation of the attenuation of a light beam passing through a bare substrate (left) and through a substrate covered by a film (right).

---

For a bare substrate, the beam passes through air/substrate and then substrate/air interfaces. When the beam passes through a bare substrate, transmittance due to the substrate can be expressed as:

$$T_{substrate} = I_0 T_1 T'_2 \quad (2.21)$$

Knowing that the air/substrate and substrate/air interfaces are equivalent, equation 2.21 becomes:

$$T_{substrate} = I_0 (T_1)^2 \quad (2.22)$$

$$T_1 = \sqrt{T_{substrate}} \quad (2.23)$$

The transmittance for a film deposited onto a substrate can be expressed in a similar form, but we must consider the air/substrate, substrate/film and film/air interfaces. The total transmittance of a beam of intensity  $I_0$  after passing through a film deposited onto a substrate can be expressed as:

$$T_{total} = I_0 T_1 T_2 T_3 \quad (2.24)$$

The contribution of the substrate is only a fraction of the total transmittance, therefore:

$$\frac{T_{substrate}}{T_{total}} = \frac{T_1^2}{T_1 T'_2 T_3} = \frac{T_1}{T'_2 T_3} \quad (2.25)$$

$T_2$  and  $T_3$  are due to the film but as we cannot measure or separate the contribution of  $T'_2$ , we consider that it has a negligible influence in the total transmittance. With the approximation that  $T'_2=1$ , equation 2.25 becomes:

$$\frac{T_{substrate}}{T_{total}} = \frac{T_1}{T_3} = \frac{T_1}{T_{film}} \quad (2.26)$$

$$\frac{T_{substrate}}{T_{total}} = \frac{\sqrt{T_{substrate}}}{T_{film}} \quad (2.27)$$

$$T_{film} = \frac{T_{total}}{\sqrt{T_{substrate}}} \quad (2.28)$$

---

### 2.4.5.1. Absorption coefficient

The absorption coefficient  $\alpha$  describes the amount of radiation absorbed by a material at a specific wavelength. When a radiation beam with intensity  $I_0$  passes through a layer with thickness  $l$ , it exits with an attenuated intensity  $I_1$ . The attenuation can be due to absorption or scattering by the film. Due to the configuration of the spectrophotometer, it is not possible to evaluate at the same time both phenomena and the absorption coefficient measured can be slightly higher than the real value. However, using a complementary device, it is possible to measure the reflectance that corresponds to the main part of the scattered radiation.

The absorption coefficient follows the Beer-Lambert law, and it can be expressed as:

$$T = \frac{I}{I_0} = e^{-\alpha l} \quad (2.29)$$

With transmittance measurements, it is possible to estimate  $\alpha$ :

$$\alpha = \frac{1}{l} \ln \frac{1}{T_{film}} \quad (2.30)$$

If we consider the reflected radiation,  $\alpha$  can be expressed more accurately as follows:

$$\alpha = \frac{1}{l} \ln \frac{(1-R)^2}{T_{film}} = \frac{1}{l} \ln \frac{1}{T_{film}} + \frac{2}{l} \ln(1-R) \quad (2.31)$$

### 2.4.5.2. Tauc plot

The absorption coefficient and the absorption bandgap transition ( $E_{g(abs)}$ ) in semiconductors can be related using the following relationship:

$$\alpha = A(h\nu - E_g)^m \quad (2.32)$$

Where  $A$  is a constant that includes the electron effective mass,  $h\nu$  and  $E_{g(abs)}$  are incident photon and absorption bandgap energy, respectively, both in eV.  $m = \frac{1}{2}$  is the coefficient for semiconductors with direct allowed transition, such as ZnO.

---

With the absorption coefficient ( $\alpha$ ) it is possible to extract the  $E_{g(abs)}$  for each film using the Tauc plot method. Multiplying the equation 2.32 by  $h\nu$  and taking into account the value of  $m$  for direct bandgap semiconductors, we obtain the following expression:

$$h\nu\alpha = B(h\nu - E_g)^{1/2} \quad (2.33)$$

When plotting  $(h\nu\alpha)^2$  vs  $h\nu$ , the intercept with the x-axis gives  $E_{g(abs)}$ .

### 2.4.5.3. Urbach energy

In the near edge the light absorption spectrum of a semiconductor can be described as the sum of different independent contributions and it could be divided into two or three main regions<sup>30-35</sup>. (i) At energies higher than  $E_{g(abs)}$  the material can be described by the tauc plot relationship where it is possible to obtain directly the bandgap of the films. (ii) At energies below  $E_{g(abs)}$ , the absorption should be equal to zero but it is possible to detect an absorption tail that follows an exponential behavior. It can be described by the Urbach rule, an empirical relationship:

$$\alpha = \alpha_0 \exp(\sigma(E - E_0)/kT) \quad (2.34)$$

$\alpha_0$  and  $E_0$  are constants that depends of each material,  $\sigma$  is the steepness parameter that depends on the temperature and of each material<sup>31,126-129</sup>. This expression is valid for ionic crystals as for covalent compounds.

Equation 2.34 can be rewritten as:

$$\alpha = A \exp(h\nu/Eu), \quad \text{with } Eu = \frac{kT}{\sigma} \quad (2.35)$$

In a logarithmic plot of  $\alpha$  versus photon energy ( $h\nu$ ), the slope corresponds to the Urbach energy, as is shown in equation 2.35.

The width of the Urbach tail can be due to thermal fluctuations and structural disorders that lead to intraband transitions. The steepness  $\sigma$  parameter can be expressed as in equation 2.36.

---


$$\sigma = \sigma_0 \left( \frac{2k_B T}{E_p} \right) \tanh \left( \frac{E_p}{2k_B T} \right) \quad (2.36)$$

$\sigma_0$  is a factor that does not depend on temperature but on each material. It has been found that it is inversely proportional to the ionic character<sup>127</sup>.  $E_p$  is the phonon energy and for some II-VI semiconductors its value depends on the temperature range. For temperatures up to 80 K,  $E_p$  fits the energy of the longitudinal acoustic (LA) phonons. From that temperature it fits the energy of the longitudinal optic (LO) phonons; examples of this behavior can be found in CdS, ZnS or ZnSe<sup>30,130</sup>. In general, the steepness parameter can be understood as a function of electron and/or exciton interactions with phonons in materials.

#### 2.4.6. Ellipsometry

With the use of ellipsometry spectroscopy it is possible to extract information about the optical properties of a given material. However, it is an indirect method that consists of the acquisition of raw data, the proposition of a model, the fitting of the data and finally the extraction of the optical parameters.

When a polarized beam is reflected on a sample, there is a change in the polarization that can be followed by the changes in the parallel and perpendicular components of the electric field of the incident radiation after the interaction with the sample (fig. 2.18).

The change in polarization is given by the following relationship:

$$\rho = \tan(\Psi) e^{i\Delta} \quad (2.37)$$

It was used the UVISEL spectroscopic phase-modulated ellipsometer from HORIBA Scientific to analyze the samples. Ellipsometry measures the parameters  $I_s$  and  $I_c$  that are related with luminosity flux intensity and are linked to the ellipsometry angles  $\Psi$  and  $\Delta$ .

$$I_s = \Psi \cdot \sin 2 \sin \Delta \quad (2.38)$$

$$I_c = \Psi \cdot \sin 2 \cos \Delta \quad (2.39)$$

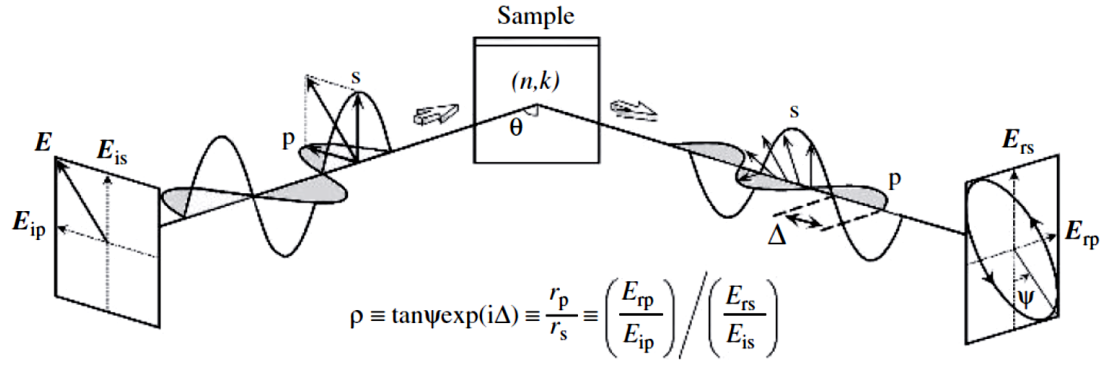


FIG. 2.18 schematic of the experimental configuration used for ellipsometry measurements<sup>131</sup>.

It is necessary to consider the characteristics of each sample to propose a good model to fit the dispersion data.

For homogeneous semiconductor films there are several methods as the Lorentz, Tauc-Lorentz, the Forouhi-Bloomer or the Tanguy model used to extract optical parameters and each one has advantages and disadvantages.

To fit the raw data of homogenous films, we used the Forouhi-Bloomer (*FB*) model<sup>132,133</sup>. In the FB model, the fitting parameter can be related with the refractive index  $n$  and the extinction coefficient  $k$ . The absorption coefficient is related with extinction coefficient as follows  $\alpha = \frac{4\pi k}{\lambda}$ , and the absorption bandgap energy was determined from the Tauc plot.

The values of  $n$  and  $k$  can be expressed in the real and imaginary parts of the dielectric constant as follows:

$$\varepsilon_1 = n^2 - k^2 \quad (2.40)$$

$$\varepsilon_2 = 2nk \quad (2.41)$$

In heterogeneous systems (composites), where two or more phases are involved, it is necessary to consider that the optical response is the contribution of all components (ZnO and Au in our nanocomposite films). In the effective medium approximation, the effective dielectric constant relates the dielectric constant of each component with its fraction within the material.

---

The most frequent models used for the characterization of inhomogeneous materials are the Maxwell-Garnett (*MG*) and the Bruggeman (*BM*) models and used to obtain the effective dielectric function ( $\epsilon_{eff}$ ).

The *MG* considers the presence of a component *i* in a host matrix while the *BM* considers that both contribute in a direct way to the properties of the nanocomposite. The *MG* (*BM*) model is the most used when the percentage of the component *i* is low (high) enough to consider the particles are well separated (percolate).

To determine the roughness of the films, it is often used a mixture of the models treating independently the film surface and the bulk. Using the Bruggeman model, the surface can be considered as an heterogeneous system composed of air and the material. More details about the ellipsometry models can be found in the annex A.

#### **2.4.7. Photoluminescence spectroscopy**

In photoluminescence spectroscopy (PL), a sample is exposed to a beam of specific wavelength to excite the material and an inverse process occurs from the relaxation of the material releasing photons. From PL measurements it is possible to obtain information about the electronic transitions in a material.

In semiconductors, the photoluminescence is used to determine the energy related to the emission energy bandgap energy ( $E_{g(ems)}$ ) and the intraband transitions caused by defects, impurities or doping agents. PL measurements require to use an optical excitation with an energy higher than  $E_{g(abs)}$  of the semiconductor. For ZnO, analyses were conducted at room and low temperatures measuring the emitted radiations in the UV and visible ranges using a laser excitation at 325 nm.

In ZnO, at room temperature the exciton-phonon interaction leads to broadening of the photoluminescence peak and it is possible an overlapping of close energy transitions. Therefore, low temperature measurements enable to obtain more information about free excitons and about close energy levels. The setup for low temperature PL measurements only varies from that of room temperature measurements by the

necessity to use an Oxford open cycle He cryostat that can cool a metallic finger receiving the sample down to 2 K. The usual temperature that can be reached is 5 K.

### 2.4.8. Raman spectroscopy

In optical transmission or photoluminescence, the wavelength  $\lambda$  (nm) is used to describe the beam energy and the optical response. In Raman spectroscopy, it is preferred to use the frequency  $\nu$  ( $s^{-1}$ ) or the wave-number  $\bar{\nu}$  ( $cm^{-1}$ ) to describe the energy transitions. Here we remind that:

$$\Delta E = h \frac{c}{\lambda} = h\nu = hc\bar{\nu} \quad (2.42)$$

Raman spectroscopy is concerned with the rotational and vibrational transitions in the spectral region from  $10^4$  to  $10^2$   $cm^{-1}$ . The sample is irradiated with a laser beam of frequency ( $\nu_0$ ) and the scattered light is measured.

The scattered light can be the result of an elastic or an inelastic process with the sample. For the elastic process, the incident photon excites an electron from a ground vibrational level to a temporal “virtual state”. In the relaxation, process the scattered photon has the same frequency ( $\nu_0$ ) as the incident photon and the phenomenon is known as Rayleigh scattering. Most of the scattering is elastic, hence the signal is strong.

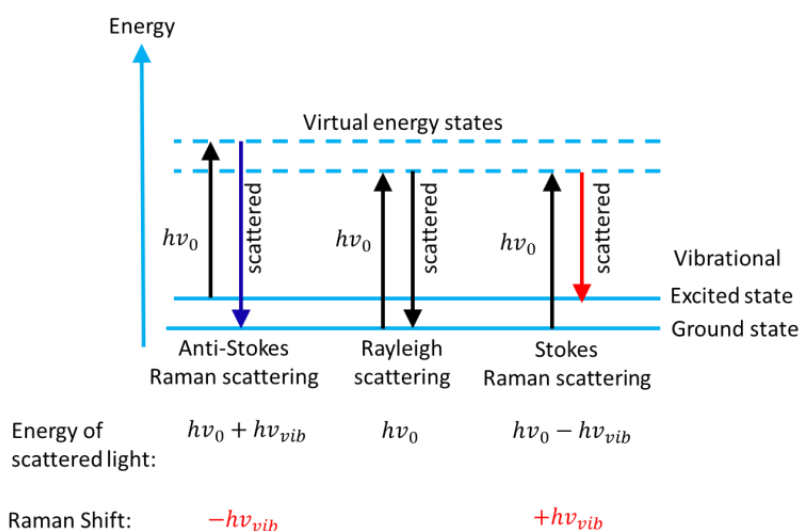


FIG. 2.19. Representation of the scattering processes in Raman measurements.

---

If the incident photon transfers energy to the material, the frequency of the scattered photon decreases (fig. 2.19). This effect is called Stoke shift. On the other hand, if the photon receives energy from the material, the frequency of the scattered photon will increase, this process is called anti Stoke shift. In both processes, there is the intermediation of lattice optical phonons. These shifts are the basis of Raman spectroscopy.

For the Raman and PL measurements was used an IHR 320 Raman spectroscope from JobinYvon, with HeCd laser at different wavelength for excitation, gratings 150 lines/mm with a blaze at 400 nm. The detection is done by a CCD cooled at  $-70^{\circ}\text{C}$ .

---

# Chapter 3

## 3. ZnO thin films: Synthesis and characterization

ZnO is a promising material for application as a transparent electrode or luminescent layer in optoelectronic devices such as solar cells, UV light-emitting diodes and electrochromic devices. Their performances strongly depend on the electrical and optical properties of the films<sup>37,39,134</sup>, that are affected by the structure and microstructure. Magnetron sputtering is a traditional method for the deposition of ZnO but sputter-deposition of ZnO is often based on RF-sputtering of ZnO targets and uses thermal assistance to grow high quality films. In contrast, the growth of ZnO films using reactive DC magnetron sputtering is little considered although it may present some interests from fundamental and applicative point of views for tuning both the defect chemistry and the microstructure. The first objective of this chapter is to illustrate these possibilities. These possibilities can then serve as a platform to study the resulting optical properties in order to rationalize the large scatter of optical data reported in the literature.

In this chapter, we investigate the influence of experimental conditions on the growth and optical properties of ZnO thin films. The chapter is divided in two main parts. In a first part we investigate the possibility to obtain single-domain epitaxial ZnO thin films without thermal assistance on (0001)-sapphire substrates using reactive DC magnetron sputtering. In the second part of the chapter we describe the evolution of the optical response and the underlying role of the chemical defects present using different growth conditions. In order to change the Ar-O<sub>2</sub> mixture composition, the oxygen flow rate (*OFR*) was modified. To consider the influence of the substrate and its interaction with the ZnO growing films we used (0001)-sapphire, showing epitaxial relationships with ZnO, and fused silica as crystalline and amorphous substrates, respectively. We also

---

deposited ZnO thin films onto (111)-Silicon to perform room and low temperature photoluminescence measurements in order to avoid any interference from the luminescence by sapphire and fused silica with that of ZnO films.

The results are interpreted to the light of the defect chemistry and recent insights into the condensation mechanisms during reactive magnetron sputtering of ZnO.

### **3.1. Elaboration of zinc oxide thin films**

Deposition runs were performed in a 40 L deposition chamber equipped with 3 magnetron guns. A schematic and description of the deposition setup is given in chapter 2, section 2.3. ZnO films were grown on fused silica, (0001)-sapphire and silicon substrates by DC sputter-deposition from a 2 inches diameter target positioned at a target-substrate distance of 50 mm in Ar-O<sub>2</sub> reactive gas mixtures. The target was placed off-axis relatively to the rotating substrate holder axis, which enables ensuring a good lateral homogeneity in thickness and composition of the films<sup>135</sup>. The samples were positioned on the circumference of the substrate-holder facing the magnetron axis. The argon flow rate was fixed to 50 standard cubic centimeters per minute (sccm) and the oxygen flow rate (*OFR*) was varied in the range of 5-15 sccm O<sub>2</sub>, corresponding to an injected composition in the range 9-23 vol % O<sub>2</sub> and a total pressure close to 0.4 Pa. The surface of the samples was activated *in situ* using Radiofrequency polarization (60 W, 2 minutes) in the reactive ambiance just before deposition. The discharge current was fixed at 0.07 A. This low discharge current was used to prevent substantial self-heating of the film during bombardment by fast particles impinging the substrates after their production at, or reflection by, the target surface. The substrate temperature was evaluated using thermal level stripes (Thermax) positioned on the same circumference as the substrates on the substrate-holder and was below 40°C (the lower detection limit of the thermal level stripes) for all conditions. The deposition time was set such that the resulting film thickness, measured by tactile profilometry, was 150 nm ± 20 nm for all deposition conditions. The evolution of the chemical composition was determined by energy dispersive X-ray spectroscopy (EDSX) (see chapter 2, section 2.4.3) with

---

amplification of the signal originating from light elements (oxygen in this case) and using a stoichiometric ZnO powder (NIST) as reference. The presence of defects and the determination of the emission bandgap energy were investigated by photoluminescence measurements (see chapter 2, section 2.4.7) in the UV and visible ranges with laser excitation at 325 nm.

### 3.2. ZnO crystal growth

When measuring the growth rate and the discharge voltage as a function of the increase of the oxygen flow rate, it is observed a decrease in both parameters as observed in fig. 3.1. ZnO exhibiting higher surface binding energy and secondary electron emission yield than metallic zinc, these evolutions are explained by a progressive transition of the chemical nature of the target surface from metallic to oxidized. Hence the *OFR* interval from 5 to 15 sccm lays in the transition region from metallic to compound sputtering mode. Moreover, both the deposition rate and discharge voltage tend to saturate to a low value as the *OFR* approaches 15 sccm, indicating nearly complete oxidation of the target is reached. Indeed, the selected range of *OFR*s ensures we can probe the influence of the progressive chemical oxidation of the target on the microstructure and properties of deposited films.

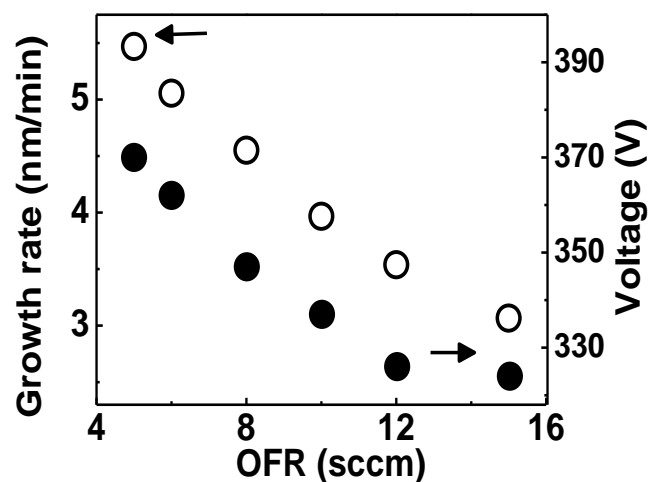


FIG. 3.1 Growth rate (white dots) and discharge voltage (black dots) as a function of the *OFR*.

The characterization of the ZnO thin films starts with a quick look at the optical transmittance response of the films. Fig. 3.2 shows the evolution of the optical transmittance in the UV and visible ranges for all films synthesized within this study. A transition from semi-transparent to highly transparent states is observed as the *OFR* is increased from 5 to 8 sccm and above. This transition results from the oxidation of zinc atoms as the *OFR* is increased as shown using X-ray absorption spectroscopy at the Zn-K edge<sup>136</sup>. In the case of Al-doped zinc oxide films, a modification of the film microstructure from random orientation of the crystallites to a strong preferential growth along the *c*-axis of the wurtzite cell has been observed during this transition<sup>137</sup>. This may indicate a modification of the condensation energetics. Considering the change of the transmittance signal during oxidation of the target surface, we investigate in this part on the influence of this transition on the microstructure of undoped ZnO in the extreme cases of amorphous substrates (fused silica) and (0001) sapphire. The latter is known to enable epitaxial growth of ZnO at temperatures higher than typically 300°C using MOVPE, MBE, PLD<sup>44–47</sup>

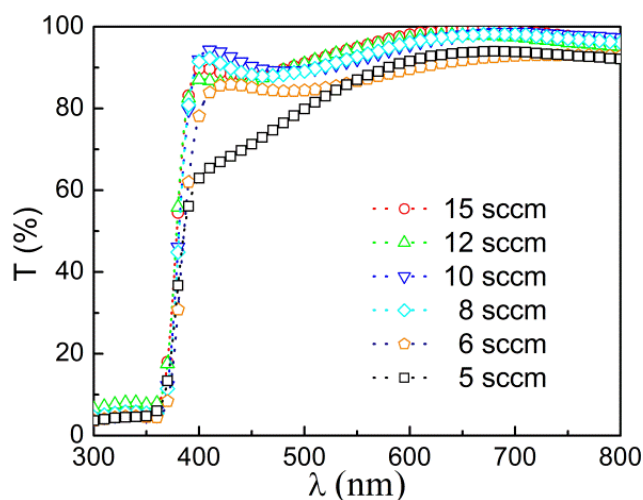


FIG. 3.2. Optical transmission spectra for ZnO films deposited on fused silica at different oxygen flow rates.

### 3.2.1. Structure and microstructure

The region of interest of X-ray diffractograms of all synthesized films collected in  $\theta$ - $2\theta$  configurations is displayed on fig. 3.3a. The diffraction peak corresponding to the signature of the (0002) planes of the ZnO wurtzite ( $P6_3mc$ ) crystal structure is observed close to  $34.4^\circ$  for all samples. A peak close to  $72.0^\circ$  was systematically observed, which

is ascribed to the diffraction by the (0004) planes of the same structure (Annex A). Only the thin films produced with the lowest *OFR* of 5 sccm exhibit other peaks, corresponding to the diffraction by  $\{10\bar{1}1\}$  and  $\{10\bar{1}0\}$  planes and a slightly darkish color characteristic of noticeable oxygen sub-stoichiometry. Hence, as observed for reactively sputtered Al-doped ZnO films<sup>137</sup>, a transition exists in the condensation process allowing the growth to develop exclusively along the *c*-axis of the wurtzite cell provided the *OFR* is high enough, this orientation being the most reported in the literature<sup>16,52,134</sup>.

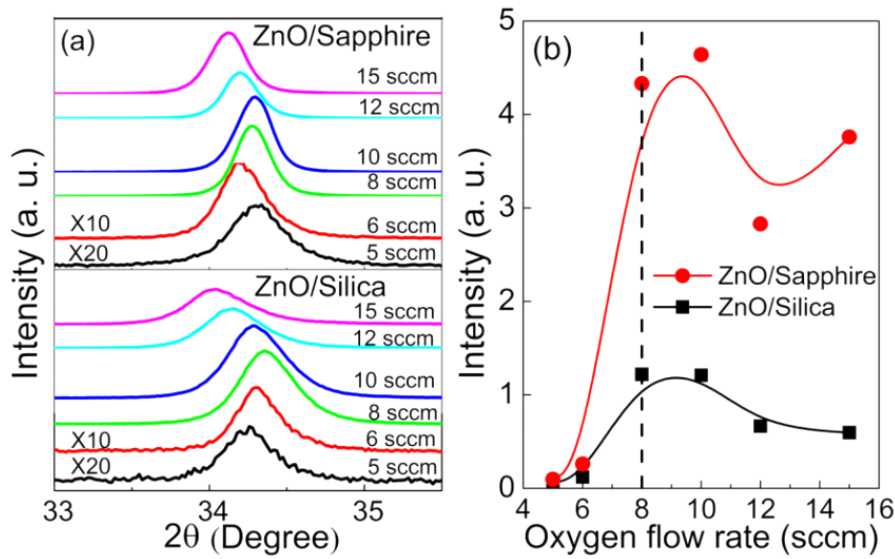


FIG. 3.3. Region of interest of the X-ray diffractograms of ZnO films deposited on fused silica and *c*-oriented sapphire for different *OFRs* (a). Evolution of the diffracted intensity with the *OFR* for films deposited on fused silica and (0001)-sapphire (b). The vertical dashed line indicates the critical oxygen flow rate (*c-OFR*).

This transition is accompanied by a strong increase of the diffracted intensity that sets to a nearly constant value for *OFRs* above or equal to 8 sccm on both substrates (fig. 3.3b). Indeed, the crystallinity is modified by the gas composition and resulting processes. In the following, we will verify that 8 sccm can be considered as a critical *OFR* (*c-OFR*) from the microstructural point of view as well. Although the trends for the evolution of the crystallinity with the *OFR* are similar for ZnO films deposited on fused silica and sapphire, the intensity diffracted by ZnO is approximately four-fold higher on sapphire. As all the films are of the same thickness, this result suggests a strong

interaction between the ZnO and sapphire crystal networks. Such an interaction is expected to increase the grain size by facilitating coherent in-plane growth.

Fig. 3.4a plots the evolution of the length of coherence domains  $L$  with the  $OFR$ .  $L$  has been evaluated from the full width at half maximum (FWHM) of the (0002) diffraction peak using the Scherrer formula<sup>138</sup>. Here, the difference of behaviors on fused silica and sapphire is striking. For the lowest  $OFR$ ,  $L$  is nearly the same on both substrates, i.e. around 30 nm. It increases slightly as the  $OFR$  is increased from 6 sccm. Starting from the  $c$ - $OFR$  of 8 sccm,  $L$  tends to stabilize to low and high values around 25 and 50 nm on fused silica and sapphire, respectively. Indeed, the growth conditions are clearly modified near the  $c$ - $OFR$ . Moreover, these results confirm a strong ZnO-sapphire interaction activated through the  $OFR$ , which is further investigated in the following.

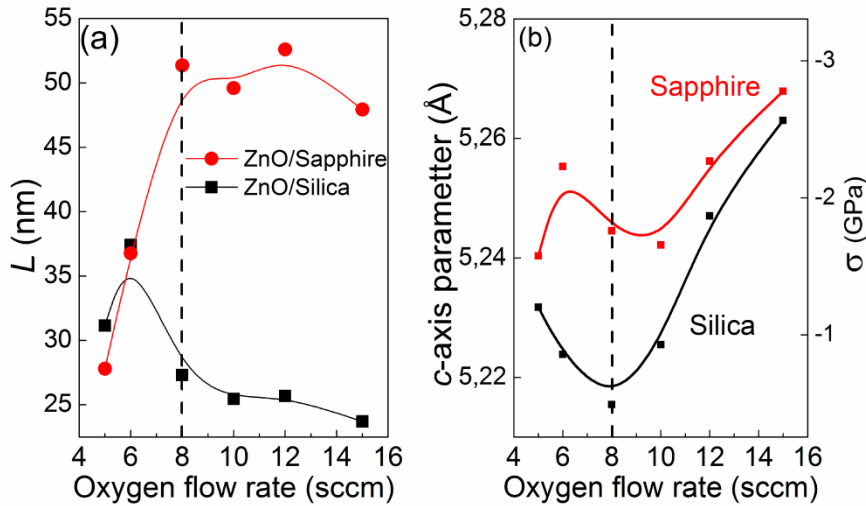


FIG. 3.4. Evolution of the length of coherence domains (a) and of the  $c$ -axis parameter of the wurtzite cell structure (b) with the oxygen flow rate of ZnO films deposited on fused silica and (0001)-sapphire. The vertical dashed line indicates the critical oxygen flow rate ( $c$ - $OFR$ ).

Looking more carefully at fig. 3.3a, it is observed that the (0002) diffraction peak is shifted towards lower values of  $2\theta$  for all investigated deposition conditions with reference to  $34.43^\circ$  for bulk ZnO. Moreover, the magnitude of the shift is depending on the synthesis conditions. According to the well-known Bragg's law, this corresponds to an elongation of the  $c$ -axis parameter, which evolution with the  $OFR$  is plotted on fig.

---

3.4b for both substrates. In-plane XRD measurements (Annex A) have been conducted and allowed to evaluate the a-axis parameter of the films deposited at 10 sccm on fused silica. A value of 3.2527 Å was found, against 3.2539 Å for bulk ZnO. Therefore, the out of plane elongation of the *c*-axis parameter is accompanied by a contraction in-plane. Indeed, in-plane compressive stresses  $\sigma$  are in action. The magnitude of these stresses was evaluated for all deposition conditions using the average uniform strain  $e_{zz}$  along the *c*-axis parameter and a biaxial in-plane strain model:

$$e_{zz} = \frac{c - c_0}{c_0} \quad (3.1)$$

$$\sigma = \left[ C_{13} - \frac{(C_{11} + C_{12})C_{33}}{2C_{13}} \right] e_{zz} \quad (3.2)$$

With  $c_0$  (5.2042 Å) the bulk and  $c$  the experimental *c*-axis parameters,  $C_{ij}$  the elastic stiffness constants ( $C_{11} = 2.1 \times 10^{11}$  N/m<sup>2</sup>,  $C_{33} = 2.1 \times 10^{11}$  N/m<sup>2</sup>,  $C_{12} = 1.2 \times 10^{11}$  N/m<sup>2</sup>, and  $C_{13} = 1.05 \times 10^{11}$  N/m<sup>2</sup>)<sup>134,139</sup>.

The evolution of  $\sigma$  with the *OFR* is displayed on fig. 3.4b for all deposition conditions on both types of substrates;  $\sigma$  is compressive in all cases. As the semi-transparent film produced with an *OFR* of 5 sccm can contain a significant amount of metallic zinc it is not considered for the discussion. Doing so, an asymmetric reverse bell-shape with a minimum close to the *c-OFR* is observed for deposition on both fused silica and sapphire substrates (fig. 3.4b). Due to the amorphous character of silica, the presence of epitaxial conditions for this substrate cannot explain this evolution. Moreover, a possible influence of thermal stresses can be ruled out since the deposition temperature is very close to room temperature. Hence, the observed behavior on fused silica should be related with the presence of crystal defects and impurities<sup>140</sup>. We can then propose that the *c-OFR* corresponds to the condition enabling to obtain the closest composition to stoichiometric ZnO. It is therefore likely related to the change in condensation mechanisms upon increasing the *OFR* as hypothesized above. Here, it is necessary to precise that the defect densities corresponding to stoichiometric ZnO in normal conditions cannot be reached with room temperature magnetron sputtering due to high associated cooling rates that favor the presence of point defects. At the zinc-rich side, the magnitude of  $\sigma$  on sapphire is 3 to 4-fold that on fused silica (-1.8 GPa on sapphire

---

and -0.5 GPa on fused silica at the *c*-*OFR*). The difference is less pronounced and tends to nullify at the oxygen-rich side. Since the condensing particles are supposed to impinge similarly the fused silica and sapphire substrates during growth, higher values of  $\sigma$  on sapphire could be related to the lattice mismatch between ZnO and sapphire within epitaxial growth conditions. Previous works have shown it is possible to obtain an heteroepitaxial growth of single-oriented ZnO on (0001) sapphire at relatively low temperature (<100 °C). The mechanism responsible for this growth is related with the formation of an O-Zn=O-Al interface and was proposed to involve energetic species produced during sputtering and high mobility of Zn surface atoms in zinc-rich conditions<sup>141,142</sup>. Structural and microstructural signatures of epitaxial growth are therefore investigated hereinafter.

$\varphi$ -angle scan X-ray diffractograms (see chapter 2, sections 2.4.1) can be used to differentiate if a film is textured or if it grows in epitaxy with the sapphire substrate. Fig. 3.5 shows  $\varphi$ -scan X-ray diffractograms using the  $2\theta$  angles corresponding to the diffraction by the  $\{10\bar{1}1\}$  planes of ZnO and  $\{10\bar{1}4\}$  planes of sapphire for the films deposited on sapphire. The signal for a film deposited on fused silica was used for comparison. Two peaks separated by 120° are visible on the diffractograms of sapphire, which is characteristic of the 3-fold symmetry around the *c*-axis of the rhombohedral structure of sapphire. No specific symmetry is apparent for ZnO films deposited on silica and weak signal is observed for the semi-transparent and slightly absorbent films deposited with the two lowest *OFR*s of 5 and 6 sccm on sapphire. In contrast, the 6-fold symmetry characteristic of single-domain epitaxial wurtzite ZnO becomes significant at the *c*-*OFR* and above and the diffracted intensity increases with the *OFR*.

To confirm the epitaxial growth and the absence of macles or twins, XRD pole figures (see chapter 2, section 2.4.1.) of the (0002) and the  $\{11\bar{2}2\}$  planes of hexagonal ZnO have been collected. The pole figure of the  $\{11\bar{2}2\}$  ZnO planes (fig. 3.6) confirms the hexagonal ZnO 6-fold symmetry despite broad peaks are observed. The small dots and the narrow peaks in the pole figure correspond to the diffraction by  $\{21\bar{3}4\}$  and  $\{30\bar{3}0\}$  peaks of the -sapphire substrate. The detection of a single peak in the center of the stereographic representation of the (0002) ZnO plane reveals the absence of twins.

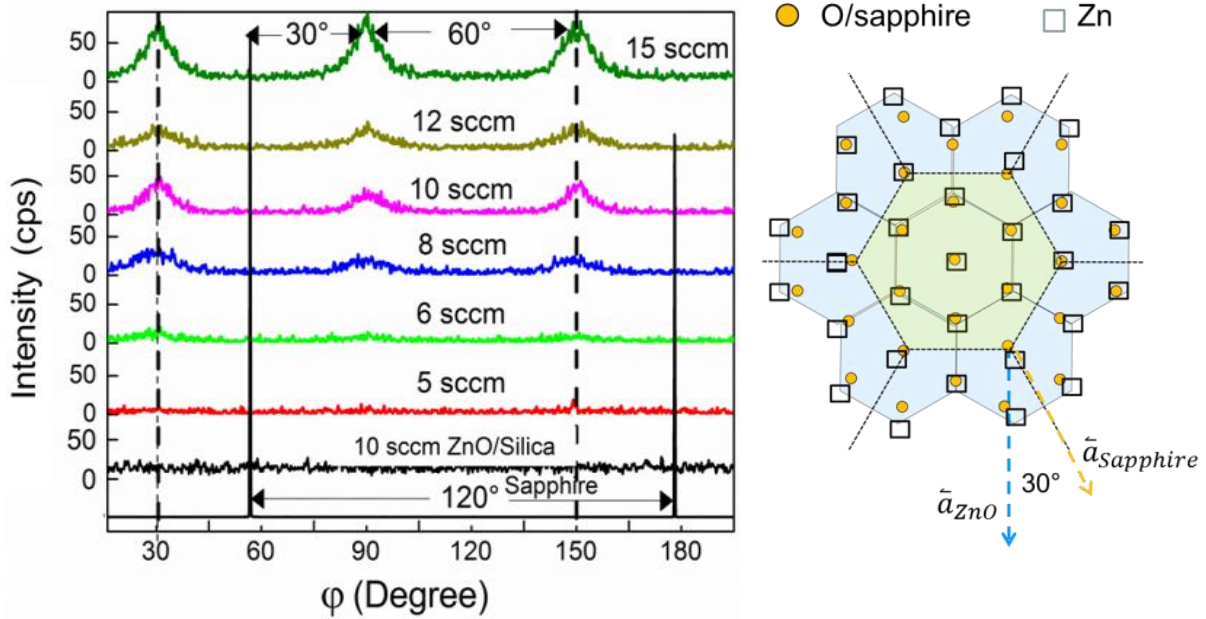


FIG. 3.5. (left) X-ray diffraction  $\phi$ -scans for the signal originating from  $\{10\bar{1}1\}$  ZnO films deposited on (0001)-sapphire for different oxygen flow rates. The signal from the  $\{10\bar{1}4\}$  planes of sapphire and from a ZnO film deposited on silica are used as references. (Right) Representation of the in-plane lattice orientation of ZnO with respect to the  $\text{Al}_2\text{O}_3$  substrate showing the  $30^\circ$  shift. The yellow lattice corresponds to the sapphire and the blue corresponds to the ZnO lattice. The yellow dots are oxygen atoms in the sapphire structure and black squares are the Zn atoms in the ZnO film.

Recalling the  $\phi$ -angle scan results, we can consider that there are different possible epitaxial relationships between  $c$ -axis oriented sapphire and  $c$ -axis oriented wurtzite zinc oxide crystals, but a rotation of  $30^\circ$  of the  $a$ -axis of ZnO with respect to the sapphire substrate is usual and allows the lowest strain in the ZnO film<sup>143-146</sup>. This situation is observed here since the  $\{10\bar{1}1\}$  peaks of ZnO are displaced by  $30^\circ$  with respect to the  $\{10\bar{1}4\}$  peaks of sapphire. The epitaxial relationships describing this situation are  $\text{ZnO}[0001]/\text{Al}_2\text{O}_3[0001]$  out of plane and  $\text{ZnO}[10\bar{1}0]/\text{Al}_2\text{O}_3[11\bar{2}0]$  in-plane. These relationships lead to a theoretical lattice mismatch of 1.4 % that can be partially accommodated by in-plane compressive stresses. Indeed, higher in-plane compressive stresses on sapphire (see fig. 3.4b) are explained by the development of single-domain epitaxial growth of ZnO at low temperature.

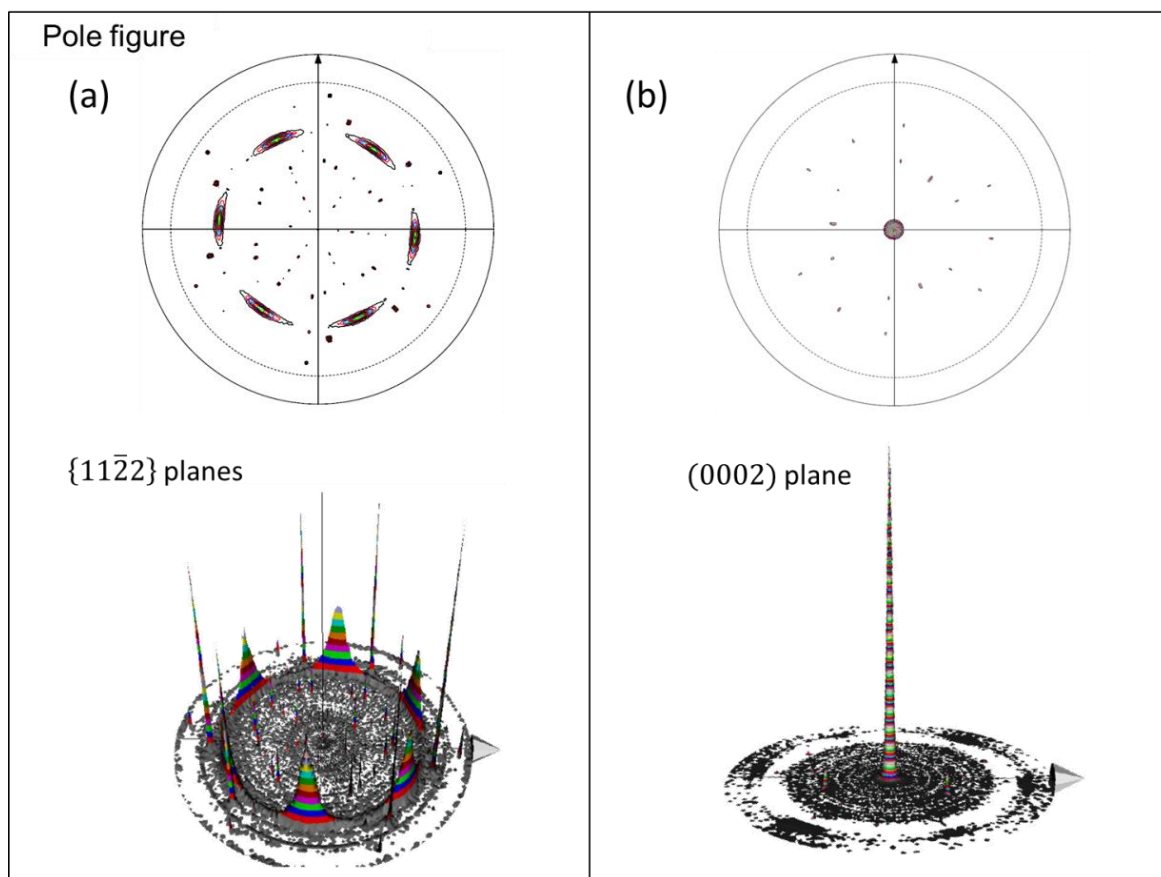


FIG. 3.6. Pole figure and 3D representation of the (a)  $\{11\bar{2}2\}$  and (b) (0002) diffraction planes of a ZnO film grown at an *OF*R of 15 sccm.

TEM analyses were performed for direct observations of the microstructure for the most different growth conditions on sapphire substrates. For the film deposited with the lowest *OF*R, a columnar growth microstructure is observed on the bright and dark field images (fig. 3.7a and fig. 3.7c). The selected area electron diffraction (SAED) pattern (fig. 3.7b) shows the presence of spots located on 3 rings corresponding to the diffraction by the (0002),  $\{10\bar{1}1\}$  and  $\{10\bar{1}0\}$  planes of ZnO. This is consistent with a polycrystalline microstructure and the absence of a clear in-plane 6-fold symmetry in the  $\varphi$ -scan of this sample (fig. 3.5). In contrast, the bright and dark field images obtained with the highest *OF*R (15 sccm) do not reveal the presence of grain boundaries (fig. 3.7d and fig. 3.7f).

Nevertheless, fluctuations of the diffracted contrast are obvious, which indicate the presence of microstrains. The latter can result from the relaxation in the FIB lamella of

compressive stresses  $\sigma$  developed during film growth (see fig. 3.4). The SAED pattern obtained placing the diaphragm as illustrated by the red circle on fig. 3.7d and with  $[\bar{1}2\bar{1}0]$  ZnO and  $[1\bar{1}00]$  Al<sub>2</sub>O<sub>3</sub> in zone axis condition, is shown in fig. 3.7e. It is constituted of sharp spots corresponding to the diffraction by the ZnO and sapphire crystal networks with their *c*-axis oriented parallel to the growth direction and the  $\{10\bar{1}0\}$  planes of ZnO and  $\{11\bar{2}0\}$  planes of sapphire parallel to each others. These measurements are fully consistent with the epitaxial orientations derived from  $\varphi$ -scan X-ray measurements (fig. 3.5). The same conclusions were drawn from the SAED analysis of the film synthesized at the *c*-OFR of 8 sccm which, nevertheless, showed less localized diffraction spots for ZnO. Hence, a simple variation of the gas composition sets the conditions for single-domain epitaxial growth along the *c*-axis of wurtzite ZnO without any thermal assistance.

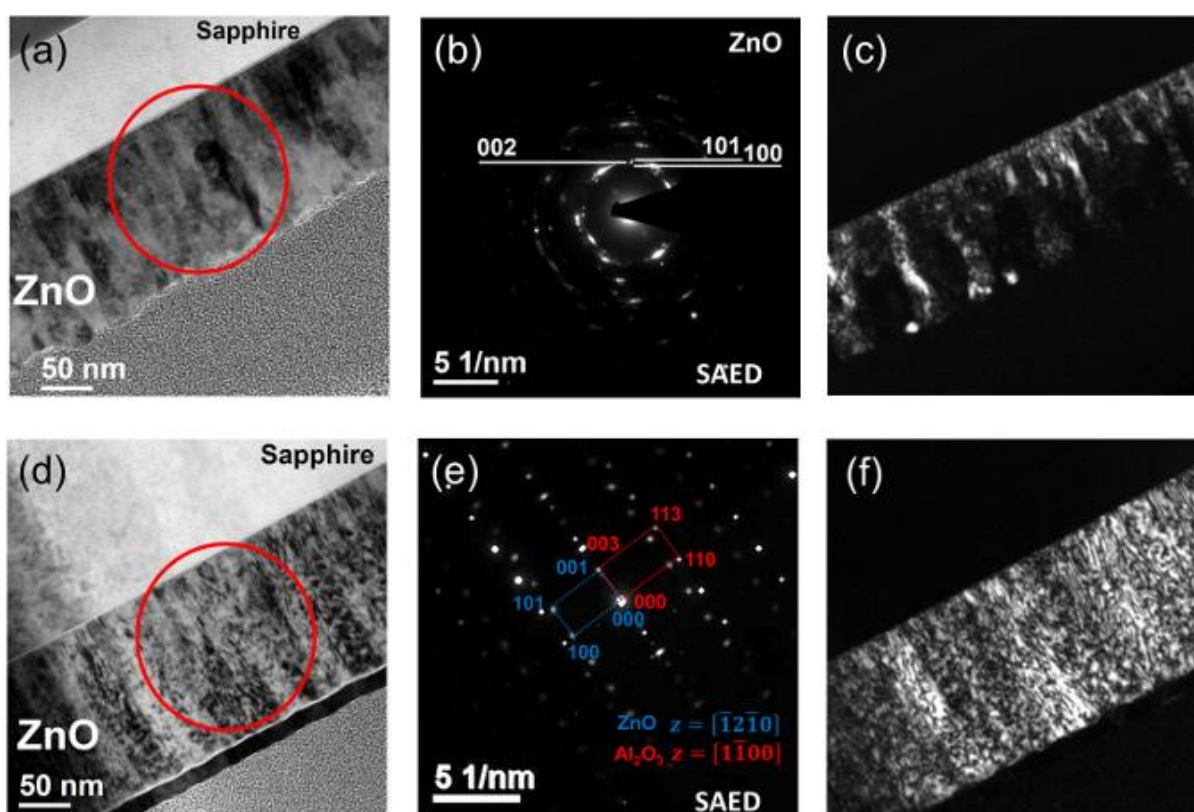


FIG. 3.7. Bright field, dark field images and selected area electron diffraction pattern of ZnO films deposited on (0001)-oriented sapphire at oxygen flow rates of 5 sccm (a-c) and 15 sccm (d-f).

---

### 3.2.2. Composition and defect chemistry

In reactive magnetron sputtering experiments the composition of the reactive gas mixture influences the film and target surface composition. Fig. 3.8a shows the evolution of the oxygen composition of the films  $C_O^F$  with the *OFR*. Progressive oxygen enrichment is observed as the gas composition is made more oxidative up to an *OFR* of 12 sccm at which saturation of the chemical composition is observed. Although these measurements result from a calibration and each point is the average of ten collections, it should not be taken as quantitative but give the trend for the evolution of the oxygen content. These results along with optical measurements of fig. 3.2 likely indicate a transition of the oxygen content from sub- to over-stoichiometry with the *OFR*, which will be further discussed in the next paragraph using the results of photoluminescence spectroscopy measurements. The inset displays the discharge voltage  $V_d$  with the *OFR*. As already mentioned above, the decrease in  $V_d$  from  $\sim 370$  V to  $\sim 320$  V as the *OFR* is increased from 5 to 15 sccm, indicates a modification of the average oxidation state of the zinc target surface accompanied by an increase of the secondary electron emission yield<sup>108,147</sup>. Indeed, compositions of the film and target surface evolve simultaneously.

In order to evaluate the consequence of the modification of the oxygen content in the films on the formation of chemical defects, room temperature photoluminescence spectra have been collected. These are displayed in fig. 3.8b for different values of the *OFR*. A near band edge (*NBE*) emission centered around 380 nm, usually ascribed to the recombination of free excitons, and a broad visible emission, ascribed to the recombination of bound excitons, are observed for all conditions. The intensity of the *NBE* emission decreases upon oxidation of the films, which is certainly related to a change in the density of free carriers and defect chemistry. Additionally, the visible emission has been deconvoluted in three contributions carrying information on the defect chemistry. Contribution P1 (maximal intensity at 527 nm-green) is ascribed to the transition between a shallow level ( $Zn_i$ ) and an oxygen vacancy ( $V_o$ ) level, while contribution P2 (560 nm-yellow) is ascribed to the transition between the conduction band and the deep level of oxygen interstitial ( $O_i$ )<sup>148,149</sup>. Contribution P3 (648 nm-orange-red) has not clearly been ascribed so far but could be related to a modification of the *c*-axis parameter and to a transition from a shallow level to the  $O_i$  level<sup>150,151</sup>.

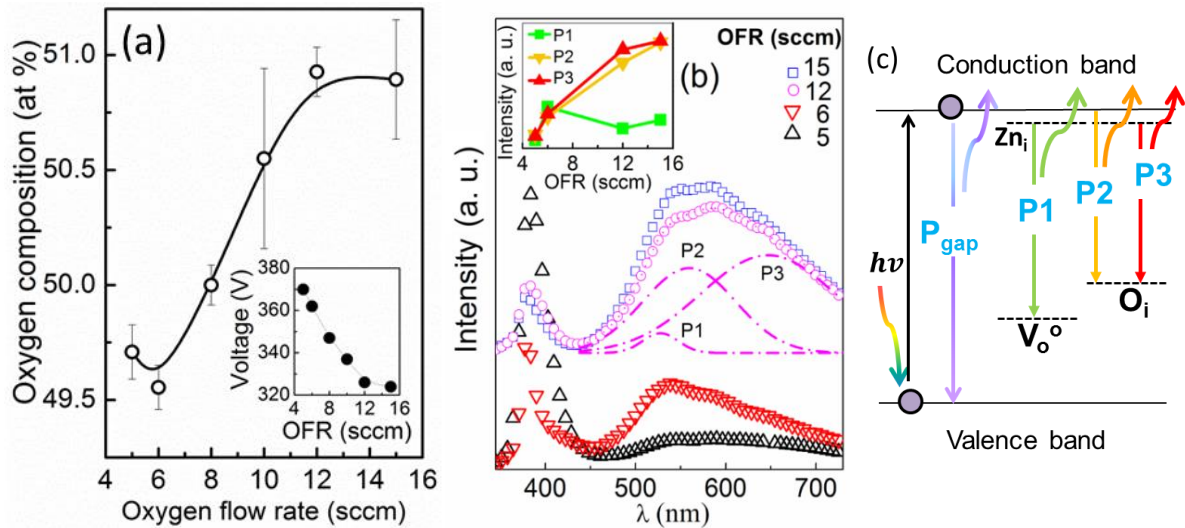


FIG. 3.8. Evolution of the oxygen content and discharge voltage  $V_d$  (insert) with the oxygen flow rate for all synthesized films (a). The vertical dashed line indicates the critical oxygen flow rate ( $c$ -OFR). Photoluminescence spectra of ZnO films deposited at different oxygen flow rates (b). An example for the deconvolution of the visible signal in three contributions is shown for the oxygen flow rate of 12 sccm. The insert shows the evolution of the maximal intensity of each contribution with the oxygen flow rate. (c) Schematic diagram showing the interband and intraband transitions in the ZnO films.

The evolution of the intensity of P1-P3 with the OFR is plotted as inset of fig. 3.8b. P1 tends to decrease with the OFR, which logically indicates the least presence, in more oxidative synthesis conditions, of chemical defects usually associated to oxygen substoichiometry. Complementary, P2 and P3 increase with the OFR, following a trend similar to the oxygen content. Hence, it is proposed that the oxidation of the film proceeds in a significant extent by generation of oxygen interstitial defects (fig 3.8c).

In order to gain more confidence on the defect chemistry assumed from the previous investigations, low temperature PL measurements have been performed near the band edge. Those measurements also carry information on the defect chemistry<sup>152,153</sup>. The low-temperature-PL spectrum of ZnO can be divided in four main energy regions according the nature of each emission process (fig. 3.9a). Region I, ranging from 3.37 to 3.42 eV, corresponds to the emission related to the A, B and C free excitons ( $FX_i$ , with  $i = A, B$  or C) recombinations. Region II, ranging from 3.37 to 3.33 eV, correspond to neutral

donor and/or acceptor defect bound-excitons ( $DX_i$  and/or  $AX_i$  with  $i = A, B$  or  $C$  exciton) emissions. From 3.33 to 3.30 eV, we find region III comprising the two electrons satellite effect and longitudinal optical phonon (LO) emissions and, at lower energies (region IV), LO replicas.

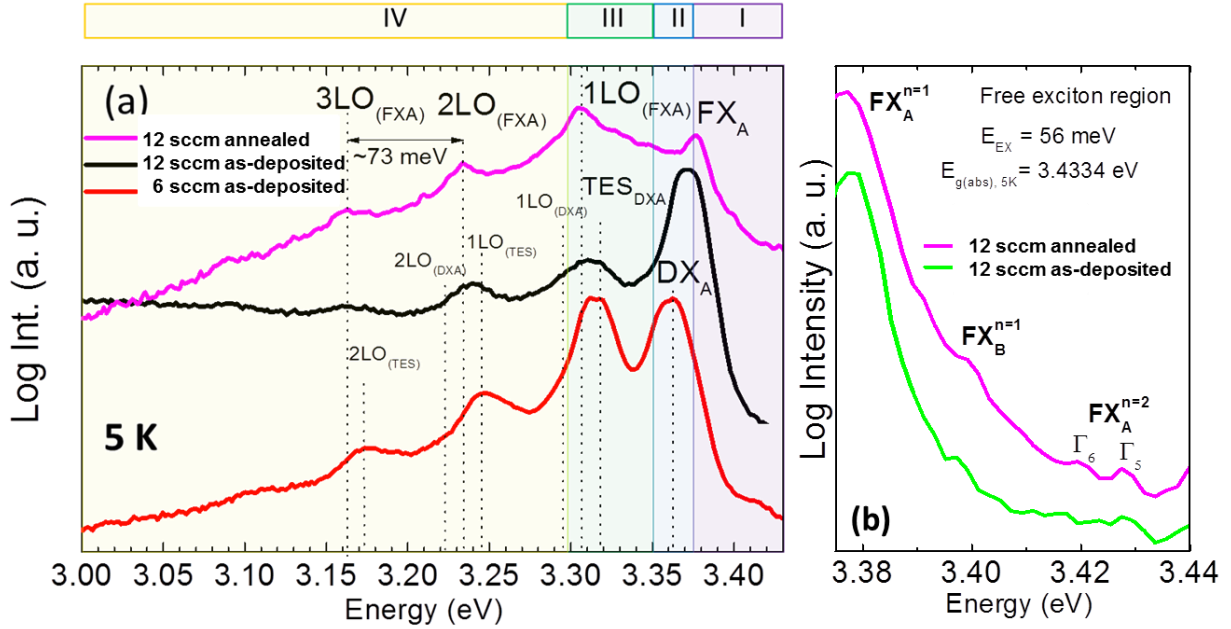


FIG. 3.9. (a) Photoluminescence spectrum at 5 K of ZnO grown at *OFRs* of 6 and 12 sccm. (b) Zoom of the photoluminescence spectrum at 5 K in the free exciton region for an annealed and an as-deposited ZnO films.

The photoluminescence spectra of as-deposited ZnO films synthesized with *OFRs* of 6 and 12 sccm and a of a film synthesized at 12 sccm and annealed at 300 °C under air for 1h are shown in fig. 3.9. The main contributions at 3.36 eV and 3.31 eV for the film as-deposited at 6 sccm correspond to electron transition from neutral donor defect to bound A exciton ( $DX_A$ ) and to its  $TES$  effect ( $TES_{DXA}$ ), respectively<sup>134,152</sup>. This confirms the predominance of donor defects at low *OFR*, as concluded from room temperature PL measurements. Consistently, phonon replicas of the  $TES_{DXA}$  are clearly identified in region IV. Signal from the A free exciton is not clearly identified but might be present at the high energy side of the  $DX_A$  peak, which is supported by the large width of the phonon signals. For the film deposited at 12 sccm, the  $TES_{DXA}$  signal is much weaker and the maximum of the exciton peak is shifted up close to the energy of the  $FX_A$  energy. This

---

is again in line with a lower density of donor defects. Therefore, low temperature PL measurements are consistent with room temperature PL measurements and confirm a least presence of donor defects in films synthesized at high *OFR*. After annealing the film deposited at 12 sccm, peaks are narrower and the spectrum is dominated by emissions subsequent to the recombination of free A excitons ( $FX_A$ ) and its phonon replica. Indeed, most of the donor defects appear to be cured by the annealing process in air at 300°C and the free exciton-*LO* Phonon interaction is strong. The latter point will be further discussed in the sections 3.3 and after.

From these low temperature measurements, it is also possible to extract the phonon energy and exciton binding energy in order to compare the data with those corresponding to typical ZnO films. In ZnO, the valence band splits in three valence states denoted as A, B and C<sup>134,152,153</sup> (see chapter 1, section 1.1.2), giving rise to the corresponding free exciton emissions ( $FX_i$ , with  $i = A, B$  or  $C$ ). At the high energy side of the PL spectra (fig. 3.9b), it is possible to detect the free exciton emissions<sup>152</sup>. After an annealing treatment, we observe the signal ground state of the A-free exciton emission ( $FX_A^{n=1}$ ) at 3.3773 eV and at a higher energy (3.4275 eV), a weak signal coming from the A-free exciton excited state ( $FX_A^{n=2}$ ) for the  $\Gamma_5$  band symmetry, The ( $FX_A^{n=2}$ ) signal corresponding to the  $\Gamma_6$  symmetry of the A-free exciton excited state appears at 3.4194 eV<sup>134</sup>. The difference in energy between the  $FX_A^{n=1}$  and the  $FX_A^{n=2}$  signals is related with the exciton binding energy as  $\Delta E = \frac{4}{3} E_{Exciton}$ <sup>134,154</sup>.  $E_{Exciton}$  is evaluated at 57 meV in our case, in agreement with the typical reported value of 60 meV in ZnO. The signal that appears at 3.3991 eV corresponds to the B-free exciton, the C-free exciton is not detected. In fig. 3.9a, near 3.31 eV we observe the ZnO *LO* phonon of the free exciton ( $LO_{(FXA)}$ ) signal and, at lower energies, its replicas separated by 73 meV. This separation corresponds to a frequency of 588  $cm^{-1}$  typical of the  $E_1$ -*LO* phonon.

From room temperature PL measurements it was possible to detect three main defects: the shallow donor zinc interstitial ( $Zn_i$ ), the deep donor oxygen vacancy ( $Vo$ ) and the deep acceptor oxygen interstitial ( $O_i$ )<sup>148,149</sup>. A brief description of each defect follows.

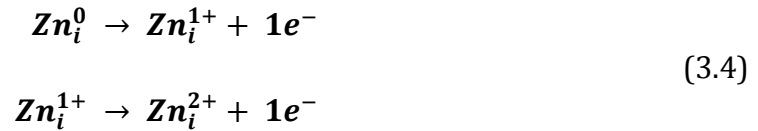
---

In zinc-rich conditions,  $V_O$  is the most stable defect and is present as a deep donor:



It is not involved in n-type conduction since its energy is at distance of at least 1 eV from the bottom of the conduction band<sup>16</sup>.

When  $Zn_i$  is inserted along the  $c$ -axis in a deformed octahedral configuration it reaches its most thermodynamically stable form. This stabilization is explained by a lower repulsion between atoms as shown by the atom distance, obtained from DFT calculations, for  $Zn_i-Zn$  is  $1,22d_0$  and for  $Zn_i-O$  is  $1,02d_0$ <sup>155</sup>. At zinc-rich conditions,  $Zn_i$  is relatively stable and, according to calculations, its energy level is located near the bottom of the conduction band. This means it can be involved in the n-type conduction as shallow donor defect (eq.3.4), eventually coupled to  $V_O$ <sup>21,156,157</sup> as also concluded from our room temperature PL measurements (fig. 3.9b).



$O_i$  exist in significant amount mainly at oxygen-rich conditions. It exists in three forms depending on the position in the unit cell<sup>158,159</sup>. For  $n$ -ZnO films, the most stable form is a two-bonded oxygen in a rotated bell-shape that is a deep acceptor defect:

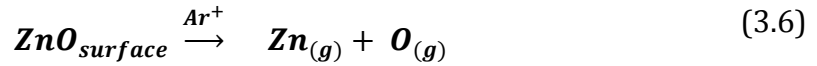


Based on the previous results, we can state that the density of this defect appears higher above a critical oxygen flow rate in the transition between the elementary and compound sputtering regimes. Based on the results presented above, it can be stated that the possibility to achieve single-domain epitaxy of wurtzite zinc oxide films on (0001) sapphire near-room temperature with reactive magnetron sputtering goes on with the transition from sub- to over-stoichiometric films and an evolution of the compressive stresses that reach a minimum near the film stoichiometry. The following section discusses the possible origin of the observed evolutions.

---

### 3.2.3. Oxygen ion bombardment.

As oxygen atoms are sputtered from the partially or fully oxidized target surface, it can capture a secondary electron emitted by the target<sup>160,161</sup>, leading to the formation of  $O^-$  ions :



Such ions can be further accelerated in the cathode sheath (fig. 3.10).

The flux of  $O^-$  species is very difficult to quantify but an empirical, though apparently universal, expression can be used to evaluate its dependency to the discharge voltage  $V_d$  for sputter-deposition of oxides<sup>161</sup>:

$$\gamma(O^-) = c * N(O) * \exp\left(\frac{1}{V_d}\right) \quad (3.8)$$

With  $\gamma(O^-)$  and  $N(O)$  the fluxes of  $O^-$  ions emitted by the target and sputtered oxygen atoms, respectively;  $c$  is a constant. We see that the flux of  $O^-$  ions emitted upon surface oxidation of the zinc target increases as  $N(O)$  rises from zero and as  $V_d$  decreases (fig. 3.8a). Indeed, the emission of  $O^-$  ions dramatically increases during the transition from metallic to compound sputtering regimes. We can estimate the number of collisions experienced by these emitted ions during their drift from the target surface to the substrate. The mean free path for the collisions of the oxygen projectile and the argon background gas  $\lambda_{O-Ar}$  can be approached by:

$$\lambda_{O-Ar} = \frac{k T_g}{\sqrt{2}(\pi r_O^2 + \pi r_{Ar}^2) P_{Ar}} \quad (3.9)$$

With the atomic radii  $r_O = 48$  pm,  $r_{Ar} = 71$  pm,  $P_{Ar} = 0.5$  Pa,  $k$  the Boltzmann constant and  $T_g = 300$  K, we find  $\lambda_{O-Ar} = 250$  mm, which by far exceeds the target-substrate distance. Therefore, fast oxygen particles impinge the surface of the growing film with a kinetic energy close to  $V_d$ , as confirmed by recent experiments with a similar pressure and target-substrate distance<sup>162</sup>. It can also be considered that a small portion (we estimate

to 6 % using the Monte Carlo SRIM code<sup>163</sup>) of the  $O_2^+$  species formed in the bulk of the plasma phase are neutralized, dissociated and reflected by the target surface. The kinetic energy of the so formed neutral O species is close to  $0.2 V_d$ , i.e. 60 eV<sup>162</sup>. It is known that the bombardment of ZnO by fast oxygen particles generates point defects to accommodate oxygen enrichment above the equilibrium stoichiometry of ZnO<sup>164</sup>. Using SRIM, we find that these particles have an implantation probability close to 90 % and locate within the first 5 nm below the film surface for the experimental conditions used. This estimate is in line with the observed oxygen over-stoichiometry above the *c-OFR* (fig. 3.8a). As evidenced by PL measurements, the chemical/structural defect associated to this over-stoichiometry is very likely oxygen interstitial. Complementarily, the density of zinc interstitials can be significant at low oxygen pressure and high Zn pressure in the metallic mode under non-equilibrium conditions<sup>155,165,166</sup>. Both interstitial defects generate local strains in the wurtzite cell and easily explain the reverse bell-shape evolution of  $\sigma$  with the *OFR* and the minimal stress state near the *c-OFR*.

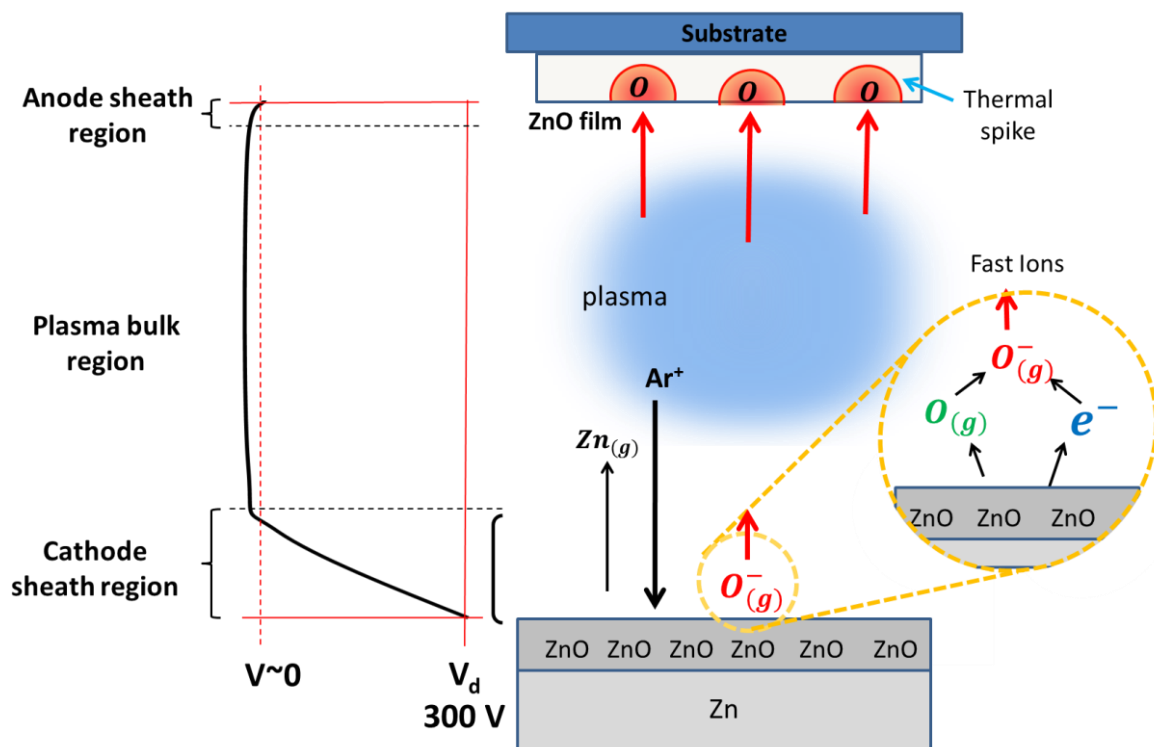


FIG. 3.10. Scheme of the oxygen ion bombardment mechanism after the critical-*OFR*.

---

Achieving epitaxial growth requires that the condensing Zn and O atoms have sufficient surface mobilities to position at the optimal thermodynamic and crystallographic sites. It can be achieved through different phenomena following the impact of the fast particles on the film surface. The kinetic energy carried by the fast O<sup>-</sup> ions (around 300 eV upon impact with the film surface) emitted by the target can easily displace chemisorbed and bulk Zn and O atoms because it by far exceeds the upper limit of the bulk displacement energy of zinc  $E_d(\text{Zn}) = 65 \text{ eV}$  and oxygen  $E_d(\text{O}) = 50 \text{ eV/at}^{167}$ . Simulations showed that implantation events induce displacement cascades at the 100 femtosecond timescale followed by a picosecond timescale thermal spike phase in the perturbed volume during which the mobility of atoms is very high<sup>116</sup>. Subsequently, thermal phonons travel away from the initial cascades zone also facilitating the diffusion on their path. As these events occur very close to the vacuum-film interface, it can strongly enhance the adatom mobility.

We propose that the possibility to form epitaxial ZnO at such a low temperature is explained by the transformation of the kinetic energy of fast oxygen particles into the mobility of the adatoms. A simplified scheme of the ion bombardment mechanism can be seen in fig. 3.10.

Fig. 3.11 summarizes the most important results of the previous sections. Increasing the oxygen flow rate fed into the deposition chamber results in a transition from sub- to over-stoichiometric ZnO films. This transition is accompanied by a change in the defect chemistry as oxygen interstitials are incorporated in the wurtzite cell. Within this transition, single-domain epitaxy of wurtzite ZnO develops on sapphire as probed with  $\varphi$ -scan X-ray diffraction and transmission electron microscopy. The ZnO single crystal is systematically oriented with the *c*-axis along the growth direction and ZnO[10 $\bar{1}$ 0]/Al<sub>2</sub>O<sub>3</sub>[11 $\bar{2}$ 0] relationship in-plane. The possibility to form epitaxial ZnO at such a low temperature is explained by the transformation of the kinetic energy of fast oxygen particles into the mobility of the adatoms. Zinc interstitial atoms and oxygen vacancies are present in large proportions in zinc-rich conditions while the density of oxygen interstitials increases as the gas mixture is made progressively more oxidative.

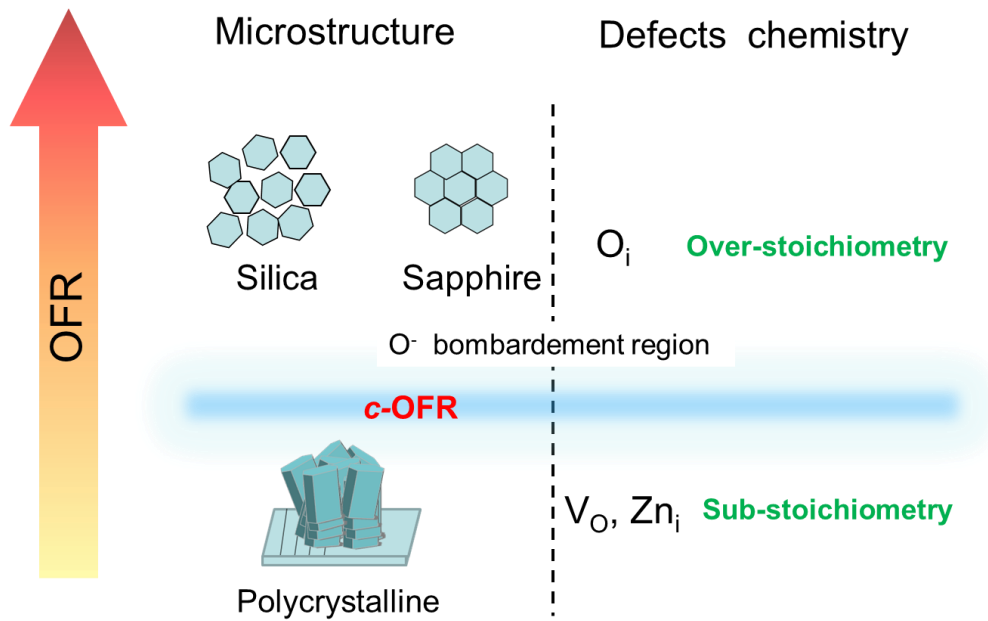


FIG. 3.11. Scheme of the in microstructure and defect chemistry evolution as a function of the *OFR* for ZnO thin films grown on fused silica and (0001)-Sapphire substrates.

### 3.3. Near absorption edge optical properties

Due to the importance of the optical properties of ZnO thin films, it is necessary to have an accurate determination of the bandgap energy ( $E_g$ ). However, in the literature there is a large scatter in the reported values of  $E_g$ <sup>168-174</sup>, suggesting several factors related with the synthesis route and experimental parameters influence the bandgap energy. Changes in  $E_g$  are often explained by changes in the carrier density through the Burstein-Moss (*BM*) effect and bandgap narrowing (*BGN*). Besides, it is important to point out that the obtained values can differ significantly depending on the measurement method. The absorption bandgap energy ( $E_{g(abs)}$ ) can be extracted from spectrophotometry measurements following the Tauc approach (see chapter 2, section 2.4.5), while the emission bandgap energy ( $E_{g(ems)}$ ) can be accessed using, for instance, photoluminescence spectroscopy PL and is referred as the near band edge (*NBE*) emission already described in the previous section.

---

We discussed in the first part of this chapter how modifications of the *OFR* and the nature of the substrate determine the microstructure of the ZnO films. Moreover, it was shown that the stoichiometry and related defect chemistry depend directly on the synthesis conditions and affect the optical response of the film (see fig. 3.2 and fig. 3.8). In this section we discuss the role of the chemical defects in the ZnO thin films optical response.

### 3.3.1 ZnO Urbach energy

It has already been commented above that near-room temperature synthesis of thin films with magnetron sputtering introduces a large density of defects due to highly energetic particles bombarding the film surface<sup>175-177</sup> and high cooling rate associated to the condensation mechanism. The presence of defects may have a deep and complex impact on the thin film properties and, particularly, on the optical and electrical properties<sup>178,179</sup>. The presence of cracks, pores or precipitates (3D defects), grain boundaries (2D defects), dislocations (1D defects) or vacancies or interstitial sites (0D defects) affect the microstructure and optical response of thin films but it is difficult to determine the contribution of each defect in the material<sup>134,180</sup>.

In ZnO thin films grown at low and high *OFR* we did not find evidence of 3D defects by TEM. All measured films were found densely packed with columnar growth or monocrystalline character depending on the synthesis parameters (fig. 3.7 gives representative situations). More particularly no evidence of precipitation of a second phase has been found neither with XRD or SAED. Therefore, the influence of 3D defects on optical properties is *a priori* neglected.

From fig. 3.12, it is observed that the absorption tail below the absorption edge is characterized by a higher absorption coefficient and is wider for films grown at low *OFR* than for films grown at high *OFR*, whatever the nature of substrate used (fused silica or sapphire). It is also observed that the nature of substrate have little influence on the tail shape. This is also true for the edge position. This reveals that the length of coherence domains  $L$  (see fig. 3.4) and, therefore, the grain size does not affect significantly the

optical absorption meanwhile the *OFR* is the main factor that changes the absorption response in this energy range. Hence, this discards a strong influence of grain boundaries (2D defects) on the optical response. As a consequence, we study in the following only the influence of point defects (electrically active or inactive) such as vacancies or interstitial atoms on the bandgap energy for films deposited on fused silica.

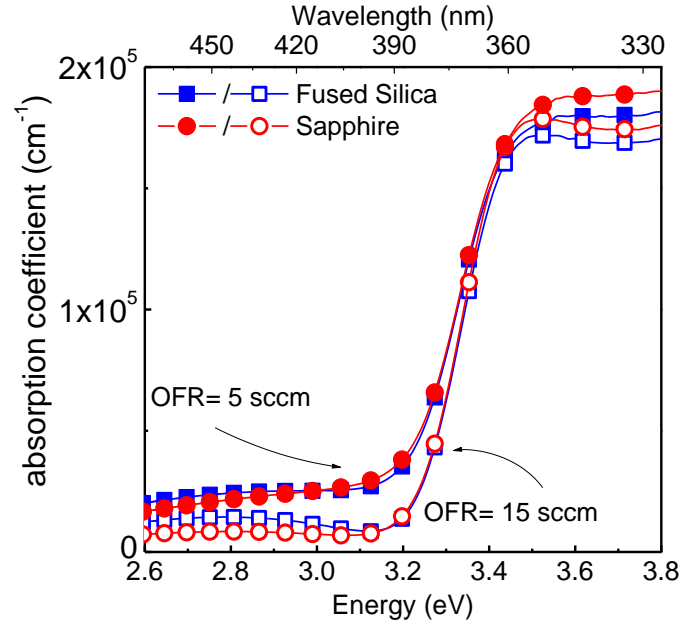


FIG. 3.12. Evolution of the absorption coefficient of ZnO films deposited on fused silica (blue squares) and (0001)-sapphire (red circles) at *OFRs* of 5 sccm (filled symbol) and 15 sccm (open symbol).

In chapter 2, section 2.4.5.3 we discussed about the exponential tails at the edges of optical interband that occurs in semiconductors and can be characterized by the Urbach energy<sup>181</sup>. The understanding of this behavior could give information about changes in  $E_g$  of a semiconductor. It has been shown that there is a relationship between the absorption coefficient and the Urbach energy ( $E_u$ ) that universally fits the absorption tail in semiconductors<sup>30,182</sup>:

$$\alpha = A \exp(h\nu/E_u), \quad \text{with } E_u = \frac{kT}{\sigma} \quad (3.10)$$

To describe the influence of electrically active impurities, Dow and Redfield proposed a refinement of the Urbach model<sup>183-185</sup>, in which electrical impurities could produce

---

electric field microfluctuations affecting the Urbach energy. According to this model, the presence of microfields perturbs the internal, relative motion of the exciton, leading to an electric-field-induced ionization of the exciton. In a detailed form, the absorption coefficient depends on the photon energy ( $h\nu$ ), the electric field ( $F$ ) and the probability  $P$  to find a field with magnitude  $F$ . The average of all the microfield source contributions can be expressed from the root mean square electric field strength ( $F_{RMS}$ ):

$$F_{rms} = \frac{2\varepsilon_0}{\sqrt{3\varepsilon^*\pi ea}} \coth \left[ \frac{E_p}{2kT} \right] \quad (3.11)$$

Whit  $\varepsilon^*$  the polaron effective dielectric constant expressed as  $\varepsilon^* = (1/\varepsilon_\infty - 1/\varepsilon_0)^{-1}$ ,  $E_p$  the phonon energy and  $a$  the 1s exciton radius (related with the binding energy). In general, in the absorption edge it is possible to confirm that:

$$\alpha \propto e^{C(E-E_0)/F_{rms}} \quad (3.12)$$

Showing that the Urbach energy is proportional to the field strength

$$E_u \propto \frac{F_{rms}}{C} \quad (3.13)$$

The introduction of electrically active defects increases  $F_{RMS}$  and, therefore,  $E_u$ . Equations 3.11 and 3.13 shows that such influence can be followed experimentally by the determination of the polaron effective dielectric constant  $\varepsilon^*$ . The lower  $\varepsilon^*$  the higher  $F_{RMS}$  and  $E_u$ , meaning that there is a stronger interaction between the defects and the exciton.

Fig. 3.13a presents the evolution of  $E_u$  as a function of the *OFR* for as-deposited and annealed films. For as-deposited films,  $E_u$  decreases rapidly while changing the *OFR* from 5 to 6 sccm. It keeps decreasing at higher *OFR*s but much slower with the *OFR*. After annealing the films in air at 300°C,  $E_u$  is nearly constant and lower than in as-deposited films (a slight decrease with the *OFR* is still observed at low *OFR*s).

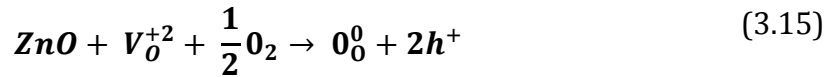
The main difference in annealed films is a higher magnitude of  $\varepsilon^*$  in the zinc-rich region. Consistently with the results from the previous section, this can be interpreted as a decrease in the density of electrically active donor defects, leading to a more covalent ZnO than as-deposited intrinsically doped-ZnO. From a chemical perspective this can be explained by the fact that, in zinc-rich conditions, an increase in temperature leads to

consumption of  $Zn_i$  eased by its high diffusion coefficient compared to other defects, which may be related with its ionic radius (74 pm)<sup>186-188</sup>.



We note that this process consumes electrons and should, therefore, render the films more resistive.

Annealing in air also leads to a decrease in the density of oxygen vacancies:



The evolutions of the Urbach energy in the case of the coatings deposited within this study can be understood knowing that the electric microfield strength increases with with heavy doping<sup>185</sup>. Consistently, it was only possible to estimate the carrier density at  $3,1 \times 10^{19} \text{ cm}^{-3}$  in the film of higher  $\epsilon^*$  as-deposited at 5 sccm, which is a similar value to some doped ZnO films<sup>174,189,190</sup>. Moreover, annealing this film in air as well as all other deposition conditions led to too resistive films to be measured.

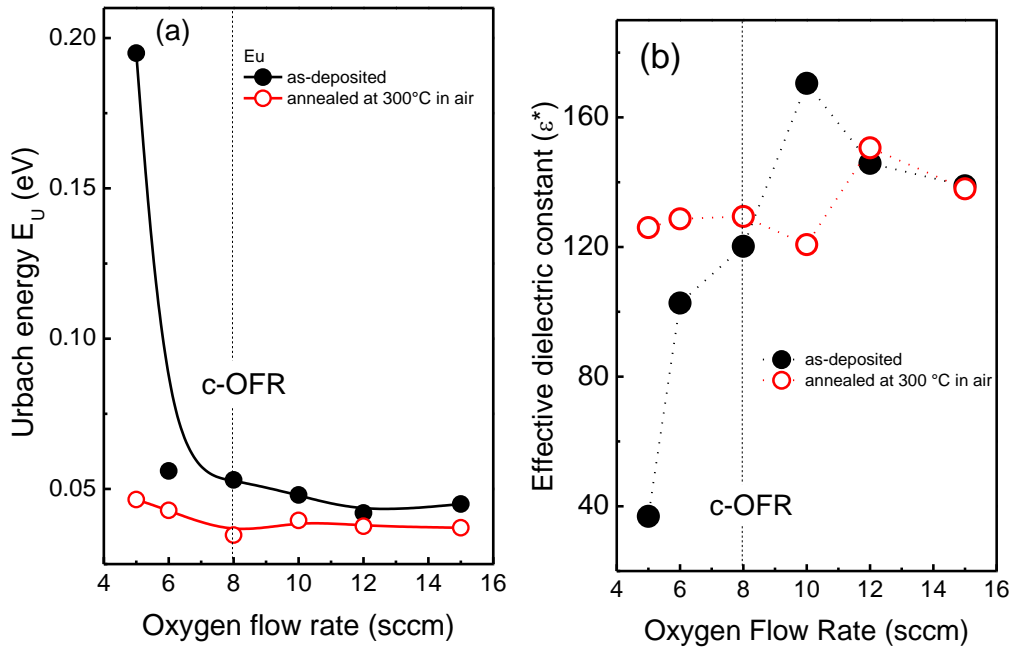


FIG. 3.13. (a). Evolution of the Urbach energy with the *OFR*. (b) The polaron effective dielectric constant  $\epsilon^* = (\epsilon_\infty^{-1} - \epsilon_0^{-1})^{-1}$  of ZnO films deposited at different *OFRs* as measured by spectroscopic ellipsometry. Full circles correspond to as deposited films and empty circles to ZnO films annealed in air at 300 °C, 1h.

### 3.3.2. ZnO bandgap energy

We discussed above how the introduction of shallow donor defects such as  $Zn_i$  can affect the near-edge absorption, increasing the Urbach energy in the zinc-rich condition. However, our main purpose is to rationalize the variations of  $E_g$  reported in the literature. Fig. 3.14 plots, for as deposited and annealed films, the evolution with the *OFR* of  $E_{g(abs)}$  and  $E_{g(ems)}$  obtained from emission PL and ellipsometry measurements using the Forouhi-Bloomer model (see annex B), respectively. Differences in the magnitude of  $E_{g(abs)}$  and  $E_{g(ems)}$  is obvious for both as-deposited and annealed films.

In the as-deposited state, from absorption and emission measurements, we observe that  $E_{g(abs)}$  and  $E_{g(ems)}$  are both rather stable in the oxygen-rich region and close to 3.35 eV and 3.23 eV, respectively. In contrast, upon decreasing the *OFR* in the zinc-rich region,  $E_{g(abs)}$  strongly increases up to 3.55 eV while  $E_{g(ems)}$  only weakly increases to around 3.27 eV. After annealing,  $E_{g(abs)}$  decreases while  $E_{g(ems)}$  increases and are nearly stable around 3.32 eV and 3.26 eV, respectively.

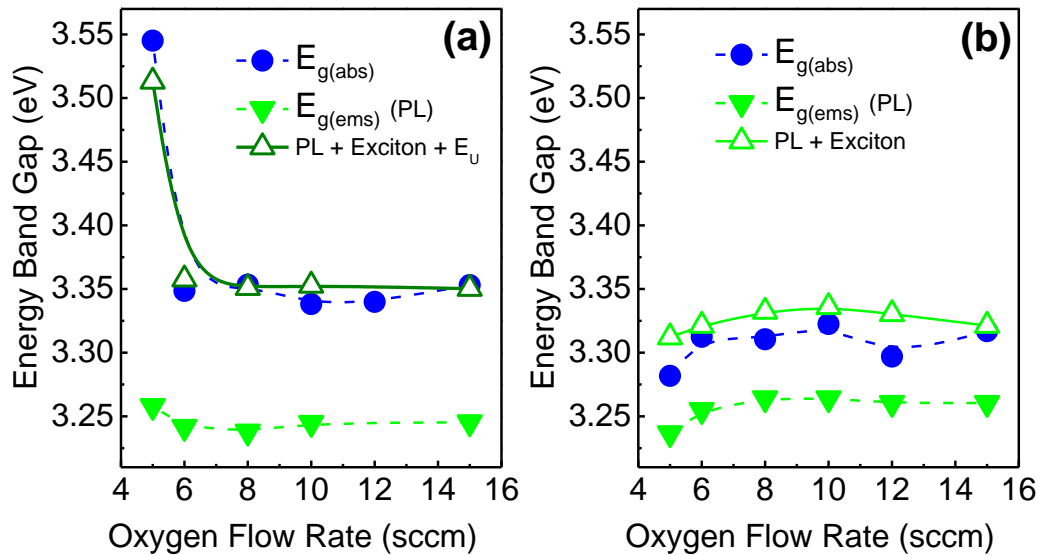


FIG. 3.14. Evolution of the bandgap energy of ZnO thin films with the OFR determined by photoluminescence (emission) (-▼-), ellipsometry (absorption) (-●-) and fit to the data with expressions 3.13 and 3.14 (-Δ-) for (left) as deposited films in the exciton-defects regime and (right) annealed films in the exciton-phonon regime.

---

In a perfect undoped ZnO crystal, the *NBE* emission, i.e.  $E_{g(ems)}$ , is supposed to be separated from the bottom of the conduction band, i.e.  $E_{g(abs)}$ , by the free exciton binding energy (see fig. 3.15a).

$$E_{g(abs)} \approx E_{g(ems)} + E_{exciton} \quad (3.16)$$

This expression rather well describes the situation after annealing (fig. 3.14b), even though the calculated absorption gap slightly overestimates experimental data.

For as deposited films, expression 3.16 does not reflect the reality and it is necessary to introduce the contribution of the Urbach energy  $E_u$  as follows:

$$E_{g(abs)} \approx E_{g(ems)} + E_{exciton} + E_{Urbach} \quad (3.17)$$

Such approach allows fitting very well the experimental data (fig. 3.14a). The results can be explained by taking into account (i) the influence of the introduction of shallow defects may affect the band tails above a certain defect density and that (ii) the exciton-phonon or exciton-defect interactions is dominating the *NBE* and highlights the importance of the Urbach energy as an experimental parameter to extract correlations between the defect chemistry and  $E_{g(abs)}$  using  $E_{g(ems)}$  as a reference state.

At low density of shallow defect states, there are highly localized states and the exciton-shallow defect interaction is weak. In such case the *NBE* emission is expected to be separated from the conduction band minimum by the exciton binding energy and equation 3.16 applies. Since ZnO is a ionic crystal, in absence of strong doping the free exciton is expected to strongly interact with phonons<sup>183,185</sup>, which is verified by low temperature PL measurements in annealed films (see fig. 3.9).

When the shallow defect concentration is large enough, the levels near the conduction and valence bands changes from localized to delocalized states, band tails develop and equation 3.16 is no more valid (fig. 3.14b) to describe the relationship between  $E_{g(abs)}$  and  $E_{g(ems)}$ . The high concentration of shallow donor defects leads also to a strong exciton-donor defects interaction as is confirmed by the low temperature PL measurements (see fig. 3.9). As a result, the exciton energy level is localized below the Urbach tail and equation 3.14 describes well the relationship between  $E_{g(abs)}$  and  $E_{g(ems)}$  by taking into account  $E_u$ .

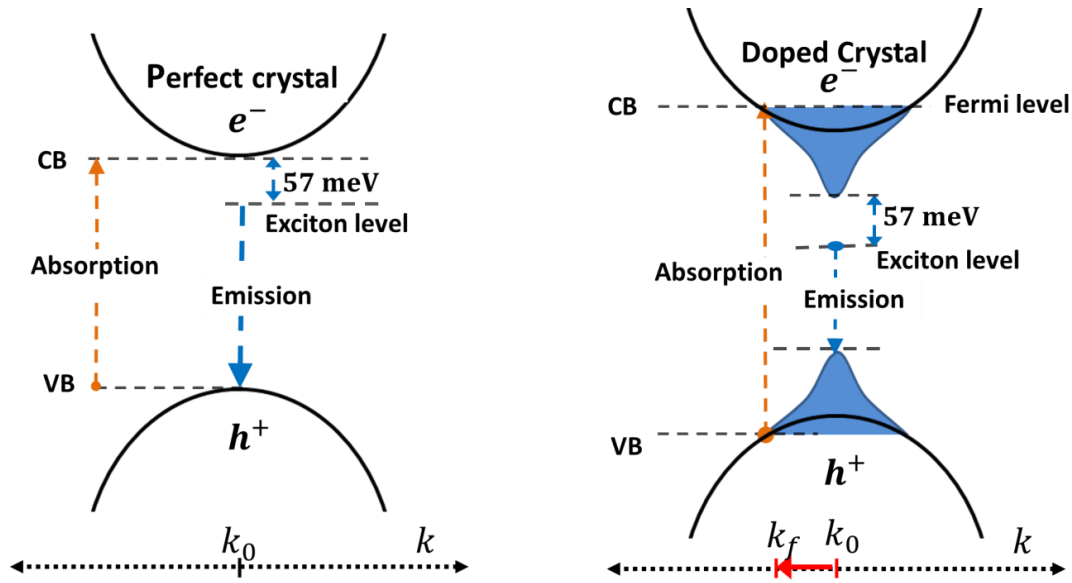


FIG. 3.15. Representation of electronic band structure for (a) perfect ZnO crystal and (b) a highly ZnO doped crystal.

The electrostatic repulsion between the valence and conduction bands increases  $E_{g(abs)}$  distance and simultaneously the delocalized defect could make the  $E_{g(ems)}$  lower than in a low-doped crystal. This can explain the slightly lower emission  $E_g$  ZnO value for as-deposited compared to the annealed films.

Upon decreasing the *OFR*, the electrically active defects density in as-deposited films increases and so does the Urbach energy. As the Fermi level is a function of the carrier concentration<sup>191,192</sup>, it shifts close to the conduction band for n-doped films. At high doping level, the defects concentration is above the critical Mott carrier concentration<sup>172,193,194</sup> and unoccupied levels in the conduction band are filled up. The Fermi wave number  $k_f$  changes and the Fermi level is pushed into the conduction band, leading to absorption at higher energies than the usual  $E_{g(abs)}$ . This effect is known as the Burstein-Moss (BM) effect<sup>195,196</sup>. For non-doped ZnO, typical carrier concentration ( $n_e$ ) is around  $10^{16}$  to  $10^{17}$   $\text{cm}^{-3}$  and depends on the growth technique<sup>134</sup>. The critical Mott density (threshold to activate the BM effect) for ZnO varies between  $1,3 \times 10^{18}$  to  $3,7 \times 10^{19}$   $\text{cm}^{-3}$  depending on the model used to calculate it<sup>134,152,197</sup>. For the *OFR* of 5sccm, the carrier concentration in as-deposited ZnO could be estimated to  $3,1 \times 10^{19}$   $\text{cm}^{-3}$  using hall-effect measurements; which is similar to the density obtained with some doped ZnO

---

films<sup>174,189,190</sup>. For highly-doped crystal, the band structure can be represented as in fig. 3.15b. The shift from a  $k_0$  to a  $k_f$  wave vector is related to the increase in carrier concentration. As the Urbach tails are related with the shallow donor defects and, therefore with states below the conduction band, the relationship between  $E_{g(abs)}$  and  $E_{g(ems)}$  can be described by equation 3.17.

Present results show that variations of  $E_u$  can, at least in the present case, account very well for the BM. This parameter is often overlooked but we see it holds relevant information.

For annealed films, the relationship between  $E_{g(abs)}$  and  $E_{g(ems)}$  is described by the equation 3.16 (dotted line in fig. 3.14b), meaning that the decrease in shallow defect density during annealing eliminates the defect-exciton interaction and the Urbach energy decreases. The band diagram of a perfect crystal better describes the situation (fig. 3.15a).

### 3.4. Conclusion

In this chapter we found experimental conditions to tune the microstructural and optical properties of ZnO thin films by using reactive sputtering technique and by controlling experimental parameters as the *OFR* and nature of the growth substrate. It was shown it is possible to achieve single domain epitaxial growth of ZnO onto sapphire at high *OFR* (oxygen-rich conditions) without in-situ annealing and at self-established substrate temperatures very close to room temperature. Upon changing the *OFR*, was also observed a change in the defect chemistry that is dominated by shallow donor defects in zinc-rich conditions to domination by oxygen interstitials under oxygen-rich conditions. The possibility to vary the defect chemistry in epitaxial films opens possibilities to study the influence of point defects on the properties of the ZnO films in absence of grain boundaries.

The study of the optical properties put some light to understand the close relationship between the emission and absorption bandgap energies. The results allow a better

---

understanding of the large scattering of the bandgap energy of ZnO reported in the literature by proposing a model taking into account the chemical defects. More particularly, was highlighted the need to consider the Urbach energy in the optical behavior of ZnO films showing a large density of point defects.

---

# Chapter 4

## 4. ZnO-Au nanocomposite films

In the previous chapter we described the main features of ZnO films grown under different *OF*Rs and substrates, revealing the possibility to tune their microstructural and optical properties. In this chapter, we describe the synthesis and characterization of ZnO-Au nanocomposite films grown by reactive DC magnetron co-sputtering and show which is the influence of the incorporation of gold and of the *OF*R on the microstructural, optical and physical properties of the nanocomposite films.

### 4.1. Synthesis and characterization

The synthesis of the nanocomposite films was performed using reactive DC magnetron co-sputtering of Zn and Au targets. The experimental setup (see chapter 2, section 2.3) for the elaboration of these films is the same as used for ZnO films deposition but a second magnetron has been equipped with a Au target.

There are two parameters to be evaluated in the elaboration of the ZnO-Au nanocomposite films: the oxygen gas proportion fed to the deposition chamber  $O_2\% = \frac{O_2}{Ar+O_2} \times 100$  and the atomic gold content defined as  $\frac{Au}{Au+Zn} \times 100$ . The gas proportion has been controlled by the argon and oxygen flow rates. The argon flow rate was fixed at 50 sccm, while the *OF*R has been varied from 6 sccm (10.7 vol %) to 15 sccm (23.1 vol %). This resulted in a total pressure in the range of 0.43 to 0.52 Pa.

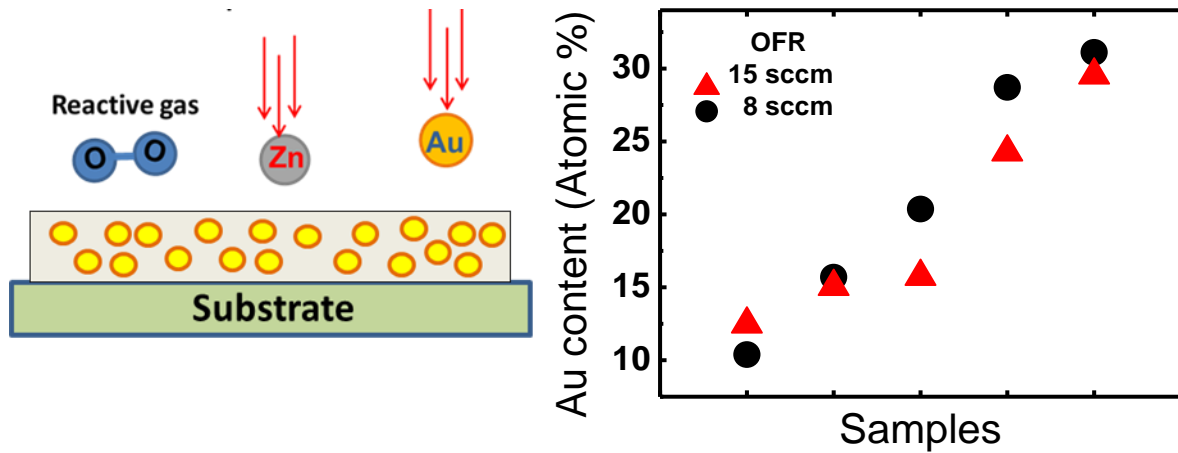


FIG. 4.1. (Left) Representation of the formation of ZnO-Au nanocomposite films. (Right) Au content obtained for ZnO-Au nanocomposite thin films grown at 8 sccm and at 15 sccm. Other samples have also been grown under different conditions that can be consulted in annex C.

The current applied to the zinc target ( $I_{Zn}$ ) was kept constant at 0.07 A, while that applied to the gold target ( $I_{Au}$ ) was changed from 0.015 to 0.006 A (the lowest reachable current for the Au target). As the sputtering yield (see chapter 2, section 2.1.3) is higher for the Au than for the Zn target, especially when Zn is oxidized, it is not possible to reach low Au contents only by setting the lowest possible value of  $I_{Au}$ . It was, therefore, necessary to modify the target to substrate-holder distance ( $D_{ts}$ ) (see chapter 2, fig. 2.8) in order to adjust the deposition rate ( $R$ ) that roughly obey to a propagation law:

$$R \propto \frac{1}{(D_{ts})^2} \quad (4.1)$$

Adjusting both  $I_{Au}$  and  $D_{ts}$ , the Au content could be varied from 10 to 30 % at two different OFRs, as is observed in fig. 4.1.

The deposition time was set such that the nanocomposite grown films have a thickness of 150 nm  $\pm$ 40 whatever the chemical composition, as measured using tactile profilometry (see chapter 2, section 2.3).

In table 4.1 are summarized the experimental parameters of 6 samples representative for a wide range of gold contents.

Table 4.1. Selected Experimental parameters for the elaboration of ZnO-Au nanocomposite films.

Sample	<i>OFR</i> (sccm)	$I_{Au}$ (A)	<i>Dts</i> (mm)	$\left(\frac{Au}{Au + Zn} \times 100\right)$	<i>Thickness</i> (nm)	<i>Total pressure</i> (Pa)
1	8	0.006	55	10.4	166	0.445
2	8	0.010	55	20.4	110	0.434
3	8	0.012	55	28.7	158	0.448
4	15	0.006	100	12.5	162	0.516
5	15	0.006	120	15.7	196	0.513
6	15	0.009	55	29.6	125	0.513

## 4.2. Structure and microstructure

In the last chapter, it was stated that factors such as the *OFR* and the nature of the substrate have a strong influence on the microstructure and properties of ZnO films. In order to compare the behavior of ZnO and ZnO-Au, thin films have been grown under similar conditions at the zinc target in order to evaluate the influence of gold introduction into the ZnO matrix. Therefore, we study the influence of the *OFR*, of the gold content and annealing process on the structure and microstructure of the ZnO-Au nanocomposite films. The film structure and microstructure were evaluated by XRD measurements (see chapter 2, section 2.41) and TEM analyses. Fig. 4.2 compares the X-ray diffractograms of ZnO thin films grown on silica and [0001]-oriented sapphire with a *OFR* of 8 sccm (previously shown in chapter 3, fig. 3.2) with those of a ZnO-Au nanocomposite film with the lowest gold content of our set of samples (Au 10 %) grown

on same substrates with the same *OF*R. A striking influence of the introduction of Au on the crystallinity of the matrix is observed as a decrease of 2 orders of magnitude in the intensity of the (0002) ZnO peak is observed. This indicates a decrease in the crystal quality of the matrix. Another feature of the XRD pattern is the shift of the peak position to lower values with reference to pure ZnO, which will be discussed in section 4.2.2.

We showed in chapter 3, section 3.2.1 that there can be a strong influence of the nature of substrate for ZnO films, due to the possibility to achieve single-domain epitaxy. The diffractograms for pure ZnO clearly highlight this effect. In contrast, there is no marked difference in intensity, width or peak position of the (0002) ZnO diffraction peak for ZnO-Au nanocomposite films grown on fused silica and sapphire. This indicates little, if any, influence of the nature of the substrate on the film properties. Indeed, for practical and economical reasons, we selected fused silica as substrate for the following studies.

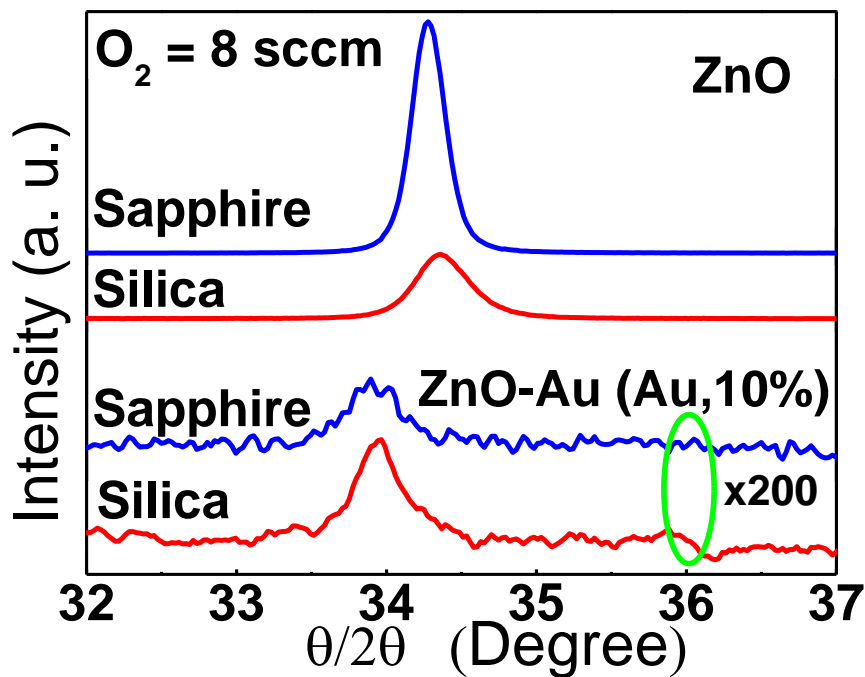


FIG. 4.2. X-ray diffractograms of ZnO and of ZnO-Au (10 % Au) films grown on sapphire (blue lines) and on fused silica (red lines). The ZnO-Au diffracted intensity is magnified by 200 times. All the films were grown with an *OF*R of 8 sccm. Diffractograms are offset on the y-axis for clarity.

#### 4.2.1. Influences of the Au content and OFR

In order to evaluate the influence of the gold loading and of the OFR on the microstructure of the films, the gold content has been increased up to 30% at two different OFRs.

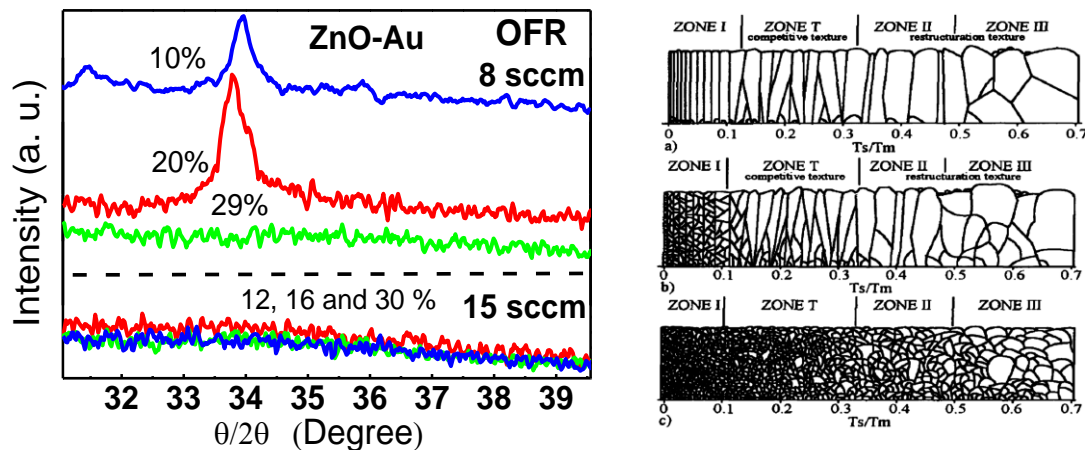


FIG. 4.3. (Left) X-ray diffractograms of ZnO-Au nanocomposite thin films with different Au contents. The films were grown at OFRs of 8 sccm (above the dotted line) and 15 sccm (below the dotted line). The main diffraction peak corresponds to the diffraction by (0002) ZnO planes. Diffractograms are offset on the y-axis for clarity. (Right) Barna and Adamik model showing the influence of the impurities level in the crystalline growth (from top to bottom) at low, medium and high contents<sup>114</sup>.

Fig. 4.3 (left) shows the X-ray diffractograms of ZnO-Au nanocomposite thin films with different Au contents grown at OFRs of 8 sccm and 15 sccm, considered in the following as low and high OFR, respectively. At low OFR, the (0002) ZnO diffraction peak is detected up to 20 % Au with a slight increase in the diffracted intensity as the gold content was increased from 10% to 20% gold. However, the diffracted intensity remains extremely weak compared to pure ZnO (fig. 4.2) and no diffraction signal of crystalline ZnO is detected at 29 % Au. The diffractogramm of the film containing 10% Au also exhibits a weak peak at 31.5° and a fluctuation around 35.9° that could correspond to the {1000} and the {10 $\bar{1}$ 1} planes of the ZnO hexagonal structure, respectively. Such

---

peaks can also be detected in poorly crystalline ZnO films<sup>198</sup>. After deposition at high *OFR*, no diffraction peak of ZnO could be detected for any of the Au contents. Indeed, the detrimental effect of gold on the ZnO matrix crystallinity appears stronger at high *OFR*. In order to interpret these data we can refer to the observations of chapter 3. It has effectively been observed that increasing the *OFR* from 8 to 15 sccm induces a drop in the diffracted intensity and length of coherence domains (chapter 3, fig. 3.3 and fig. 3.4) of pure ZnO films. Hence, part of the degradation of the matrix crystallinity with the *OFR* in nanocomposite films may be related to the bombardment by fast oxygen particles around the critical *OFR* of 8 sccm, as proposed in chapter 3. Nevertheless, this effect alone does not explain the disappearance of the diffraction peaks. In summary, the XRD analysis indicate that both the incorporation of gold and increase of the *OFR* tend to degrade the crystallinity of the ZnO matrix.

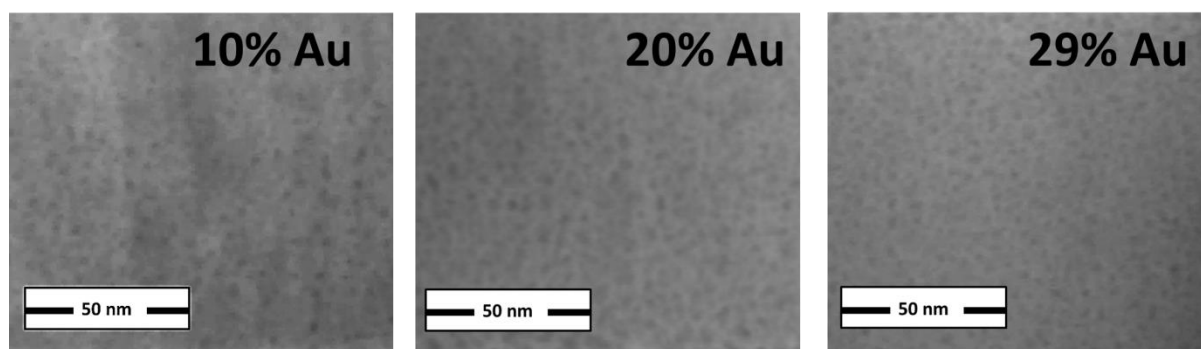


FIG. 4.4. STEM bright field images of transversal cut of ZnO-Au thin nanocomposite films grown with an *OFR* of 8 sccm with Au contents of (a) 10 %, (b) 20 % and (c) 29 %.

Several processes related to the incorporation of gold can influence the crystallinity of the ZnO matrix. First, Au atoms may be present in the ZnO matrix, as suggested by recent investigations on RF sputter-deposited ZnO-Au films<sup>199</sup>, which can induce local strains. This point will be further discussed in section 4.2.2. Second, it could also be explained by the interference of impurities with crystal growth during film growth, as proposed by Barna and Adamik<sup>113,114</sup>. Such impurities could be present in the form of isolated or clustered gold atoms. Given the sought information concerns the nanometer or atom scale, the limits of X-ray diffraction sensitivity are reached and other methods are required to better understand the microstructure of ZnO-Au thin films.

From the bright field Scanning transmission electron microscopy (STEM) images of fig. 4.4, it is possible to observe that the coatings are dense with homogeneously distributed small dark spherical dots. The contrast reveals a difference in the local volume mass and the dark spots that likely correspond to Au NPs, as will be verified in the following paragraph. The higher the Au content the higher the density of Au NPs. However, the average size of dark spots stays nearly constant at about 2-3 nm.

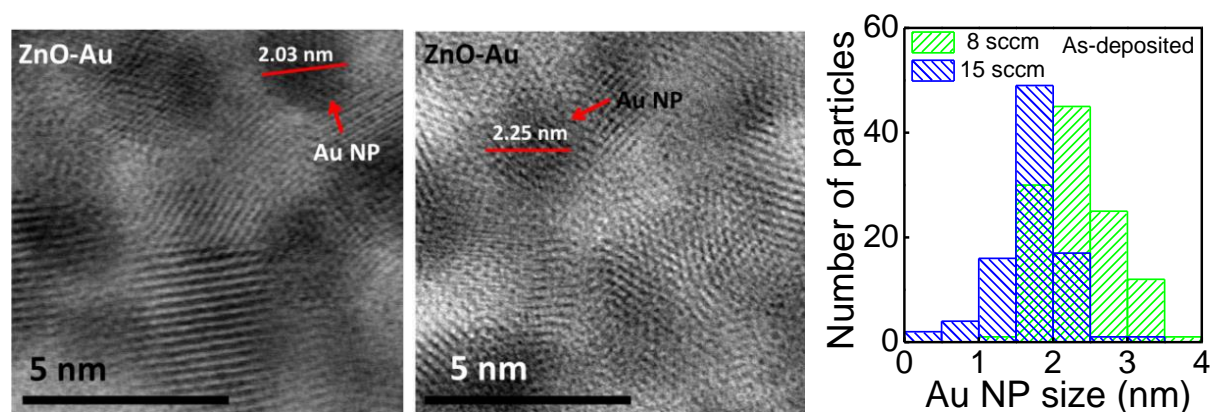


FIG. 4.5. HR-TEM bright field images of ZnO-Au thin nanocomposite films with an Au content of 20 % grown with *OFRs* of (left) 8 sccm and (center) 15 sccm. (Right) size distribution of Au NPs in as-deposited films (extracted from several images collected in different regions of the TEM lamellae).

High resolution TEM (HR-TEM) has been used to extract more information on the microstructure, and to evaluate the influence of the *OFR* on the micro and nanostructure of the films. For this purpose, two samples with a gold content close to 20 % and grown with *OFRs* of 8 or 15 sccm have been selected. Fourier transform has been used to obtain the electron diffraction patterns and confirm the presence of nanocrystalline gold (see fig. 4.11) and NPs are clearly identified on the bright field images of fig. 4.5. The NPs size distributions have been extracted and exhibit a maximum close to 2 nm in for both. No clear signal from crystalline ZnO could be detected, highlighting the poor crystallinity of the matrix.

#### 4.2.2. Influence of the annealing temperature

As the crystal quality of the ZnO matrix appears to be low according to XRD analyses, and in view to modify the physical properties, thermal annealing in air was performed for the ZnO-Au nanocomposite films grown at low and high *OFRs* using different temperatures. In this section, we describe the influence of the annealing temperature on the microstructure of the ZnO-Au nanocomposite thin films.

TEM bright field images of fig. 4.6 show the microstructure of films grown at low (8 sccm) and high (15 sccm) *OFRs* for the same Au content of 30 % and annealed in air at 300°C. The most visible effect of the annealing process is the increase of the size of Au *NPs*. this can be, at least partially, explained by the Ostwald ripening mechanism<sup>200</sup>. It is also possible that gold atoms trapped in the ZnO cell are released and diffuse to the *NPs*, promoting their growth. The histograms show comparable size distributions in both films, with a maximum at 4-5 nm. In addition, for the films grown with an *OFR* of 15 sccm, dark (Au-rich) and clear (Au-poor) regions of about 20 nm in size can be detected. Punctual EDSX analyses indicate these correspond to local enrichment and impoverishment in gold. As Au-rich and Au-poor domains are close to each others in the samples, their formation could be induced by the transfer of gold atoms from Au-poor to Au-rich regions by Ostwald ripening. Such regions were not considered to build the histograms of annealed nanocomposite films grown at 15 sccm.

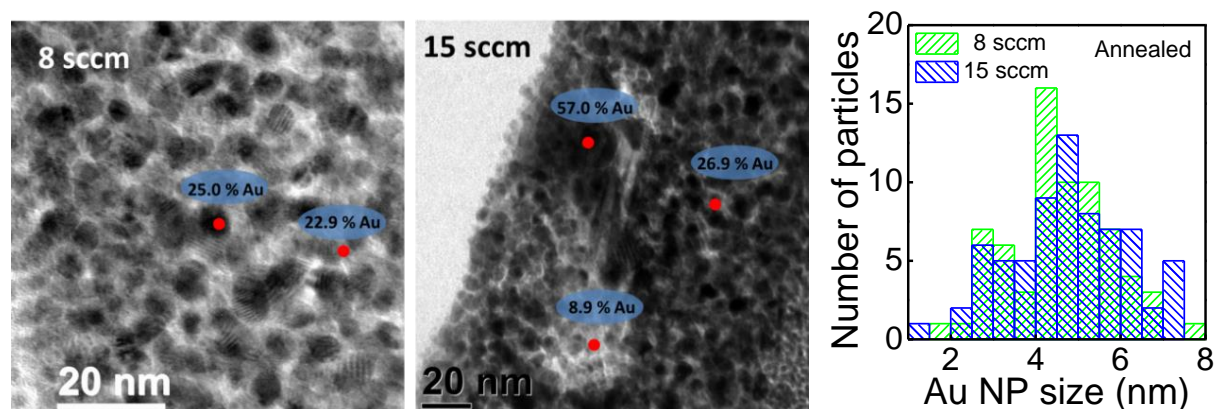


FIG. 4.6. TEM images of 300°C annealed (1h) ZnO-Au nanocomposite thin films with Au contents close to 30% grown with *OFRs* of 8 sccm (left) and 15 sccm (center) Corresponding size distribution of the Au *NPs* (right).

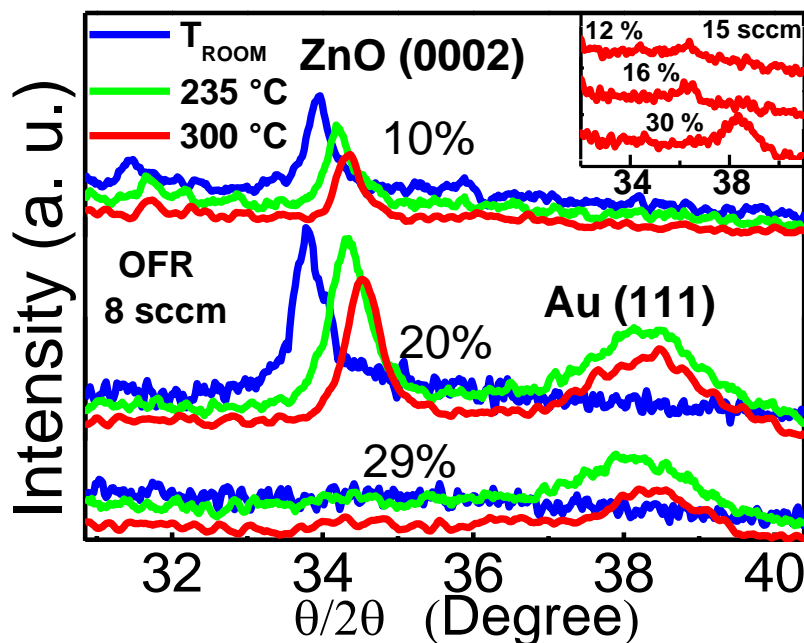


FIG. 4.7. X-ray diffractograms of ZnO-Au nanocomposite thin films grown with an *OFR* of 8 sccm with different Au contents. In the inset: films grown with an *OFR* of 15 sccm with 12%, 16% and 30 % Au. For all graphics: Blue line is for as-deposited film, green and red lines are for the films after an annealing process of 1h in air at 235 °C and 300 °C, respectively. Diffratogramms are offset on the y-axis for clarity.

To complement these analyses, ZnO-Au films with different gold contents grown at low and high *OFR*s were measured by XRD after annealing at two different temperatures (230 and 300 +/- 5 °C) and compared with the as-deposited films. In fig. 4.7 we can observe that for a low *OFR* (8 sccm), one of the most important features of the X-ray diffractogram is the signal that peaks around 38.5 ° and corresponds to the {111} planes of crystalline fcc Au. It is only detected in films with Au contents higher than 20% and after annealing above 200 °C. These results are in line with the increase of NPs size detected by HRTEM analyses. It is also possible that the quality and/or volume fraction of crystalline metallic gold improve upon annealing and enables a better definition of the {111} diffraction peak. Such informations are unfortunately hardly accessible. The inset of fig. 4.7 displays the X-ray diffractograms of films grown with an *OFR* of 15 sccm and with Au contents of 12, 16 and 30% annealed in air at 300 °C. it is possible to observe the {111} peak of Au only for the highest Au content and after an higher annealing

temperature of 300 °C than with films synthesized at low *OFR*. It can be interpreted by a more difficult growth of the *NPs* at high *OFR*. The possible origin of such phenomenon will be discussed in the next section.

As discussed in section 4.2.1, the Au content influences the microstructure of the ZnO matrix. So does the annealing temperature too. We have also discussed in the same section on the possible presence of gold atoms in the ZnO crystal cell. Fig. 4.7 reveals that for the *OFR* of 8 sccm, the (0002) ZnO diffraction peak shifts with the Au content and the annealing temperature, indicating a variation of the *c*-axis parameter. We can follow in fig. 4.8 the evolution of the ZnO *c*-axis parameter with the Au content and the annealing temperature for this *OFR*. Increasing the gold content or the annealing temperature of nanocomposite films have opposite effects as it increases and decreases the *c*-axis parameter, respectively. The annealing treatment enables reaching a *c*-axis parameter close to that of a pure bulk ZnO (5.2042 Å) for all gold contents but requires different holding temperature depending on the gold content. There are several possible explanations to these observations.

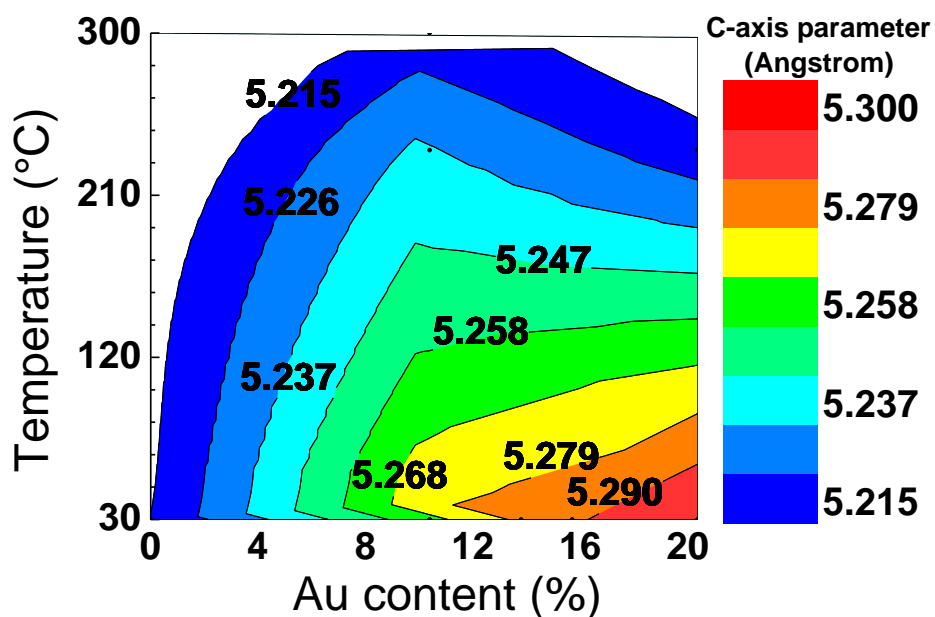


FIG. 4.8. 2D Contour plot of the *c*-axis parameter determined using the (0002) ZnO diffraction peak of ZnO and ZnO-Au nanocomposite films grown at 8 sccm as a function of the temperature and the gold content.

Within the ZnO biaxial in-plane strain model (see chapter 3, section 3.2.1), the elongation (compression) of the  $c$ -axis parameter can be interpreted as in-plane compressive (tensile) stress states. In order to verify the validity of this model in the present situation, stress measurements have been performed using the curvature method<sup>201</sup> (fig. 4.9). All as-deposited films exhibit a compressive stress state but, in contradiction with the biaxial in-plane strain interpretation of the data of fig. 4.8, the magnitude of the compressive stress decreases as the gold content is increased for both *OFRs*. Compressive stresses almost disappear at 30% Au. Nevertheless, the curvature method gives global information about the film in-plane stress state, while the position of the (0002) diffraction peak reveals information on the strain in the matrix only.

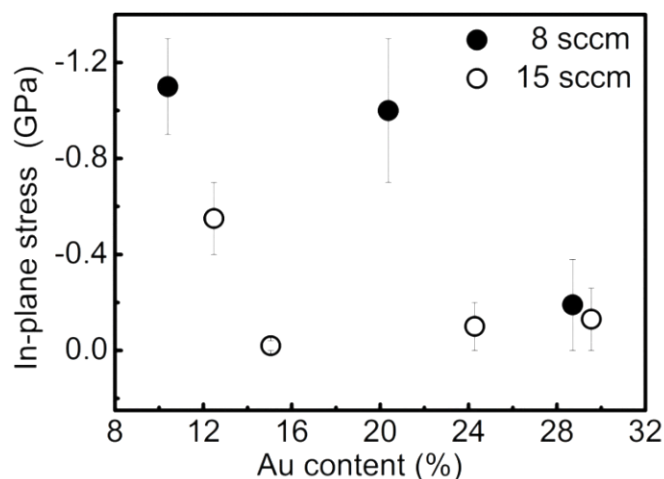


FIG. 4.9. Stress measurements using the curvature method for ZnO-Au nanocomposite films as a function of the Au content and grown with *OFrs* of 8 sccm (filled circles) and 15 sccm (empty circles).

It is well known that Au exhibits a ductile behavior. Hence, due to the contribution of “soft” metallic Au *NPs*, the Young modulus of Au-ZnO nanocomposite films is expected to be lower than that of the ZnO matrix alone (111 GPa)<sup>202</sup>, as observed with the YSZ-Au system<sup>203</sup>. However, it has been recently discovered that Au *NPs* can become stiffer than bulk Au when decreasing their size<sup>204–206</sup>.

It is possible to propose a mechanism explaining both the  $c$ -axis variations and evolution of the stress state with the gold content and annealing treatment. As mentioned earlier

---

(section 4.2.1), a possible origin of the degradation of the crystallinity of the ZnO matrix is the presence of gold atoms in the crystal lattice of ZnO, as reported recently for RF sputter-deposited ZnO-Au films. More particularly, the gold atoms were found to substitute zinc atoms<sup>199</sup>. These “trapped” atoms could indeed expand the ZnO lattice due to their much larger atomic or ionic radius than Zn atoms. In the framework of this interpretation, XRD measurements give us information about the probability to find trapped Au atom, which is found to increase upon increasing the Au content. These atoms could be released from the ZnO structure during the annealing treatment, diffusing to the Au *NPs*, decreasing the deformation of ZnO and increasing the ductility of the material.

We indeed suggest that both results (*c*-axis evolution and stress state) are not contradictory but give different informations on the influence of gold on the microstructure and mechanical properties of the films, respectively.

It is possible to use the FWHM of the {111} fcc Au diffraction peak of fig. 4.7 to estimate the length of coherence domains *L* by neglecting other contributions to the FWHM such as the distribution in size of the *NPs* and stress state. Fig. 4.10 plots the results as a function of the gold content. First, it is observed that the magnitude of *L* is similar to, even higher than, the average size of *NPs* found by HRTEM at high gold loading after annealing at 300°C (see fig. 4.6). It indicates the *NPs* are likely monocrystalline. This is typically what we observed during all our HRTEM investigations. Nevertheless, a value of *L* higher than the particle size is not realistic and shows the applied procedure overestimates *L*. Nevertheless, we can elaborate on the trends. Similar values of *L* are found after annealing at 230°C of the films deposited at low *OFR* and containing nearly 20% and 29% Au. In contrast, *L* is much higher for the highest gold loadings if the annealing temperature is rose to 300°C. It clearly shows particle growth is faster for the highest gold loading. We explain this by the release of a higher content of gold atoms trapped in the ZnO lattice that fastens the growth by Ostwald ripening. Consistently, the annealing temperature required to relax the ZnO lattice to its bulk geometry is lower at high overall gold content (fig. 4.8). From fig. 4.8 we can estimate the gold content to activate such mechanism around 8-10% Au. For the films synthesized at high *OFR*, the thermally stimulated growth of Au *NPs* appears to be canceled up to 20% Au and retarded at 30% Au.

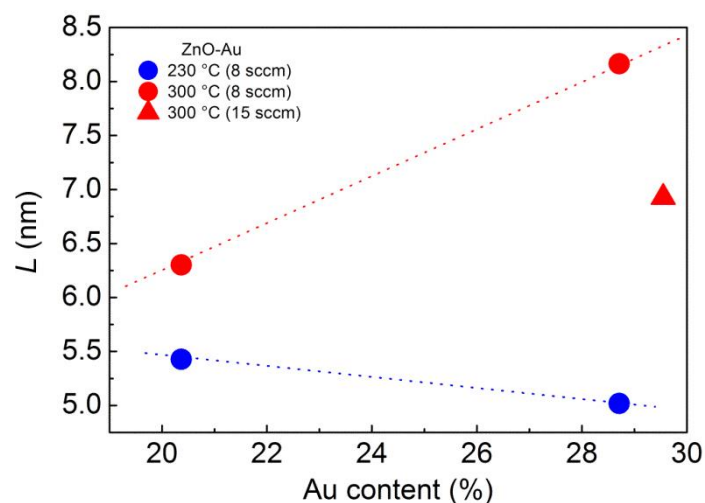


FIG. 4. 10. Length of coherence domains of crystalline gold estimated from X-ray diffractograms of annealed ZnO-Au films for two gold contents and two  $OFR_s$ .

In summary, the incorporation of Au into ZnO leads to strong changes in the microstructure of the films. The crystallinity of the ZnO matrix decreases with the Au content but this effect is stronger when the  $OFR$  increases. At low  $OFR$ , the incorporation of Au leads to  $c$ -axis elongation that can be reduced when the films are annealed. This is associated to a decrease in the overall in-plane compressive stress state. The evolution of internal stress as well as evolutions of the  $c$ -axis parameter of ZnO is explained by the presence of gold  $NPs$  relaxing the compressive stress and by the presence in, and release from, the ZnO crystal cell of isolated Au atoms, respectively. Annealing the films in air induces an increase of the average size of Au  $NPs$ , which is more pronounced at high gold loadings and delayed to higher temperatures for films grown at higher  $OFRs$ .

As an approach to understand the role of the interfaces on the film properties, we discuss in the next section the possibility to have oxidize Au  $NPs$  at high  $OFRs$

### 4.3. Au $NPs$ oxidation

The investigation of the microstructural properties of ZnO-Au films in section 4.2 evidenced a strong influence of the introduction of gold and of the  $OFR$  on the

crystallinity of the ZnO matrix and growth of *NPs*. This is supported by the fact a higher annealing temperature is needed to detect Au *NPs* by XRD in the films deposited under high *OFR*. This calls for a deeper investigation of the interaction between the *NPs* and ZnO matrix. The formation of a shell blocking (or slowing down) the diffusion of gold atoms can be considered. As the *OFR* appears to be the relevant parameter to retard the growth of *NPs*, such a shell could be in the form of a gold oxide. For this formation to be possible it must to be favored energetically.

Gold oxides are known to be thermodynamically unstable in normal conditions, but their formation at the surface of *NPs* could depend on an increased reactivity of the Au *NPs* at small sizes (see chapter 1, section 1.5).

If we model Au *NPs* by spheres, it is possible to express their Gibbs free energy of formation ( $\Delta G$ ) as two contributions: one related to the surface area and the other to the bulk volume of *NPs*.

$$\Delta G = -\frac{4}{3}\pi r^3 \Delta G_V + 4\pi r^2 \sigma \quad (4.2)$$

With  $\Delta G_V$  the volume free energy of formation of solid gold starting from a reference state such as gold atoms in the gas phase or trapped in the ZnO cell, and  $\sigma$  the interfacial tension between the *NPs* and ZnO. Using the size distribution of Au *NPs* for as-deposited and annealed nanocomposite films (fig. 4.5 and 4.6), and considering a spherical shape, it is possible to calculate the distribution of the ratio from surface area to the volume of the Au *NP* before and after annealing ( see fig. 4.11).

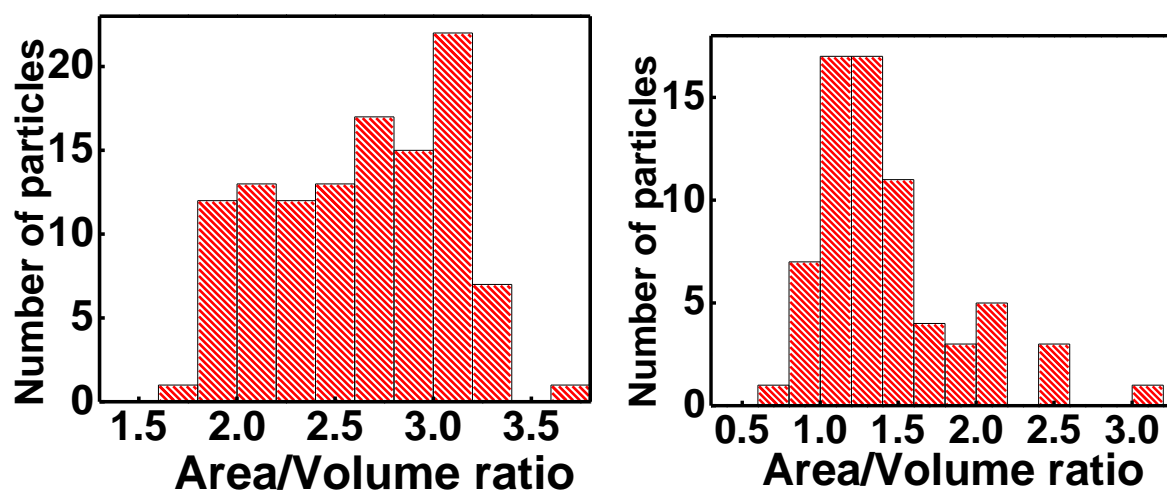


FIG. 4.11. Ratio of surface area to volume of Au *NPs* in nanocomposite films grown at 8 sccm. (left) As-deposited and (right) annealed at 300 °c, 1h in air.

---

In the as-deposited films the surface area is three times the bulk volume. In contrast, in the annealed films the surface/volume ratio is close to one. This suggests a higher reactivity in the as-deposited samples. As a working hypothesis, to be confirmed in section 4.3.2, we can suppose that the *NPs* are in a purely metallic form after annealing, i.e. similar to the bulk stable equilibrium state. Hence, smaller fully metallic particles would be in a less energetically favorable thermodynamic state. The formation of a gold oxide shell could compensate the unbalanced surface forces<sup>54,207</sup> in small particles if it acts as a buffer layer between the metallic core of *NPs* and ZnO matrix and leads to a lower interfacial tension (lower value of  $\sigma$ ). This could explain the formation of an Au<sub>2</sub>O<sub>3</sub> shell around small particles in presence of a sufficiently high concentration of oxygen during growth. Tracking down a direct evidence of such an effect is far beyond the scope of the present study. Nevertheless, in the two next sections we provide more information on the structure and chemistry of gold particles in the films in order to confirm the presence of an Au oxide shell.

#### 4.3.1. Electron diffraction patterns

HRTEM analyzes have been conducted in order to track down the eventual presence of gold oxide in nanocomposite films synthesized at high *OFR*. It was unfortunately impossible to either evidence or discard the presence of gold oxide from bright field images due to the overlap of signal from the different particles on the 2D plane view projection of the probed volume in the TEM lamellae. Nevertheless, the electron diffraction (ED) patterns obtained from the FFT of HRTEM images of ZnO-Au nanocomposite films grown at high *OFR* are different from those obtained with as-deposited films grown at low *OFR* (fig. 4.12). The ED pattern for a film deposited at 8 sccm shows a broad diffraction ring possibly owing to the nanocrystalline ZnO matrix. The ring covers interplanar distances ranging between 0.190 and 0.265 nm we attribute to contributions by the (0002) planes of the hexagonal ZnO structure and, possibly, to contributions by the {10 $\bar{1}$ 1} and {10 $\bar{1}$ 0} planes. There are also bright spots with an interplanar distance of 0.230 nm that correspond to the {111} planes of fcc Au. This crystal structure is confirmed by the presence of spots at interplanar distances of 0.115,

0.140 and 0.120 nm corresponding to {222}, {220} and {311} planes of fcc Au<sup>208,209</sup>, respectively.

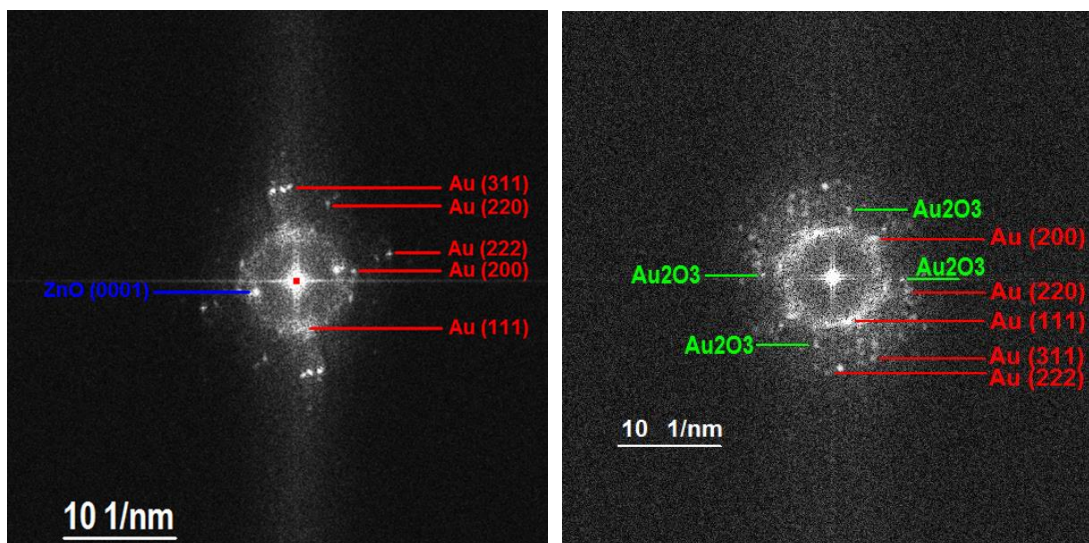


Fig. 4.12. Indexation of the electron diffraction pattern obtained using FFT of HRTEM images of ZnO-Au nanocomposite films grown at low (left) and high (right).

The diffraction pattern obtained with a film deposited at an *OF*R of 15 sccm shows a broader diffraction ring for ZnO than for 8 sccm, in line with the lower crystallinity of the matrix, as suggested by XRD on films grown at high *OF*R. The clear signature of fcc Au is also observed. It is also possible to identify several isolated spots with an average interplanar distance of 0.154 nm that could not be indexed neither by wurtzite ZnO nor by fcc Au diffraction planes. From the PDF card (00-043-1039), it is possible to assign this distance to the (460) and the (280) planes of the orthorhombic Au<sub>2</sub>O<sub>3</sub> phase with interplanar distances of 0.154 and 0.153 nm, respectively. Nevertheless, it is difficult to conclude definitely on the presence of Au<sub>2</sub>O<sub>3</sub> on the basis of these results only.

#### 4.3.2. Au<sub>2</sub>O<sub>3</sub>/Au shell/core structure

The Au 4f core level electronic structure of selected samples has been evaluated by XPS. In the literature, it is reported to present a doublet with a spin orbit splitting of 3.7 eV with binding energies of 84.0 and 87.6 eV, that correspond to the 4f<sub>7/2</sub> and the 4f<sub>5/2</sub> states, respectively.

Looking in fig. 4.13 at the electronic structure of the films grown at 8 sccm, we find two strong signals related to the Au spin split doublet separated by nearly 3.7 eV. A clear shift to lower binding energies (BE) is observed compared to the positions reported in the literature for Au<sup>0</sup> and this shift increases with the Au content. Shifts to lower BE are generally related with negatively charged atoms (anions), while shifts to higher BE are related with positively charged atoms (cations).

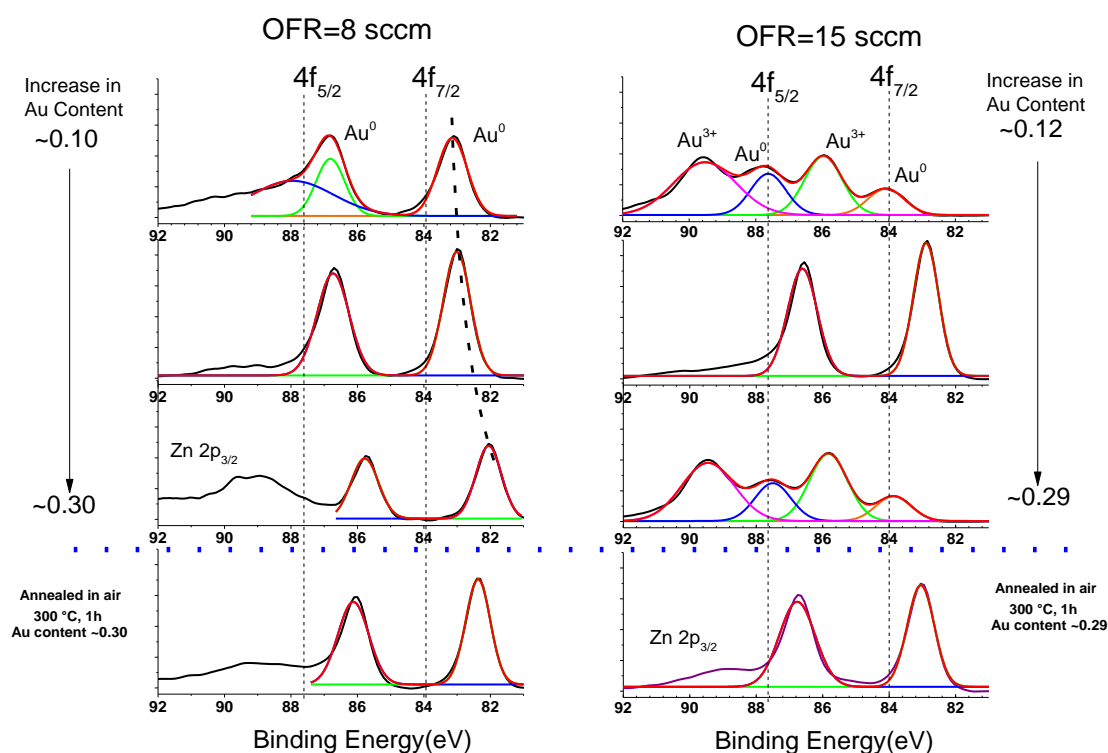


FIG. 4.13. Au-4f core level spectra obtained by XPS measurements of ZnO-Au thin films grown at an *OFR* of 8 sccm and 15 sccm with different Au contents. The vertical dashed lines represent the 4f level of bulk Au<sup>0</sup>. Below the dotted blue line are shown the spectra of annealed ZnO-Au nanocomposite thin films at the highest Au content of the each series.

Shifts in the Au 4f BE could also be due to different factors such as particle size effects<sup>210,211</sup>, alloy formation<sup>212</sup> or charge transfer<sup>213</sup>. AuZn alloys are discarded because, although Zn could transfer charges to the Au atoms (nearly 0.25e), the Au<sup>0</sup> peaks would be shifted to higher BE<sup>212</sup>. Moreover, decreasing the particle size into the nanometer range induces a decrease in the average coordination number that also leads to a shift to

---

higher energies<sup>214</sup>. Hence, it can be discarded as well in our case. Therefore, the charge exchange between the ZnO matrix and Au NPs likely explains the observed shift to lower BE. It is supported by the fact charge transfer from substrate to supported Au NPs has been found for substrates with a reducing behavior<sup>215</sup> as well as for electronegatively charged Au NPs<sup>216</sup>.

Looking at the spectra of the films grown with an *OF*R of 15 sccm, we find three main differences with those of films grown at low *OF*R. Four peaks are observed and, due to their separation of 3.7 eV by pairs, they can be assigned to the gold 4f level and separated in two groups of peaks. The first pair with contributions at 84.0 and 87.6 eV corresponds to the Au<sup>0</sup> signal. In contrast to the films grown at low *OF*R, there is no shift to lower BE with reference to the bulk Au<sup>0</sup> state. By XPS it is possible to differentiate the possible oxidation states of Au<sup>217</sup>. The signal corresponding to the second pair of peaks located at 85.4 and at 89.4 eV corresponds to the Au<sup>3+</sup> oxidation state of Au<sub>2</sub>O<sub>3</sub>. The formation of gold oxides has already been observed under extreme oxidizing conditions as anodic formation or after UV/ozone treatments<sup>218</sup> of gold where is obtained a mixture of Au (I) and Au(III) oxides. Furthermore, sputtering Au in oxygen atmosphere leads to pure Au(III) oxide films<sup>218</sup>. The second sample at high *OF*R has a different behavior to the films in the same series, which could be due to heating of the samples with the X-ray beam during measurement.

The present results strongly support that Au NPs oxidation occurs and leads to an Au<sub>2</sub>O<sub>3</sub>/Au shell/core structure. Such structure has also been reported for Au NPs on oxide supports such as SiO<sub>2</sub> and TiO<sub>2</sub> and presents a different thermal stability depending on the chemical behavior of the support. On a reducing support, as reduced TiO<sub>2</sub><sup>219</sup>, the Au<sub>2</sub>O<sub>3</sub> shell is less stable than on a less reducing support as SiO<sub>2</sub>.

In the previous chapter, we stated that for films grown at low *OF*R, there is predominance in ZnO of donor defects such as interstitial zinc or oxygen vacancies, while at high *OF*R there is predominance of acceptor defects such as zinc vacancies or interstitial oxygen. Therefore, zinc-rich ZnO films have donor defects, forming a reducing ZnO surface, while oxygen-rich ZnO films have a higher content of acceptor defects forming an oxidizing surface. The Au NPs and atoms are expected to interact differently with these two types of surfaces. We can propose a model (fig. 4.14) in which oxygen vacancies ( $V_o$ ) or zinc interstitial ( $Zn_i$ ) at the ZnO (0001) surface are active sites

for the Au adsorption. When an Au NP interacts with a donor rich-ZnO surface, there is charge transfer (electrons) from the donor defects to the Au NP, charging negatively the NP and shifting the XPS signal to lower BE. This oxide-metal charge transfer has been observed at ZnO|Au interfaces when the ZnO surface has a donor behavior<sup>220-222</sup> and the interface behaves as an ohmic contact. For samples synthesized at high OFR, ZnO (0001) surfaces have a large density of  $V_{Zn}$  sites that favor the adsorption and subsequent ionization of Au only stable as  $Au^{1+}$  ion<sup>223</sup>. However, it is necessary to recall that sputtering is a technique that can lead to far from thermodynamic equilibrium material configurations. Hence, it could enable reaching higher oxidation states. Within our model, the charge transfer from the Au NP to the acceptor defects leads to the oxidation of the surface Au atoms, forming an  $Au_2O_3$  shell (confirmed by the  $Au^{3+}$  XPS signals). The shell isolates the  $Au^0$  atoms in the bulk of NPs from ZnO and inhibits the charge transfer from ZnO to Au. This is strongly supported by the fact BEs of the  $Au^0$  peaks are the same as for bulk  $Au^0$ .

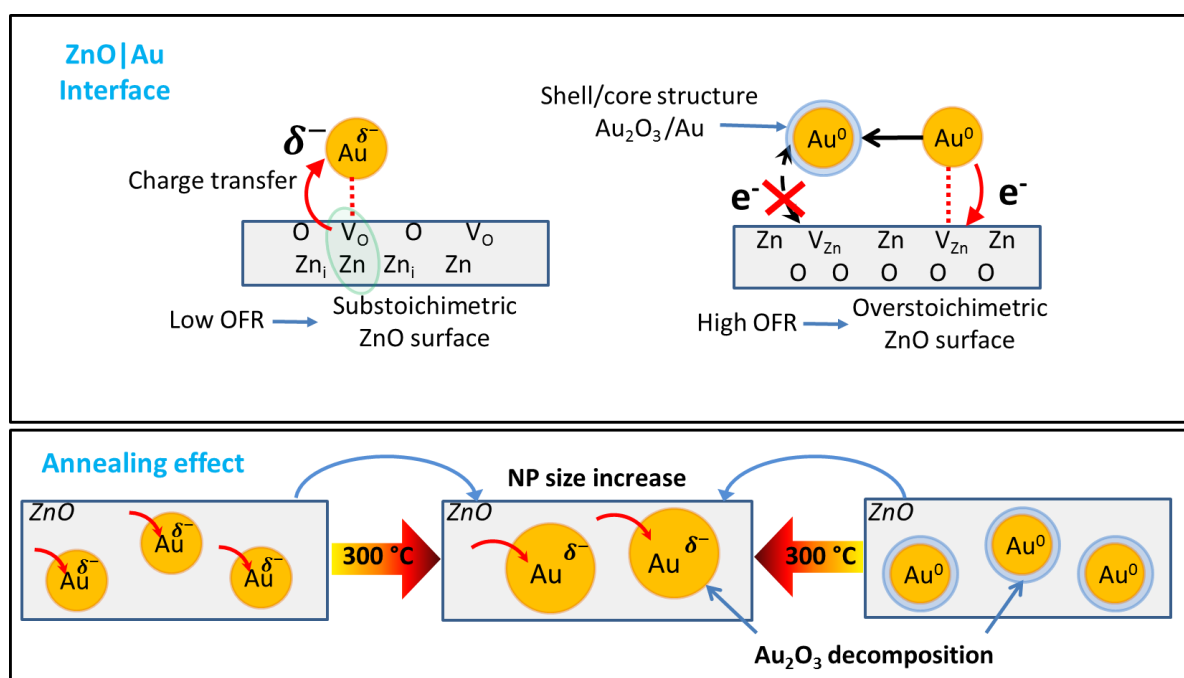


FIG. 4.14. Top. ZnO|Au interface showing the Au NPs-ZnO matrix interaction for nanocomposites grown with an OFR of 10 sccm and below (left) and films grown at OFRs of 12 and 15 sccm (right). Bottom: Interaction of the Au NPs with the ZnO matrix after annealing at 300 °C, 1h in air.

---

Based on this model, the film with an Au content of 20% grown at high *OFR* is expected to present two pairs of peaks but presents only the Au<sup>0</sup> signal shifted to lower BE. We attribute this contradictory result to a heating and decomposition of the Au<sub>2</sub>O<sub>3</sub> shell in the film during XPS measurements<sup>224</sup>. Effectively Au<sub>2</sub>O<sub>3</sub> is very sensitive to the temperature. Au<sub>2</sub>O<sub>3</sub> powders were found to decompose below 200 °C<sup>225</sup> in reducing conditions such as H<sub>2</sub> atmosphere and Au<sub>2</sub>O<sub>3</sub> nanometric layers decompose at even lower temperature<sup>226</sup>. In the literature, Au<sub>2</sub>O<sub>3</sub> is reported as thermodynamically unstable in normal conditions and to decompose spontaneously. However, in nanocomposite films, the ZnO matrix with oxidizing defects seems to stabilize the Au oxide although the phase cannot withstand the annealing treatment. One of the consequences of this shell decomposition, is that the Au<sup>0</sup> atoms are again in contact with the ZnO matrix, allowing the charge transfer from ZnO to Au and shifting the BE to lower energies.

Annealing the films deposited at low *OFR* induces a slight shift of the peaks towards the position of the Au<sup>0</sup>, but without reaching it. The difference in the BE between as-deposited and annealed films (82.05 and 82.4 eV, respectively for the lower energy peak) can be explained by the fact the charge transfer occurs at the interface. Effectively, there is a higher surface/volume ratio (as is shown in fig. 4.11) for Au *NPs* before annealing and it is expected that the charge transfer per atom is more important in small Au *NPs*.

From XPS data we can extract the FWHM of the different contributions, which can reveal information about the crystal quality of the phases present at Au *NPs* (fig. 4.15). The FWHM of Au<sup>0</sup> is found to decrease with the Au content, passing from 1.06 at 10% to 0.91 at 29% and from this value to 0.87 after annealing treatment. At high *OFR*, the Au<sup>0</sup> FWHM value decreases from 1.28 at 12% to 1.24 at 30% Au and from this value to 0.90 after annealing, showing a clear improvement of the crystallinity. This is in agreement with the increase of the size of Au particles found by XRD and TEM analyses after annealing. The Au<sup>3+</sup> FWHM value shows little variation as a function of the Au content passing from 1.32 at 12% to 1.35 at 30%, which indicates similar crystallinity of shell thickness in all conditions where its signature is found.

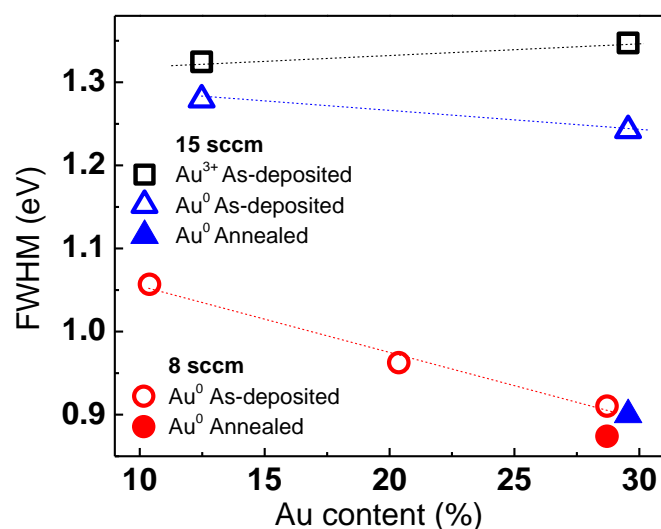


FIG. 4.15. Evolution of the XPS FWHM signal of the Au<sup>0</sup> and Au<sup>3+</sup> peaks of films grown at an *OF<sub>R</sub>*s of 8 sccm and 15 sccm as a function of the gold content and influence of the annealing treatment at 300°C. The dotted lines are shown as a visual guide.

#### 4.4. Optical properties of ZnO-Au nanocomposite thin films

As shown previously, the incorporation of Au, the growth conditions (*OF<sub>R</sub>*) and the annealing treatment have a strong impact on the microstructure of the ZnO-Au nanocomposite films. These factors are expected to affect the optical properties of the films. To evaluate the influence of the *OF<sub>R</sub>* and gold content on the optical properties, ZnO-Au nanocomposite films elaborated varying the *OF<sub>R</sub>* from 6 to 15 sccm have been characterized for their optical properties by optical transmittance and spectroscopic ellipsometry.

##### 4.4.1. Localized surface plasmon resonance and absorption background

The localized surface plasmon resonance (*LSPR*) of isolated Au *NPs* can be detected in the visible range<sup>67,75,218,227</sup> in different dielectric surrounding media. Its presence can be

revealed by extracting the absorption coefficient from spectrophotometry measurements (see chapter 2, section 2.4.5). The main purpose of this section is to study the influence of the microstructure and local chemistry of ZnO-Au nanocomposite thin films on the *LSPR* behavior.

Fig. 4.16 plots the optical absorption for films grown under low and high *OFRs* with three different Au contents before and after annealing at 230 and 300 +/- 5 °C. For the as-deposited films (blue line), there is no absorption band detected in the visible range. The absorption in the near UV corresponds to the valence to conduction band transition of the ZnO matrix. However, the characteristic absorption peak related to free excitons is not visible, likely due to a low crystallinity of the matrix. It is possible to observe that increasing the *OFR* from 8 to 15 sccm decreases the absorption in the visible range (referred in the following as background absorption). These observations will be discussed in the next section.

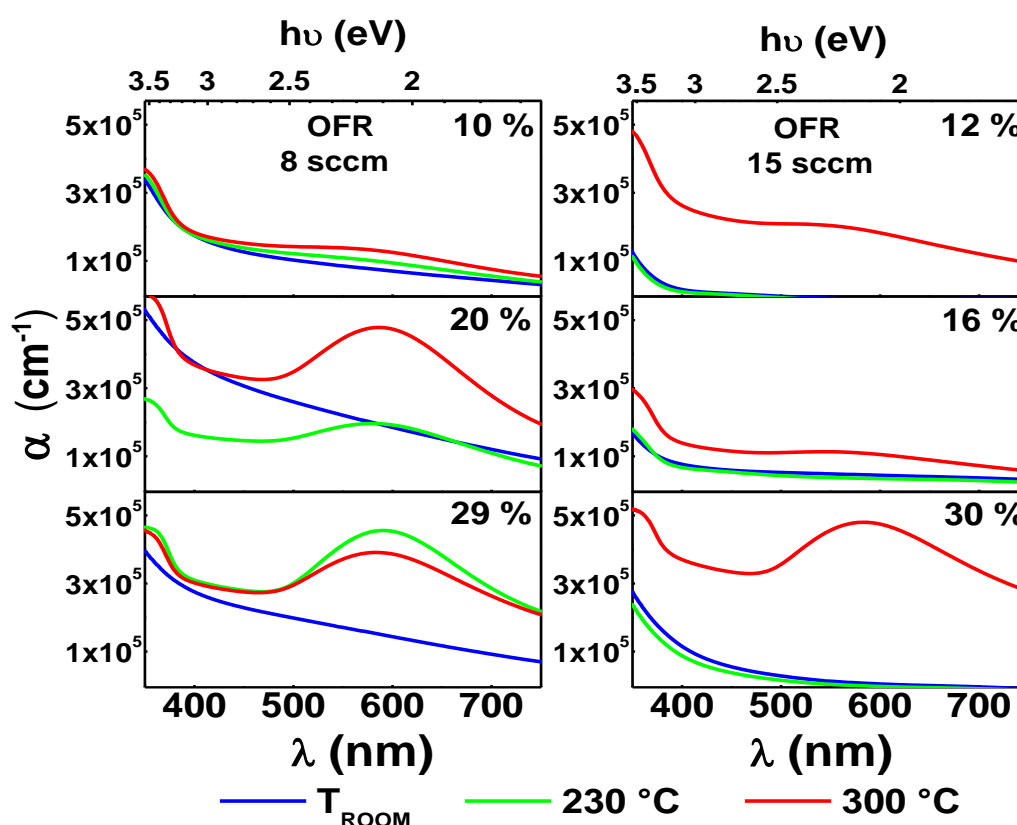


FIG. 4.16. Absorption coefficient dispersion curves of ZnO-Au nanocomposite thin films grown with an *OFR* of 8 sccm or 15 sccm with different Au contents. For all graphics: Blue line is for as-deposited film, green and red lines are for the films after an annealing process for 1h in air at 235 °C and 300 °C, respectively.

Furthermore, fig. 4.16 informs us that the annealing process has two main consequences on the absorption properties of the coatings: (i) it promotes the development of the *LSPR* band, which the amplitude depends on the gold content, and (ii) steepens the bandgap transition of the ZnO matrix. Nevertheless, these effects are delayed to higher temperatures at high *OFR* as the absorption spectra remain almost unchanged after annealing the coatings at 230°C.

Once developed, the *LSPR* band has similar characteristics at low and high *OFRs* (centered near 590 nm and FWHM  $\sim$  170 nm for the highest gold loading). There is a difference with the *LSPR* band of isolated Au *NPs* in air centered around 539 nm<sup>67</sup>. The redshift observed with our films arises from a different dielectric function of the embedding medium<sup>36-40</sup>, as clearly established in the Mie scattering theory (see chapter 1, section 1.5).

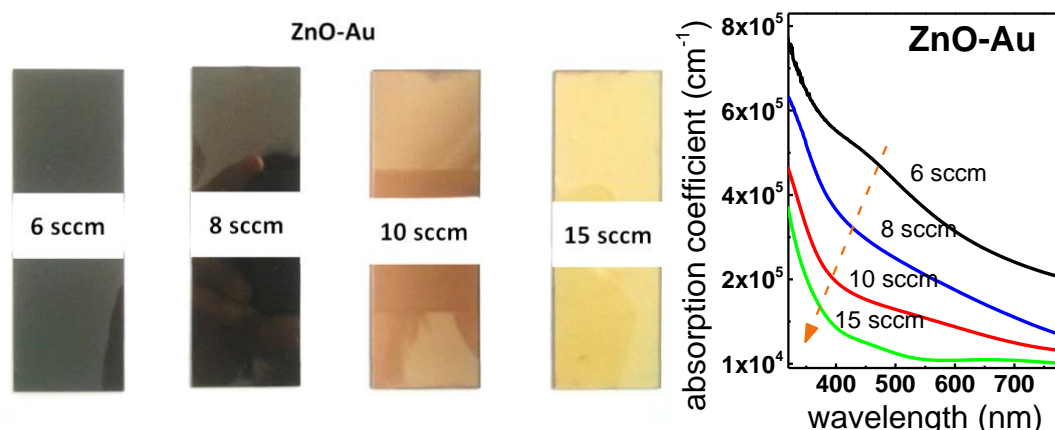


FIG. 4.17. As-deposited ZnO-Au nanocomposite thin film grown with different *OFRs*. (Left) Photographs of the films from low to high *OFR*. (Right) dispersion curves of the absorption coefficient of the corresponding films.

The absorption spectrum of pure gold films is dominated by valence electrons and the  $5d^{10} \rightarrow 6sp^0$  interband transition located around  $\sim$ 1.8 eV<sup>67,68</sup> but is not related to a sharp signal and can describe the background absorption in the spectra of fig 4.16. A surprising feature of fig 4.16 is the increase of the background absorption upon annealing the films synthesized with an *OFR* of 15 sccm. Fig. 4.17 shows the absorption curves for ZnO-Au nanocomposite films with an Au content higher than 16%, a

comparable thickness but grown with different *OFRs*. In the picture (left) we observe how the films are getting more transparent as they are grown with higher *OFRs*. It is confirmed by the absorption curves (right) where the decrease of the Au metallic absorption reaches differences in amplitude of at least one order of magnitude. Given the high transparency of ZnO films grown under similar conditions (see chapter 3, fig. 3.2), we can be confident that this behavior does not arise from the oxidation of the matrix. During growth, Au atoms or clusters interact with recently formed ZnO surfaces and are sensitive to the chemical state of such surface.

Considering an Au<sub>2</sub>O<sub>3</sub> shell forms on the metallic Au *NPs* under oxygen-rich conditions, it is possible to explain the change in the amplitude of the background absorption with the *OFR*. Only the free electrons of the Au 5*d* level are involved in the background absorption. In Au<sub>2</sub>O<sub>3</sub>, the 5*d* level is hybridized with the Oxygen 2*p* levels and the 5*d* electrons cannot participate to the interband transition<sup>228</sup>.

We used spectroscopic ellipsometry to obtain more information about the dielectric constant of the ZnO-Au nanocomposite films using a dedicated model (see Annex B). Investigations by spectroscopic ellipsometry confirm the main results obtained by UV-Vis spectrophotometry for the absorption dispersion curves. Effectively, it is observed how the films get weakly absorbent after an *OFR* higher than 10 sccm but the background absorption rises and the *LSPR* absorption band appears after annealing at 300 °C for 1h in air the (fig. 4.18).

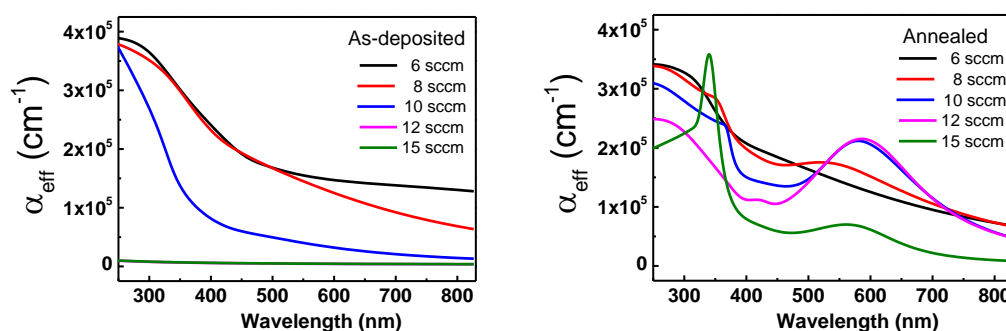


FIG. 4.18. Absorption coefficient of ZnO-Au nanocomposite thin films obtained from ellipsometric measurements and fitting of the data for films grown in the *OFR* interval from 6 to 15 sccm. The Au content is higher than 15 % in all the films. (Left) As-deposited films. (Right) Annealed films for 1h in air at 300 °C.

Upon fitting the data, it was not necessary to introduce the Au *NPs* Drude equation to describe the effective dielectric function for as-deposited films grown at 12 and 15 sccm, as if there was no gold present in the film. This can be directly related with the presence of the Au<sub>2</sub>O<sub>3</sub> shell that screens the contribution of metallic Au. After annealing, it was necessary to introduce the Au *NPs* dielectric function for all the *OFR* conditions of synthesis and the *LSPR* owing to Au *NPs* is detected as with optical transmittance measurements.

The real ( $\epsilon_{effr}$ ) and imaginary ( $\epsilon_{effi}$ ) parts of the effective dielectric function show the optical response of the nanocomposites in the visible and the near UV region (fig. 4.19). It is possible to observe a clear difference between the non-absorbent films grown at 12 and 15 sccm and the absorbent films grown under *OFRs* of 10 sccm and below. For the non-absorbent layers,  $\epsilon_{effr}$  can be directly related with the refractive index (if  $\epsilon_{effi} = 0$  then  $\epsilon_{effr} = n^2$ ) and the average refractive index is 2.17, close to that of pure ZnO. For as-deposited layers in the near UV region (*OFR* < 10 sccm), it is possible to observe an increase in the light absorption attributed to interband transitions in the ZnO matrix. However, there is a blue shift of this absorption when increasing the *OFR* that could be related to the nanocrystalline character of the ZnO matrix. Effectively, the confinement effect at the nanometer scale<sup>229,230</sup> increases  $E_{g(abs)}$ .

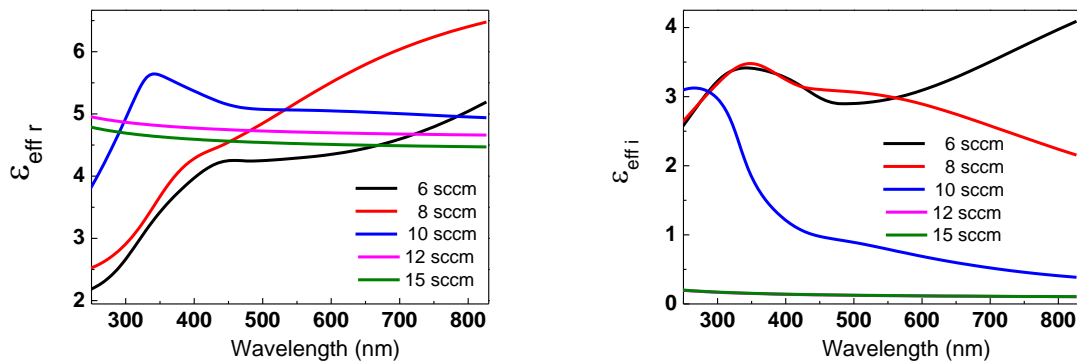


FIG. 4.19. (Left) Real and (right) imaginary parts of the effective dielectric function of as-deposited ZnO-Au nanocomposite thin films grown in the *OFR* interval from 6 to 15 sccm. The Au content is higher than 15 % in all the films.

From the model used, it was also possible to extract the dielectric function of the ZnO matrix alone and to compare it with that of a pure ZnO film (fig 4.20). It is evident, looking at the imaginary part of the matrix dielectric function ( $\epsilon_{mi}$ ), that the introduction

of gold affects the optical response of the ZnO matrix. For as-deposited films, the polarization amplitude increases compared to that of ZnO films and peaks at a different wavelength depending on the *OFR*. Moreover, the absorption tail (Urbach energy, see chapter 3, section 3.3.1) is more important than for pure ZnO films. The effect is more marked at low *OFR*. Indeed, it is possible that the donor defects concentration is increased for all conditions upon gold incorporation but higher at low *OFR*. After annealing, the polarization amplitude depends on the *OFR*, lower (higher) than for pure ZnO at low (High) *OFR* but approaches that of pure ZnO films.

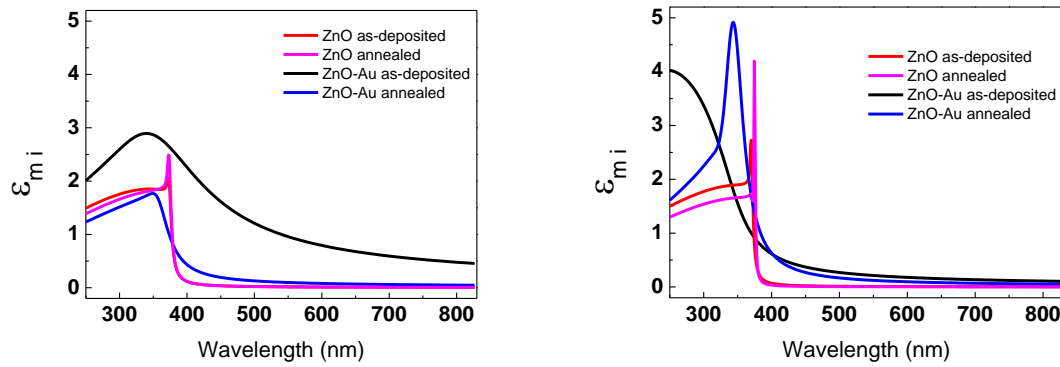


FIG. 4.20. Imaginary part of the ZnO dielectric function in as-deposited and annealed ZnO and ZnO-Au nanocomposite thin films grown at low (left) and high (right) *OFRs*.

The Maxwell Garnett (*MG*) model (see Annex B) is valid for metallic *NPs* with a radius higher than 1 nm. For the as-deposited samples, the Au *NPs* are already above the threshold of validity of the model. For annealed samples the Au *NPs* have an average radius of 2-3 nm, therefore the *MG* is valid. The *MG* model is mainly used for embedded/matrix configurations (see chapter 1, section 1.3 and annex B). Having in mind this consideration, using the *MG* model, it is possible to separate the contributions of the Au *NPs* and of the ZnO matrix to the effective dielectric function.

For the real part of the Au dielectric function ( $\epsilon_{NP_r}$ ), in as-deposited films, there are two characteristic features. First, model it is not required to include the contribution from the Au *NPs* in the *MG* model at high *OFR*. Therefore, it is not possible to extract the Au dielectric function. Second, the *OFR* influences  $\epsilon_{NP_r}$  (fig. 4.21). The decrease in *OFR* leads to an increase in the  $\epsilon_{NP_r}$  value, especially for wavelengths higher than 550 nm in the region where interband transitions characteristic Au occur.

In annealed nanocomposite films, it is possible to extract the  $\epsilon_{NP_r}$  for all the *OFRs*. We observe a similar trend than in as-deposited films:  $\epsilon_{NP_r}$  increases when decreasing the *OFR*.

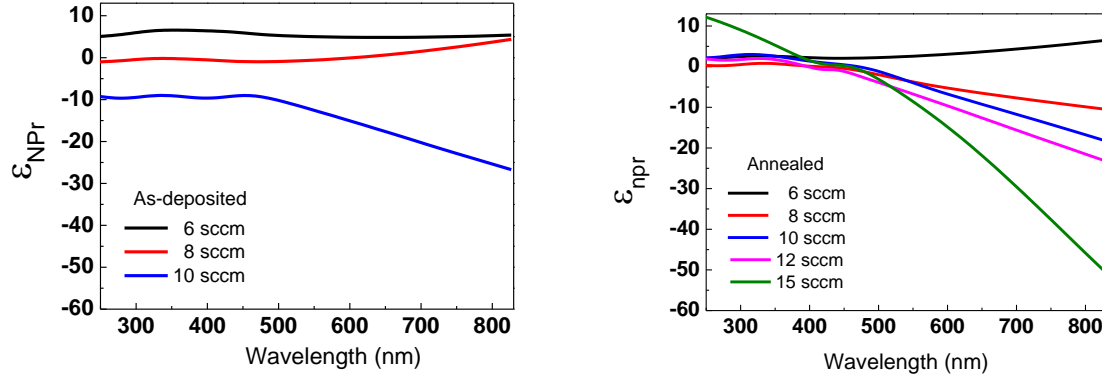


FIG. 4.21. Real part of the Au *NPs* dielectric function in as-deposited (left) and annealed at 300°C (right) ZnO-Au nanocomposite thin films grown at different *OFRs*.

$\epsilon_{NP_r}$  is directly inversely proportional to the damping constant ( $\Gamma$ ) of the Drude model (see Annex B). This can be related to a confinement due to the decrease of the Au *NPs* radius but also to a broader size dispersion of Au *NPs* or to the presence of chemical bonds at the Au|matrix interface (chemical damping)<sup>231</sup>.

As the size of Au *NPs* does not exhibit strong variations with the *OFR* in as deposited samples (see fig. 4.4), a confinement effect is not likely the main responsible for the change in the amplitude of  $\epsilon_{NP_r}$ . The formation of an Au<sub>2</sub>O<sub>3</sub> shell at high *OFR* uses 5*d* electrons of gold to form the oxide bonds characterized by the hybridization of the Au 5*d* with O 2*p* states. Knowing the *LSPR* of gold *NP* is largely influenced by 5*d* electrons, the presence of the Au<sub>2</sub>O<sub>3</sub> shell can inhibit the plasmon resonance<sup>232</sup>. Moreover, the 5*d*<sup>10</sup>→6*sp*<sup>0</sup> interband transitions responsible for the absorption background can be damped for the same reason. This can explain why above 10 sccm metallic Au does not contribute directly to the effective dielectric constant. According to our interaction model (fig. 4.14), below an *OFR* of 10 sccm the Au *NPs* interact with the donor rich-ZnO surface and there is a charge transfer (electrons) from the donor defects of ZnO to the Au *NPs*. Hence, the decrease in the  $\epsilon_{NP_r}$  likely represents the damping process due to the strong interaction between the Au *NPs* and ZnO. Putting together the results from this

---

section with the microstructural characterizations reported above, we can affirm that the *LSPR* absorption band appears in the visible range only after an annealing treatment that promotes the increase of the size of gold *NPs* from most likely size close to 3 to approximately 5 nm. The absence of the *LSPR* at low Au *NP* size can be explained by a high damping factor that decreases the amplitude of the resonance as reported in several works<sup>65,67</sup>. The red-shift of the *LSPR* absorption peak is explained by the higher dielectric constant of the ZnO matrix. Moreover, the difference in background absorption and in the thermal threshold for the development of the *LSPR* band at different *OF*Rs supports the presence of a strong chemical interaction between gold *NPs* and the ZnO matrix to form Au<sub>2</sub>O<sub>3</sub> shell at high *OF*Rs, as was deduced from XPS measurements.

#### **4.5. Physical properties of ZnO-Au nanocomposite films**

Physical properties of materials are to a large extent influenced by their microstructure and chemical state of their constitutive elements. Based on the results from the previous sections, strong differences in the physical properties of ZnO-Au nanocomposite films deposited at low and high *OF*Rs are expected. We evaluate hereinafter some optical, electrical and vibrational properties of the synthesized films.

##### **4.5.1. Conductivity**

ZnO-Au nanocomposites could be used in the future in optoelectronic devices. Therefore, it is important to assess the electrical behavior of the nanocomposite films with different microstructural characteristics. We evaluate the influence of the Au introduction, the *OF*R and the annealing treatment of ZnO-Au nanocomposite films compared to pure ZnO thin film.

Using the four-probe method we have measured the electrical resistivity and calculated the electrical conductivity. For the ZnO thin films, only the film grown at an *OF*R of 6 sccm has a measurable conductivity ( $\rho < 10^6$  ohm-cm), films grown at higher *OF*Rs are non-measurable (NM). Fig. 4.22 shows the electrical conductivity of as-deposited (blue bar) and annealed (red bar) ZnO-Au nanocomposite films grown at *OF*Rs 6, 8 and 15

sccm with different Au contents and compares it to that of the pure zinc oxide film grown at low *OFR* (6 sccm).

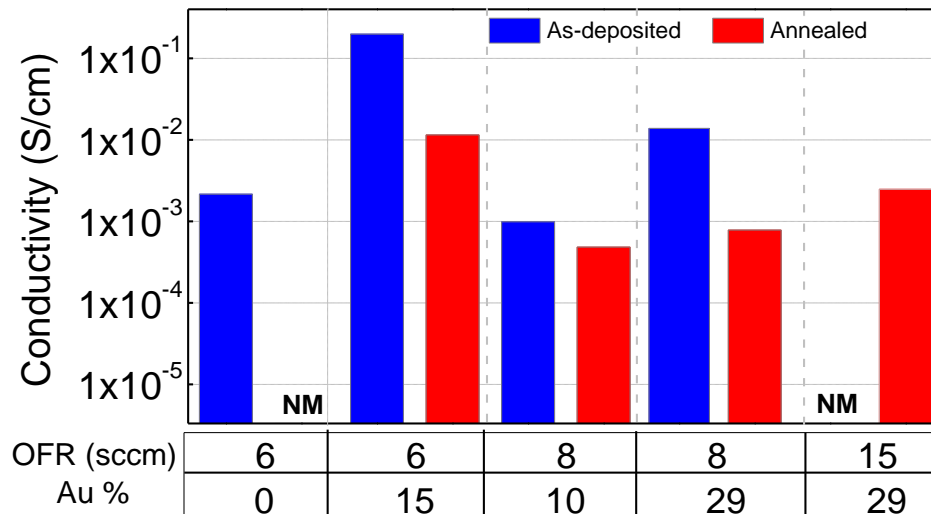


FIG. 4.22. Electrical conductivity of as-deposited and annealed ZnO and ZnO-Au nanocomposite films grown at 6, 8 and 15 sccm with different Au content NM stands for samples non-measurable ( $\rho > 10^7$  ohm-cm)

The introduction of gold is found to increase the electrical conductivity of the nanocomposite films grown at 6 and 8 sccm, but for the *OFr* of 15 sccm the films is still non-measurable. If we look at the nanocomposites grown at 8 sccm, we can clearly see how an increase in the Au content also increases the electrical conductivity when passing from 10 to 29 % Au. This is likely not explained by a percolation effect given that we could apply the Maxwell Garnett ellipsometric model for all synthesis and annealing conditions (see Annex B). It can be explained by a higher density of gold nanoparticles (see fig. 4.4) that leads to shorter distance between the *NPs* and subsequent decreased electrical resistance of the ZnO phase separating it or to improved electron tunneling. It is also evident from the figure that the annealing treatment (red bars) reduces the electrical conductivity for all the films except for the nanocomposite films grown at the highest *OFr* (15 sccm) that passes from a non-measurable to a conductive state. The resistivity of the nanocomposite is highly influenced by the ZnO matrix behavior showing that varying the *OFr* from 6 to 8 sccm the electrical conductivity decreases and we can relate it with the decrease of the carrier concentration as was discussed previously (see chapter 3, section 3.3). This leads us to prioritize the interpretation of

---

the results by a classical electron transport between the *NPs* rather than on the basis of the tunnel effect. The annealing treatment in air has been shown to have a strong influence on the matrix (ZnO) chemistry and crystallinity and on the size of *NPs*. The treatment has opposite effects on the electrical conduction of, on the one hand, ZnO and ZnO-Au films grown at low *OFR* and, on the other hand, of ZnO-Au films grown at high *OFR*. The oxidation of ZnO film upon annealing decreases the carrier concentration in films deposited at low *OFRs*, therefore increasing the resistivity of the films to a non-measurable state. We can suppose that the same mechanism is in action to reduce the conductivity of the nanocomposite film synthesized with the same *OFR*. We can therefore understand the reduction in conductivity after annealing of ZnO-Au films deposited at low *OFRs*.

The resistivity of as-deposited nanocomposite film grown at the highest *OFR* cannot be measured ( $\rho > 10^7$  ohm-cm) whatever the Au content. To the light of the results discussed in the previous sections, we ascribe it to the presence of the Au<sub>2</sub>O<sub>3</sub> shell consuming the Au valence conduction electrons and to a very poor crystallinity of the ZnO matrix. Annealing the film increases the conductivity, which is perfectly in line with the decomposition of the Au<sub>2</sub>O<sub>3</sub> shell that leads to the recovery of the metallic behavior at the surface of *NPs*.

As the matrix oxidation decreases the conductivity, the slight increase is not due to the ZnO. Let's remind that the ZnO-Au nanocomposite films grown with a high *OFR* are transparent certainly due to the Au<sub>2</sub>O<sub>3</sub> shell that does not allow the 5d-6sp transitions in gold. After 1h annealing at 300 °C in air takes place the decomposition of the Au<sub>2</sub>O<sub>3</sub> shell and the partial recovery of the Au metallic behavior at the ZnO|Au interface. The reduction of the Au<sub>2</sub>O<sub>3</sub> shells also allows the interband transitions represented by the color change from transparent to reddish films related with the plasmon presence and the detection of the *LSPR* absorption peak.

#### **4.5.2. vibrational properties**

The vibrational properties of the ZnO-Au nanocomposite films should be sensitive to the presence of an Au<sub>2</sub>O<sub>3</sub> shell surrounding Au *NPs*. Raman scattering measurements have been conducted in order to investigate such influence. Fig. 4.23 shows the Raman

---

spectra obtained using laser excitation at 633 nm of a ZnO film grown at low *OF*R and ZnO-Au nanocomposite films grown at low and at high *OF*Rs as-deposited and annealed. From the spectrum of pure ZnO, we can identify three main vibrational contributions consisting of two peaks located 438, 480 and a broad peak at 573 cm<sup>-1</sup>. These correspond to the  $E_2^{High}$ , the  $A_1(2LA)$  multiphonon vibration and possibly to an overlapping of the  $A_1(LO)$  and the  $E_1(LO)$  modes, respectively<sup>15,233,234</sup>.

The response of ZnO-Au nanocomposite films is different from that of pure ZnO although bulk metallic gold does not show a vibrational signature in Raman. We first observe a strong enhancement of the overall intensity compared to the ZnO film we will discuss in the next paragraph. Second, the film deposited at low *OF*R presents essentially the same broad band as pure ZnO ascribed the overlapping of  $A_1(LO)$  and  $E_1(LO)$  but shifted to lower wavenumbers. Increasing the *OF*R, leads to a completely different signal with a broad contribution showing a maximum near 630 cm<sup>-1</sup>. This signal has been identified as a possible vibrational state of Au<sub>2</sub>O<sub>3</sub><sup>235</sup> and HREELS measurements confirmed that it corresponds to the stretching of Au-O bonds<sup>236</sup>. Indeed, the presence of Au<sub>2</sub>O<sub>3</sub> in Au-ZnO films detected by electronic structure measurements using XPS (section 4.3.2) is supported by the vibrational signature in Raman scattering. The spectra of annealed ZnO-Au films synthesized at low and high *OF*Rs present similar features that can be assigned to the same contributions as for pure ZnO, This is in line with the fact that an annealing treatment at 300°C produces similar microstructures and chemical states in films deposited with different *OF*Rs (see section 4.3). Such observations on the shape and position of the contributions assigned to the ZnO matrix may have several origins. First, quantum confinement of the optical phonons<sup>237</sup> upon decreasing the crystal diameter of ZnO leads to a broadening of the optical phonon lines as well as shift to lower frequencies. For the films annealed at 300 °C grown at low *OF*Rs, the length coherence domains of ZnO changes with the Au content. There is a decrease from 34 to 22 nm (calculated for the FWHM of the (0002) peak in fig. 4.7) when increasing the Au content from 10 to 20 %, and has a similar value to those obtained in pure ZnO grown on silica. Nevertheless, this explanation does not stand for the shift observed between the as deposited and annealed states of the ZnO-Au film deposited at low *OF*R because the crystallinity of ZnO is not degraded by the annealing process (see section 4.2.2, fig. 4.7). We propose that the oxidation of the ZnO matrix during annealing decreases the carrier

concentration, in line with conductivity measurements, which is represented by a shift to lower frequencies of the  $A_1(LO)$  mode<sup>238</sup>.

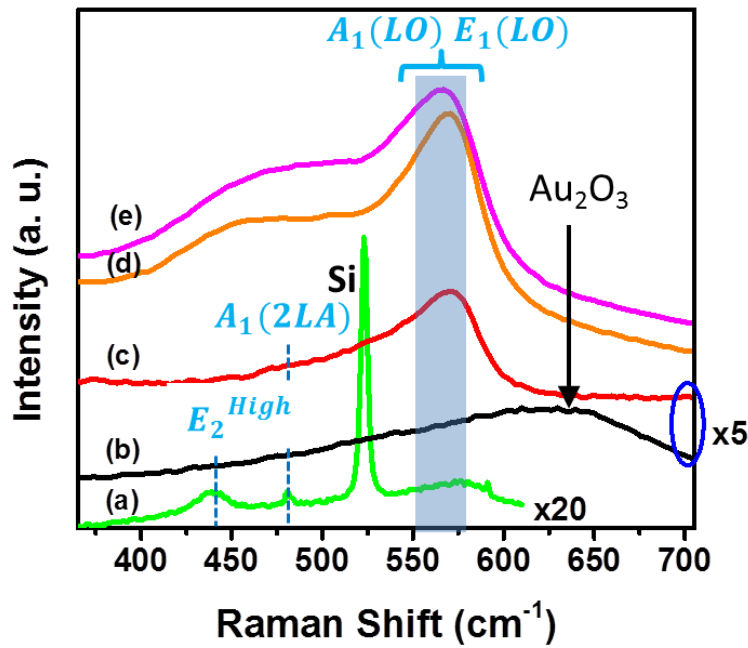


FIG. 4. 23. Raman shift spectra obtained with a 633 nm laser excitation of (a) as-deposited ZnO film grown at 6 sccm, (b) as-deposited ZnO-Au film grown at 15 sccm, (c) ZnO-Au film grown at 15 sccm after an annealing at 300 °C, 1h in air, (d) annealed ZnO-Au film grown at 6 sccm and (e) as-deposited ZnO-Au film grown at 6 sccm. All the ZnO-Au nanocomposite films have an Au content of nearly 20 %. (a) is amplified by a factor of 20 and (b) and (c) are amplified by a factor of 5.

The large increase in the overall intensity between pure ZnO and ZnO-Au nanocomposite (at most by a factor of 230) films can be explained by considering that the signal is enhanced by the presence of Au NPs. We can refer to data from the literature showing that, owing to the surface enhancement of Raman scattering (*SERS*), the band corresponding to  $A_1(LO)$  and  $E_1(LO)$  can be dramatically exalted for ZnO quantum dots placed on a substrate covered by Au NPs of 15 nm in diameter.<sup>239</sup> Such effect, known as plasmonic enhancement of Raman scattering, is due to the large local electric field around the NPs induced by the collective oscillation of electrons upon light excitation in *LSPR* (see chapter 1, section 1.5). As the *LSPR* band appears in the

absorption spectra after annealing of the Au-ZnO films (section 4.4), this effect explains well the Raman data obtained after annealing. Nevertheless, signal enhancement is also observed in as-deposited Au-ZnO films whereas no *LSPR* band could be detected in the absorption spectra of the corresponding films. Unfortunately, it was not possible to find data in the literature concerning the *SERS* by ultrafine Au *NPs* as those present in our films. In order to further investigate on a possible *SERS* effect in those samples, Raman scattering has been performed using different laser excitation wavelengths of 325, 633 and 784 nm (fig. 4.24). The first being well below the *LSPR* absorption band of samples where it can be detected, while the two others are in the *LSPR* band range (see section 4.4). Laser excitation at 325 nm produces spectra dominated by the band corresponding to  $A_1(LO)$  and  $E_1(LO)$  both in the sample having Au *NPs* in a metallic state (low *OFR*) and in the sample showing a shell/core  $Au_2O_3/Au$  configuration (high *OFR*). This band is known to be exalted using a laser of 325 nm of energy higher than the ZnO bandgap energy due to the exciton-phonon interaction that is stronger in *LO* than in *TO* phonons<sup>240</sup>. Additional weak signal corresponding to the vibrational signature of  $Au_2O_3$  could be detected in the film synthesized at high *OFR*.

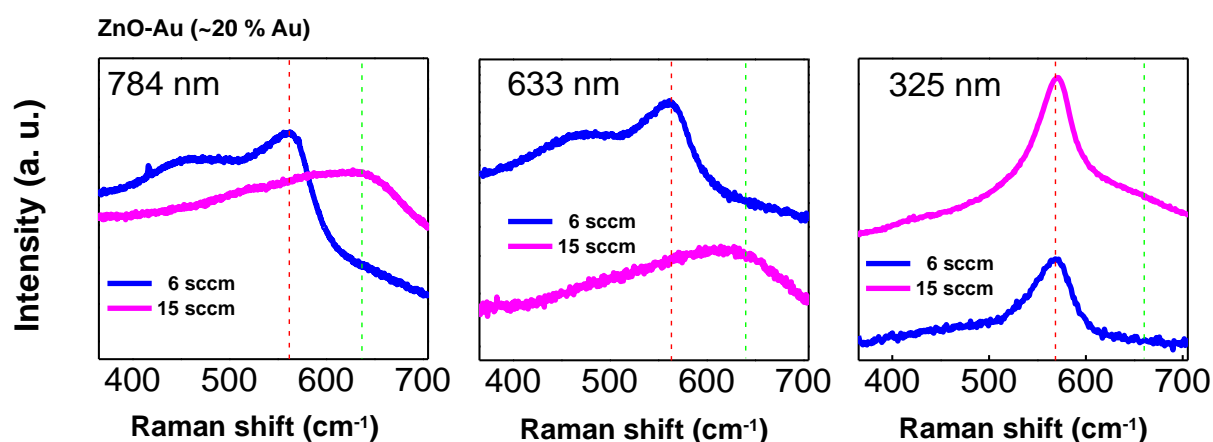


FIG. 4.24. Raman shift spectra measured with three different laser excitations (784, 633 and 325 nm) of as-deposited ZnO-Au nanocomposite films grown with an *OFR* of 6 sccm (blue) and 15 sccm (violet). The red and green dashed lines represent the position of the ZnO and  $Au_2O_3$  vibration modes respectively.

With laser excitations at 633 or 784 nm, the  $A_1(LO)$ - $E_1(LO)$  still appears with a high intensity in the films deposited at low *OFR* and is supplemented by the  $E_2^{High}$  mode and the  $A_1(2LA)$  multiphonon vibration. In contrast, the spectra corresponding to the film

---

synthesized at high *OFR* is dominated by the signature of  $\text{Au}_2\text{O}_3$  of much higher intensity than at 325 nm excitation.

Considering that a fraction of the Au particles experience *LSPR* for excitations at 633 and 784 nm (included in the broad *LSPR* band when it can be detected) although no *LSPR* band is observed in the absorption spectra, we can propose a simple model to explain this behavior.

At 325 nm, the sample are measured in conventional Raman mode and the properties and the  $A_1(LO)$ - $E_1(LO)$  band dominate the spectra due to the exaltation of the exciton-phonon interaction<sup>240</sup>. At 633 and 784 nm, metallic Au experience *LSPR* at some particles and exalt the signal of their environment, i.e. the ZnO matrix at low *OFR* and the  $\text{Au}_2\text{O}_3$  shell at high *OFR*.

### 4.5.3. Photoluminescence

Photoluminescence (PL) is an important feature of ZnO for applications such as ultra-violet (UV) detectors<sup>241</sup>, UV and blue light emitting devices<sup>242-244</sup>. It is based on the optical signals originating from recombination of free excitons near the bandgap energy and the recombination of excitons bound to defects that manifests by a broad emission band in the visible range in room temperature experiments. PL has been used in the previous chapter to investigate the presence of point defects in ZnO films and gain knowledge on the value of  $E_{g(ems)}$ . Here we look at the emission properties in order to investigate the influence of the ZnO-Au film microstructure on the emission signal. The PL spectra of the ZnO-Au nanocomposite films presented on fig. 4.25 for films synthesized at low *OFR* do not show a clear near-band edge emission (*NBE*) peak of ZnO (see chapter 3, section 3.2.2). However, a broad band is observed in the visible region, which intensity increases with the Au content. For films deposited at high *OFR* this dependency is not clear.

When annealing the samples, the emission in the visible range increases strongly and sets to a similar intensity for both *OFRs*. It is worth to notice that the near-band edge excitonic emission of ZnO is more pronounced after annealing but also there exist several signals at higher energies than the ZnO excitonic peak. These peaks can be

assigned to the *LO* phonon and its replicas since the energy separation between two consecutive peaks is of 72 meV, i.e. the *LO* phonon energy in ZnO. It is not a classical feature of ZnO PL that can be attributed to Raman excitation with the 325 nm laser<sup>245</sup>, likely facilitated by the presence of Au *NPs*.

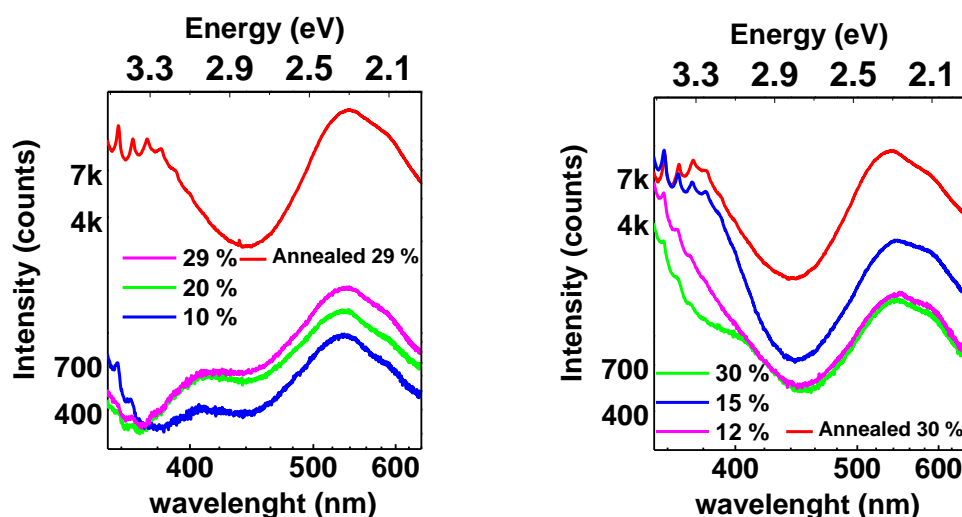


FIG. 4.25. Photoluminescence spectra of as-deposited and annealed ZnO-Au nanocomposite thin films grown with an *OFR* of 8 sccm with different Au contents (left) and an *OFR* of 15 sccm with different Au contents (right). For both graphs: red line is for the highest Au content ZnO-Au nanocomposite film after an annealing process for 1h in air at 300 °C.

Several works have shown an enhancement of the ZnO *NBE* emission for Au *NPs* or films on ZnO substrate<sup>246</sup> but in detriment to the visible emission<sup>247,248</sup>. It is explained by the inhibition of the defects radiative process due to transfer of the electrons (associated to donor defects) to the Au *NPs* and then to the conduction level of ZnO, thereby allowing the interband transition<sup>246,249</sup>. However, in our sample this process is likely incomplete due to the low crystallinity of the matrix and associated high density of point defects.

The PL measurements show how the ZnO-Au nanocomposite films have a different optical response than ZnO and also that it is sensitive to the Au content and the presence of the Au<sub>2</sub>O<sub>3</sub> shell. However, at this point there is not enough information to describe in details the interactions between, on one side, the ZnO shallow and deep defects and, on the other side, the Au *NPs* and their influence on the *LSPR* effect. Such informations could help to clarify the influence of the embedded Au *NPs* in ZnO as matrix.

---

## 4.6. Conclusion

In this chapter we observed how deeply are influenced the structural, microstructural, optical and physical properties by the incorporation of gold into ZnO as matrix when compared to pure ZnO. Moreover, the chemical behavior of ZnO can also strongly affect the behavior of the Au *NPs* as was observed from the optical properties.

The changes in the different properties let us observe the strong interaction between both components, revealing that a change in one of them affects the properties of the other. However, there are interactions between the Au *NPs* and the ZnO matrix enhanced by the electromagnetic radiation that are still not fully understood and need to be studied in more details.

We believe that this study will help understanding how to obtain conductive nanocomposites from a ZnO resistive matrix. Moreover, according to the results of Raman spectroscopy analysis, a broad *LSPR* region could be benefit to, produce SERS substrate that could be activated with different laser wavelengths with the possibility to enhance or not specific vibrational modes.

---

# General conclusions

Wide bandgap semiconductors and metal/oxide nanocomposite films are building blocks for the development of a novel generation of devices in the field of optoelectronic and plasmonics. This work studied the microstructure and chemistry of ZnO and ZnO-Au nanocomposite films in order to better understand their functional properties with a focus on the optical properties.

ZnO and ZnO-Au thin films have been synthesized by reactive magnetron sputtering and studied for their microstructural and optical properties. It is found that the structure, microstructure, optical and physical properties are strongly influenced by experimental parameters or the nature of the substrate.

The first chapter of this work was dedicated to a literature review on the general properties of ZnO, gold in the form of nanoparticles (with a special attention paid to the localized surface plasmon resonance phenomenon) and recent studies dedicated to ZnO-Au thin films.

The second chapter described the principles of the reactive magnetron sputtering method and of the characterization methods used for the study of the material properties.

The third chapter was dedicated to the study of ZnO thin films with two main interests related to the microstructure and the optical properties of ZnO, respectively. It has been shown it is possible to achieve single domain epitaxial growth of ZnO onto sapphire at high oxygen flow rate fed into the deposition chamber (oxygen-rich conditions) without in-situ annealing and at self-established substrate temperatures very close to room temperature. The epitaxy only occurs on (0001)-sapphire substrates and we propose it is eased by an O<sup>-</sup> bombardment mechanism that occurs only after a critical-*OFR* as the target surface is oxidized. Upon changing the *OFR*, was also observed by photoluminescence spectroscopy a change in the defect chemistry from a situation where it is dominated by shallow donor defects in zinc-rich conditions to a situation where oxygen interstitials dominates under oxygen-rich conditions. The possibility to vary the defect chemistry in epitaxial films opens possibilities to study the influence of point

---

defects on the properties of the ZnO films in absence of grain boundaries. The study of the optical properties put some light onto the understanding of the close relationship between the emission and absorption bandgap energies. The results allow a better understand the large scatter of the bandgap energy of ZnO reported in literature by proposing a model taking into account the chemical defects. More particularly, was highlighted the need to consider the Urbach energy in the optical behavior of ZnO films showing a large density of point defects. A simple relationship that connects the absorption and emission bandgap energies was proposed on the basis on the theory of the Urbach energy involving exciton-phonons and exciton-defects interactions.

The last chapter of this work was dedicated to the synthesis and study of ZnO-Au nanocomposite films. It has been evaluated how the incorporation of gold in the ZnO matrix can influence the structural, microstructural, optical and physical properties of the nanocomposites when compared to pure ZnO. The chemical behavior of ZnO (reducing or oxidizing), which depends on the defect chemistry, can also change the behavior of the Au NPs as was observed from the optical properties. The most striking results are the strong decrease in crystallinity compared to pure ZnO and the change from highly absorbent layers at low *OFR* (Zinc-rich conditions) to more transparent films when the *OFR* is increased to reach oxygen-rich conditions. The data indicate that the incorporation of gold in the ZnO lattice deforms the crystal lattice and decreases its the crystallinity and, simultaneously, the presence of donor (acceptor) defects in the ZnO matrix is found to reduce (oxidize) the Au NPs changing the properties of both components. These two phenomena and other changes in the different properties let us observe the strong interaction among both components, revealing that modifications in one of it affect the properties of the other. However, there some interactions between the Au NPs and the ZnO matrix enhanced by the electromagnetic radiation are still not completely understood and need to be studied in more details.

This work could serve as a platform to further develop the applications of ZnO-Au nanocomposite films thanks to the understanding it provides on the particle/matrix interactions.

---

# Annexes

## Annex A

### Determination of the a lattice parameter by in-plane X-ray diffraction

To determine if there is in-plane stress in the ZnO thin films (chapter 2, section 2.2), it was necessary to know if an elongation along the  $c$ -axis in the ZnO films is accompanied by a contraction in the  $a$  lattice parameter. Using the Bragg law, it is possible to determine the interplanar distance  $d$  of a specific ZnO diffraction plane and to relate it with the  $a$  lattice parameter of ZnO:

$$\frac{1}{d^2} = \frac{4}{3} \left( \frac{h^2 + hk + k^2}{a^2} \right) + \frac{l^2}{c^2} \quad (\text{A.1})$$

We selected the {1000} ZnO planes for this purpose. Equation A.1 then becomes:

$$a = \sqrt{\frac{4}{3} d^2} \quad (\text{A.2})$$

To reach this objective we performed in-plane XRD measurement for the ZnO film grown at an *OF*R of 10 sccm on fused silica (see fig. A.1) showing a large elongation in the  $c$ -axis direction. An accurate value of the  $\theta$  diffraction angle of the selected plane has to be extracted. For that, the {11 $\bar{2}$ 0} sapphire diffraction plane was used as reference to ensure the peak position corresponding to diffraction by {1000} ZnO planes represents the actual geometry of the crystal cell. We used an X'Pert Pro MPD diffractometer. The X-rays were generated from a Cu anode, which has a characteristic emission wavelength of 1.5406 Å. The determination of the  $\theta$  position was extracted using gaussian fitting.

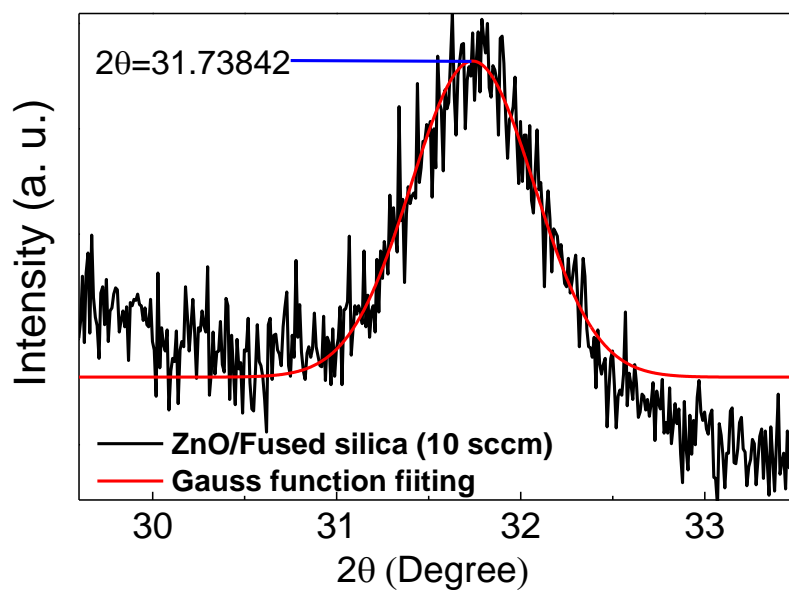


FIG. A.1. In-plane X-ray diffractogram of a ZnO film grown at an *OF*R of 10 sccm on fused silica. The peak corresponds to the diffraction by {1000} planes of wurtzite ZnO. The red line corresponds to a Gauss function in order to determine with precision the peak position.

The obtained value of 3.2527 Å for the *a* lattice parameter is lower than the bulk value of 3.2539 Å. This confirms in-plane contraction at the origin of an elongation along the *c*-axis.

---

## X-ray diffractogram of ZnO thin film in the complete scan range measured

In order to affirm that the films have a preferential growth along the  $c$ -axis we show one X-ray diffractogram between 15 and 85 degrees. In fig. A.2 the diffractogram (in logarithmic scale) shows two signals, one very intense compared to the second one. The signals peak at 34 and 72 degrees that correspond to diffraction by the (0002) and (0004) planes of the ZnO wurtzite structure.

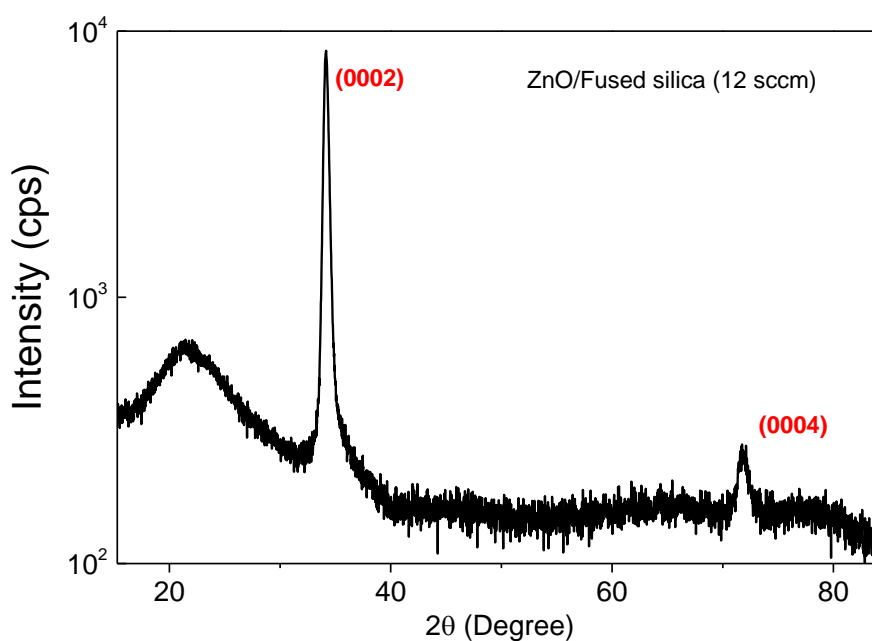


FIG. A.2. X-ray diffractogram (full range) of a ZnO thin film grown at an *OF*R of 12 sccm on fused silica. Only the (0002) and (0004) planes are detectable in the diffractogram.

The intensity is in a logarithmic scale.

---

## Annex B

### Ellipsometry dispersion laws

While UV-Vis spectrophotometry gives the overall optical behavior of the nanocomposite films, further details on the individual contribution of the ZnO matrix and gold nanoparticles can be extracted by modelling spectroscopic ellipsometry measurements. Measurements and modelling have been performed in collaboration with the LCP-A2MC research group belonging to the “Institut Jean Barriol” of “Université de Lorraine” in Metz, France.

#### ZnO thin films

As mentioned in chapter 2, section 2.4.6, for homogeneous semiconductor films, such as the ZnO films, there are several methods used to extract optical parameters. In our work, to fit the raw data of homogeneous films and obtain the optical constants, we used the Forouhi-Bloomer (*FB*) dispersion model<sup>132,133</sup>. Dispersion formulas are mathematical expressions setting the energy dependence of a material optical parameters ( $n$ ,  $k$ ) or dielectric function ( $\varepsilon_r$ ,  $\varepsilon_i$ )<sup>250</sup>. Parameters of the *FB* model can be related using the following expressions:

$$n(E) = \sqrt{\varepsilon^\infty} + \frac{B_0 \times E + C_0}{E^2 - B \times E + C}, \quad (\text{B.1})$$

$$k(E) = \begin{cases} \frac{A \times (E - E_{gFB})^2}{E^2 - B \times E + C} & E > E_{gFB} \\ 0 & E \leq E_{gFB} \end{cases} \quad (\text{B.2})$$

$$B_0 = \frac{A}{Q} \times \left( -\frac{B^2}{2} + E_g \times B - E_{gFB}^2 + C \right) \quad (\text{B.3})$$

$$C_0 = \frac{A}{Q} \times \left( (E_{gFB}^2 + C) \times \frac{B}{2} - 2E_{gFB} \times C \right) \quad (\text{B.4})$$

$$Q = \frac{1}{2} \sqrt{4 \times C - B^2} \quad (\text{B.5})$$

---

The determination of the  $A, B, C, E_{g_{FB}}$  and  $\varepsilon^\infty$  fitting parameters allows to characterize the optical response of the film.

- $E_{g_{FB}}$  is the bandgap energy. However, in case of Urbach tails it underestimates the bandgap. For this reason, it was not used for the discussions.
- $\varepsilon^\infty$  is the dielectric function at high-frequency of the.
- $A, B, C$  are constants that define the position, the amplitude and the width of the absorption peak.

From the fitting procedure, we obtain  $n$  and  $k$ . It is then possible to obtain the dielectric function ( $\varepsilon_r, \varepsilon_i$ ), calculate the absorption coefficient ( $\alpha$ ).  $E_{g(ABS)}$  has been extracted using the Tauc plot on the dispersion curve of the absorption coefficient (see chapter 2).

### **Au NPs**

The dielectric function of noble metal *NPs* such as silver and gold consists of two contributions. One accounts for interband transitions (due to the *5d* electrons response). The other is the intraband contribution that takes into account the free electron response.

In a classical approach, electron confinement effects appear when the mean free path of conduction electron is limited by the size of *NPs*. Assuming that only the free electrons are affected by this effect, the dielectric function of metallic *NPs* can be expressed in the following way:

$$\varepsilon(\omega) = \varepsilon_{bulk} - \frac{\omega_p^2}{-\omega^2 + i\omega\Gamma_0} + \frac{\omega_p^2}{-\omega^2 + i\omega(\Gamma_0 + \frac{Av_f}{R})} \quad (\text{B.6})$$

With  $\varepsilon_{bulk}, \omega_p, v_f$  and  $\Gamma_0$  the dielectric function, the plasma frequency, the Fermi velocity of free electrons and electron damping parameter, respectively.  $A$  is a parameter that depends on the material and is fixed to 1 in our case.  $R$  is the radius of *NPs*.

---

## Effective medium models for heterogeneous composites

In chapter 2, section 2.4.6 we indicated that in heterogeneous systems (composites), it is necessary to consider that the optical response is the contribution of all components. In the effective medium approximation, the effective dielectric function ( $\epsilon_{eff}$ ) relates the dielectric function of each component to its volume fraction within the material. In this work we use two effective medium approaches, The Maxwell-Garnett (*MG*) and the Bruggeman (*BM*) effective medium models, to obtain  $\epsilon_{eff}$ .

The *MG* considers the presence of a component in a host, while the *BM* does not considers a host/embedded system and both components contribute in an independent way to the properties of the nanocomposite (see fig. B.1). The first model is most used when the percentage of the component *i* is low enough to consider the particles are well separated. If particles are in contact, the *BM* model better describe the optical behavior.

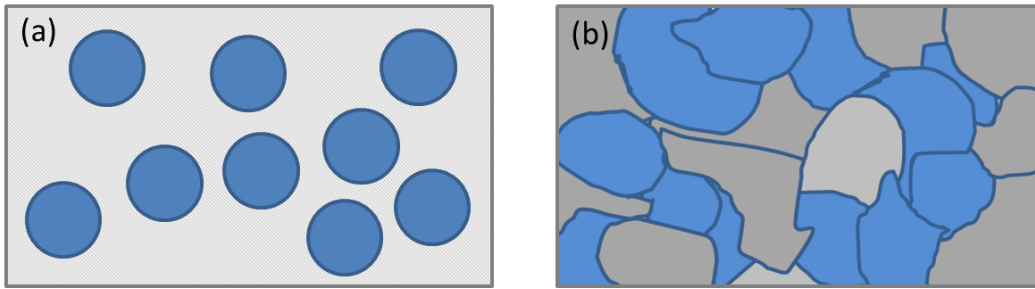


FIG. B.1. Topology of composite medium corresponding to the (a) Maxwell-Garnett and (b) Bruggeman effective medium models.

The Maxwell-Garnett effective medium model relates the dielectric constants by:

$$\frac{\epsilon_{eff} - \epsilon_a}{\epsilon_{eff} + 2\epsilon_a} = (1 - f_a) \frac{\epsilon_b - \epsilon_a}{\epsilon_b + 2\epsilon_a} \quad (\text{B.7})$$

The expression for the Bruggeman effective medium model is:

$$f_a \frac{\epsilon_a - \epsilon_{eff}}{\epsilon_a + 2\epsilon_{eff}} + (1 - f_a) \frac{\epsilon_b - \epsilon_{eff}}{\epsilon_b + 2\epsilon_{eff}} = 0 \quad (\text{B.8})$$

In both expressions,  $\epsilon_a$ ,  $\epsilon_b$  and  $\epsilon_{eff}$  are the dielectric constants of the components *a*, *b* and of the effective medium, respectively.  $f_a$  and  $(1 - f_a)$  are the volume fractions of each component.

---

The extraction of  $\epsilon_{eff}$  is achieved after the following steps:

- The first step allows obtaining the dielectric function of the matrix (ZnO). In this case, it has been extracted by fitting the data obtained by measurement of the pure ZnO films grown at equivalent experimental conditions than the ZnO-Au nanocomposite film to analyze.
- With the ZnO dielectric function fixed, it is possible to obtain the A/R ratio of equation B.6 and the volume fraction of gold.
- With the gold dielectric function fixed, the ZnO dielectric function parameters are adjusted. Successive iterations enable fitting the experimental data with a good accuracy.

### Ellipsometric models

For ZnO thin films, the ellipsometric model (fig. B.2) is composed of two films of thickness  $d$  and  $d_r$ , respectively, on a silicon substrate. The upper film represents the ZnO roughness and is modeled by the Bruggeman effective medium approximation with a ZnO volume fraction fixed at 50 %. The ZnO thin film is modeled using the FB dispersion model.

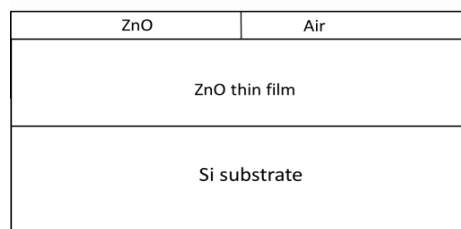


Fig. B.2. Ellipsometric model representing a ZnO thin film. Top layer models the roughness and the bottom layer represents the ZnO film and is treated with the *FB* dispersion model. The silicon substrate has a known contribution.

Fig. B.3 shows an exemple of the fitting, using the model described above, of the experimental ellipsometric parameters obtained by measurement of a ZnO film deposited with an OFR of 6 sccm.

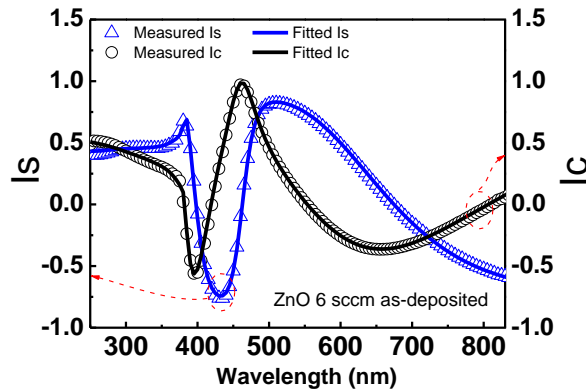


Fig. B.3. Experimental (symbols) and calculated (lines)  $I_s$  and  $I_c$  ellipsometric parameters measured at  $70^\circ$  for as-deposited ZnO thin films grown at an *OFR* of 6 sccm.

The ellipsometric model applied to represent the microstructure of ZnO-Au nanocomposite thin films is composed of two layers: an upper layer that represents the roughness of the film and the *BM* model is used as for ZnO films. The second layer, with gold and ZnO, describes the core of the nanocomposite film. It allows to separate the contribution of the dielectric functions of gold and ZnO. The *MG* effective medium model is used for that, assuming that gold *NPs* are embedded into ZnO and the domains are spatially separated<sup>131,251</sup>, as observed experimentally using HRTEM (chapter 4, fig. 4.5).

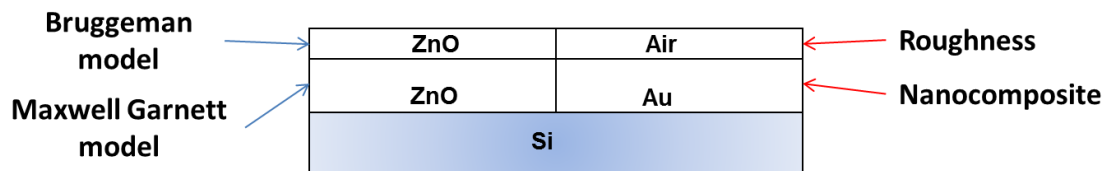


Fig. B.4. Ellipsometric model used to represent the microstructure of a ZnO-Au nanocomposite film. Top layer models the roughness and is treated with the *BM* model and the bottom layer represents the core of the nanocomposite and is treated with the *MG* model. The silicon substrate contribution is known.

$I_s$  and  $I_c$  are the experimental data obtained from the ellipsometry measurements (chapter 2, section 2.4.8).

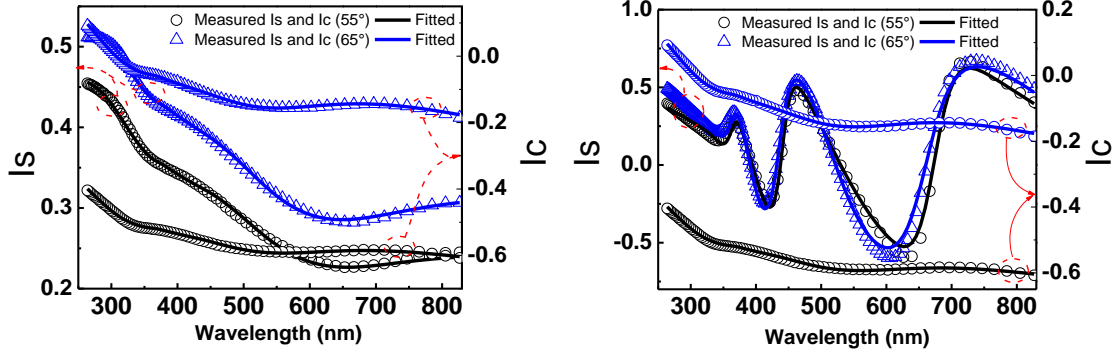


Fig. B.5. Experimental (symbols) and calculated (lines)  $|S|$  and  $|C|$  ellipsometric parameters measured at  $55^\circ$  and  $65^\circ$  for ZnO-Au nanocomposite films grown at low (left) and high (right) *OFR*.

The data are the values to be fitted by the proposed model. In figure B.5 are shown as examples the experimental data for a ZnO-Au nanocomposite thin film grown at low *OFR* (left) and at high *OFR* (right). The measurements were performed by changing the incident beam angle from  $55$  to  $75^\circ$  with a step of  $5^\circ$  (fig. B.5 only shows the fitting for  $55$  and  $65^\circ$ ). It is clear that the fitting has a good correspondence with the experimental data in both films while the optical response is different for both conditions.

### Polaron effective Dielectric function ( $\epsilon^*$ )

As seen in chapter 3, section 3.2.3 the polaron effective dielectric constant ( $\epsilon^*$ ) is define as:

$$\epsilon^* = \left( \frac{1}{\epsilon^\infty} - \frac{1}{\epsilon^0} \right)^{-1} \quad (\text{B.9})$$

With  $\epsilon^\infty$  the high-frequency dielectric constant and  $\epsilon^0$  the static dielectric constant.  $\epsilon^\infty$  is defined in, and obtained directly by, the *FB* model. To extract  $\epsilon^0$ , it is necessary to make an extrapolation considering that there are no characteristic ZnO bands in the infrared region. This approximation is valid given that the carrier concentration is too low to consider any plasmon resonance<sup>136</sup>.

---

## Annex C

### Experimental parameters for ZnO-Au nanocomposite films deposition

In this work, we elaborated two series of ZnO-Au nanocomposite films for their characterization and study. In the first series we varied the gold content at two fixed *OFRs* (8 and 15 sccm). Samples 6 to 10 are shown in chapter 4, fig. 4.1 and were elaborated to verify the Au content variation with the Au target density and the target-substrate distance (*Dts*). No other measurements were made for these films. The second series was elaborated with the aim to investigate in detail the influence of the *OFR* for nanocomposite films with relatively large Au quantities. The slight variation in the total pressure compared to the first series is due to a change of the pressure gauge in the lapse between the elaborations of the two series.

Sample	<i>OFR</i> (sccm)	$I_{Au}$ (A)	<i>Dts</i> (mm)	$\left(\frac{Au}{Au + Zn} \times 100\right)$	Thickness (nm)	Total pressure (Pa)
1 <sup>st</sup> series (Au content variation)						
1	8	0.006	55	10.4	166	0.445
2	8	0.010	55	20.4	110	0.434
3	8	0.012	55	28.7	158	0.448
4	15	0.006	100	12.5	162	0.516
5	15	0.006	120	15.7	196	0.513
6	15	0.009	55	29.6	125	0.513
7	8	0.009	55	15.70	180	0.431
8	8	0.015	55	31.11	110	0.446
9	15	0.006	85	15.05	172	0.513
10	15	0.006	55	24.27	162	0.511
2 <sup>nd</sup> series ( <i>OFR</i> variation)						
11	6	0.017	55	16.6	206	0.268
12	8	0.015	55	22.0	196	0.278
13	10	0.010	55	21.2	167	0.306
14	12	0.010	55	24.2	216	0.314
15	15	0.010	55	28.7	245	0.364

---

# Bibliography

- (1) Strong, A. B. *Fundamentals of Composites Manufacturing, Second Edition: Materials, Methods and Applications*; Society of Manufacturing Engineers, 2008.
- (2) Ebrahimi, F. *Nanocomposites - New Trends and Developments*; InTech, 2012.
- (3) Basu, T. S.; Ghosh, S.; Gierlotka, S.; Ray, M. Collective Charge Transport in Semiconductor-Metal Hybrid Nanocomposite. *Appl. Phys. Lett.* **2013**, *102*, 053107.
- (4) Cozzoli, P. D.; Comparelli, R.; Fanizza, E.; Curri, M. L.; Agostiano, A.; Laub, D. Photocatalytic Synthesis of Silver Nanoparticles Stabilized by TiO<sub>2</sub> Nanorods: A Semiconductor/Metal Nanocomposite in Homogeneous Nonpolar Solution. *J. Am. Chem. Soc.* **2004**, *126*, 3868–3879.
- (5) Cassagneau, T.; Hix, G.; Jones, D.; Mairelestorres, P.; Rhomari, M.; Roziere, J. Nano-Nanocomposite Systems - in-Situ Growth of Particles and Clusters of Semiconductor-Metal Sulfides in Porous Silica-Pillared Layered Phosphates. *J. Mater. Chem.* **1994**, *4*, 189–195.
- (6) Granitzer, P.; Rumpf, K.; Poelt, P.; Albu, M.; Chernev, B. The Interior Interfaces of a Semiconductor/metal Nanocomposite and Their Influence on Its Physical Properties. *Phys. Status Solidi C* **2009**, *6*, 2222–2227.
- (7) Gries, T.; Catrin, R.; Migot, S.; Soldera, F.; Endrino, J.-L.; Landa-Cánovas, A. R.; Cleymand, F.; Mangin, D.; Mücklich, F.; Horwat, D. Local Modification of the Microstructure and Electrical Properties of Multifunctional Au-YSZ Nanocomposite Thin Films by Laser Interference Patterning. *ACS Appl. Mater. Interfaces* **2014**.
- (8) Kim, K. H.; Baek, Y.-K.; Jeon, H.-J.; Srinivasarao, M.; Jung, H.-T. Cylindrical Posts of Ag/SiO<sub>2</sub>/Au Multi-Segment Layer Patterns for Highly Efficient Surface Enhanced Raman Scattering. *Nanotechnology* **2012**, *23*, 315302.
- (9) Dhas, V.; Muduli, S.; Lee, W.; Han, S.-H.; Ogale, S. Enhanced Conversion Efficiency in Dye-Sensitized Solar Cells Based on ZnO Bifunctional Nanoflowers Loaded with Gold Nanoparticles. *Appl. Phys. Lett.* **2008**, *93*, 243108.
- (10) Dong, W.; Li, Y.; Niu, D.; Ma, Z.; Gu, J.; Chen, Y.; Zhao, W.; Liu, X.; Liu, C.; Shi, J. Facile Synthesis of Monodisperse Superparamagnetic Fe<sub>3</sub>O<sub>4</sub> Core@hybrid@Au Shell Nanocomposite for Bimodal Imaging and Photothermal Therapy. *Adv. Mater.* **2011**, *23*, 5392–5397.
- (11) Klingshirn, C.; Meyer, B. K.; Waag, A. *ZnO: From Fundamental Properties towards Novel Applications*; Springer Verlag, 2010.
- (12) Brüesch, P. *Phonons: Theory and Experiments I - Lattice Dynamics and Models of Interatomic Forces*; 1982.
- (13) Serrano, J.; Romero, A. H.; Manjón, F. J.; Lauck, R.; Cardona, M.; Rubio, A. Pressure Dependence of the Lattice Dynamics of ZnO: An Ab Initio Approach. *Phys. Rev. B* **2004**, *69*, 094306.

- 
- (14) Manjón, F. J.; Marí, B.; Serrano, J.; Romero, A. H. Silent Raman Modes in Zinc Oxide and Related Nitrides. *J. Appl. Phys.* **2005**, *97*, 053516.
- (15) Cuscó, R.; Alarcón-Lladó, E.; Ibáñez, J.; Artús, L.; Jiménez, J.; Wang, B.; Callahan, M. Temperature Dependence of Raman Scattering in ZnO. *Phys. Rev. B* **2007**, *75*.
- (16) Janotti, A.; Van de Walle, C. G. Fundamentals of Zinc Oxide as a Semiconductor. *Rep. Prog. Phys.* **2009**, *72*, 126501.
- (17) Madelung, P. D. O. *Semiconductors — Basic Data*; Madelung, P. D. O., Ed.; Springer Berlin Heidelberg, 1996.
- (18) Birman, J. L. Polarization of Fluorescence in CdS and ZnS Single Crystals. *Phys. Rev. Lett.* **1959**, *2*, 157–159.
- (19) Mang, A.; Reimann, K.; Rübénacke, S. Band Gaps, Crystal-Field Splitting, Spin-Orbit Coupling, and Exciton Binding Energies in ZnO under Hydrostatic Pressure. *Solid State Commun.* **1995**, *94*, 251–254.
- (20) Meyer, B. K.; Alves, H.; Hofmann, D. M.; Kriegseis, W.; Forster, D.; Bertram, F.; Christen, J.; Hoffmann, A.; Straßburg, M.; Dworzak, M.; et al. Bound Exciton and Donor–acceptor Pair Recombinations in ZnO. *Phys. Status Solidi B* **2004**, *241*, 231–260.
- (21) Ellmer, K.; Klein, A.; Rech, B. *Transparent Conductive Zinc Oxide Basics and Applications in Thin Film Solar Cells*; Springer: Berlin, 2008.
- (22) Pelant, I.; Valenta, J. *Luminescence Spectroscopy of Semiconductors*; Oxford University Press, 2012.
- (23) Amirtharaj, P. M.; Seiler, D. G. Optical Properties of Semiconductors. *Handb. Opt.* **1995**, *2*, 36–1.
- (24) Dong, J.; Drabold, D. A. Band-Tail States and the Localized-to-Extended Transition in Amorphous Diamond. *Phys. Rev. B* **1996**, *54*, 10284.
- (25) Cohen, M. H.; Fritzsche, H.; Ovshinsky, S. R. Simple Band Model for Amorphous Semiconducting Alloys. *Phys. Rev. Lett.* **1969**, *22*, 1065–1068.
- (26) Kim, K.-K.; Niki, S.; Oh, J.-Y.; Song, J.-O.; Seong, T.-Y.; Park, S.-J.; Fujita, S.; Kim, S.-W. High Electron Concentration and Mobility in Al-Doped N-ZnO Epilayer Achieved via Dopant Activation Using Rapid-Thermal Annealing. *J. Appl. Phys.* **2005**, *97*, 066103.
- (27) Jullien, M.; Horwat, D.; Manzeh, F.; Escobar Galindo, R.; Bauer, P.; Pierson, J. F.; Endrino, J. L. Influence of the Nanoscale Structural Features on the Properties and Electronic Structure of Al-Doped ZnO Thin Films: An X-Ray Absorption Study. *Sol. Energy Mater. Sol. Cells* **2011**, *95*, 2341–2346.
- (28) Walsh, A.; Da Silva, J.; Wei, S.-H. Origins of Band-Gap Renormalization in Degenerately Doped Semiconductors. *Phys. Rev. B* **2008**, *78*.
- (29) Mohanty, B. C.; Yeon, D. H.; Das, S. N.; Kwak, J. H.; Yoon, K. H.; Cho, Y. S. Unusual near-Band-Edge Photoluminescence at Room Temperature in Heavily-Doped ZnO:Al Thin Films Prepared by Pulsed Laser Deposition. *Mater. Chem. Phys.* **2013**, *140*, 610–615.
- (30) Samuel, L.; Brada, Y.; Burger, A.; Roth, M. Urbach Rule in Mixed Single Crystals of  $Zn_xCd_{1-x}Se$ . *Phys. Rev. B* **1987**, *36*, 1168.
-

- 
- (31) Ates, A.; Yildirim, M. A.; Kundakci, M.; Yildirim, M. Investigation of Optical and Structural Properties of CdS Thin Films. *Chin. J. Phys.* **2007**, *45*.
- (32) Ilican, S.; Caglar, Y.; Caglar, M. Preparation and Characterization of ZnO Thin Films Deposited by Sol-Gel Spin Coating Method. *J Optoelectron Adv Mater* **2008**, *10*, 2578–2583.
- (33) Krajewski, T. A.; Dybko, K.; Luka, G.; Wachnicki, L.; Witkowski, B. S.; Duzynska, A.; Kopalko, K.; Lusakowska, E.; Kowalski, B. J.; Godlewski, M.; et al. Electrical and Optical Properties of Zinc Oxide Layers Grown by the Low-Temperature Atomic Layer Deposition Technique. *Phys. Status Solidi B* **2010**, *247*, 1653–1657.
- (34) Rai, R. C.; Guminiak, M.; Wilser, S.; Cai, B.; Nakarmi, M. L. Elevated Temperature Dependence of Energy Band Gap of ZnO Thin Films Grown by E-Beam Deposition. *J. Appl. Phys.* **2012**, *111*, 073511.
- (35) Kasap, S.; Capper, P. *Springer Handbook of Electronic and Photonic Materials*; Springer, 2006.
- (36) Vlasenko, L. S.; Watkins, G. D. Optical Detection of Electron Paramagnetic Resonance in Room-Temperature Electron-Irradiated ZnO. *Phys. Rev. B* **2005**, *71*, 125210.
- (37) Zamfirescu, M.; Kavokin, A.; Gil, B.; Malpuech, G.; Kaliteevski, M. ZnO as a Material Mostly Adapted for the Realization of Room-Temperature Polariton Lasers. *Phys. Rev. B* **2002**, *65*, 161205.
- (38) Baltakesmez, A.; Tekmen, S.; Tuzemen, S. ZnO Homojunction White Light-Emitting Diodes. *J. Appl. Phys.* **2011**, *110*, 054502.
- (39) Grabowska, J.; Meaney, A.; Nanda, K. K.; Mosnier, J. P.; Henry, M. O.; Duclere, J. R.; McGlynn, E. Surface Excitonic Emission and Quenching Effects in ZnO Nanowire/nanowall Systems: Limiting Effects on Device Potential. *Phys. Rev. B* **2005**, *71*, 115439.
- (40) Özgür, U.; Alivov, Y. I.; Liu, C.; Teke, A.; Reshchikov, M. A.; Doğan, S.; Avrutin, V.; Cho, S.-J.; Morkoç, H. A Comprehensive Review of ZnO Materials and Devices. *J. Appl. Phys.* **2005**, *98*, 041301.
- (41) Singh, N.; Kumari, B.; Sharma, S.; Chaudhary, S.; Upadhyay, S.; Satsangi, V. R.; Dass, S.; Shrivastav, R. Electrodeposition and Sol-gel Derived Nanocrystalline N-ZnO Thin Films for Photoelectrochemical Splitting of Water: Exploring the Role of Microstructure. *Renew. Energy* **2014**, *69*, 242–252.
- (42) Sun, J.; Gong, Y.; Liu, K.; Li, Y.; Du, G. Investigation of ZnO Nanostructures Grown on Si and GaAs Substrates by Low-Temperature CBD Method. *Phys. Status Solidi A* **2014**, *211*, 625–629.
- (43) Schmidt-Mende, L.; MacManus-Driscoll, J. L. ZnO-nanostructures, Defects, and Devices. *Mater. Today* **2007**, *10*, 40–48.
- (44) Robin, I. C.; Ribeaud, A.; Brochen, S.; Feuillet, G.; Ferret, P.; Mariette, H.; Ehrentraut, D.; Fukuda, T. Low Residual Doping Level in Homoepitaxially Grown ZnO Layers. *Appl. Phys. Lett.* **2008**, *92*, 141101.
- (45) Kim, Y.-J.; Lee, J.-H.; Yi, G.-C. Vertically Aligned ZnO Nanostructures Grown on Graphene Layers. *Appl. Phys. Lett.* **2009**, *95*, 213101.
-

- 
- (46) Kaidashev, E. M.; Lorenz, M.; Wenckstern, H. von; Rahm, A.; Semmelhack, H.-C.; Han, K.-H.; Benndorf, G.; Bundesmann, C.; Hochmuth, H.; Grundmann, M. High Electron Mobility of Epitaxial ZnO Thin Films on c-Plane Sapphire Grown by Multistep Pulsed-Laser Deposition. *Appl. Phys. Lett.* **2003**, *82*, 3901–3903.
- (47) Prellier, W.; Fouchet, A.; Mercey, B.; Simon, C.; Raveau, B. Laser Ablation of Co:ZnO Films Deposited from Zn and Co Metal Targets on (0001) Al<sub>2</sub>O<sub>3</sub> Substrates. *Appl. Phys. Lett.* **2003**, *82*, 3490–3492.
- (48) Ong, H. C.; Dai, J. Y.; Du, G. T. Studies of Electronic Structure of ZnO Grain Boundary and Its Proximity by Using Spatially Resolved Electron Energy Loss Spectroscopy. *Appl. Phys. Lett.* **2002**, *81*, 277–279.
- (49) Seto, J. Y. W. The Electrical Properties of Polycrystalline Silicon Films. *J. Appl. Phys.* **1975**, *46*, 5247–5254.
- (50) Thornton, J. A. Magnetron Sputtering: Basic Physics and Application to Cylindrical Magnetrons. *J. Vac. Sci. Technol.* **1978**, *15*, 171–177.
- (51) De Gryse, R.; Haemers, J.; Leroy, W. P.; Depla, D. Thirty Years of Rotatable Magnetrons. *Thin Solid Films* **2012**, *520*, 5833–5845.
- (52) Ellmer, K. Magnetron Sputtering of Transparent Conductive Zinc Oxide: Relation between the Sputtering Parameters and the Electronic Properties. *J. Phys. -Appl. Phys.* **2000**, *33*, R17–R32.
- (53) Savage, N. Resources: Mine, All Mine! *Nature* **2013**, *495*, S2–S3.
- (54) Nanda, K.; Maisels, A.; Kruis, F.; Fissan, H.; Stappert, S. Higher Surface Energy of Free Nanoparticles. *Phys. Rev. Lett.* **2003**, *91*.
- (55) Mostafa, S.; Behafarid, F.; Croy, J. R.; Ono, L. K.; Li, L.; Yang, J. C.; Frenkel, A. I.; Cuenya, B. R. Shape-Dependent Catalytic Properties of Pt Nanoparticles. *J. Am. Chem. Soc.* **2010**, *132*, 15714–15719.
- (56) Mayoral, A.; Barron, H.; Estrada-Salas, R.; Vazquez-Duran, A.; José-Yacamán, M. Nanoparticle Stability from the Nano to the Meso Interval. *Nanoscale* **2010**, *2*, 335–342.
- (57) Staykov, A.; Nishimi, T.; Yoshizawa, K.; Ishihara, T. Oxygen Activation on Nanometer-Size Gold Nanoparticles. *J. Phys. Chem. C* **2012**, *116*, 15992–16000.
- (58) Shang, C.; Liu, Z.-P. Origin and Activity of Gold Nanoparticles as Aerobic Oxidation Catalysts in Aqueous Solution. *J. Am. Chem. Soc.* **2011**, *133*, 9938–9947.
- (59) Liu, Y.; Tsunoyama, H.; Akita, T.; Xie, S.; Tsukuda, T. Aerobic Oxidation of Cyclohexane Catalyzed by Size-Controlled Au Clusters on Hydroxyapatite: Size Effect in the Sub-2 Nm Regime. *ACS Catal.* **2011**, *1*, 2–6.
- (60) Huang, W.; Ji, M.; Dong, C.-D.; Gu, X.; Wang, L.-M.; Gong, X. G.; Wang, L.-S. Relativistic Effects and the Unique Low-Symmetry Structures of Gold Nanoclusters. *ACS Nano* **2008**, *2*, 897–904.
- (61) Schwerdtfeger, P.; Boyd, P. D. W.; Brienne, S.; Burrell, A. K. Relativistic Effects in Gold Chemistry. 4. Gold(III) and gold(V) Compounds. *Inorg. Chem.* **1992**, *31*, 3411–3422.
- (62) Freestone, I.; Meeks, N.; Sax, M.; Higgitt, C. The Lycurgus Cup — A Roman Nanotechnology. *Gold Bull.* **2007**, *40*, 270–277.
-

- 
- (63) Mie, G. Beiträge Zur Optik Trüber Medien, Speziell Kolloidaler Metallösungen. *Ann. Phys.* **1908**, *330*, 377–445.
- (64) Link, S.; El-Sayed, M. A. Shape and Size Dependence of Radiative, Non-Radiative and Photothermal Properties of Gold Nanocrystals. *Int. Rev. Phys. Chem.* **2000**, *19*, 409–453.
- (65) Battie, Y.; Resano-Garcia, A.; Chaoui, N.; Zhang, Y.; Naciri, A. E. Extended Maxwell-Garnett-Mie Formulation Applied to Size Dispersion of Metallic Nanoparticles Embedded in Host Liquid Matrix. *J. Chem. Phys.* **2014**, *140*, 044705.
- (66) Quinten, M. Optical Constants of Gold and Silver Clusters in the Spectral Range between 1.5 eV and 4.5 eV. *Z. Für Phys. B Condens. Matter* **1996**, *101*, 211–217.
- (67) Alvarez, M. M.; Khoury, J. T.; Schaaff, T. G.; Shafigullin, M. N.; Vezmar, I.; Whetten, R. L. Optical Absorption Spectra of Nanocrystal Gold Molecules. *J. Phys. Chem. B* **1997**, *101*, 3706–3712.
- (68) Kreibig, P. D. U.; Vollmer, P. D. M. Theoretical Considerations. In *Optical Properties of Metal Clusters*; Springer Series in Materials Science; Springer Berlin Heidelberg, 1995; pp. 13–201.
- (69) Eustis, S.; El-Sayed, M. A. Why Gold Nanoparticles Are More Precious than Pretty Gold: Noble Metal Surface Plasmon Resonance and Its Enhancement of the Radiative and Nonradiative Properties of Nanocrystals of Different Shapes. *Chem. Soc. Rev.* **2006**, *35*, 209.
- (70) Yoshino, T.; Takanezawa, S.; Ohmori, T.; Masuda, H. Preparation of ZnO/Au Nanocomposite Thin Films by Electrodeposition. *Jpn. J. Appl. Phys. Part 2-Lett.* **1996**, *35*, L1512–L1514.
- (71) Pal, U.; Aguila, E.; Vazquez, O.; Koshizaki, N.; Sasaki, T.; Terauchi, S. Synthesis and Characterization of Au/ZnO Nanocomposites. *Mod. Phys. Lett. B* **2001**, *15*, 679–682.
- (72) Pal, U.; Almanza, E. A.; Cuchillo, O. V.; Koshizaki, N.; Sasaki, T.; Terauchi, S. Preparation of Au/ZnO Nanocomposites by Radio Frequency Co-Sputtering. *Sol. Energy Mater. Sol. Cells* **2001**, *70*, 363–368.
- (73) Pal, U.; García-Serrano, J.; Casarrubias-Segura, G.; Koshizaki, N.; Sasaki, T.; Terauchi, S. Structure and Optical Properties of M/ZnO (M=Au, Cu, Pt) Nanocomposites. *Sol. Energy Mater. Sol. Cells* **2004**, *81*, 339–348.
- (74) Bajaj, G.; Soni, R. K. Nanocomposite ZnO/Au Formation by Pulsed Laser Irradiation. *Appl. Surf. Sci.* **2010**, *256*, 6399–6402.
- (75) Han, Z.; Wei, L.; Zhang, Z.; Zhang, X.; Pan, H.; Chen, J. Visible-Light Photocatalytic Application of Hierarchical Au-ZnO Flower-Rod Heterostructures via Surface Plasmon Resonance. *Plasmonics* **2013**, *8*, 1193–1202.
- (76) Li, Y.; Zhang, B.-P.; Zhao, J.-X. Enhanced Photocatalytic Performance of Au–Ag Alloy Modified ZnO Nanocomposite Films. *J. Alloys Compd.* **2014**, *586*, 663–668.
- (77) Ali, H.; Iliadis, A. *Au/Zno-nanocomposite/(100)Si N-P Heterojunction Diodes for Gas Sensors*; Ieee: New York, 2007.
- (78) Della Gaspera, E.; Guglielmi, M.; Martucci, A.; Giancaterini, L.; Cantalini, C. Enhanced Optical and Electrical Gas Sensing Response of Sol–gel Based NiO–Au
-

- 
- and ZnO–Au Nanostructured Thin Films. *Sens. Actuators B Chem.* **2012**, *164*, 54–63.
- (79) Della Gaspera, E.; Martucci, A.; Post, M. ZnO–NiO Thin Films Containing Au Nanoparticles for CO Optical Sensing. *Sens. Lett.* **2011**, *9*, 600–604.
- (80) Della Gaspera, E.; Guglielmi, M.; Perotto, G.; Agnoli, S.; Granozzi, G.; Post, M. L.; Martucci, A. CO Optical Sensing Properties of Nanocrystalline ZnO–Au Films: Effect of Doping with Transition Metal Ions. *Sens. Actuators B-Chem.* **2012**, *161*, 675–683.
- (81) Argibay, N.; Prasad, S. V.; Goeke, R. S.; Dugger, M. T.; Michael, J. R. Wear Resistant Electrically Conductive Au–ZnO Nanocomposite Coatings Synthesized by E-Beam Evaporation. *Wear* **2013**, *302*, 955–962.
- (82) Argibay, N.; Goeke, R. S.; Dugger, M. T.; Rodriguez, M. A.; Michael, J. R.; Prasad, S. V. Electrical Resistivity of Au–ZnO Nanocomposite Films. *J. Appl. Phys.* **2013**, *113*, 143712.
- (83) Schoepfner, R. L.; Bahr, D. F.; Jin, H.; Goeke, R. S.; Moody, N. R.; Prasad, S. V. Wear Behavior of Au–ZnO Nanocomposite Films for Electrical Contacts. *J. Mater. Sci.* **2014**, *49*, 6039–6047.
- (84) Sun, L.; Zhao, D.; Ding, M.; Zhao, H.; Zhang, Z.; Li, B.; Shen, D. A White-Emitting ZnO–Au Nanocomposite and Its SERS Applications. *Appl. Surf. Sci.* **2012**, *258*, 7813–7819.
- (85) Mishra, Y. K.; Mohapatra, S.; Singhal, R.; Avasthi, D. K.; Agarwal, D. C.; Ogale, S. B. Au–ZnO: A Tunable Localized Surface Plasmonic Nanocomposite. *Appl. Phys. Lett.* **2008**, *92*, 043107.
- (86) Harsha, K. S. *Principles of Vapor Deposition of Thin Films*; Elsevier, 2005.
- (87) Ohring, M. *The Materials Science of Thin Films*; Academic Press: Boston, 1992.
- (88) Bunshah, R. F. *Handbook of Deposition Technologies for Films and Coatings Science, Technology, and Applications*; Noyes Publications: Park Ridge, N.J., 1994.
- (89) Al Kahlout, A.; Al Dahoudi, N.; Heusing, S.; Moh, K.; Karos, R.; de Oliveira, P. W. Structural, Electrical and Optical Properties of Aluminum Doped Zinc Oxide Spin Coated Films Made Using Different Coating Sols. *Nanosci. Nanotechnol. Lett.* **2014**, *6*, 37–43.
- (90) Uchida, S.; Sameshima, S.; Hirata, Y. Processing of Y-Doped Ceria Film by Doctor Blade Method. *J. Ceram. Soc. Jpn.* **2001**, *109*, 100–105.
- (91) Yang, Z.; Xu, Q.; Li, C. Self-Assembly of Large Scale and High-Quality Colloidal Particle Films by Spin-Coating. In *Materials Processing Technology, Pts 1-3*; Liu, X. H.; Jiang, Z.; Han, J. T., Eds.; Trans Tech Publications Ltd: Stafa-Zurich, 2012; Vol. 418-420, pp. 876–879.
- (92) Yang, H.; Jiang, P. Large-Scale Colloidal Self-Assembly by Doctor Blade Coating. *Langmuir* **2010**, *26*, 13173–13182.
- (93) Sigmund, P. Theory of Sputtering. I. Sputtering Yield of Amorphous and Polycrystalline Targets. *Phys. Rev.* **1969**, *184*, 383.
- (94) Thompson, M. W. II. The Energy Spectrum of Ejected Atoms during the High Energy Sputtering of Gold. *Philos. Mag.* **1968**, *18*, 377–414.
-

- 
- (95) Wasa, K. Sputtering Phenomena. In *Handbook of Sputter Deposition Technology*; Elsevier, 2012; pp. 76–144.
- (96) Sheridan, J., T.E.; Goree, J. . Analytic Expression for the Electric Potential in the Plasma Sheath. *IEEE Trans. Plasma Sci.* **1989**, *17*, 884–888.
- (97) Anders, A. Fundamentals of Pulsed Plasmas for Materials Processing. *Surf. Coat. Technol.* **2004**, *183*, 301–311.
- (98) Anders, A.; Andersson, J.; Ehasarian, A. High Power Impulse Magnetron Sputtering: Current-Voltage-Time Characteristics Indicate the Onset of Sustained Self-Sputtering. *J. Appl. Phys.* **2007**, *102*, 113303.
- (99) Robertson, S. Sheaths in Laboratory and Space Plasmas. *Plasma Phys. Control. Fusion* **2013**, *55*, 093001.
- (100) Ellmer, K.; Welzel, T. Reactive Magnetron Sputtering of Transparent Conductive Oxide Thin Films: Role of Energetic Particle (ion) Bombardment. *J. Mater. Res.* **2012**, *27*, 765–779.
- (101) Lieberman, M. A.; Lichtenberg, A. J. *Principles of Plasma Discharges and Materials Processing*; John Wiley & Sons, Inc., 2005.
- (102) Eckstein, D. W. *Computer Simulation of Ion-Solid Interactions*; Springer Series in Materials Science; Springer Berlin Heidelberg, 1991.
- (103) Yamamura, Y.; Tawara, H. Energy Dependence of Ion-Induced Sputtering Yields from Monatomic Solids at Normal Incidence. *At. Data Nucl. Data Tables* **1996**, *62*, 149–253.
- (104) Depla, D.; Mahieu, S.; Greene, J. E. Chapter 5 - Sputter Deposition Processes. In *Handbook of Deposition Technologies for Films and Coatings (Third Edition)*; Martin, P. M., Ed.; William Andrew Publishing: Boston, 2010; pp. 253–296.
- (105) Phelps, A. V.; Petrovic, Z. L. Cold-Cathode Discharges and Breakdown in Argon: Surface and Gas Phase Production of Secondary Electrons. *Plasma Sources Sci. Technol.* **1999**, *8*, R21.
- (106) Oechsner, H. Electron Yields from Clean Polycrystalline Metal Surfaces by Noble-Gas-Ion Bombardment at Energies around 1 keV. *Phys. Rev. B* **1978**, *17*, 1052–1056.
- (107) Depla, D.; Buyle, G.; Haemers, J.; De Gryse, R. Discharge Voltage Measurements during Magnetron Sputtering. *Surf. Coat. Technol.* **2006**, *200*, 4329–4338.
- (108) Depla, D.; Heirwegh, S.; Mahieu, S.; Haemers, J.; Gryse, R. D. Understanding the Discharge Voltage Behavior during Reactive Sputtering of Oxides. *J. Appl. Phys.* **2007**, *101*, 013301.
- (109) Depla, D.; Haemers, J.; De Gryse, R. Discharge Voltage Measurements during Reactive Sputtering of Oxides. *Thin Solid Films* **2006**, *515*, 468–471.
- (110) Safi, I. Recent Aspects Concerning DC Reactive Magnetron Sputtering of Thin Films: A Review. *Surf. Coat. Technol.* **2000**, *127*, 203–218.
- (111) Thornton, J. A. High Rate Thick Film Growth. *Annu. Rev. Mater. Sci.* **1977**, *7*, 239–260.

- 
- (112) Thornton, J. A. Influence of Apparatus Geometry and Deposition Conditions on the Structure and Topography of Thick Sputtered Coatings. *J. Vac. Sci. Technol.* **1974**, *11*, 666–670.
- (113) Barna, P. B.; Adamik, M. Fundamental Structure Forming Phenomena of Polycrystalline Films and the Structure Zone Models. *Thin Solid Films* **1998**, *317*, 27–33.
- (114) Barna, P. B.; Adamik, M. Growth Mechanisms of Polycrystalline Thin Films. *Sci. Technol. Thin Films* **1995**, 1–28.
- (115) Messier, R. Revised Structure Zone Model for Thin Film Physical Structure. *J. Vac. Sci. Technol. Vac. Surf. Films* **1984**, *2*, 500.
- (116) Anders, A. A Structure Zone Diagram Including Plasma-Based Deposition and Ion Etching. *Thin Solid Films* **2010**, *518*, 4087–4090.
- (117) Horwat, D.; Billard, A. Effects of Substrate Position and Oxygen Gas Flow Rate on the Properties of ZnO: Al Films Prepared by Reactive Co-Sputtering. *Thin Solid Films* **2007**, *515*, 5444–5448.
- (118) Graef, M. D.; McHenry, M. E. *Structure of Materials: An Introduction to Crystallography, Diffraction and Symmetry*; Cambridge University Press, 2007.
- (119) Pecharsky, V. K.; Zavalij, P. Y. *Fundamentals of Powder Diffraction and Structural Characterization of Materials*; Springer: New York, 2005.
- (120) Detavernier, C.; Özcan, A. S.; Jordan-Sweet, J.; Stach, E. A.; Tersoff, J.; Ross, F. M.; Lavoie, C. An off-Normal Fibre-like Texture in Thin Films on Single-Crystal Substrates. *Nature* **2003**, *426*, 641–645.
- (121) Wenk, H.-R.; Houtte, P. V. Texture and Anisotropy. *Rep. Prog. Phys.* **2004**, *67*, 1367.
- (122) Adamik, M.; Barna, P. B.; Tomov, I. Correlation between Texture and Average Grain Size in Polycrystalline Ag Thin Films. *Thin Solid Films* **2000**, *359*, 33–38.
- (123) Williams, D. B.; Carter, C. B. *Transmission Electron Microscopy a Textbook for Materials Science*; Springer: New York, 2009.
- (124) Watts, J. F.; Wolstenholme, J. *An Introduction to Surface Analysis by XPS and AES*; Wiley-Interscience: Hoboken, NJ, 2005.
- (125) Würth, C.; Grabolle, M.; Pauli, J.; Spieles, M.; Resch-Genger, U. Relative and Absolute Determination of Fluorescence Quantum Yields of Transparent Samples. *Nat. Protoc.* **2013**, *8*, 1535–1550.
- (126) Abay, B.; Güder, H. S.; Efeuglu, H.; Yogurtçu, Y. K. Urbach-Martienssen's Tail in Layered Ternary Semiconductor T L GaS 2. *Turk J Phys* **2001**, *25*, 543–549.
- (127) Chichibu, S.; Mizutani, T.; Shioda, T.; Nakanishi, H.; Deguchi, T.; Azuhata, T.; Sota, T.; Nakamura, S. Urbach–Martienssen Tails in a Wurtzite GaN Epilayer. *Appl. Phys. Lett.* **1997**, *70*, 3440.
- (128) Rai, R. C. Analysis of the Urbach Tails in Absorption Spectra of Undoped ZnO Thin Films. *J. Appl. Phys.* **2013**, *113*, 153508.
- (129) Rakhshani, A. E. Study of Urbach Tail, Bandgap Energy and Grain-Boundary Characteristics in CdS by Modulated Photocurrent Spectroscopy. *J. Phys. Condens. Matter* **2000**, *12*, 4391.
-

- 
- (130) Eom, S.-H. E.; Yu, Y.-M.; Choi, Y. D. Optical Absorption Spectra in Zn<sub>0.93</sub>Mn<sub>0.07</sub>Se Epilayers. *Journal of the Korean Physical Society*. 2005, pp. 508–511.
- (131) Fujiwara, H. Principles of Spectroscopic Ellipsometry. In *Spectroscopic Ellipsometry*; John Wiley & Sons, Ltd, 2007; pp. 81–146.
- (132) Forouhi, A. R.; Bloomer, I. Optical Dispersion Relations for Amorphous Semiconductors and Amorphous Dielectrics. *Phys. Rev. B* **1986**, *34*, 7018–7026.
- (133) Forouhi, A. R.; Bloomer, I. Optical Properties of Crystalline Semiconductors and Dielectrics. *Phys. Rev. B* **1988**, *38*, 1865–1874.
- (134) Özgür, U.; Alivov, Y. I.; Liu, C.; Teke, A.; Reshchikov, M. A.; Doğan, S.; Avrutin, V.; Cho, S.-J.; Morkoç, H. A Comprehensive Review of ZnO Materials and Devices. *J. Appl. Phys.* **2005**, *98*, 041301.
- (135) Horwat, D.; Pierson, J. F.; Billard, A. Magnetron Sputtering of NASICON (Na<sub>3</sub>Zr<sub>2</sub>Si<sub>2</sub>P<sub>0</sub>12) Thin Films: Part II: A Novel Approach. *Surf. Coat. Technol.* **2007**, *201*, 7060–7065.
- (136) Jullien, M.; Horwat, D.; Manzeh, F.; Escobar Galindo, R.; Bauer, P.; Pierson, J. F.; Endrino, J. L. Influence of the Nanoscale Structural Features on the Properties and Electronic Structure of Al-Doped ZnO Thin Films: An X-Ray Absorption Study. *Sol. Energy Mater. Sol. Cells* **2011**, *95*, 2341–2346.
- (137) Horwat, D.; Billard, A. Effects of Substrate Position and Oxygen Gas Flow Rate on the Properties of ZnO: Al Films Prepared by Reactive Co-Sputtering. *Thin Solid Films* **2007**, *515*, 5444–5448.
- (138) Klug, H. P.; Alexander, L. E. *X-Ray Diffraction Procedures for Polycrystalline and Amorphous Materials*; Wiley: New York, 1974.
- (139) Jogai, B. Effect of in-Plane Biaxial Strains on the Band Structure of Wurtzite GaN. *Phys. Rev. B* **1998**, *57*, 2382–2386.
- (140) Menon, R.; Gupta, V.; Tan, H. H.; Sreenivas, K.; Jagadish, C. Origin of Stress in Radio Frequency Magnetron Sputtered Zinc Oxide Thin Films. *J. Appl. Phys.* **2011**, *109*, 064905.
- (141) Vinnichenko, M.; Shevchenko, N.; Rogozin, A.; Groetzschel, R.; Muecklich, A.; Kolitsch, A.; Moeller, W. Structure and Dielectric Function of Two- and Single-Domain ZnO Epitaxial Films. *J. Appl. Phys.* **2007**, *102*, 113505.
- (142) Ruthe, K. C.; Cohen, D. J.; Barnett, S. A. Low Temperature Epitaxy of Reactively Sputtered ZnO on Sapphire. *J. Vac. Sci. Technol. A* **2004**, *22*, 2446–2452.
- (143) Perrière, J.; Millon, E.; Seiler, W.; Boulmer-Leborgne, C.; Craciun, V.; Albert, O.; Loulergue, J. C.; Etchepare, J. Comparison between ZnO Films Grown by Femtosecond and Nanosecond Laser Ablation. *J. Appl. Phys.* **2002**, *91*, 690–696.
- (144) Narayan, J.; Dovidenko, K.; Sharma, A. K.; Oktyabrsky, S. Defects and Interfaces in Epitaxial ZnO/ $\alpha$ -Al<sub>2</sub>O<sub>3</sub> and AlN/ZnO/ $\alpha$ -Al<sub>2</sub>O<sub>3</sub> Heterostructures. *J. Appl. Phys.* **1998**, *84*, 2597–2601.
- (145) Vispute, R. D.; Talyansky, V.; Trajanovic, Z.; Choopun, S.; Downes, M.; Sharma, R. P.; Venkatesan, T.; Woods, M. C.; Lareau, R. T.; Jones, K. A.; et al. High Quality Crystalline ZnO Buffer Layers on Sapphire (001) by Pulsed Laser Deposition for III–V Nitrides. *Appl. Phys. Lett.* **1997**, *70*, 2735–2737.
-

- 
- (146) Millon, E.; Albert, O.; Loulergue, J. C.; Etchepare, J.; Hulin, D.; Seiler, W.; Perrière, J. Growth of Heteroepitaxial ZnO Thin Films by Femtosecond Pulsed-Laser Deposition. *J. Appl. Phys.* **2000**, *88*, 6937–6939.
- (147) Depla, D.; Li, X. Y.; Mahieu, S.; Gryse, R. D. Determination of the Effective Electron Emission Yields of Compound Materials. *J. Phys. Appl. Phys.* **2008**, *41*, 202003.
- (148) Alvi, N. ul H.; Hussain, S.; Jensen, J.; Nur, O.; Willander, M. Influence of Helium-Ion Bombardment on the Optical Properties of ZnO Nanorods/p-GaN Light-Emitting Diodes. *Nanoscale Res. Lett.* **2011**, *6*, 628.
- (149) Alvi, N. H.; Hasan, K. ul; Nur, O.; Willander, M. The Origin of the Red Emission in N-ZnO Nanotubes/p-GaN White Light Emitting Diodes. *Nanoscale Res. Lett.* **2011**, *6*, 130.
- (150) Tam, K. H.; Cheung, C. K.; Leung, Y. H.; Djurisić, A. B.; Ling, C. C.; Beling, C. D.; Fung, S.; Kwok, W. M.; Chan, W. K.; Phillips, D. L.; et al. Defects in ZnO Nanorods Prepared by a Hydrothermal Method. *J. Phys. Chem. B* **2006**, *110*, 20865–20871.
- (151) GOMI, M.; OOHIRA, N.; OZAKI, K.; KOYANO, M. Photoluminescent and Structural Properties of Precipitated ZnO Fine Particles. *Jpn. J. Appl. Phys.* **2003**, *42*, 481–485.
- (152) Meyer, B. K.; Alves, H.; Hofmann, D. M.; Kriegseis, W.; Forster, D.; Bertram, F.; Christen, J.; Hoffmann, A.; Straßburg, M.; Dworzak, M.; et al. Bound Exciton and Donor–acceptor Pair Recombinations in ZnO. *Phys. Status Solidi B* **2004**, *241*, 231–260.
- (153) Meyer, B.; Sann, J.; Lautenschläger, S.; Wagner, M.; Hoffmann, A. Ionized and Neutral Donor-Bound Excitons in ZnO. *Phys. Rev. B* **2007**, *76*.
- (154) Morkoç, H.; Özgür, U. *Zinc Oxide: Fundamentals, Materials and Device Technology*; Wiley-VCH: Weinheim, 2009.
- (155) Janotti, A.; Van de Walle, C. G. Native Point Defects in ZnO. *Phys. Rev. B* **2007**, *76*, 165202.
- (156) Kim, Y.-S.; Park, C. Rich Variety of Defects in ZnO via an Attractive Interaction between O Vacancies and Zn Interstitials: Origin of N-Type Doping. *Phys. Rev. Lett.* **2009**, *102*.
- (157) Kim, D.-H.; Lee, G.-W.; Kim, Y.-C. Interaction of Zinc Interstitial with Oxygen Vacancy in Zinc Oxide: An Origin of N-Type Doping. *Solid State Commun.* **2012**, *152*, 1711–1714.
- (158) Janotti, A.; Van de Walle, C. G. Oxygen Vacancies in ZnO. *Appl. Phys. Lett.* **2005**, *87*, 122102.
- (159) Erhart, P.; Klein, A.; Albe, K. First-Principles Study of the Structure and Stability of Oxygen Defects in Zinc Oxide. *Phys. Rev. B* **2005**, *72*.
- (160) Mahieu, S.; Depla, D. Correlation between Electron and Negative O<sup>-</sup> Ion Emission during Reactive Sputtering of Oxides. *Appl. Phys. Lett.* **2007**, *90*, 121117.
- (161) Mahieu, S.; Leroy, W. P.; Aeken, K. V.; Depla, D. Modeling the Flux of High Energy Negative Ions during Reactive Magnetron Sputtering. *J. Appl. Phys.* **2009**, *106*, 093302.

- 
- (162) Welzel, T.; Ellmer, K. The Influence of the Target Age on Laterally Resolved Ion Distributions in Reactive Planar Magnetron Sputtering. *Surf. Coat. Technol.* **2011**, *205, Supplement 2*, S294–S298.
- (163) Ziegler, J. M.; Ziegler, M. D.; Biersack, J. P. *Monte Carlo Code SRIM-2008.04*; 2008.
- (164) Butkhuzi, T. V.; Bureyev, A. V.; Georgobiani, A. N.; Kekelidze, N. P.; Khulordava, T. G. Optical and Electrical Properties of Radical Beam Gettering Epitaxy Grown N- and P-Type ZnO Single Crystals. *J. Cryst. Growth* **1992**, *117*, 366–369.
- (165) Kim, Y.-S.; Park, C. Rich Variety of Defects in ZnO via an Attractive Interaction between O Vacancies and Zn Interstitials: Origin of N-Type Doping. *Phys. Rev. Lett.* **2009**, *102*.
- (166) Zeng, H.; Duan, G.; Li, Y.; Yang, S.; Xu, X.; Cai, W. Blue Luminescence of ZnO Nanoparticles Based on Non-Equilibrium Processes: Defect Origins and Emission Controls. *Adv. Funct. Mater.* **2010**, *20*, 561–572.
- (167) Lorenz, K.; Alves, E.; Wendler, E.; Bilani, O.; Wesch, W.; Hayes, M. Damage Formation and Annealing at Low Temperatures in Ion Implanted ZnO. *Appl. Phys. Lett.* **2005**, *87*, 191904.
- (168) Washington, P. L.; Ong, H. C.; Dai, J. Y.; Chang, R. P. H. Determination of the Optical Constants of Zinc Oxide Thin Films by Spectroscopic Ellipsometry. *Appl. Phys. Lett.* **1998**, *72*, 3261.
- (169) Siraj, K.; Javaid, K.; Pedarnig, J. D.; Bodea, M. A.; Naseem, S. Electron Beam Induced Nanostructures and Band Gap Tuning of ZnO Thin Films. *J. Alloys Compd.* **2013**, *563*, 280–284.
- (170) Yuste, M.; Galindo, R. E.; Caretti, I.; Torres, R.; Sánchez, O. Influence of the Oxygen Partial Pressure and Post-Deposition Annealing on the Structure and Optical Properties of ZnO Films Grown by Dc Magnetron Sputtering at Room Temperature. *J. Phys. Appl. Phys.* **2012**, *45*, 025303.
- (171) Serdobintsev, A. A.; Veselov, A. G.; Kiryasova, O. A. Properties of Zinc Oxide Films Synthesized in Low-Temperature Plasma Discharge under Conditions of Bombardment with Plasma Components. *Semiconductors* **2008**, *42*, 486–489.
- (172) Sernelius, B. E.; Berggren, K.-F.; Jin, Z.-C.; Hamberg, I.; Granqvist, C. G. Band-Gap Tailoring of ZnO by Means of Heavy Al Doping. *Phys. Rev. B* **1988**, *37*, 10244–10248.
- (173) Krajewski, T. A.; Dybko, K.; Luka, G.; Wachnicki, L.; Witkowski, B. S.; Duzynska, A.; Kopalko, K.; Lusakowska, E.; Kowalski, B. J.; Godlewski, M.; et al. Electrical and Optical Properties of Zinc Oxide Layers Grown by the Low-Temperature Atomic Layer Deposition Technique. *Phys. Status Solidi B* **2010**, *247*, 1653–1657.
- (174) Mazilu, M.; Tigau, N.; Musat, V. Optical Properties of Undoped and Al-Doped ZnO Nanostructures Grown from Aqueous Solution on Glass Substrate. *Opt. Mater.* **2012**, *34*, 1833–1838.
- (175) Welzel, T.; Naumov, S.; Ellmer, K. Ion Distribution Measurements to Probe Target and Plasma Processes in Electronegative Magnetron Discharges. I. Negative Ions. *J. Appl. Phys.* **2011**, *109*, 073302.
-

- 
- (176) Depla, D.; De Gryse, R. Influence of Oxygen Addition on the Target Voltage during Reactive Sputtering of Aluminium. *Plasma Sources Sci. Technol.* **2001**, *10*, 547.
- (177) Chamorro, W.; Horwat, D.; Pigeat, P.; Miska, P.; Migot, S.; Soldera, F.; Boulet, P.; Mücklich, F. Near-Room Temperature Single-Domain Epitaxy of Reactively Sputtered ZnO Films. *J. Phys. Appl. Phys.* **2013**, *46*, 235107.
- (178) Can, M. M.; Ismat Shah, S.; Doty, M. F.; Haughn, C. R.; Firat, T. Electrical and Optical Properties of Point Defects in ZnO Thin Films. *J. Phys. Appl. Phys.* **2012**, *45*, 195104.
- (179) Hai-Bo, F.; Shao-Yan, Y.; Pan-Feng, Z.; Hong-Yuan, W.; Xiang-Lin, L.; Chun-Mei, J.; Qin-Sheng, Z.; Yong-Hai, C.; Zhan-Guo, W. Investigation of Oxygen Vacancy and Interstitial Oxygen Defects in ZnO Films by Photoluminescence and X-Ray Photoelectron Spectroscopy. *Chin. Phys. Lett.* **2007**, *24*, 2108.
- (180) Kosacki, I.; Anderson, H. U. Microstructure—Property Relationships in Nanocrystalline Oxide Thin Films. *Ionics* **2000**, *6*, 294–311.
- (181) Urbach, F. The Long-Wavelength Edge of Photographic Sensitivity and of the Electronic Absorption of Solids. *Phys. Rev.* **1953**, *92*, 1324–1324.
- (182) Chichibu, S.; Mizutani, T.; Shioda, T.; Nakanishi, H.; Deguchi, T.; Azuhata, T.; Sota, T.; Nakamura, S. Urbach–Martienssen Tails in a Wurtzite GaN Epilayer. *Appl. Phys. Lett.* **1997**, *70*, 3440.
- (183) Dow, J. D.; Redfield, D. Electroabsorption in Semiconductors: The Excitonic Absorption Edge. *Phys. Rev. B* **1970**, *1*, 3358.
- (184) Rai, R. C. Analysis of the Urbach Tails in Absorption Spectra of Undoped ZnO Thin Films. *J. Appl. Phys.* **2013**, *113*, 153508.
- (185) Dow, J. D.; Redfield, D. Toward a Unified Theory of Urbach’s Rule and Exponential Absorption Edges. *Phys. Rev. B* **1972**, *5*, 594–610.
- (186) Ellmer, K.; Klein, A.; Rech, B. *Transparent Conductive Zinc Oxide Basics and Applications in Thin Film Solar Cells*; Springer: Berlin, 2008.
- (187) Tomlins, G. W.; Routbort, J. L.; Mason, T. O. Zinc Self-Diffusion, Electrical Properties, and Defect Structure of Undoped, Single Crystal Zinc Oxide. *J. Appl. Phys.* **2000**, *87*, 117.
- (188) Shan, F. K.; Liu, G. X.; Lee, W. J.; Shin, B. C. The Role of Oxygen Vacancies in Epitaxial-Deposited ZnO Thin Films. *J. Appl. Phys.* **2007**, *101*, 053106.
- (189) Lu, J. G.; Fujita, S.; Kawaharamura, T.; Nishinaka, H.; Kamada, Y.; Ohshima, T.; Ye, Z. Z.; Zeng, Y. J.; Zhang, Y. Z.; Zhu, L. P.; et al. Carrier Concentration Dependence of Band Gap Shift in N-Type ZnO:Al Films. *J. Appl. Phys.* **2007**, *101*, 083705.
- (190) Kim, K.-K.; Niki, S.; Oh, J.-Y.; Song, J.-O.; Seong, T.-Y.; Park, S.-J.; Fujita, S.; Kim, S.-W. High Electron Concentration and Mobility in Al-Doped N-ZnO Epilayer Achieved via Dopant Activation Using Rapid-Thermal Annealing. *J. Appl. Phys.* **2005**, *97*, 066103.
- (191) Neamen, D. *Semiconductor Physics And Devices*; McGraw-Hill Education, 2003.
- (192) Manasreh, O. *Semiconductor Heterojunctions and Nanostructures*; Nanoscience and Technology.
- (193) Mott, N. F.; Davis, E. A. *Electronic Processes in Non-Crystalline Materials*; Oxford University Press, 2012.
-

- 
- (194) Hamberg, I.; Granqvist, C. G.; Berggren, K.-F.; Sernelius, B. E.; Engström, L. Band-Gap Widening in Heavily Sn-Doped In<sub>2</sub>O<sub>3</sub>. *Phys. Rev. B* **1984**, *30*, 3240–3249.
- (195) Burstein, E. Anomalous Optical Absorption Limit in InSb. *Phys. Rev.* **1954**, *93*, 632–633.
- (196) Moss, T. S. The Interpretation of the Properties of Indium Antimonide. *Proc. Phys. Soc. Sect. B* **1954**, *67*, 775.
- (197) Klingshirn, C.; Hauschild, R.; Fallert, J.; Kalt, H. Room-Temperature Stimulated Emission of ZnO: Alternatives to Excitonic Lasing. *Phys. Rev. B* **2007**, *75*.
- (198) Chamorro, W.; Horwat, D.; Pigeat, P.; Miska, P.; Migot, S.; Soldera, F.; Boulet, P.; Mücklich, F. Near-Room Temperature Single-Domain Epitaxy of Reactively Sputtered ZnO Films. *J. Phys. Appl. Phys.* **2013**, *46*, 235107.
- (199) Xu, Y.; Yao, B.; Li, Y. F.; Ding, Z. H.; Li, J. C.; Wang, H. Z.; Zhang, Z. Z.; Zhang, L. G.; Zhao, H. F.; Shen, D. Z. Chemical States of Gold Doped in ZnO Films and Its Effect on Electrical and Optical Properties. *J. Alloys Compd.* **2014**, *585*, 479–484.
- (200) Hannon, J. B.; Klünker, C.; Giesen, M.; Ibach, H.; Bartelt, N. C.; Hamilton, J. C. Surface Self-Diffusion by Vacancy Motion: Island Ripening on Cu(001). *Phys. Rev. Lett.* **1997**, *79*, 2506–2509.
- (201) Mézin, A. Coating Internal Stress Measurement through the Curvature Method: A Geometry-Based Criterion Delimiting the Relevance of Stoney's Formula. *Surf. Coat. Technol.* **2006**, *200*, 5259–5267.
- (202) Morkoç, H.; Özgür, U. *Zinc Oxide: Fundamentals, Materials and Device Technology*; Wiley-VCH: Weinheim, 2009.
- (203) Voevodin, A. A.; Hu, J. J.; Fitz, T. A.; Zabinski, J. S. Tribological Properties of Adaptive Nanocomposite Coatings Made of Yttria Stabilized Zirconia and Gold. *Surf. Coat. Technol.* **2001**, *146–147*, 351–356.
- (204) Gu, Q. F.; Krauss, G.; Steurer, W.; Gramm, F.; Cervellino, A. Unexpected High Stiffness of Ag and Au Nanoparticles. *Phys. Rev. Lett.* **2008**, *100*, 045502.
- (205) Liu, X. J.; Zhou, Z. F.; Yang, L. W.; Li, J. W.; Xie, G. F.; Fu, S. Y.; Sun, C. Q. Correlation and Size Dependence of the Lattice Strain, Binding Energy, Elastic Modulus, and Thermal Stability for Au and Ag Nanostructures. *J. Appl. Phys.* **2011**, *109*, 074319.
- (206) Ouyang, G.; Zhu, W. G.; Sun, C. Q.; Zhu, Z. M.; Liao, S. Z. Atomistic Origin of Lattice Strain on Stiffness of Nanoparticles. *Phys. Chem. Chem. Phys.* **2010**, *12*, 1543–1549.
- (207) Gucci, L.; Beck, A.; Pászti, Z. Gold Catalysis: Effect of Particle Size on Reactivity towards Various Substrates. *Catal. Today* **2012**, *181*, 26–32.
- (208) Aldea, N.; Marginean, P.; Rednic, V.; Pintea, S.; Barz, B.; Gluhoi, A.; Nieuwenhuys, B. E.; Xie, Y.; Aldea, F.; Neumann, M. Crystalline and Electronic Structure of Gold Nanoclusters Determined by EXAFS, XRD and XPS Methods. *J. Optoelectron. Adv. Mater.* **2007**, *9*, 1555–1560.
- (209) Yazid, H.; Adnan, R.; Hamid, S. A.; Farrukh, M. A. Synthesis and Characterization of Gold Nanoparticles Supported on Zinc Oxide via the Deposition-Precipitation Method. *Turk J Chem* **2010**, *34*, 639–650.
- (210) Anderson, D. P.; Alvino, J. F.; Gentleman, A.; Qahtani, H. A.; Thomsen, L.; Polson, M. I. J.; Metha, G. F.; Golovko, V. B.; Andersson, G. G. Chemically-Synthesised,
-

- 
- Atomically-Precise Gold Clusters Deposited and Activated on Titania. *Phys. Chem. Chem. Phys.* **2013**, *15*, 3917.
- (211) Cuenya, B. R.; Baeck, S.-H.; Jaramillo, T. F.; McFarland, E. W. Size- and Support-Dependent Electronic and Catalytic Properties of Au<sup>0</sup>/Au<sup>3+</sup> Nanoparticles Synthesized from Block Copolymer Micelles. *J. Am. Chem. Soc.* **2003**, *125*, 12928–12934.
- (212) Thomas, T. D.; Weightman, P. Valence Electronic Structure of AuZn and AuMg Alloys Derived from a New Way of Analyzing Auger-Parameter Shifts. *Phys. Rev. B* **1986**, *33*, 5406.
- (213) Jiang, Z.; Zhang, W.; Jin, L.; Yang, X.; Xu, F.; Zhu, J.; Huang, W. Direct XPS Evidence for Charge Transfer from a Reduced Rutile TiO<sub>2</sub>(110) Surface to Au Clusters. *J. Phys. Chem. C* **2007**, *111*, 12434–12439.
- (214) Mason, M. G. Electronic Structure of Supported Small Metal Clusters. *Phys. Rev. B* **1983**, *27*, 748.
- (215) Hore, S.; Kaiser, G.; Hu, Y.-S.; Schulz, A.; Konuma, M.; Götz, G.; Sigle, W.; Verhoeven, A.; Maier, J. Carbonization of Polyethylene on Gold Oxide. *J. Mater. Chem.* **2008**, *18*, 5589.
- (216) Knecht, J.; Fischer, R.; Overhof, H.; Hensel, F. ESCA Study of Compounds of Gold in the Oxidation State –I. *J. Chem. Soc. Chem. Commun.* **1978**, 905–906.
- (217) Schmidbaur, H.; Mandl, J. R.; Wagner, F. E.; Vondel, D. F. V. de; Kelen, G. P. V. der. ESCA and Mössbauer Study of Compounds of Gold in the Oxidation States +I, +II, and +III. *J. Chem. Soc. Chem. Commun.* **1976**, 170–172.
- (218) Liu, Y.-L.; Fang, C.-Y.; Yu, C.-C.; Yang, T.-C.; Chen, H.-L. Controllable Localized Surface Plasmonic Resonance Phenomena in Reduced Gold Oxide Films. *Chem. Mater.* **2014**, *26*, 1799–1806.
- (219) Ono, L. K.; RoldanCuenya, B. Formation and Thermal Stability of Au<sub>2</sub>O<sub>3</sub> on Gold Nanoparticles: Size and Support Effects. *J. Phys. Chem. C* **2008**, *112*, 4676–4686.
- (220) Ip, K.; Thaler, G. T.; Yang, H.; Youn Han, S.; Li, Y.; Norton, D. P.; Pearton, S. J.; Jang, S.; Ren, F. Contacts to ZnO. *J. Cryst. Growth* **2006**, *287*, 149–156.
- (221) Bora, T.; Kyaw, H. H.; Sarkar, S.; Pal, S. K.; Dutta, J. Highly Efficient ZnO/Au Schottky Barrier Dye-Sensitized Solar Cells: Role of Gold Nanoparticles on the Charge-Transfer Process. *Beilstein J. Nanotechnol.* **2011**, *2*, 681–690.
- (222) Brillson, L. J.; Lu, Y. ZnO Schottky Barriers and Ohmic Contacts. *J. Appl. Phys.* **2011**, *109*, 121301.
- (223) Phala, N. S.; Klatt, G.; van Steen, E.; French, S. A.; Sokol, A. A.; Catlow, C. R. A. The Nature of the Oxidation States of Gold on ZnO. *Phys. Chem. Chem. Phys.* **2005**, *7*, 2440.
- (224) Koslowski, B.; Boyen, H.-G.; Wilderotter, C.; Kästle, G.; Ziemann, P.; Wahrenberg, R.; Oelhafen, P. Oxidation of Preferentially (1 1 1)-Oriented Au Films in an Oxygen Plasma Investigated by Scanning Tunneling Microscopy and Photoelectron Spectroscopy. *Surf. Sci.* **2001**, *475*, 1–10.
- (225) Szlachetko, J.; Sá, J.; Nachtegaal, M.; Hartfelder, U.; Dousse, J.-C.; Hoszowska, J.; Abreu Fernandes, D. L.; Shi, H.; Stampfl, C. Real Time Determination of the
-

- 
- Electronic Structure of Unstable Reaction Intermediates during Au<sub>2</sub>O<sub>3</sub> Reduction. *J. Phys. Chem. Lett.* **2014**, *5*, 80–84.
- (226) Tsai, H.; Hu, E.; Perng, K.; Chen, M.; Wu, J.-C.; Chang, Y.-S. Instability of Gold Oxide Au<sub>2</sub>O<sub>3</sub>. *Surf. Sci.* **2003**, *537*, L447–L450.
- (227) Kim, J. I.; Jung, D.-R.; Kim, J.; Nahm, C.; Byun, S.; Lee, S.; Park, B. Surface-plasmon-Coupled Photoluminescence from CdS Nanoparticles with Au Films. *Solid State Commun.* **2012**, *152*, 1767–1770.
- (228) Shi, H.; Asahi, R.; Stampfl, C. Properties of the Gold Oxides Au<sub>2</sub>O<sub>3</sub> and Au<sub>2</sub>O: First-Principles Investigation. *Phys. Rev. B* **2007**, *75*.
- (229) Kosacki, I.; Anderson, H. U. Microstructure—Property Relationships in Nanocrystalline Oxide Thin Films. *Ionics* **2000**, *6*, 294–311.
- (230) Mosquera, A. A.; Horwat, D.; Rashkovskiy, A.; Kovalev, A.; Miska, P.; Wainstein, D.; Albella, J. M.; Endrino, J. L. Exciton and Core-Level Electron Confinement Effects in Transparent ZnO Thin Films. *Sci. Rep.* **2013**, *3*.
- (231) Hövel, H.; Fritz, S.; Hilger, A.; Kreibig, U.; Vollmer, M. Width of Cluster Plasmon Resonances: Bulk Dielectric Functions and Chemical Interface Damping. *Phys. Rev. B* **1993**, *48*, 18178–18188.
- (232) Cottancin, E.; Celep, G.; Lermé, J.; Pellarin, M.; Huntzinger, J. R.; Vialle, J. L.; Broyer, M. Optical Properties of Noble Metal Clusters as a Function of the Size: Comparison between Experiments and a Semi-Quantal Theory. *Theor. Chem. Acc.* **2006**, *116*, 514–523.
- (233) Damen, T. C.; Porto, S. P. S.; Tell, B. Raman Effect in Zinc Oxide. *Phys. Rev.* **1966**, *142*, 570.
- (234) Sander, T.; Eisermann, S.; Meyer, B. K.; Klar, P. J. Raman Tensor Elements of Wurtzite ZnO. *Phys. Rev. B* **2012**, *85*.
- (235) Niaura, G.; Gaigalas, A. K.; Vilker, V. L. Surface-Enhanced Raman Spectroscopy of Phosphate Anions: Adsorption on Silver, Gold, and Copper Electrodes. *J. Phys. Chem. B* **1997**, *101*, 9250–9262.
- (236) Pireaux, J. J.; Liehr, M.; Thiry, P. A.; Delrue, J. P.; Caudano, R. Electron Spectroscopic Characterization of Oxygen Adsorption on Gold Surfaces: II. Production of Gold Oxide in Oxygen DC Reactive Sputtering. *Surf. Sci.* **1984**, *141*, 221–232.
- (237) Lin, K.-F.; Cheng, H.-M.; Hsu, H.-C.; Hsieh, W.-F. Band Gap Engineering and Spatial Confinement of Optical Phonon in ZnO Quantum Dots. *Appl. Phys. Lett.* **2006**, *88*, 263117.
- (238) Huang, Y.; Liu, M.; Li, Z.; Zeng, Y.; Liu, S. Raman Spectroscopy Study of ZnO-Based Ceramic Films Fabricated by Novel Sol-gel Process. *Mater. Sci. Eng. B* **2003**, *97*, 111–116.
- (239) Rumyantseva, A.; Kostcheev, S.; Adam, P.-M.; Gaponenko, S. V.; Vaschenko, S. V.; Kulakovich, O. S.; Ramanenka, A. A.; Guzatov, D. V.; Korbutyak, D.; Dzhagan, V.; et al. Nonresonant Surface-Enhanced Raman Scattering of ZnO Quantum Dots with Au and Ag Nanoparticles. *ACS Nano* **2013**, *7*, 3420–3426.
-

- 
- (240) Rajalakshmi, M.; Arora, A. K.; Bendre, B. S.; Mahamuni, S. Optical Phonon Confinement in Zinc Oxide Nanoparticles. *J. Appl. Phys.* **2000**, *87*, 2445.
- (241) Liu, K.; Sakurai, M.; Aono, M. ZnO-Based Ultraviolet Photodetectors. *Sensors* **2010**, *10*, 8604–8634.
- (242) Ryu, Y.; Lee, T.-S.; Lubguban, J. A.; White, H. W.; Kim, B.-J.; Park, Y.-S.; Youn, C.-J. Next Generation of Oxide Photonic Devices: ZnO-Based Ultraviolet Light Emitting Diodes. *Appl. Phys. Lett.* **2006**, *88*, 241108.
- (243) Guillet, T.; Brimont, C.; Valvin, P.; Gil, B.; Bretagnon, T.; Médard, F.; Mihailovic, M.; Zúñiga-Pérez, J.; Leroux, M.; Semond, F.; et al. Laser Emission with Excitonic Gain in a ZnO Planar Microcavity. *Appl. Phys. Lett.* **2011**, *98*, 211105.
- (244) Tsukazaki, A.; Kubota, M.; Ohtomo, A.; Onuma, T.; Ohtani, K.; Ohno, H.; Chichibu, S. F.; Kawasaki, M. Blue Light-Emitting Diode Based on ZnO. *Jpn. J. Appl. Phys.* **2005**, *44*, L643–L645.
- (245) Kumar, B.; Gong, H.; Chow, S. Y.; Tripathy, S.; Hua, Y. Photoluminescence and Multiphonon Resonant Raman Scattering in Low-Temperature Grown ZnO Nanostructures. *Appl. Phys. Lett.* **2006**, *89*, 071922.
- (246) Zhang, Y.; Li, X.; Ren, X. Effects of Localized Surface Plasmons on the Photoluminescence Properties of Au-Coated ZnO Films. *Opt. Express* **2009**, *17*, 8735–8740.
- (247) Ruiz Peralta, M. D. L.; Pal, U.; Zeferino, R. S. Photoluminescence (PL) Quenching and Enhanced Photocatalytic Activity of Au-Decorated ZnO Nanorods Fabricated through Microwave-Assisted Chemical Synthesis. *ACS Appl. Mater. Interfaces* **2012**, *4*, 4807–4816.
- (248) Saravanan, K.; Panigrahi, B. K.; Krishnan, R.; Nair, K. G. M. Surface Plasmon Enhanced Photoluminescence and Raman Scattering of Ultra Thin ZnO-Au Hybrid Nanoparticles. *J. Appl. Phys.* **2013**, *113*, 033512.
- (249) Zhang, N.; Tang, W.; Wang, P.; Zhang, X.; Zhao, Z. In Situ Enhancement of NBE Emission of Au–ZnO Composite Nanowires by SPR. *CrystEngComm* **2013**, *15*, 3301.
- (250) Keita, A.-S.; Naciri, A. E.; Delachat, F.; Carrada, M.; Ferblantier, G.; Slaoui, A. Spectroscopic Ellipsometry Investigation of the Optical Properties of Nanostructured Si/SiNx Films. *J. Appl. Phys.* **2010**, *107*, 093516.
- (251) Jepsen, P. U.; Fischer, B. M.; Thoman, A.; Helm, H.; Suh, J. Y.; Lopez, R.; Haglund, R. F. Metal-Insulator Phase Transition in a VO<sub>2</sub> Thin Film Observed with Terahertz Spectroscopy. *Phys. Rev. B* **2006**, *74*, 205103.

---

# Abstract

## **Microstructure, chemistry and optical properties of ZnO and ZnO-Au nanocomposite thin films grown by DC-reactive magnetron co-sputtering**

Composite materials can exhibit properties that none of the individual components show. Moreover, composites at the nanoscale can present new properties compared to the bulk state or to macro-composites due to confinement and quantum size effects. The semiconductor/metal nanocomposites are highly interesting due to their unique catalytic and optoelectronic properties and the possibility to tune them easily. This PhD work gives insight into the specific interactions and resulting physical properties occurring in ZnO and ZnO-Au nanocomposite films grown by reactive DC magnetron sputtering. The results can be summarized in two points:

First, it was possible to tune the microstructural and optical properties of ZnO. Epitaxial growth of ZnO onto sapphire was achieved for the first time in O<sub>2</sub>-rich conditions without thermal assistance. Also, a study of the optical properties highlights the close relationship between the bandgap energy ( $E_g$ ) and the defect chemistry in ZnO films. A model was proposed to explain the large scatter of the  $E_g$  values reported in the literature.

Second, the deep influence of the incorporation of gold into the ZnO matrix on important material properties was revealed. Moreover, the presence of donor (acceptor) defects in the matrix is found to give rise to the reduction (oxidation) of the Au nanoparticles.

This research work contributes to a better understanding of semiconductor/metal nanocomposites revealing the key role of the state of the semiconductor matrix.

**Keywords:** ZnO, reactive sputtering, epitaxial growth, nanocomposites, ZnO-Au, Localized surface plasmon resonance (LSPR).

---

# Zusammenfassung

## **Mikrostruktur, Chemie und optische Eigenschaften von ZnO- und ZnO-Au-Nanokompositdünnschichten hergestellt durch reaktives DC-Magnetron-Co-Sputtern**

Kompositmaterialien können Eigenschaften zeigen, die keine der individuellen Komponenten zeigt. Außerdem können Nanokomposite im Vergleich zu Materialien im Bulk-Zustand oder Makrokompositen der gleichen Komponenten aufgrund von Confinement und Quanteneffekten neue Eigenschaften zeigen. Halbleiter/Metall-Nanokomposite sind sehr interessant aufgrund ihrer einzigartigen katalytischen und optoelektronischen Eigenschaften. Diese Doktorarbeit gibt Einblick in die spezifischen Wechselwirkungen und die daraus resultierenden physikalischen Eigenschaften, die in durch reaktives DC-Magnetron-Sputtern hergestellten ZnO- und ZnO-Au-Nanokompositschichten auftreten. Die Ergebnisse lassen sich in zwei Punkten zusammenfassen:

Zum einen war es möglich die mikrostrukturellen und optischen Eigenschaften von ZnO-Schichten anzupassen. Epitaktisches Wachstum von ZnO auf Saphir wurde zum ersten Mal in O<sub>2</sub>-reichen Bedingungen ohne thermische Unterstützung erreicht. Außerdem zeigt eine Studie der optischen Eigenschaften die enge Beziehung zwischen der Bandlücke und der Defektchemie in ZnO-Schichten.

Zum anderen wurde der starke Einfluss des Zusatzes von Au in die ZnO-Matrix auf wichtige Materialeigenschaften aufgedeckt. Außerdem wurde gezeigt, dass die Anwesenheit von Donator(Akzeptor)-Defekten zur Reduktion (Oxidation) der Au Nanopartikel führt.

Diese Arbeit trägt zum besseren Verständnis von Halbleiter/Metall-Nanokompositen bei und unterstreicht dabei die Wichtigkeit des Zustandes der Halbleitermatrix.

**Stichworte:** ZnO, reaktives Sputtern, Epitaxiewachstum, Nanokomposite, ZnO-Au, lokalisierte Oberflächenplasmonenresonanz (LSPR).

---

# Résumé

## Microstructure, chimie et propriétés optiques de films minces ZnO et nanocomposites ZnO-Au synthétisés par pulvérisation cathodique magnétron réactive

Les matériaux composites peuvent présenter des propriétés qu'aucun des composants individuels ne présente. En outre, à l'échelle du nanomètre les nanocomposites peuvent présenter de nouvelles propriétés par rapport à l'état massif ou à des macrocomposites des mêmes composants en raison d'effets de confinement et d'effets quantiques liés à la taille. Les nanocomposites semi-conducteur/métal sont très intéressants en raison de leurs uniques propriétés catalytiques et opto-électroniques et la possibilité de les ajuster facilement.

Ce travail de thèse étudie les interactions spécifiques et les propriétés physiques qui se manifestent dans les films minces de ZnO et nanocomposites ZnO-Au synthétisés par pulvérisation magnétron réactive continue. Premièrement, il est observé qu'il est possible d'ajuster les propriétés microstructurales et optiques des couches de ZnO en réglant les paramètres expérimentaux. La croissance épitaxiale de ZnO sur saphir a été réalisée pour la première fois dans des conditions riches en oxygène sans assistance thermique. En outre, une étude des propriétés optiques met en évidence la relation étroite entre les propriétés optiques et de la chimie des défauts dans les couches minces de ZnO. Un modèle a été proposé pour expliquer la grande dispersion des valeurs de gap rencontrées dans la littérature.

Deuxièmement, il a été possible de révéler l'influence profonde de l'incorporation de l'or dans la matrice de ZnO sur des propriétés importantes dans des films nanocomposites. En outre, la présence de défauts donneurs (accepteurs) au sein de la matrice ZnO se permet de réduire (oxyder) les nanoparticules d'or. Ce travail de recherche contribue à une meilleure compréhension des nanocomposites semi-conducteurs/métal et révèle le rôle important de l'état de la matrice semi-conductrice et de la surface des particules pour les propriétés finales du matériau.

**Mots clés:** ZnO, pulverization cathodic reactive, croissance épitaxiale, nanocomposites, ZnO-Au, résonance des plasmons de surface localisés (LSPR).